# Parallelle optische interconnecties geïntegreerd met gedrukte schakelingen

# Parallel Optical Interconnections Integrated on a Printed Circuit Board

Geert Van Steenberge

Promotor: prof. dr. ir. P. Van Daele
Proefschrift ingediend tot het behalen van de graad van
Doctor in de Ingenieurswetenschappen: Elektrotechniek

Vakgroep Informatietechnologie
Voorzitter: prof. dr. ir. P. Lagasse
Faculteit Ingenieurswetenschappen
Academiejaar 2005 - 2006

ISBN 90-8578-098-5
NUR 959
Wettelijk depot: D/2006/10.500/56

Promotor:

Prof. dr. ir. P. Van Daele

Onderzoeksgroep TFCG Microsystems
Vakgroep Informatietechnologie
Technologiepark 914A
B-9052 Zwijnaarde

# Dankwoord

Vier jaar onderzoek leverde niet alleen de beoogde resultaten op, het schonk me ook meerdere boeiende ervaringen, die ik niet snel zal vergeten. De avond van het tot stand komen van de slagzin *TeF-Cee-Gee is okee olee olee* was zeer zeker een climax, het bezwarend beeldmateriaal achteraf, zeer zeker een anti-climax. Naast dit semi-professioneel randgebeuren zijn de verschillende hoogtepunten op professioneel gebied te danken aan een heel aantal personen.

In de eerste plaats bedank ik mijn promotor Peter Van Daele voor de technische ondersteuning en begeleiding vooral bij aanvang van mijn onderzoek, voor het vertrouwen, voor de kansen die ik heb gekregen, en voor de beschamende kerstman foto's uit Rovaniemi.

Andre Van Calster voor het beschikbaar stellen van de infrastructuur binnen de onderzoeksgroep, voor het verzorgen van de aangename werksfeer, voor het sponsoren van de BBQ's, en voor het integreren van *den optische kant* binnen TFCG.

Paul Lagasse voor het beschikbaar stellen van de infrastructuur binnen de vakgroep alsook de nodige kredieten via projectonderzoek.

Peter Geerinck voor het aanbrengen van optische lagen, voor het prepareren van SEM samples, en voor het werk rond vezel klieven. Steven Van Put voor het onderhouden van het contact met Optec, voor het ableren van golfgeleider bordjes, voor het klieven van vezels, en voor het structureren van allerlei andere samples. Nina Hendrickx en Erwin Bosman voor hun interesse en motivatie om dit onderzoek verder uit te bouwen.

Mijn bureaugenoten voor de discussies, om het draaien van al dan niet Studio Brussel, om wie de eerste pot koffie 's morgens zal zetten, om wat wel of niet stinkt, om de combinatie bejaarden en openbaar vervoer, om hoe belachelijk een gsm tune kan zijn, om het aantal smsjes iemand van zijn lief per minuut kan krijgen, om het verschil tussen een spare rib en een ribstuk, om al die andere levensbelangrijke vragen . . . Wim, ik zorg nog wel voor die grote groene riet-

plant, wedden dat ik beter doe dan Jonathan en Nadine? Tom, Ann, (ex-) bureaugenoten next door, spring gerust eens binnen. Alle andere technologen en designers, dankjewel voor die tussendoortjes.

Verder collega's van de Photonics onderzoeksgroep: Hendrik Sergeant voor de praktische hulp bij het opzetten van een eigen meetopstelling. Kris Naessens voor zijn input omtrent laser ablatie, en voor het ter beschikking stellen van zijn lens writing software. De bewoners van *den 39 zaliger* voor de leuke babbels tijdens het gependel naar *den 41*. Het TDC United gedeelte van *den 41*, voor al dat vlot scorend geweld, en voor het mooie gele shirt.

Collega's van TONA (VUB): in het bijzonder Hugo Thienpont voor zijn engagement in microphotonics. Heidi Ottevaere en Jürgen Van Erps voor ruwheids- en profielmetingen. Christof Debaes en Michael Vervaeke voor de vlotte samenwerking.

Verder een aantal mensen uit de industrie: Jan Watte (Tyco Electronics) voor de technische discussies en ondersteuning bij het opmeten van gekliefde vezel facetten. Jan Van Koestem en Danny Morlion (FCI 's Hertogenbosch) voor de technische discussies omtrent optische vezelconnectoren. Markus Riester (Motorola) for the technical discussions on structuring polymer layers. Reto Fries (PPC Electronic) for the technical discussions on how to handle and process thin glass foils.

Mijn beste vrienden inclusief hun partner . . . horen zeker thuis in dit VIP lijstje . . . der Jaan (de bibliothecaris), Galle (de want-to-be-a-manager-but-am-rather-michael-jackson), Wimmen (de ingenieur uit sector 7G), Hilde (de licentiate kunst geschiedenis alias boerinneke), Anneleen (de onderwijzeres alias stadsmadam), Brammen, Roeli, Vladdy, Duis, en al die anderen die ik graag meer zou zien.

Mama en papa, Karolien en Hans, omdat het deugd doet dat jullie er steeds voor me zijn, ook al heb ik weinig tijd voor onze *Buxus Sempervirens*, en zal het moeilijk zijn om ooit zelf met een hectare *Betula Pendula Fastigiata* te beginnen.

Mijn allerliefste Elsje, om aan die journalisten uit te leggen dat je om te doctoreren geen patiënten nodig hebt, om al die leuke momenten samen, omdat je niet tevreden bent met de woorden: ik jou ook.

Geert Van Steenberge
Sint-Amandsberg, augustus 2006

# Contents


**1 Introduction** **1**
1.1 Short distance interconnections . . . . . . . . . . . . . . . . . . . . . . 1
1.2 Box-to-box optical interconnections . . . . . . . . . . . . . . . . . . . . 4
1.3 In-box optical interconnections . . . . . . . . . . . . . . . . . . . . . . 4
1.3.1 Fiber based approaches . . . . . . . . . . . . . . . . . . . . . . 4
1.3.2 Waveguide based approaches . . . . . . . . . . . . . . . . . . . 6
1.3.3 Free-space based approaches . . . . . . . . . . . . . . . . . . . 7
1.4 Research context . . . . . . . . . . . . . . . . . . . . . . . . . . . . . . 7
1.5 Publications . . . . . . . . . . . . . . . . . . . . . . . . . . . . . . . . 9

**2 Optical waveguide materials** **17**
2.1 Introduction . . . . . . . . . . . . . . . . . . . . . . . . . . . . . . . . 17
2.2 Thin glass sheets . . . . . . . . . . . . . . . . . . . . . . . . . . . . . . 18
2.3 Polymers . . . . . . . . . . . . . . . . . . . . . . . . . . . . . . . . . . 19
2.3.1 Optical loss . . . . . . . . . . . . . . . . . . . . . . . . . . . . . 19
2.3.2 Environmental performance . . . . . . . . . . . . . . . . . . . 21
2.3.3 Compatibility with standard PCB manufacturing . . . . . . 21
2.3.4 Overview of novel optical polymers . . . . . . . . . . . . . . 22
2.4 Ormocer®s . . . . . . . . . . . . . . . . . . . . . . . . . . . . . . . . . 28
2.5 Truemode™ . . . . . . . . . . . . . . . . . . . . . . . . . . . . . . . . . 33
2.6 Conclusions . . . . . . . . . . . . . . . . . . . . . . . . . . . . . . . . 36

**3 Laser ablation** **41**
3.1 Laser set-up . . . . . . . . . . . . . . . . . . . . . . . . . . . . . . . . 41
3.1.1 Beam delivery unit . . . . . . . . . . . . . . . . . . . . . . . . . 41
3.1.2 Part mounting, motion, and control . . . . . . . . . . . . . . 44
3.2 Ablating polymers: some fundamentals and experimental results . 45
3.2.1 Ablation rate and ablation threshold . . . . . . . . . . . . . . 45
3.2.2 Ablative photodecomposition . . . . . . . . . . . . . . . . . . 47
3.2.3 Thermal ablation . . . . . . . . . . . . . . . . . . . . . . . . . . 49
3.2.4 Efficient ablation . . . . . . . . . . . . . . . . . . . . . . . . . . 52

3.2.5 Plume effects and debris . . . . . . . . . . . . . . . . . . . . . . 54
3.2.6 Surface quality . . . . . . . . . . . . . . . . . . . . . . . . . 59
3.2.7 Surface roughness . . . . . . . . . . . . . . . . . . . . . . . 61
3.2.8 Dynamic ablation . . . . . . . . . . . . . . . . . . . . . . . . 64
3.3 Ablating glass materials . . . . . . . . . . . . . . . . . . . . . . . 64
3.4 Conclusions . . . . . . . . . . . . . . . . . . . . . . . . . . . . . 69

**4 Planar waveguides 75**
4.1 Introduction . . . . . . . . . . . . . . . . . . . . . . . . . . . . . 75
4.2 Technology overview . . . . . . . . . . . . . . . . . . . . . . . . . 77
4.3 Fabrication . . . . . . . . . . . . . . . . . . . . . . . . . . . . . . 82
4.4 Characterization . . . . . . . . . . . . . . . . . . . . . . . . . . . 86
4.4.1 Surface roughness . . . . . . . . . . . . . . . . . . . . . . . 86
4.4.2 Measurement set-up . . . . . . . . . . . . . . . . . . . . . . 88
4.4.3 Waveguide propagation loss . . . . . . . . . . . . . . . . . . 90
4.4.4 Spectral attenuation . . . . . . . . . . . . . . . . . . . . . . 99
4.5 Single mode waveguides . . . . . . . . . . . . . . . . . . . . . . . 100
4.6 Conclusions . . . . . . . . . . . . . . . . . . . . . . . . . . . . . 102

**5 Coupling structures 107**
5.1 O/E coupling . . . . . . . . . . . . . . . . . . . . . . . . . . . . . 107
5.2 Embedded $45^o$ micromirrors . . . . . . . . . . . . . . . . . . . . 111
5.2.1 Technology overview . . . . . . . . . . . . . . . . . . . . . . 111
5.2.2 Fabrication . . . . . . . . . . . . . . . . . . . . . . . . . . . 113
5.2.3 Characterization . . . . . . . . . . . . . . . . . . . . . . . . 120
5.3 Laser ablated cavities for hybrid integration . . . . . . . . . . . . . 125
5.3.1 Inserts with in-plane optical functionality . . . . . . . . . . 125
5.3.2 Inserts with out-of-plane coupling optical functionality . . . 127
5.4 Accessing embedded optical layers . . . . . . . . . . . . . . . . . . 130
5.5 Conclusions . . . . . . . . . . . . . . . . . . . . . . . . . . . . . 132

**6 Board-to-board coupling interface 139**
6.1 Introduction . . . . . . . . . . . . . . . . . . . . . . . . . . . . . 139
6.2 Microlenses . . . . . . . . . . . . . . . . . . . . . . . . . . . . . . 140
6.2.1 Technology overview . . . . . . . . . . . . . . . . . . . . . . 140
6.2.2 Excimer laser ablation . . . . . . . . . . . . . . . . . . . . . 141
6.2.3 $CO_2$ laser polishing . . . . . . . . . . . . . . . . . . . . . . . 142
6.2.4 Characterization . . . . . . . . . . . . . . . . . . . . . . . . 145
6.3 MT compatible coupling . . . . . . . . . . . . . . . . . . . . . . . 146
6.3.1 Fabrication . . . . . . . . . . . . . . . . . . . . . . . . . . . 146
6.3.2 Misalignment tolerances . . . . . . . . . . . . . . . . . . . . 152
6.4 Conclusions . . . . . . . . . . . . . . . . . . . . . . . . . . . . . 153

**7 Fiber cleaving** **159**
7.1 Introduction . . . 159
7.2 Termination of optical fibers . . . 159
7.2.1 Using mechanical cleavers . . . 159
7.2.2 Using $CO_2$ lasers . . . 160
7.2.3 Using UV lasers . . . 161
7.3 Excimer laser ablation of glass fiber . . . 161
7.4 Design of the fiber holder . . . 162
7.5 Experimental results . . . 164
7.5.1 Single fiber . . . 164
7.5.2 Fiber ribbon . . . 166
7.6 Characterization . . . 166
7.7 Termination of PCB embedded optical fibers . . . 170
7.8 $CO_2$ laser polishing and splicing of fibers . . . 170
7.9 Conclusions . . . 172

**8 Conclusions and outlook** **177**
8.1 Main achievements . . . 177
8.2 Future work . . . 178

# List of Tables

2.1 Loss of optical polymers to be used for board-level interconnections - part 1 . . . . . 23
2.2 Loss of optical polymers to be used for board-level interconnections - part 2 . . . . . 24
2.3 Process flow for the application of one Ormocer® layer . . . . . . 30
2.4 Process flow for the application of one Truemode™ layer . . . . . . 34

4.1 Patterning techniques for optical polymers to be used for board-level interconnections . . . . . 78
4.2 Process flow for the definition of waveguides by laser ablation . . . 83
4.3 Process flow for the definition of waveguides by photolithography 83
4.4 Truemode™ and Ormocer® indices of refraction . . . . . . . . . . 90
4.5 Propagation loss optimization at 850 nm for varying KrF excimer laser pulse repetition rate (Truemode™) . . . . . . . . . . . . . . . 90
4.6 Propagation loss as a function of wavelength (Truemode™) . . . . 100

5.1 Process flow for the fabrication of metal coated mirrors embedded in the optical layer (Ormocer®) . . . . . . . . . . . . . . . . . . . . 117
5.2 Process flow for the fabrication of metal coated mirrors embedded in the optical layer (Truemode™) . . . . . . . . . . . . . . . . . . . 121
5.3 Surface roughness optimization of 45$^o$ coated mirrors (Ormocer®) 122
5.4 Mirror coupling loss (dB) . . . . . . . . . . . . . . . . . . . . . . . 125

7.1 Parameters for a KrF excimer laser induced scratch . . . . . . . . . 165
7.2 Angle deviation for perpendicular cleaved fibers . . . . . . . . . . . 169
7.3 Surface roughness of $CO_2$ laser polished fiber facets . . . . . . . . . 171

# List of Figures


1.1 The growth of data transport as a driving market force for both optics and electronics (source: Caspian Networks) . . . . . . . . . . 2
1.2 Copper versus optoelectronic crossover zone (source: iNEMI [14]) 3
1.3 Fiber based optical interconnections integrated on a PCB (source: ACTS-PLATO-project) . . . . . . . . . . . . . . . . . . . . . . . . . 5

2.1 Low optical loss of borosilicate glass (D263T) over a broad spectrum (source: Schott [3]) . . . . . . . . . . . . . . . . . . . . . . . . 18
2.2 Surface roughness of a 70 $\mu$m thick glass sheet, measured using a non-contact optical profiler (Wyko NT2000) . . . . . . . . . . . . . 19
2.3 Temperature and pressure during FR4 lamination [9] . . . . . . . 22
2.4 Principle of solgel reaction of alkoxysilanes to organically modified inorganic oligomers (source: Fraunhofer Institute [14]) . . . . 29
2.5 Spin curves for Ormocer® . . . . . . . . . . . . . . . . . . . . . . . 30
2.6 Planarization properties of Ormocer®, measured using a Tencor Alphastep-200 stylus profiler . . . . . . . . . . . . . . . . . . . . . 31
2.7 Surface roughness of one Ormocer® cladding layer integrated on FR4 . . . . . . . . . . . . . . . . . . . . . . . . . . . . . . . . . . 32
2.8 Cross-section showing electrical tracks covered by an Ormocer® layer integrated on a halogen-free FR4 substrate . . . . . . . . . . 32
2.9 Optical transparency of Truemode™ (source: Exxelis [11]) . . . . 33
2.10 Non-uniformity of spincoated Truemode™ layers . . . . . . . . . 34
2.11 Cross-section of a Truemode™ undercladding, core, and uppercladding stack, integrated on an FR4 substrate . . . . . . . . . . . 35

3.1 Laser set-up . . . . . . . . . . . . . . . . . . . . . . . . . . . . . . 42
3.2 Schematic of the $CO_2$ laser beam path [5] . . . . . . . . . . . . . . 43
3.3 Schematic of the excimer laser beam path [5] . . . . . . . . . . . . 44
3.4 Excimer laser ablation rate for Ormocer® core and cladding material . . . . . . . . . . . . . . . . . . . . . . . . . . . . . . . . . . 46

3.5 Linear relation between number of pulses and ablation depth for Ormocer® . . . 46
3.6 Ablative photodecomposition during KrF excimer laser ablation of Truemode™ . . . 48
3.7 Nd-YAG laser ablation of Truemode™ . . . 50
3.8 Nd-YAG laser ablation of Ormocer® . . . 51
3.9 Redeposition of ablation products on or around the ablated area (Ormocer®) . . . 55
3.10 Poor adhesion of debris (Ormocer®) . . . 56
3.11 Influence of fume extraction direction with respect to ablation direction to the vertical sidewall surface quality (Ormocer®) . . . 57
3.12 Laser cleaning of surfaces contaminated with debris (Ormocer®) 58
3.13 Formation of microstructures on the bottom surface of the ablated area (Ormocer®) . . . 60
3.14 Smooth surface after annealing of $CO_2$ laser induced microstructures (Ormocer®) . . . 61
3.15 Smooth KrF excimer laser ablated sidewall (Truemode™) . . . 63
3.16 Roughness of a KrF excimer laser ablated sidewall (Truemode™) 63
3.17 Optical absorption properties of dehydrated synthetic silica glass under ArF laser irradiation [39] . . . 65
3.18 KrF excimer laser ablation of a 70 $\mu$m thick borosilicate glass sheet 66
3.19 Nd-YAG laser ablation of a 70 $\mu$m thick borosilicate glass sheet . . 67
3.20 $CO_2$ laser cutting of a 70 $\mu$m thick borosilicate glass sheet . . . 68

4.1 Array of waveguides in a 70 $\mu$m thick borosilicate glass sheet defined by HF etching (source: PPC Electronic [38]) . . . 82
4.2 SEM images of excimer laser ablated waveguides (Truemode™) . 84
4.3 Cross-section of an excimer laser ablated waveguide (Truemode™) 85
4.4 Microscope image of an array of KrF excimer laser ablated waveguides on a pitch of 125 $\mu$m (Truemode™) . . . 85
4.5 Microscope image of an array of $45 \times 120\,\mu m^2$ waveguides on a pitch of 250 $\mu$m defined by photolithography (Ormocer®) . . . 86
4.6 Sidewall surface roughness as a function of pulse repetition rate for KrF excimer laser ablated waveguides (Truemode™) . . . 87
4.7 Optical loss measurement set-up . . . 89
4.8 Loss of KrF excimer laser ablated waveguides (Truemode™) at 850 nm for a pulse repetition rate of 50 Hz . . . 91
4.9 Loss of KrF excimer laser ablated waveguides (Truemode™) at 850 nm for a pulse repetition rate of 100 Hz . . . 92
4.10 Loss of KrF excimer laser ablated waveguides (Truemode™) at 850 nm for a pulse repetition rate of 200 Hz . . . 93
4.11 Loss of KrF excimer laser ablated waveguides (Truemode™) at 850 nm as a function of pulse energy . . . 94

4.12 Loss of KrF excimer laser ablated waveguides (Truemode™) at 850 nm for optimum ablation parameters . . . 95
4.13 1×12 arrays of KrF excimer laser ablated parallel optical interconnections integrated on a 10×10 $cm^2$ PCB . . . 96
4.14 Loss of waveguides defined by photolithography (Ormocer®) at 850 nm . . . 97
4.15 Loss of waveguides defined by photolithography (Ormocer®) at 980 nm . . . 98
4.16 Relative loss spectrum of a KrF excimer laser ablated waveguide (Truemode™) . . . 99
4.17 Microscope image of an array of single mode waveguides defined by photolithography (Ormocer®) . . . 101
4.18 Loss of photolithographic defined single mode waveguides at 1310 nm (Ormocer®), based on samples provided by the Fraunhofer IOF Institute . . . 101

5.1 The use of vertical emitters calls for an additional $90^o$ bend in the signal path (source: IBM [4]) . . . 109
5.2 Schematic view of two coupling concepts . . . 113
5.3 SEM image of a cross-section of a TIR micromirror fabricated in Ormocer® using a KrF excimer laser . . . 114
5.4 Reflectance of different metals to be used for mirror coating . . . 116
5.5 Au reflectance as a function of angle of incidence $\theta_i$ . . . 116
5.6 Process flow for the fabrication of a metal coated mirror embedded in the optical layer . . . 117
5.7 Result of ultrasound agitation and spincoating at 4000 rpm on filling up an angled optical via with Ormocer® cladding . . . 118
5.8 SEM image of a cross-section of a metal coated micromirror fabricated in Ormocer® . . . 119
5.9 WYKO plot to analyze surface flatness above an embedded metal coated mirror . . . 120
5.10 Surface roughness of a micromirror fabricated in Ormocer® using KrF excimer laser ablation . . . 121
5.11 Dektak stylus angle measurement of a $45^o$ micromirror . . . 123
5.12 Vertical coupling loss measurements performed on a 10×10 $cm^2$ optical PCB . . . 124
5.13 Laser ablated cavities defined in Ormocer® . . . 125
5.14 Microscope image of a KrF excimer laser ablated large area cavity 126
5.15 Basic fabrication processes of deep lithography with protons (source: VUB, FirW-TONA [42]) . . . 128
5.16 Microscope image of an out-of-plane coupling component fabricated with DLP (source: VUB, FirW-TONA [38]) . . . 128

5.17 Demonstrator board containing laser ablated cavities for the introduction of out-of-plane coupling DLP inserts . . . . . . . . . . 129
5.18 Out-of-plane coupler inserted in the laser ablated cavity (source: VUB, FirW-TONA) . . . . . . . . . . . . . . . . . . . . . . . . . . 130
5.19 SEM image of KrF excimer laser ablated fiber reinforced epoxy, laminated on top of a thin glass sheet . . . . . . . . . . . . . . . . 131
5.20 SEM image of $CO_2$ laser ablated fiber reinforced epoxy, laminated on top of a thin glass sheet . . . . . . . . . . . . . . . . . . . 131

6.1 Coupling approach based on passive and mechanical alignment of a standard MT type connector . . . . . . . . . . . . . . . . . . . 140
6.2 $CO_2$ laser polishing of KrF excimer laser ablated microlenses in Ormocer® . . . . . . . . . . . . . . . . . . . . . . . . . . . . . 143
6.3 Ormocer® microlens fabricated by KrF excimer laser ablation, $CO_2$ laser polishing, and thermal annealing . . . . . . . . . . . . . 144
6.4 Microlens aligned with a TIR micromirror . . . . . . . . . . . . . . 145
6.5 Active writing of microlenses in a 250 $\mu$m thick PC plate . . . . . 146
6.6 1×8 microlens array defined in a PC plate . . . . . . . . . . . . . . 147
6.7 700 $\mu$m hole matching the pins of the MT ferrule . . . . . . . . . . 148
6.8 PC plate containing an array of 1×12 microlenses (250 $\mu$m pitch) and two 700 $\mu$m holes that match the pins of the MT ferrule . . . 149
6.9 Mechanical alignment of the MT ferrule with respect to the lens plate . . . . . . . . . . . . . . . . . . . . . . . . . . . . . . . . . 150
6.10 PC plate of 500 $\mu$m thickness surrounding the lens plate to reduce the stress on the optical layers . . . . . . . . . . . . . . . . . . . . 150
6.11 Proof-of-principle demonstrator board providing for board-to-board coupling . . . . . . . . . . . . . . . . . . . . . . . . . . . . 151
6.12 Ray-tracing simulation of the coupling interface . . . . . . . . . . 152
6.13 Simulated alignment tolerances of the coupling interface . . . . . 153

7.1 Refraction of the laser light in the glass fiber due to the circular geometry of the fiber that acts as a lens . . . . . . . . . . . . . . . . 162
7.2 Schematic cross-section of the fiber holder, the fiber is stretched over an anvil in order to generate stress that opens up the crack . 163
7.3 Picture of the fiber holder which is placed on the translation table of the laser ablation set-up . . . . . . . . . . . . . . . . . . . . . . 164
7.4 SEM image of an end facet of a laser cleaved glass fiber . . . . . . 165
7.5 SEM image of a 1×8 array of laser cleaved glass fibers . . . . . . . 167
7.6 Statistical distribution of the surface profile of laser cleaved fibers 168
7.7 Typical interference fringes of some defects (source: Arden Photonics [10]) . . . . . . . . . . . . . . . . . . . . . . . . . . . . . . 169
7.8 Optical glass fibers embedded in a PCB (source: FZK [11]) . . . . 171
7.9 Surface profile of a $CO_2$ laser polished fiber endfacet . . . . . . . 172

# Samenvatting

In de huidige elektronische systemen neemt door de toenemende prestatie van CMOS gebaseerde microprocessoren de hoeveelheid informatie die tussen componenten uitgewisseld wordt, alsmaar toe, wat in de nabije toekomst voor een interconnectie flessenhals zal zorgen. Een recent rapport vanuit de halfgeleiderindustrie voorspelt chip input-output datasnelheden tot 9.5 GHz tegen het jaar 2010, en tot 29 GHz tegen het jaar 2015. Alhoewel het onzeker is wanneer de limieten van bestaande koper gebaseerde interconnectietechnologieën bereikt zullen zijn, lijkt het heel waarschijnlijk dat er andere oplossingen nodig zijn. Eén van deze oplossingen is de introductie van parallelle optische interconnecties.

Het fundamenteel voordeel van optische verbindingen is dat het product van propagatie afstand en bandbreedte veel groter is dan haalbaar met elektrische verbindingen. Dit was één van de drijfveren voor de transformatie van de telecommunicatiewereld over de laatste tientallen jaren, en ligt aan de basis van de transformatie van verbindingen over korte afstand (>10 m) binnen zeer performante computer systemen. Ondanks het feit dat de technologische voordelen van optische interconnecties binnen systemen reeds meer dan 20 jaar gekend zijn, worden optische kanalen nog steeds niet geïntegreerd met gedrukte schakelingen of printkaarten. De belangrijkste reden hiervoor is de kostprijs. Alleen voor voldoend hoge datasnelheden duikt de optische kostprijs onder de elektrische kostprijs. Afgezien van de correlatie tussen prijs en volumeproductie, wordt prijs direct bepaald door het aanbieden van geschikte technologische oplossingen. Dit is de belangrijkste doelstelling van dit werk: een flexibele technologie ontwikkelen die de fabricage van goedkope optische interconnecties geïntegreerd met gedrukte schakelingen moet toelaten, en dit gebaseerd op het gebruik van optische golfgeleiderstructuren.

De vereisten waaraan kandidaat optische materialen moeten voldoen worden beschreven in Hoofdstuk 2. Nadruk ligt op optische verliezen, stabiliteit, en compatibiliteit met standaard fabricageprocessen van klassieke elektrische gedrukte schakelingen. Dunne glasplaten met een dikte van 70 $\mu$m zijn een zeer aantrekkelijk materiaal, vermits hun gedrag onder invloed van temperatuur en vochtigheid superieur is ten opzichte van polymeren. Bovendien vertonen

zij lage optische verliezen over een zeer breed golflengte gebied. Grootste uitdaging is de fabricage van multimodale golfgeleiderstructuren. Verder wordt een overzicht gegeven van kandidaat polymere materialen die een maximum propagatieverlies van 0.1 dB/cm bezitten. Zowel polysiloxanen (Ormocer®) als acrylaten (Truemode™) worden onderzocht binnen dit werk. Proces parameters voor het aanbrengen van 50 $\mu$m dikke kern en cladding lagen worden bepaald. De oppervlakteruwheid van de lagen is opgemeten met een optische profilometer (Wyko NT2000), resulterend in gemiddelde ruwheden van 3–4 nm.

De nadruk lag tijdens dit werk op het gebruik van laser ablatie om structuren aan te brengen in de optische lagen. In Hoofdstuk 3 wordt de mogelijkheid onderzocht om met behulp van een KrF excimeer laser, een frequentie verdrievoudigde Nd-YAG laser, en een $CO_2$ laser, micrometer structuren te ableren in Ormocer®, Truemode™ en 70 $\mu$m dik borosilicaat glas. Er wordt aangetoond dat vooral de combinatie KrF excimeer laser en Truemode™ veel potentieel biedt. De geableerde structuren bezitten zeer vlakke zijwanden, met een gemiddelde oppervlakteruwheid van ongeveer 20 nm. De generatie van debris, en de aanwezigheid van microstructuren zijn twee fundamentele problemen bij KrF excimeer laser ablatie van Ormocer®. Nd-YAG lasers zijn in staat om ondiepe structuren aan te brengen in zowel Truemode™ als Ormocer®, met zeer vlakke zijwanden. Bij diepere structuren van typisch 50 $\mu$m wordt thermische schade geconstateerd. $CO_2$ lasers kunnen gebruikt worden om polymere oppervlakken te polijsten, maar introduceren thermische schade wanneer ze gebruikt worden in een ablatie regime. De beste resultaten voor de dunne glasplaten worden verkregen met de $CO_2$ laser, met een minimum aan debris, en onder de geschikte omstandigheden, zonder microscheurtjes.

Experimentele resultaten van KrF excimeer laser geableerde golfgeleiders in Truemode™ worden voorgesteld in Hoofdstuk 4. Rijen van $50\times50\,\mu m^2$ multimodale golfgeleiders op een afstand van 125 $\mu$m zijn geïntegreerd op $10\times10\,cm^2$ printkaarten, met propagatieverliezen van 0.11 dB/cm bij een golflengte van 850 nm. Het spectrum toont ook lage verliezen bij langere golflengtes, wat mogelijkheden opent voor telecommunicatie toepassingen op niveau van printkaarten. Fotolithografisch gedefinieerde golfgeleiders in Ormocer® vertonen een propagatieverlies van 0.08 dB/cm bij 850 nm, en 0.22 dB/cm bij 980 nm. Het principe van monomodale golfgeleiders geïntegreerd met FR4 gebaseerde gedrukte schakelingen is aangetoond, zonder optimalisatie van kern diameter. Propagatieverliezen van 0.62 dB/cm zijn opgemeten bij 1.3 $\mu$m, gebruik makend van fotolithografisch gedefinieerde golfgeleiders in Ormocer®. Ondanks het feit dat laser ablatie een serieel proces is, laat het toe om simultaan rijen van golfgeleiders te maken, en is het proces schaalbaar naar grotere printkaart dimensies. Het gebruik van fotolithografie kan toegepast worden wanneer massaproductie belangrijk wordt.

In Hoofdstuk 5 worden verschillende configuraties besproken voor het in- en

uitkoppelen van licht, ten aanzien van het vlak van de optische golfgeleiders. Nadruk ligt op de fabricage van gemetalliseerde 45$^o$ spiegeltjes, ingebed in de optische lagen. Spiegeltjes in Truemode$^{TM}$ vertonen een gemiddelde oppervlakteruwheid van slechts 42 nm, en een RMS ruwheid van slechts 53 nm, opgemeten in een gebied van $174 \times 52\,\mu m^2$. De 45$^o$ hoek is geverifieerd met een Dektak 8 stylus profiler. Hoek variatie bedraagt $\pm 2^o$. Koppelverliesmetingen voor zowel mono- als multimodale structuren geven spiegelverliezen van 2.2 dB, afhankelijk van de in- en uitkoppelvezel die gebruikt wordt. De fabricage van optische via's wordt beschreven, die de insertie van een externe koppelcomponent moet toelaten. Op het einde van dit hoofdstuk wordt het gebruik van $CO_2$ laser ablatie beschreven, om toegang te verstrekken tot de optische lagen doorheen een vezel versterkte epoxy laag.

De interface die moet toelaten licht te koppelen tussen golfgeleiders van verschillende printkaarten, wordt beschreven in Hoofdstuk 6. De koppelconfiguratie is gebaseerd op passieve en mechanische alignatie, gebruik makend van een 250 $\mu$m dik lensplaatje. De alignatie tussen de optische printkaart, en het lensplaatje is verwezenlijkt door gebruik te maken van referentiemarkeringen, de alignatie tussen de MT ferrule van de connector en het lensplaatje is verwezenlijkt door twee 700 $\mu$m gaten, die corresponderen met de pinnen van de MT ferrule. KrF excimeer laser ablatie van microlenzen is beschreven, gebruik makend van zowel een Polycarbonaat, als een Ormocer® substraat, en gebruik makend van $CO_2$ laser geassisteerd polijsten. Een korte misalignatie tolerantie studie van de koppelinterface laat een schatting van de koppelverliezen toe.

De ontwikkeling van een UV excimeer laser gebaseerd proces voor het klieven van glasvezel is beschreven in Hoofdstuk 7. Dit proces laat een volledig geautomatiseerd klieven toe, voor massavolume productie van optische vezel assemblages. Thermische effecten resulterend in smelten van de vezel treden niet op, wat wel het geval is bij het gebruik van $CO_2$ lasers. Een selectief geableerde kras propageert wanneer de vezel onder spanning wordt gebracht, wat zich uit in een klief van de vezel. De positie van de laser geïnduceerde kras is veel precieser dan mogelijk is met een mechanische kliever. Het proces is operator onafhankelijk, en vertoont consistente klievages. Verder onderzoek is vereist om de defecten die optreden voor rijen van vezels te minimaliseren. De hoek van loodrecht gekliefde vezels is nagemeten met een optische interferometer, en geeft een gemiddelde van 1.06$^o$, en een standaard afwijking van 0.47$^o$. Koppelverlies na het aan mekaar lassen van twee vezels bedraagt 0.03 dB, vergelijkbaar met mechanisch gekliefde vezels. Het ontwikkeld proces laat toe om glasvezels die ingebed zijn in een gedrukte schakeling (als alternatief voor optische golfgeleiders) te termineren, waarvoor momenteel geen kliefprocedure voorhanden is. Op het einde van dit hoofdstuk wordt $CO_2$ laser polijsten van glasvezel facetten voorgesteld, wat een reductie van de gemiddelde ruwheid van het vezelfacet oplevert van 50 nm naar 27 nm in een zone van 60 $\mu$m rond de kern van de vezel.

# Summary

Bottleneck in todays electronic systems is to a large extent associated with the off-chip communication. Continual efforts to increase the speed of CMOS circuitry has led to the need for higher performing interconnects. The ITRS report from 2005 predicts a chip-to-board speed up to 9.5 GHz for the year 2010 and approaching 29 GHz for the year 2015. While it is uncertain when the physical limitations of conventional interconnects will prohibit speed increases, it seems that electrical transmission lines cannot continuously scale with higher performing CMOS circuitry.

While the benefits of optics for short links within systems have been discussed for over 20 years, the opportunity for optics has never been stronger. The fundamental advantage of optics is the much larger bandwidth-distance product that can be achieved, compared to electrical links. This was one of the drivers behind the transformation of the telecommunications industry over the last several decades, and underlies the transition at shorter distances that we have seen in optics use within high-end computing systems over the last decade.

Despite the technological advantages, optics has still not made the rapid inroads onto boards and cards. The main reason for this is cost. Only for higher bandwidth-distance products, the cost of optics drops well below the cost of a comparable electrical link. Besides the inter-dependance between costs and market volumes, costs can be addressed through technical solutions directly, which is the main objective of this work, providing for a flexible technology for the fabrication of low cost board-level optical interconnections.

A lot of research is currently focused on the use of optical waveguides, being fabricated directly onto the board, or fabricated separately onto foils that are laminated into the board subsequently. A number of challenges must be overcome in order to make these waveguides a practical technology.

The requirements for optical materials to be used for board-level optical interconnections are discussed in Chapter 2. Special attention is given to optical loss, environmental stability, and compatibility with standard PCB manufacturing. Thin glass sheets are a very attractive material, as the temperature and humidity behaviour is superior to polymers, and they show a low optical loss over a broad

window. Big challenge is the fabrication of multimode waveguides in 70 $\mu$m thick glass foils. An overview of polymer candidates is presented, with propagation loss $< 0.1$ dB/cm, for datacom and telecom wavelengths. Both polysiloxanes (Ormocer®) and acrylates (Truemode™) are investigated within this work. Process parameters for the application of 50 $\mu$m thick cladding and core layers are determined. Surface roughness of the layers has been evaluated making use of a non-contact optical profiler (Wyko NT2000), showing an $R_a$ surface roughness of 3–4 nm.

During this work, emphasis was on investigating the use of laser ablation for structuring the optical layers, as it is a very flexible technology that is compatible with standard PCB manufacturing processes. Chapter 3 deals with the feasibility of KrF excimer laser-, frequency tripled Nd-YAG laser-, and $CO_2$ laser ablation for structuring Ormocer®, Truemode™ and 70 $\mu$m thick borosilicate glass sheets. It has been revealed that there is a lot of potential for the combination KrF excimer laser - Truemode™ materials, showing very smooth sidewall surfaces, with an $R_a$ roughness around 20 nm. Generation of debris, and the presence of microstructures are two fundamental limits for structuring Ormocer® materials using KrF excimer lasers. It has been shown that frequency tripled Nd-YAG lasers are capable of structuring shallow grooves with smooth surfaces, but grooves with a depth of 50 $\mu$m show thermal damage. $CO_2$ lasers can be used for smoothing polymer surfaces, but introduce serious thermal damage when ablating polymers. Optimum results for structuring glass are obtained for $CO_2$ laser ablation, minimizing the presence of debris, and under the right circumstances, without the formation of microcracks.

Experimental results on KrF excimer laser ablated waveguides in Truemode™ are presented in Chapter 4. Arrays of $50{\times}50\,\mu m^2$ multimode waveguides on a pitch of 125 $\mu$m have been integrated on $10{\times}10\,cm^2$ PCBs, showing a propagation loss of 0.11 dB/cm at a wavelength of 850 nm. The loss spectrum revealed that longer wavelengths could be used as well, opening possibilities for telecom applications at the board-level. Comparing the insertion loss at 850 nm to the insertion loss at 980 nm and 1.3 $\mu$m, gives a propagation loss of 0.015 dB/cm at 980 nm, and 0.15 dB/cm at 1.3 $\mu$m. Waveguides structured by photolithography in Ormocer®, show a propagation loss of 0.08 dB/cm at 850 nm, and 0.22 dB/cm at 980 nm. Even though laser ablation remains a serial process, it allows for a simultaneous fabrication of arrays of waveguides, and the process is scalable to larger PCB dimensions. The use of photolithography could be applied when high throughput becomes important. Proof-of-principle has been shown for the integration of single mode waveguides on FR4 based PCBs, without optimizing core dimensions. A propagation loss of 0.62 dB/cm has been measured at 1.3 $\mu$m, using Ormocer® patterned by photolithography.

Different approaches for out-of-plane coupling structures are discussed in Chapter 5. Special attention is given to the fabrication of metal coated micromirrors

embedded in the optical layer. The process being developed can be applied both for Ormocer® and for Truemode$^{TM}$ materials. Surface roughness measurements revealed that for Truemode$^{TM}$ the $R_a$ surface roughness of the mirrors can be as low as 42 nm, and the RMS roughness as low as 53 nm, measured on an area of $174\times52\,\mu m^2$. The $45^o$ angle has been verified using a Dektak 8 stylus profiler, indicating an angle variation of $\pm 2^o$. Coupling loss measurements were performed both using multimode and single mode waveguides as testbed structures. An excess mirror loss of 2.2 dB has been achieved, depending on the in- and outcoupling fiber being used. The fabrication of optical vias allowing the introduction of a pluggable component is described. Finally, the use of $CO_2$ laser ablation to access the optical layers through fiber reinforced epoxy is discussed.

The interface to allow coupling between waveguides located on different PCBs is discussed in Chapter 6. The coupling approach is based on both passive and mechanical alignment making use of a 250 $\mu$m thick lens plate. The alignment between the optical PCB and the lens plate is achieved by index alignment, the alignment of the MT ferrule and the lens plate is achieved by the two 700 $\mu$m holes that match the pins of the MT ferrule. KrF excimer laser ablation of microlenses is described, both using Polycarbonate and Ormocer® substrates, and using $CO_2$ laser assisted polishing. A misalignment tolerance study is performed estimating the loss introduced by the coupling scheme.

In Chapter 7 a UV excimer laser based cleaving procedure for silica fiber has been developed that enables automated cleaving for high-volume production of fiber-optic assemblies. Due to the typical interaction of UV excimer laser light with silica glass, thermal effects resulting in local melting of the fiber do hardly occur, as is the case with $CO_2$ lasers. A selective ablation of the glass in the form of a small rectangular cavity can serve as a fracture initiator when the fiber is placed under stress. The position of the laser induced scratch can be more precise than with a classic diamond tool used in mechanical cleavers. The system is operator independent and provides consistent high-quality cleaves on single fiber, further investigation is required to minimize lip/roll-off for ribbon configurations. The end angle of the cleaved optical fiber is measured using a non-contact optical interferometer system and had an average of $1.06^o$ and a standard deviation of $0.47^o$ for perpendicular cleavages. Insertion loss after splicing is in the range of 0.03 dB, which is compatible with mechanical cleaved fibers. The developed cleaving process is presented to enable termination of optical fibers embedded in a PCB, for which currently no cleaving process exists. Finally, $CO_2$ laser polishing of fiber facets is shown to be feasible, reducing the average surface roughness $R_a$ from 50 nm to 27 nm within a range of 60 $\mu$m from the center of the fiber.

# Notations

| Notation | Meaning |
|---|---|
| BW | Bandwidth |
| CCD | Charge Coupled Device |
| CMM | Coordinate Measurement Microscope |
| CMOS | Complementary Metal Oxide Semiconductor |
| CTE | Coefficient of Thermal Expansion |
| CWDM | Coarse Wavelength Division Multiplexing |
| DOF | Depth Of Focus |
| DWDM | Dense Wavelength Division Multiplexing |
| EMI | ElectroMagnetic Interference |
| FR4 | Flame Retardant |
| Gbps | GigaBit Per Second |
| GPIB | General Purpose Interface Bus |
| HF | HydroFluoric |
| LAN | Local Area Network |
| LIPSS | Laser Induced Periodic Surface Structures |
| MEMS | Micro Electro Mechanical System |
| MOEMS | Micro Opto Electro Mechanical System |
| MT | Mechanically Transferable |
| NA | Numerical Aperture |
| PC | Poly Carbonate |
| PCB | Printed Circuit Board |
| PMMA | PolyMethylMetAcrylate |
| PLD | Pulsed Laser Deposition |
| POF | Plastic Optical Fiber |
| RIE | Reactive Ion Etching |
| SEM | Scanning Electron Microscope |
| SMP | Symmetric MultiProcessor |
| TIR | Total Internal Reflection |
| TTL | Through The Lens |
| VCSEL | Vertical Cavity Surface Emitting Laser |
| WDM | Wavelength Division Multiplexing |

# Chapter 1

# Introduction

## 1.1 Short distance interconnections

The communications world is evolving rapidly, as voice and data networks merge to become broadband multimedia networks. The increasing prevalence of computers, the explosive growth of the Internet (see Figure 1.1), and the emergence of a strong wireless market are driving these changes, and optoelectronic components are the fundamental enablers of this transformation. The combination of both optical and electrical technologies allows data to be generated, transported and manipulated at high rates. Today, optoelectronics are being integrated into existing networks, but within a few years, all-optical networks will most likely be needed.

The fundamental advantage of optics is the much larger bandwidth-distance product that can be achieved, compared to electrical links, i.e. the losses and signal distortions for optical propagation are far more benign than those for electrical links. This was one of the drivers behind the transformation of the telecommunications industry over the last several decades, and underlies the transition at shorter distances that we have seen in optics use within high-end computing systems over the last decade.

While the benefits of optics for short links within systems have been discussed for over 20 years [1], the opportunity for optics has never been stronger. Bottleneck in todays electronics is to a large extent associated with the off-chip communication. Continual efforts to increase the speed of CMOS circuitry has led to the need for higher performing interconnects. The ITRS report from 2005 predicts a chip-to-board speed up to 9.5 GHz for the year 2010 and approaching 29 GHz for the year 2015 [2]. While there is little to do to alleviate fundamental properties of conductors (skin effect), without increasing wire cross-sections (which reduces

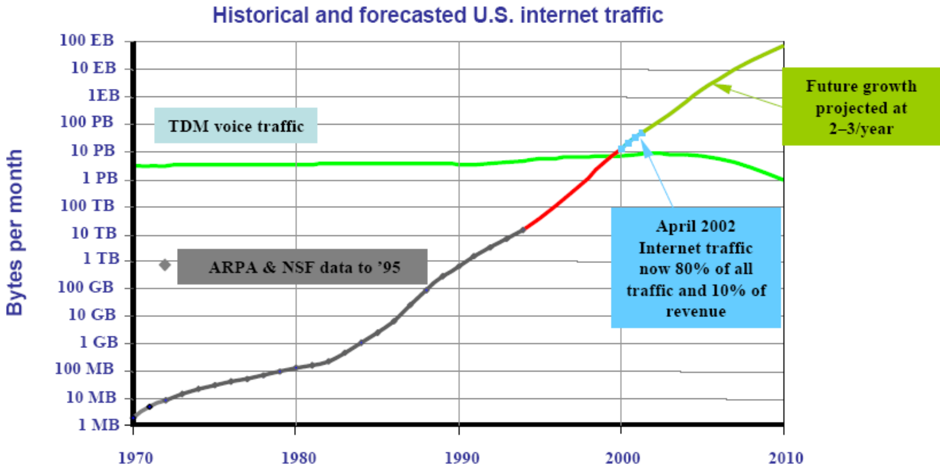


**Figure 1.1:** The growth of data transport as a driving market force for both optics and electronics (source: Caspian Networks)

wiring density), improved low loss dielectric materials, and advanced board technologies (with no or reduced vias) can improve signal propagation characteristics [3, 4]. The increasing density of circuits (available at lower cost) allows more signal processing techniques to be brought to bear on the problem, including signal pre-emphasis and equalization, decision feedback techniques and multi-level coding [5, 6, 7, 8]. The resulting impact is that electrical link performance can continue to improve, but at the expense of other important metrics. To incorporate a few high data rate links is not necessarily an issue, however multiply this by thousands of off-chip links, and the burden of utilizing these advanced circuit techniques can become a problem. Optics can alleviate these issues by greatly reducing the need for on chip signal processing [9, 10].

Electrical interconnects have other limitations that are harder to quantify but that are just as important, particularly as line density increases. They are susceptible to electromagnetic interference (EMI) from the board and rack environment, including (and especially) crosstalk from adjacent channels. These issues are particularly serious at high-density connectors which interface plug-in boards to the backplane [11, 12]. The use of dielectric rather than metal based waveguides makes optical interconnects (and corresponding connectors) immune to EMI.

Other advantages of optics include card edge density, e.g. the bandwidth per unit card edge length is much higher for optical links than for electrical. Achievable card edge density for optical interconnects is today a few times better than for electrical interconnects, and will increase further to 10$\times$ in the 10 Gbps generation [13].

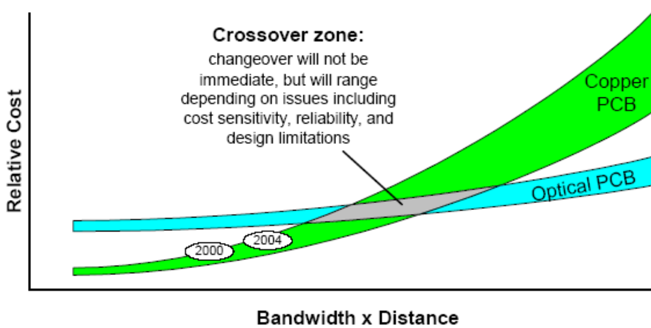


**Figure 1.2:** Copper versus optoelectronic crossover zone (source: iNEMI [14])

Optics also offers potential power savings over electrical links, especially at longer distances, but only if the optical interconnects can be more tightly integrated with the signal source. Every optics link must connect to a data source, such as a micro-processor, via an electrical link. If these electrical links need to traverse a full card length to connect to optics positioned at the card edge, then the combined electrical-optical-electrical link may offer no power advantage whatsoever. The shorter the optical link under consideration the more important it is to minimize the electrical feeder distance.

Despite the technological advantages, optics has still not made the rapid inroads onto boards and cards that have been discussed for the last two decades. The main reason for this is cost. The cost of optics (on a per Gbps basis) is still well above that of comparable electrical links. For example, even for a 10 m, $12\times2.5$ Gbps parallel link, optics is currently about $2\times$ more expensive than the corresponding electrical link [13]. Only for higher bandwidth-distance products, the cost of optics drops well below the cost of a comparable electrical link, as is shown in Figure 1.2 (iNEMI Technology Roadmap 2005 [14]).

Of course, market volumes are critical to reducing costs, and the acceptance of optical interconnections in computing systems is largely influenced by the interdependance of costs and market volumes. Without a comparable cost entry point for optics, the volume market never has a chance to develop for these shorter length links [13]. On the other hand, costs can be addressed through technical solutions directly, which is the main objective of this work, providing for a flexible technology for the fabrication of low cost board-level optical interconnections.

In what follows, optical links are classified as in-box and box-to-box interconnections. In-box interconnections include both MCM-level, board-level, and backplane-level interconnections, with distances ranging from a few centimeters up to one meter. Box-to-box interconnections cover the inter-cabinet links with distances up to tens of meters.

## 1.2 Box-to-box optical interconnections

This is obviously the most mature class of optical intra-system interconnects, which is partially due to its relation to local area network (LAN) type applications. Commercial state-of-the-art optical interconnects are using pairs of electro-optical transceiver modules, based on VCSEL arrays, interconnected by multimode fiber arrays, with MT based connectors. Speeds of individual VCSELs is at 2.5 to 3.125 Gbps, dimension is typically $1\times12$. Standardized modules are available from several vendors.

Suppliers are taking the next logical step, to 10 Gbps transmission through 12-fiber ribbons at total data rates to 120 Gbps. Agilent Laboratories has developed a system based on bottom-emitting 990 nm VCSELs, and bottom-illuminated InGaAs/InP detectors that is flip-chip bonded to integrated circuits and can transmit through 100 m of multimode fiber ribbon [15]. The IBM Watson Research Center has developed a similar system based on top-emitting 850 nm VCSELs and top-illuminated GaAs detectors [16].

It is also possible that parallel optics could evolve in more complex directions than simply increasing the channel bit rate and the width of the link. One of the most straightforward ideas is to use multiple wavelengths on a single fiber (wavelength division multiplexing, or WDM). A version of a parallel WDM transmitter and receiver has been demonstrated [17]. This system is considered coarse WDM (CWDM), since the wavelength spacing between channels is typically 10–15 nm, as opposed to the 0.5–1.0 nm channel spacing typical of the dense WDM (DWDM) systems used in long-haul telecommunications. The target overall bandwidth in the demonstrator is more than 10 Gbps in each of 48 channels. This bit rate should match or exceed the clock speed of microprocessors and so be adequate for the initial use of SMP bus optical interconnects in servers. Since the module uses a four-wavelength CWDM design to reduce the fiber count by four, an optical MUX and DEMUX are needed, adding cost and complexity.

## 1.3 In-box optical interconnections

### 1.3.1 Fiber based approaches

With the idea of using an established technology, people have considered various approaches, essentially all based on pieces of fiber, going from discrete optical fibers, to optical fibers laminated into flexible foils or into boards.

An illustration of a discrete fiber based optical layer is given in Figure 1.3a, showing an application board on which optical signals, coming from the optical backplane are routed to micromechanical all-optical switches and back to the backplane connectors. An integrated fiber based optical layer is shown in Figure

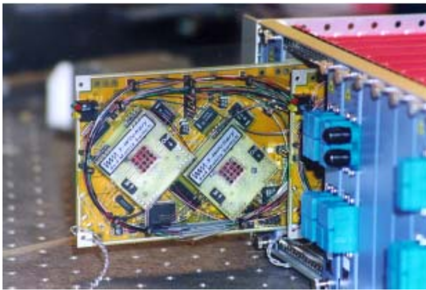

(a) Discrete fibers

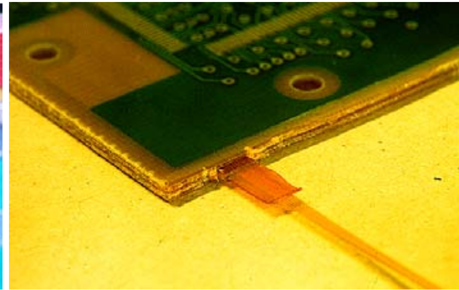

(b) Fibers integrated in a standard PCB-stack

(c) Embedded optical fibers as a passive optical backplane

**Figure 1.3:** Fiber based optical interconnections integrated on a PCB (source: ACTS-PLATO-project)

1.3b, where one can see the optical fiber ribbon extending from the edge of the board. Both demonstrators were realized within the European ACTS-PLATO-project (Photonic links in ATM and optical systems) [18, 19, 20].

Among the problems for fiber based approaches, the minimum radius of curvature of standard optical fiber is certainly the most important, causing problems both for routing of the fiber along the board, and for coupling light from the optical fibers towards optoelectronic components mounted on the board, as the fibers cannot be bended perpendicular to the surface (minimum radius of curvature 1–2 cm). Slightly bending the optical fibers towards the surface has been demonstrated within the European RACE II-HIBITS-project (High Bitrate ATM Termination and Switching) [21, 22, 23]. Mounting optoelectronic components into laser drilled holes, still requires the fabrication of the endfacet to the optical fiber, which results in some practical difficulties as traditional cleaving of the fibers can not be used. Alternative solutions as e.g. cleaving of the fibers using laser ablation are investigated within this PhD work.

Optical fibers embedded in flexible foils, offering a pure passive optical intercon-

nection, are commercially available [24, 25], aiming at optical backplane applications where no integration with the electrical backplane is required. An example realized within the European ACTS-PLATO-project can be seen in Figure 1.3c.

Switching from glass fiber towards plastic optical fiber (POF) can solve some of the above mentioned problems. POF termination does not require multi-step polishing, and the process is far more reliable than polishing of glass fiber. The smaller bending radiuses allow for the realization of very compact connectors, a concept that has been adapted in the European IST-IO-project (Interconnect by Optics) [26]. In the IO-project, a new type of POF is developed, with better absorption and temperature characteristics compared to PMMA based POF. The main market today for POF are short-distance communication links, operating at a moderated bandwidth. In such applications, the low cost aspect of POF is very important, and the fiber is typically a thick (1 mm) step-index fiber. The parallel optical interconnect link requires a different type of fiber, with a fiber core diameter of 70 $\mu$m.

All optical fiber based approaches only offer point-to-point interconnects, and complex fiber arrangements cannot be batch fabricated but have to be laid out fiber by fiber. When comparing fiber based approaches with more integrated approaches such as waveguides, an analogy to copper cables and printed circuit boards (PCBs) in the early days of electronics can be seen.

### 1.3.2 Waveguide based approaches

A lot of research is currently focused on the use of optical waveguides, being fabricated directly onto the board, or fabricated separately onto foils that are laminated into the board subsequently. A number of challenges must be overcome in order to make these waveguides a practical technology, including the following:

- optical loss of the waveguides
- stability of the waveguides during the board manufacturing process, chip attachment, and system operation
- scalability of waveguide manufacturing to larger board dimensions
- low loss optical interface between O/E module and waveguides, and between board and backplane

As the use of optical waveguides is investigated within this PhD work, a complete description will be given in the following chapters, including the challenges mentioned above.

### 1.3.3 Free-space based approaches

One of the potential advantages of using free-space optics is the low attenuation (few dB/km) if air is used as a propagation medium. There are still losses due to reflections, but these can be minimized using anti-reflection coatings. Another potential advantage is the promise of increased density by using real 2D arrays. For board integrated waveguides, few layers can be stacked on top of each other, but probably not too many, leading to 1.5D arrays, being arrays with few $\times$ many channels. In free-space optics, however, there is no need to stack individual layers and the optics will image as many channels as the field of view and the density of VCSEL arrays will allow. The limitation will more probably come from the electrical contacts of the VCSEL array and from thermal considerations.

A key limitation of free-space approaches is the alignment, which has to be maintained over time over the whole optical path, and not only at the coupling interfaces. Free-space interconnects have therefore been limited in length from centimeters to a few tens of centimeters. Compared to the routing possibilities in guided approaches, free-space offers only very limited flexibility. In order to avoid negative influences from dust and dirt, the optical path will have to be encapsulated, which will add to the complexity of the optical subsystem. Despite these reflections, free-space interconnections are expected to find breakthrough for shorther distance MCM-level interconnections.

A key implementation requirement is some method of providing optical alignment between the individual sets of transmitter-receiver elements and at the same time providing for optical signal isolation to reduce crosstalk between the various channels. The architectural approaches [27, 28, 29, 30, 31, 32, 33, 34, 35, 36, 37] can be summarized into four implementational methodologies, used individually or in some combinations: spatial separation, lensing elements, differing wavelengths, and holographic optical elements (HOE). Apart from the architectural approaches, there is a wealth of system topologies. Some examples are line of sight between adjacent boards, zig-zag propagation within glass plates, or folded systems using mirrors or prisms.

## 1.4 Research context

The research which formed the basis of this dissertation was carried out within the framework of the project Plastic for Photonics, supported by the Institute for the Promotion of Innovation by Science and Technology (IWT). The objective was to develop a technology, for the application of polymer optical layers on a standard PCB, for the fabrication of multimode optical waveguides in these layers, and for the definition of out-of-plane couplers in these waveguides. Emphasis was on investigating the use of laser ablation for structuring the polymer layers,

as it is a very flexible technology that is compatible with standard PCB manufacturing processes.

Within a bilateral project with FCI 's Hertogenbosch the aim was to establish a coupling interface between waveguides located on different PCBs, based on the widely used MT type connector.

The objective of the work performed within a bilateral project with Motorola was to optimize laser ablation for the fabrication of optical vias, to optimize the performance of the out-of-plane couplers, and to investigate the integration of both $45^o$ micromirrors and microlenses in the optical layers.

In cooperation with different partners of the European PIDEA-Project-Orbita (Optical Routing Backplanes Intranet-working for Telecom/datacom Applications) the objective was to investigate the use of laser ablation for structuring glass sheets, and to provide for an optical window, through a fiber reinforced epoxy layer, to access the embedded optical waveguiding layers.

The research work carried out in the framework of the project LIAM (high-performance low-cost interconnection components for a new generation of access network products, manufactured using new micro-optical fabrication technologies), supported by the Institute for the Promotion of Innovation by Science and Technology (IWT), the aim was to investigate UV laser cleaving of glass fibers, enabling automated cleaving for high-volume production of fiber-optic assemblies.

Within the European IST-project-Nemo (Network of Excellence on Micro-Optics), more precisely within the workpackage on Micro-Optics for PCB and MCM-level interconnects, the laser cleaving process is investigated for the termination of optical fibers embedded in a PCB, as an alternative medium to optical waveguides. Within the same workpackage, the optical vias are further investigated, to be combined with pluggable out-of-plane couplers.

## 1.5 Publications

### The following journal papers have been published

- G. Van Steenberge, P. Geerinck, S. Van Put, J. Van Koetsem, H. Ottevaere, D. Morlion, H. Thienpont and P. Van Daele. Mt-compatible laser-ablated interconnections for optical printed circuit boards. *Journal of Lightwave Technology*, 22(9):2083-2090, Sep 2004.

- G. Van Steenberge, P. Geerinck, S. Van Put, J. Watt, H. Ottevaere, H. Thienpont and P. Van Daele. Laser cleaving of glass fibers and glass fiber arrays. *Journal of Lightwave Technology*, 23(2):609-614, Feb 2005.

- G. Van Steenberge, N. Hendrickx, E. Bosman, J. Van Erps, H. Thienpont and P. Van Daele. Laser ablation of parallel optical interconnect waveguides. *Photonics Technology Letters*, 18(9):1106-1108, May 1 2006.

### The following papers have been presented at international conferences

- P. Van Daele, P. Geerinck, G. Van Steenberge and S. Van Put. Optical interconnections on pcb's: a killer application for vcsels (invited). In *Photonics Fabrication Europe'02, Proceedings SPIE 4942, VCSELs And Optical Interconnects*, pages 269–281, Apr 2002.

- P. Van Daele, P. Geerinck, G. Van Steenberge, S. Van Put and M. Cauwe. Laser ablation as an enabling technology for opto-boards. In *ECTC'03, Proceedings Electronic Components And Technology Conference*, pages 1140–1146, May 2003.

- G. Van Steenberge, P. Geerinck, S. Van Put and P. Van Daele. Integration of multimode waveguides and micro-mirror couplers in printed circuit boards using laser ablation. In *Proceedings Symposium IEEE/LEOS Benelux Chapter*, pages 285–288, Nov 2003.

- G. Van Steenberge, P. Geerinck, S. Van Put and P. Van Daele. Integration of multimode waveguides and micromirror couplers in printed circuit boards using laser ablation (invited). In *Photonics Europe'04, Proceedings SPIE 5454, Fabrication Packaging And Integration*, pages 75–84, Apr 2004.

- G. Van Steenberge, P. Geerinck, S. Van Put and P. Van Daele. Demonstration of an mt-compatible connectorisation of a laser-ablated optical interconnection on a printed circuit board. In *ECTC'04, Proceedings Electronic Components And Technology Conference*, pages 1552–1557, May 2004.

- G. Van Steenberge, P. Geerinck, S. Van Put, H. Ottevaere, H. Thienpont and P. Van Daele. Laser ablated micromirrors for optical printed circuit boards. In *Proceedings Symposium IEEE/LEOS Benelux Chapter*, pages 271–274, Dec 2004.

- G. Van Steenberge, P. Geerinck, S. Van Put, N. Hendrickx, E. Bosman, H. Ottevaere, H. Thienpont and P. Van Daele. 45 Out-of-plane turning mirrors for optical printed circuit boards. In *EMPC'05, Proceedings European Microelectronics And Packaging Conference And Exhibition*, pages 557–560, Jun 2005.

- N. Hendrickx, G. Van Steenberge, P. Geerinck, S. Van Put, E. Bosman and P. Van Daele. Multilayer optical interconnections integrated on a printed circuit board. In *EMPC'05, Proceedings European Microelectronics And Packaging Conference And Exhibition*, pages 329–333, Jun 2005.

- J. Van Erps, G. Van Steenberge, N. Hendrickx, P. Geerinck, B. Volckaerts, C. Debaes, P. Van Daele and H. Thienpont. Deep lithography with protons to prototype pluggable micro-optical out-of-plane coupling structures for multimode waveguides. In *ICOO'05, Proceedings SPIE 5956, International Congress On Optics And Optoelectronics, Integrated Optics: Theory And Applications*, Aug 2005.

- G. Van Steenberge, P. Geerinck, M. Riester and P. Van Daele. Laser ablated coupling structures for optical printed circuit boards. In *ICOO'05, Proceedings SPIE 5956, International Congress On Optics And Optoelectronics, Integrated Optics: Theory And Applications*, Aug 2005.

- N. Hendrickx, H. Suyal, G. Van Steenberge, A. McCarthy, A. Walker, M. R. Taghizadeh and P. Van Daele. Laser direct writing and laser ablation as enabling technologies for the definition of micro-optical elements. In *ICOO'05, Proceedings SPIE 5956, International Congress On Optics And Optoelectronics, Integrated Optics: Theory And Applications*, Aug 2005.

- N. Hendrickx, G. Van Steenberge, P. Geerinck and P. Van Daele. Multilayer optical interconnects integrated on a printed circuit board. In *Proceedings Symposium IEEE/LEOS Benelux Chapter*, pages 213–216, Dec 2005.

- G. Van Steenberge, N. Hendrickx, P. Geerinck, E. Bosman, S. Van Put, J. Van Erps, H. Thienpont and P. Van Daele. Development of a fabrication technology for integrating low cost optical interconnects on a printed circuit board. In *Photonics West'06, Proceedings SPIE 6126, Nanophotonic Packaging*, Jan 2006.

- G. Van Steenberge, N. Hendrickx, P. Geerinck, E. Bosman, S. Van Put and P. Van Daele. Development of a technology for fabricating low cost parallel

optical interconnects. In *Photonics Europe'06, Proceedings SPIE 6185, Micro-Optics VCSELs And Photonic Interconnects: Fabrication, Packaging And Integration*, Apr 2006.

- N. Hendrickx, G. Van Steenberge, P. Geerinck and P. Van Daele. Multilayer optical interconnects integrated on a printed circuit board. In *Photonics Europe'06, Proceedings SPIE 6185, Micro-Optics VCSELs And Photonic Interconnects: Fabrication, Packaging And Integration*, Apr 2006.
- E. Bosman, P. Geerinck, W. Christiaens, G. Van Steenberge, J.M. Vanfleteren and P. Van Daele. Optical connections on flexible substrates. In *Photonics Europe'06, Proceedings SPIE 6185, Micro-Optics VCSELs And Photonic Interconnects: Fabrication, Packaging And Integration*, Apr 2006.
- N. Hendrickx, J. Van Erps, H. Suyal, G. Van Steenberge, A. McCarthy, M.R. Taghizadeh, H. Thienpont and P. Van Daele. Roughness measurements on coupling structures for optical interconnections integrated on a printed circuit board. In *Photonics Europe'06, Proceedings SPIE 6185, Micro-Optics VCSELs And Photonic Interconnects: Fabrication, Packaging And Integration*, Apr 2006.
- J. Franc, A. Last, N. Destouches, D. Blanc, N. Hendrickx, G. Van Steenberge and O.M. Parriaux. High-efficiency diffraction grating coupler. In *Photonics Europe'06, Proceedings SPIE 6185, Micro-Optics VCSELs And Photonic Interconnects: Fabrication, Packaging And Integration*, Apr 2006.

### The following papers have been presented at national conferences

- G. Van Steenberge, P. Geerinck, S. Van Put, N. Hendrickx, H. Ottevaere, H. Thienpont and P. Van Daele. Laser ablated micromirrors for optical printed circuit boards. In *Proceedings 5th FTW PhD Symposium, Faculty Of Engineering, Ghent University*, Dec 2004.
- N. Hendrickx, G. Van Steenberge, P. Geerinck and P. Van Daele. Multilayer optical interconnects integrated on a printed circuit board. In *Proceedings 6th FTW PhD Symposium, Faculty Of Engineering, Ghent University*, Dec 2005.

### The following presentations were done at international symposia, without proceedings

- P. Van Daele, P. Geerinck, G. Van Steenberge and S. Van Put. Optics on pcb's: a dream coming true. *Symposium: Short Distance Optical Interconnects - From Backplanes To Intrachip Communication*, Mar 2003.

- G. Van Steenberge and P. Van Daele. Waveguides in boards based on ormocer®s. *DATE Workshop On Parallel Optical Interconnects Inside Electronic Systems*, Feb 2004.
- G. Van Steenberge, M. Taghizideh and P. Van Daele. Laser patterning. *Workshop On Micro-Optics - Benefits For Industry NEMO-FP6-Project*, Apr 2005.

# References


[1] J.W. Goodman, F.J. Leonberger, S.Y. Kung, and R.A. Athale. Optical interconnections for vlsi systems. *Proceedings Of The IEEE*, 72(7):850–866, Jul 1984.

[2] International Technology Roadmap for Semiconductors 2005 Edition. `http://www.itrs.net`.

[3] M. Shafer, B. Das, and G. Patel. Connector and chip vendors unite to produce a high-performance 10 gb/s nrz-capable serial backplane. In *DesignCon, Proceedings High-Performance System Design Conference*, Jan 2003.

[4] B. Chan, J. Lauffer, S. Rosser, and J. Stack. Pwb solutions for high speed systems. In *ECTC'04, Proceedings Electronic Components And Technology Conference*, May 2004.

[5] J.T. Stonick, G.Y. Wei, J.L. Sonntag, and D.K. Weinlader. An adaptive pam-4 5-gb/s backplane transceiver in 0.25-mu m cmos. *IEEE Journal Of Solid-State Circuits*, 38(3):436–443, Mar 2003.

[6] J.L. Zerbe, C.W. Werner, V. Stojanovic, F. Chen, J. Wei, G. Tsang, D. Kim, W.F. Stonecypher, A. Ho, T.P. Thrush, R.T. Kollipara, M.A. Horowitz, and K.S. Donnelly. Equalization and clock recovery for a 2.5-10-gb/s 2-pam/4-pam backplane transceiver cell. *IEEE Journal Of Solid-State Circuits*, 38(12):2121–2130, Dec 2003.

[7] T. Beukema, M. Sorna, K. Selander, S. Zier, B.L. Ji, P. Murfet, J. Mason, W. Rhee, H. Ainspan, B. Parker, and M. Beakes. A 6.4-gb/s cmos serdes core with feed-forward and decision-feedback equalization. *IEEE Journal Of Solid-State Circuits*, 40(12):2633–2645, Dec 2005.

[8] A. Adamiecki, M. Duelk, and J.H. Sinsky. 25 gbit/s electrical duobinary transmission over fr-4 backplanes. *Electronics Letters*, 41(14):826–827, Jul 7 2005.

[9] D.A.B. Miller. Physical reasons for optical interconnection. *International Journal Of Optoelectronics*, 11(3):155–168, May-Jun 1997.

[10] D.A.B. Miller. Rationale and challenges for optical interconnects to electronic chips. *Proceedings Of The IEEE*, 88(6):728–749, Jun 2000.

[11] 2 mm HM Connector Noise Analysis Differential Pair Signal Placement Comparison. Tyco Electronics Circuits and Designs. `http://www.tycoelectronics.com/products/simulation/files/papers/hmcna_2.pdf`.

[12] Z-Pack HM-Zd Connector Noise Analysis for Xaui Applications. Tyco Electronics Circuits and Designs. `http://catalog.tycoelectronics.com/TE/GeneralInfo/connector_noise_analysis.pdf`.

[13] M.A. Taubenblatt. Challenges and opportunities for integrated optics in computing systems. In *Photonics West'06, Proceedings SPIE 6124, Optoelectronic Integrated Circuits*, Jan 2006.

[14] iNEMI Technology Roadmap 2005. `http://www.inemi.org/`.

[15] L.A.B. Windover, J.N. Simon, S.A. Rosenau, K.S. Giboney, G.M. Flower, L.W. Mirkarimi, A. Grot, B. Law, C.K. Lin, A. Tandon, R.W. Gruhlke, H. Xia, G. Rankin, M.R.T. Tan, and D.W. Dolfi. Parallel-optical interconnects $>$ 100 gb/s. *Journal Of Lightwave Technology*, 22(9):2055–2063, Sep 2004.

[16] D.M. Kuchta, Y.H. Kwark, C. Schuster, C. Baks, C. Haymes, J. Schaub, P. Pepeljugoski, L. Shan, R. John, D. Kucharski, D. Rogers, M. Ritter, J. Jewell, L.A. Graham, K. Schrodinger, A. Schild, and H.M. Rein. 120-gb/s vcsel-based parallel-optical interconnect and custom 120-gb/s testing station. *Journal Of Lightwave Technology*, 22(9):2200–2212, Sep 2004.

[17] B.E. Lemoff, M.E. Ali, G. Panotopoulos, G.M. Flower, B. Madhavan, A.F.J. Levi, and D.W. Dolfi. Maui: Enabling fiber-to-the-processor with parallel multiwavelength optical interconnects. *Journal Of Lightwave Technology*, 22(9):2043–2054, Sep 2004.

[18] Photonic links in ATM and optical systems (PLATO). `http://cordis.europa.eu.int/`.

[19] K. Vandeputte, P. Van Daele, E. Hoedt, J. Van Koetsem, and J. Hossfeld. Low cost multi-fiber add/drop multiplexer demonstration system. In *ECOC'99, Proceedings European Conference On Optical Communication*, pages 112–113, Sep 1999.

[20] J. Hossfeld, W. Ehrfeld, M. Neumeier, J. Schulze, L. Weber, and A. Picard. Micro-optical components for parallel optical networks. In *IEEE/LEOS Summer Topical Meetings, Broadband Optical Networks And Technologies: An Emerging Reality/Optical MEMS/Smart Pixels/Organic Optics And Optoelectronics*, pages 39–40, Jul 1998.

[21] High Bitrate ATM Termination and Switching (HIBITS). `http://cordis.europa.eu.int/`.

[22] G. De Pestel, A. Picard, J. Vandewege, D. Morlion, Q. Tan, J. Van Koetsem, F. Migom, and P. Vetter. Parallel optical interconnections for future broad band systems, based on the fiber in board technology. In *ECTC'96, Proceedings Electronic Components And Technology Conference*, pages 264–268, May 1996.

[23] Q. Tan, J. Vandewege, G. De Pestel, P. Vetter, and F. Migom. 2.5 gb/(s-mm) optical fiber interconnections. In *ECOC'96, Proceedings European Conference On Optical Communication*, pages II55–II58, Sep 1996.

[24] Molex FlexPlane$^{TM}$ optical flex circuit. `http://www.molex.com`.

[25] AMP LIGHTRAY OFX$^{TM}$ Interconnection System. `http://amp.com`.

[26] Interconnect by Optics (IO). `http://io.intec.ugent.be`.

[27] C. Berger, X. Wang, J.T. Ekman, P.J. Marchand, H. Spaanenburg, M.M. Wang, F.E. Kiamilev, and S.C. Esener. Parallel processing demonstrator with plug-on-top free-space interconnect optics. In *Photonics West'01, Proceedings SPIE 4292, Optoelectronic Interconnects*, pages 105–116, Jan 2001.

[28] M. Chateauneuf, A.G. Kirk, D.V. Plant, T. Yamamoto, and J.D. Ahearn. 512-channel vertical-cavity surface-emitting laser based free-space optical link. *Applied Optics*, 41(26):5552–5561, Sep 10 2002.

[29] C. Debaes, M. Vervaeke, V. Baukens, H. Ottevaere, P. Vynck, P. Tuteleers, B. Volckaerts, W. Meeus, M. Brunfaut, J. Van Campenhout, A. Hermanne, and H. Thienpont. Low-cost microoptical modules for mcm level optical interconnections. *IEEE Journal Of Selected Topics In Quantum Electronics*, 9(2):518–530, Mar-Apr 2003.

[30] D.T. Neilson and E. Schenfeld. Plastic modules for free-space optical interconnects. *Applied Optics*, 37(14):2944–2952, May 10 1998.

[31] F. Lacroix, E. Bernier, M.H. Ayliffe, F.A.P. Tooley, D.V. Plant, and A.G. Kirk. Implementation of a compact, four-stage, scalable optical interconnect for photonic backplane applications. *Applied Optics*, 41(8):1541–1555, Mar 10 2002.

[32] N. McArdle, M. Naruse, H. Toyoda, Y. Kobayashi, and M. Ishikawa. Reconfigurable optical interconnections for parallel computing. *Proceedings Of The IEEE*, 88(6):829–837, Jun 2000.

[33] X.Z. Zheng, P.J. Marchand, D.W. Huang, and S.C. Esener. Free-space parallel multichip interconnection system. *Applied Optics*, 39(20):3516–3524, Jul 10 2000.

[34] K. Hirabayashi, T. Yamamoto, S. Matsuo, and Hino S. Board-to-board free-space optical interconnections passing through boards for a bookshelf-assembled terabit-per-second-class atm switch. *Applied Optics*, 37(14):2985–2995, May 10 1998.

[35] M.W. Haney, M.P. Christensen, P. Milojkovic, G.J. Fokken, M. Vickberg, B.K. Gilbert, J. Rieve, J. Ekman, P. Chandramani, and F. Kiamilev. Description and evaluation of the fast-net smart pixel-based optical interconnection prototype. *Proceedings Of The IEEE*, 88(6):819–828, Jun 2000.

[36] M. Gruber, J. Jahns, E.M. El Joudi, and S. Sinzinger. Practical realization of massively parallel fiber-free-space optical interconnects. *Applied Optics*, 40(17):2902–2908, Jun 10 2001.

[37] J. Ellis, R. Mays, D. Griffiths, H. Bi, J. Choi, W. Jiang, and R.T. Chen. Holographic optical elements for optical backplane bus targeted at high speed data transfer. In *Photonics West'06, Proceedings SPIE 6126, Nanophotonic Packaging*, Jan 2006.

# Chapter 2

# Optical waveguide materials

*In this chapter, an overview of currently available optical materials for board-level optical interconnections will be presented. Specific properties of polymer and glass materials will be discussed. Special attention will be given to optical loss, environmental stability, and compatibility with standard PCB manufacturing. Process parameters for the polymers being used in this PhD dissertation will be addressed in detail, together with surface characterization results.*

## 2.1 Introduction

Waveguiding materials to be used for board-level optical interconnections can be divided into two main categories: polymers and glass sheets. Novel optical polymers are engineered in many laboratories worldwide, and some are commercially available. Thin glass sheets are available from companies which supply into the liquid crystal display market. Key ideal requirements for waveguide materials include: low optical loss, high thermal stability, refractive index controllability, good adhesion, good dimensional stability, low birefringence and stable optical properties. Optical loss is a key selection factor and has been the major barrier to the adoption of polymer waveguides in applications for a long time. Other concerns are expressed with regard to the environmental performance: thermal and humidity stability. Thermal stability is very important particularly in applications where an optical layer is to be laminated within a conventional electrical printed circuit board. Moreover, during soldering of the board, temperature reaches 230$^o$C for a short time during solder reflow, and even higher temperatures for lead-free solders. On the other hand, polymers provide for the flexible and low cost fabrication of structures through simple application techniques and low temperature processing.

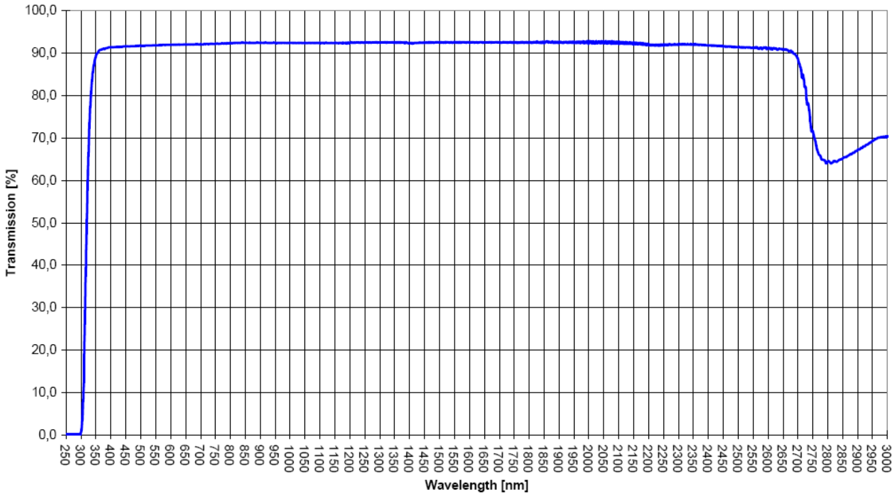


**Figure 2.1:** Low optical loss of borosilicate glass (D263T) over a broad spectrum (source: Schott [3])

## 2.2 Thin glass sheets

For decades, glass has been the most popular material for making optical components and devices. A wide range of glasses has been developed for the diverse needs of applications, from consumer products, such as lenses, and components for cameras and projectors, binoculars, and telescopes, to high-tech industrial applications, including microscopy, medical instruments, data discs, and image processing. The concept to laminate thin glass foils in between the conventionally used PCB substrate layers was developed to decrease the board-CTE [1, 2], resulting in a better thermal and mechanical stability. Moreover it is a straightforward idea that this thin glass sheet can be used as an optical layer with multimode waveguide structures of arbitrary layout as well. The advantage is that the waveguides are of high thermal reliability and low optical loss.

The glass type selected is a borosilicate glass D263T [3], manufactured using the purest raw materials, and can be manufactured in thicknesses down to 30 $\mu$m, being compatible with the 50 $\mu$m semi-standard for multimode optical interconnections. Borosilicate glass has a low coefficient of thermal expansion (CTE $= 7.2 \times 10^{-6}$ K$^{-1}$), about three times less than the other popular glass, soda-lime, which makes it useful for heating without the risk of cracking due to thermal shock. It is thermally stable up to 500$^o$C for continuous use and 600$^o$C for short periods. The thin glass sheets feature a low optical loss over a broad spectrum (Figure 2.1), superior to polymers.

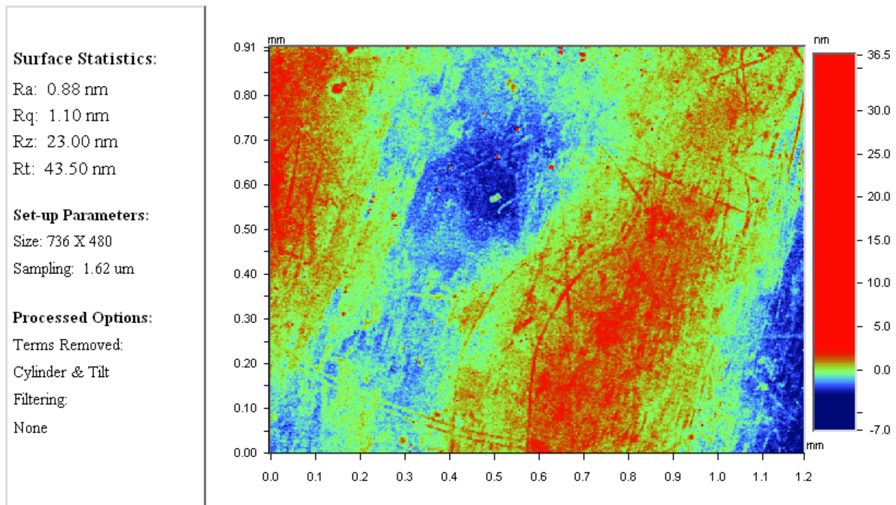


**Figure 2.2:** Surface roughness of a 70 $\mu$m thick glass sheet, measured using a non-contact optical profiler (Wyko NT2000)

The sheets have an excellent surface quality. The surface smoothness is verified using a non-contact optical profiler (Wyko NT2000), both the average roughness $R_a$ and the root mean square roughness $R_q$ are around 1 nm (Figure 2.2). D263T can be found in applications like resistive touch panels used for car navigation systems, cover glass for opto-couplers in laser diodes as found in CD players, temperature and humidity sensors in air conditioning, and packaging CCD and CMOS image sensors in the expanding market for camera phones [3]. The excellent temperature behaviour and high humidity resistance as well as life expectancy are crucial, not only in a PCB environment. Different technologies are available for patterning glass foils, as will be described in Chapter 4.

## 2.3 Polymers

### 2.3.1 Optical loss

For polymer materials, both electronic and vibrational absorptions are likely to contribute to the optical loss, as described in [4, 5, 6]. Polymeric media generally have large absorptions in the ultraviolet due to fundamental excitations of their electrons. These absorptions tend to be in the deep ultraviolet (less than 200 nm) for polymers with dominantly aliphatic hydrogen atoms, and in the near UV (200–400 nm) for polymers with significant numbers of aromatic hydrogens. Par-

tially or fully fluorinated polymers tend to have their UV absorptions at higher energies. For energies well below electronic energy levels of the polymer, where the polymer is basically transparent, weak absorption can result from a number of sources including singlet-triplet absorption, and vibration mediated absorptions inharmonic interactions [5]. In general, electronic absorptions in polymers are very unlikely to contribute significantly to optical losses in the major telecommunication windows near 1300 nm and 1550 nm. In the 1300–1600 nm range, absorptions coming from the overtones of fundamental molecular vibrations are dominant [7, 8]. Since the strength of the absorption tends to decrease by approximately an order of magnitude between each harmonic order, higher harmonics are generally weak enough not to be of concern. The highest energy vibrations are those that have high spring constants (stiff bonds, such as double bonds) and/or small reduced mass. The smallest reduced mass occurs when one of the atoms is hydrogen. Both C–H and O–H overtones are highly absorptive in the telecommunications windows, whereas C–F overtones, for example, show extremely low absorption throughout the range of interest, due to their higher harmonic order. As hydrogens are removed through partial fluorination, the absorption of optical polymers reduces significantly. In general, it is difficult to directly determine the absorption of an optical material, since, scattering contributions to the overall attenuation are often indistinguishable from those coming from absorption.

There are numerous extrinsic contributions to scattering loss in optical materials [5]. Most important are large inclusions such as particles, voids, cracks, and bubbles. Generally, an inclusion is considered large if it is greater than 1 $\mu$m in diameter, in which case the scattering intensity is largely wavelength independent. Extrinsic scattering in polymers can result from unfiltered particles, dust, dissolved bubbles, and unreacted monomer. To eliminate extrinsic scattering it is obviously necessary to follow clean procedures in the preparation of polymer formulations, and to perform all coating operations in a clean room.

Intrinsic scattering results from density fluctuations and compositional inhomogeneities, both of which occur on very short length scales (0.1 $\mu$m or less) [5]. Polymer layers are typically formed by spincoating processes in which polymers are deposited from solution and subsequently dried by heating in an oven or on a hotplate. The resulting films are generally uniform, but can have a roughness that will contribute to scattering losses. When thin films are deposited on substrates, an important aspect of the process is managing the stress that can develop. Polymer waveguides are ordinarily deposited at low temperatures, but solvent bakes and annealing often occur at moderate high temperatures. These temperature excursions, when coupled with the CTE mismatch that exists between the film and the substrate, result in stress-induced scattering.

As scattering comes from a number of sources, experimental scattering data is often fit with an empirical law of the form [5]:

$$\alpha_{scatter} = A + B/\lambda^2 + D/\lambda^4 \tag{2.1}$$

where A is the contribution from large particle scattering (i.e., $\gg \lambda$), B the contribution from inhomogeneities on the order of $\lambda$ in size (Mie scattering), and D the contribution from small inhomogeneities ($\ll \lambda$, Rayleigh-like). Within this PhD work, the different process steps for layer application and waveguide patterning are optimized in order to reduce scattering loss, however, no experimental scattering data is investigated.

### 2.3.2 Environmental performance

An important characteristic for practical applications is the thermal stability of optical properties because polymeric materials are subject to yellowing upon thermal aging. Typically, such aging results from the formation of partially conjugated molecular groups characterized by broad ultraviolet absorption bands, which tail off in intensity through the visible region [5]. This yellowing is strongly influenced by the chemical structure of the original polymer. In fully halogenated materials, yellowing becomes almost negligible at any wavelength because the absence of hydrogen prohibits the formation of H–halogen products that will result in carbon double bonds. These unsaturated double bonds are the major cause of yellowing when they are slowly oxidized under long-term thermal aging.

Requirements for telecommunications network devices have been developed with the goal of assuring operation for 20 to 25 years. The major governing documents for passive optical components are two monographs from Telecordia, the GR1209 and GR1221. The Telecordia GR1209 focuses primarily on optical performance tests and short-term reliability data (several weeks) that would apply to any manufactured lot of devices. The Telecordia GR1221 is a document that focuses on comprehensive reliability assurance, in particular vendor and device qualification, lot-to-lot quality and reliability control, storage, and handling. Of particular concern for polymers are extreme temperatures and humidities, as well as the broad range of temperatures.

### 2.3.3 Compatibility with standard PCB manufacturing

To be widely compatible with existing PCB manufacturing processes, the high pressure and temperature conditions during lamination must be taken into account. A temperature of about 170 $^o$C and higher at a pressure of about 150 N/cm$^2$ is needed to laminate FR4 material over the course of more than one hour (Figure 2.3) [9]. Moreover, further considerations regarding soldering

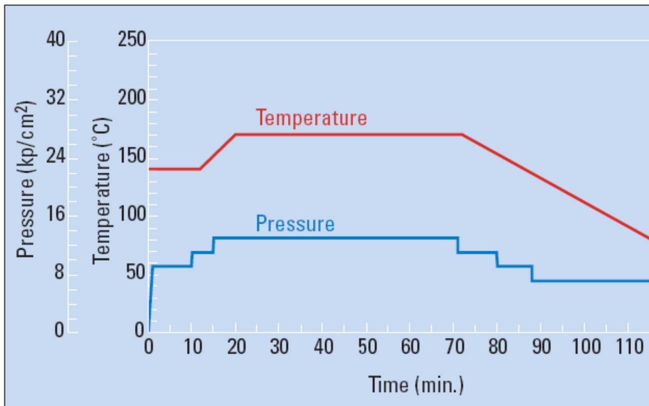


**Figure 2.3:** Temperature and pressure during FR4 lamination [9]

of the board must be taken into account when the temperature reaches 230 $^o$C for a short time during reflow, and even higher temperatures for lead-free solders. There are some further requirements that seem obvious, but that nonetheless are extremely important and merit mention. The first one is the compatibility of the waveguide material with conventional board material (FR4, flame retardent laminate made from woven glass fiber impregnated with expoy resin). Mechanical, thermal, and climate property requirements of optoelectronic PCBs must also be addressed. In order to guarantee trouble-free mounting of the active and passive components on optoelectronic PCBs, the same planarity, of the entire board as well as of the chip area itself, must be postulated, which is state-of-the-art for PCBs. Also, electrical properties such as dielectric strength and isolation resistance of the optical material must be considered.

### 2.3.4 Overview of novel optical polymers

In the past twenty years, several major families of novel optical polymers have been developed in academic and industrial laboratories. In addition to the review articles [4, 5, 6] some recent updates on developed materials will be given in this section, a summary is presented in Table 2.1, and Table 2.2. Currently, the available optical polymers are highly transparent with absorption loss values close to 0.1 dB/cm at all major communication wavelengths (840, 1310, and 1550 nm). The propagation loss given in Table 2.1, and Table 2.2 are for multimode waveguides (for datacom) and for single mode waveguides (for telecom).

| Manufacturer | Polymer Type [Trade Name] | Loss, dB/cm [wavelength, nm] | Ref |
|---|---|---|---|
| Amoco | fluorinated polyimide [Ultradel] | 0.4 [1300 nm]<br>1.0 [1550 nm] | [5] |
| Asahi Glass | perfluorovinyl ether cyclopolymer [CYTOP] | | [5, 10] |
| Corning (formerly AlliedSignal) | acrylate | 0.02 [840 nm]<br>0.3 [1300 nm]<br>0.8 [1550 nm] | [4, 5, 6] |
| | halogenated acrylate | 0.01 [840 nm]<br>0.06 [1300 nm]<br>0.2 [1550 nm] | [4, 5, 6] |
| Dow Chemical | benzocyclobutene [Cyclotene] | 0.8 [1300 nm]<br>1.5 [1550 nm] | [5, 6] |
| | perfluorocyclobutene [XU 35121] | 0.25 [1300 nm]<br>0.25 [1550 nm] | [5, 6] |
| DuPont | tetrafluoroethylene and perfluorovinyl ether copolymer [Teflon AF] | | [5, 6] |
| Exxelis (formerly Terahertz) | acrylate [Truemode$^{TM}$] | 0.04 [850 nm]<br>0.3 [1310 nm]<br>0.5 [1550 nm] | [11] |
| General Electric | polyetherimide [Ultem] | 0.24 [830 nm] | [5, 12] |
| Hitachi | fluorinated polyimide | TE: 0.5 [1300 nm]<br>TM 0.6 [1300 nm] | [5, 6] |

**Table 2.1:** Loss of optical polymers to be used for board-level interconnections - part 1

| Manufacturer | Polymer Type [Trade Name] | Loss, dB/cm [wavelength, nm] | Ref |
|---|---|---|---|
| Micro resist technology | polysiloxane [Ormocer®] | 0.05 [830 nm]<br>0.2 [1310 nm]<br>0.6 [1550 nm] | [13, 14] |
| | epoxy [EpoCore] [EpoClad] | 0.2 [850 nm] | [13, 15] |
| NTT | halogenated acrylate | 0.02 [830 nm]<br>0.07 [1310 nm]<br>1.7 [1550 nm] | [5] |
| | deuterated polysiloxane | 0.17 [1310 nm]<br>0.43 [1550 nm] | [5, 16, 17] |
| | fluorinated polyimide | TE: 0.3 [1310 nm]<br>TM 0.7 [1310 nm] | [5] |
| | epoxy | 0.1 [850 nm] | [18] |
| Luvantix | epoxy | 0.04 [850 nm] | [19] |
| Optical Crosslinks (formerly Dupont and Polymer Photonics) | acrylate [GuideLink] | 0.08 [800 nm]<br>0.2 [1300 nm]<br>0.6 [1550 nm] | [20] |
| Promerus | polynorbornene | 0.1 [820 nm] | [21] |
| RPO (formerly Redfern) | inorganic polymer glass [IPG] | 0.24 [1322 nm]<br>0.52 [1548 nm] | [22, 23] |
| Telephotonics | [OASIC] | 0.01 [840 nm]<br>0.03 [1300 nm]<br>0.1 [1550 nm] | [5] |

**Table 2.2:** Loss of optical polymers to be used for board-level interconnections - part 2

**Deuterated and halogenated polyacrylates**

Allied-Signal developed a wide variety of photo-crosslinkable, optically transparent polymers based on the combinations of multifunctional halogenated acrylate monomers and oligomers in addition to various additives. The polymers allow the creation of waveguides with low scattering losses and low polarization-dependent losses. Upon UV-exposure the monomer systems form highly crosslinked networks, which exhibit low intrinsic absorption in the wavelength range extending from 400 to 1600 nm. At 840 nm, losses are as low as 0.02 dB/cm, and 0.01 dB/cm for the halogenated acrylates. By blending and copolymerization with selected miscible monomers, this approach allows precise tailoring of the refractive index over a broad range from 1.3 to 1.6, although it can be difficult to simultaneously achieve a given refractive index and low intrinsic absorption at the same time. It is possible to tailor other physical proporties such as flexibility, toughness, surface energy, and adhesion to specific applications.

NTT has developed deuterated polyfluoromethacrylate with high transparency, low birefringence, and good processibility. They have also developed processes to fabricate low optical loss single mode and multimode optical waveguides with these polymers. The propagation loss and waveguide birefringence of the single mode waveguides were as low as 0.1 dB/cm and $-5.5\times10^{-6}$ at 1310 nm, respectively. The propagation losses of the multimode waveguides were less than 0.02 dB/cm at both 680 nm and 830 nm, and 0.07 dB/cm at 1310 nm.

Polyguide, developed by DuPont (currently Optical Crosslinks, and commercially available under the name GuideLink) has shown excellent layer quality and thickness control. GuideLink can be machined using excimer lasers to form mechanical structures with a high degree of accuracy allowing for connection to a mechanically transferable (MT type) ferrule packaged with push/pull housing connected to a multichannel standard ribbon fiber [20]. GuideLink possesses relatively high optical losses (0.08 dB/cm at 800 nm, 0.2 dB/cm at 1300 nm, and 0.6 dB/cm at 1550 nm) due to its non-halogenated acrylate structure.

Heriot-Watt University developed polyacrylate optical polymers based on sulphur containing monomers, with very high thermal stability, up to 250$^o$C or more, with a good range of refractive index and viscosity, and good adhesion to typical substrates. The Truemode$^{TM}$ materials are commercially available (Exxelis, formerly Terahertz), and are one of the investigated polymers in this PhD dissertation, discussed in more detail in Section 2.5.

**Fluorinated polyimides**

Polyimides are a proven class of polymers in the microelectronics industry due to their high thermal stability ($>300^o$C) and outstanding dielectric and mechanical properties. However, conventional polyimides are not suitable for use as optical

materials. Several types of fluorinated polyimides that feature low optical loss in the near infrared region, a broad range of refractive index control, and excellent heat resistance have been introduced by Amoco (Ultradel), General Electric (Ultem), NTT and Hitachi. Fluorinated polyimides can suppress refractive index fluctuations and the presence of pinholes, two main causes for the observed waveguide losses in conventional polyimides. One intrinsic problem that is still difficult to avoid is the large birefringence and polarization dependent loss. At 830 nm Ultem shows an optical loss of 0.24 dB/cm, it is mostly combined with BCB as a cladding layer [12].

### Perfluorocyclobutyl aryl ether polymers

For most spincoating applications, the solubility of optical polymers needs to exceed 50 wt.-% in common solvents if a reasonable film thickness and planarity is to be obtained [5]. This basic requirement severely limit the use of many fluoropolymers. However, poly (aryl ether) polymers, first developed by Dow Chemical, possess both high-performance properties and processibility [24, 25], high temperature stability ($T_g = 120–350^oC$), precisely controlled refractive index, low moisture absorption, and a low absorption at 1300 and 1550 nm ($< 0.25$ dB/cm).

### Miscellaneous highly fluorinated polymers

Perfluorinated ether-containing polymer [10], CYTOP, developed by Asihi Glass Co. and the copolymers between Teflon and fluorinated ketal Teflon AF, developed by DuPont are two interesting perfluorinated polymers that possess excellent optical properties for low loss polymer optical fibers at both visible and infrared wavelengths. Nexans Research Center has developed a new version of POF based on CYTOP, within the European IST-IO-project (Interconnect by Optics) [26], replacing copper intrasystem links with POF, at the chip-access, onboard and board-to-board levels. The graded-index fiber has an attenuation below 30 dB/km at 850 nm. However, there are some limitations for using the polymers for optical waveguide applications, such as: difficult in integrating them in multilayer waveguide structures due to poor adhesion, thermo-mechanical stability, and difficulty in waveguide processing using established fabrication techniques.

### Polysiloxanes

Inorganic polymers, polysiloxanes, have been developed by NTT (deuterated siloxanes), Fraunhofer Institute (Ormocer®s), and Redfern (currently RPO, inorganic polymer glass, IPG). NTT synthesized deuterated phenylsilyl chloride monomers as the starting materials for the waveguide core polymer. The struc-

ture of the synthesized polymer has two distinctive characteristics. One is the adoption of a polysiloxane backbone (–Si–0–) to provide high heat resistance compared with carbon–carbon (C–C) bonds. The other is the adoption of a deuterated substituent in the phenyl group with lower absorption at both 1300 and 1550 nm than that of normal (non-deuterated) phenylsilyl chloride. On the other hand, since a phenyl group has a large molecular refraction, the refractive index of the polymer can be changed by controlling the contents of the phenyl group. Single mode channel waveguides using the polymer were fabricated by dry etching. The propagation loss of the channel waveguides was 0.17 dB/cm at 1310 nm and 0.43 dB/cm at 1550 nm. The thermal and environmental stability of the waveguides was demonstrated by the fact that the propagation loss remained unchanged after tests at $> 200^o$C for 30 min, at $> 120^o$C for 1000 h, and at $> 75^o$C and 90% RH for 1000 h [16, 17].

The Ormocer® materials (ORganic MOdified CERamics), developed by the Fraunhofer Institute, and made commercially available by micro resist technology, are synthesized by organic crosslinking of polycondensed alkoxysilanes (solgel processing), which offers a tremendous flexibility in polymer synthesis by variation of catalyst, temperature, and alkoxysilane scaffold. This flexibility enable one to adjust the polymers to particular application parameters, refractive indices can be tuned over a wide range by mixing various resins. They have been proven to combine very good optical and dielectrical properties in the lower high frequency region, which makes them promising candidates for electro-optical applications. They have low transmission losses in the near infrared range for the wavelengths 830 nm, 1310 nm and 1550 nm. The material processing is compatible to conventional equipment in thin film processing, and Ormocer®s adhere very well on most substrates such as (metallized) Si wafers, inorganic glasses, polymers, and FR4 material. Their thermal stability is high enough for most of the technological applications (decomposition temperature $> 270^o$C). The Ormocer® materials are discussed in more detail in Section 2.4, together with the process parameters for the application of the optical layers.

The inorganic polymer glass (IPG), developed by Redfern (currently RPO) [22], is a reactive branched-chain polysiloxane. Georgia Institute of Technology reported IPG waveguide losses of 0.24 dB/cm at 1322 nm and 0.52 dB/cm at 1548 nm [23].

The University of Dortmund reported on two-component room temperature crosslinking polysiloxanes of Wacker Chemie GmbH. The cladding materials are standard commercial polymers, whereas the core polymer is a special development of Wacker in close cooperation with the University of Dortmund [27, 28]. Typical loss figures at 850 nm are 0.05 dB/cm. The optical layer is laminated between two FR4 boards by standard PCB processes. Good adhesion to the FR4 is achieved by using special adhesion promoters. The board stability has been tested against soldering reflow conditions by subsequent annealing at $230^o$C for 5 minutes. No degradation effects in the optical transmission could be observed.

### Epoxies

Epoxies to be used for low loss optical waveguides are developed by Luvantix, NTT, and by micro resist technology (EpoCore, EpoClad). The epoxy duromer type EpoCore and EpoClad, are new materials for optical waveguides in PCB for New Generation Interconnection Technology (NegIT) [15], and have a high heat and pressure resistance, tunable refractive index (core/cladding), and a high transmittance at 830 nm (0.1–0.2 dB/cm for lithographic defined waveguides) [13]. The UV-curable epoxy from Luvantix has a controllable refractive index (1.38–1.52), low birefringence, and a low propagation loss of 0.04 dB/cm at 830 nm [19]. NTT reported on multimode waveguides based on UV-curable epoxy, both for core and cladding, with a propagation loss of 0.1 dB/cm at 850 nm [18].

### Polynorbornenes

BFGoodrich has over three decades of experience with cyclic olefins (e.g., norbornene type monomers) and polymers derived therefrom. Recently, they have developed a novel catalyst system that allows the addition polymerization of norbornene-type monomers. The innovation of the catalyst system leads to a new generation of polycyclic olefins, enabling cyclic olefin based waveguide polymers, with intrinsically good optical, mechanical and moisture absorption properties. The intrinsic properties of the polynorbornene system include low transmission loss ($< 0.1$ dB/cm at 820 nm), wide spectral range ($< 0.4$ dB/cm at 450 nm and $< 0.1$ dB/cm at 515–870 nm), low birefringence, consistent difference in index over a wide temperature range, long-term thermal stability ($> 2000$ h at 125$^o$C), high glass transition temperature ($> 280^o$C), and low moisture absorption ($<$0.1%). Candidate materials have been identified as core and cladding components for optical waveguides. The refractive index of a typical core material is 1.53, and of a typical cladding material, 1.50 at 820 nm.

## 2.4 Ormocer®s

### The materials

The first step of the Ormocer® synthesis is a hydrolysis/condensation reaction, which starts with commercially available functionalized alkoxysilanes or novel synthesized perfluoroaryl silanes and leads to the formation of organically modified inorganic nanoscale oligomers (Figure 2.4). Their size and shape can be influenced easily by modifying the polycondensation conditions (such as, e.g., catalyst, concentration, solvent, or temperature) ([14, 29, 30]). Several organic side chains, carrying the polymerizable functionality, are appended to the inor-

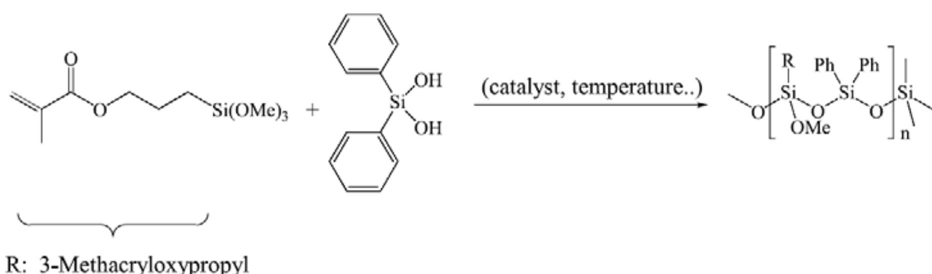


**Figure 2.4:** Principle of solgel reaction of alkoxysilanes to organically modified inorganic oligomers (source: Fraunhofer Institute [14])

ganic Si–O–Si backbone of the individual oligomers. Residual Si–OH groups can be reduced by silylating agents.

The second processing step after the addition of thermal- and/or photoinitiator contains a polymerization reaction, leading to a fully crosslinked three dimensional network. This is one of the reasons for the good structure accuracy up to temperatures of 270$^o$C in comparison to conventional thermoplast materials. The Ormocer® materials have been developed to come as ready to use photosensitive mixtures.

### Processing

The fabrication of a three-layer Ormocer® structure (undercladding, core, and uppercladding) is eased by the possibility of changing and influencing the refractive index of the materials by mixing different components. This allows both cladding and core layers to be fabricated using the same material, which facilitates the compatibility and stacking of the layers. The refractive indices are 1.5306 and 1.5475 for cladding and core, respectively, at a wavelength of 830 nm. The thickness of the optical layers is determined by the viscosity of the solution being applied. In order to change this viscosity and, hence, the thickness of the layers, the resin can be diluted (Figure 2.5). The Ormocer® layers (each 50 $\mu$m thick) are prepared by spincoating at, typically, 700 rpm for 40 sec for a dilution of 20:1 (20 Vol.% Ormocer® and 1 Vol.% propylacetate). Because the uniformity of the layers enhances at higher spin speeds, for further experiments the non-diluted solution is used. Spin speed of 1500 rpm for a 50 $\mu$m thick cladding layer, and 1800 rpm, for a 50 $\mu$m core layer. The spin speed is slightly different, because cladding and core have a different viscosity: at 25$^o$C and solvent free 2.5–4 Pa s (Ormoclad), 3–4 Pa s (Ormocore). Spincoating is used in this PhD dissertation since sample sizes are not exceeding $10 \times 10$ cm$^2$.

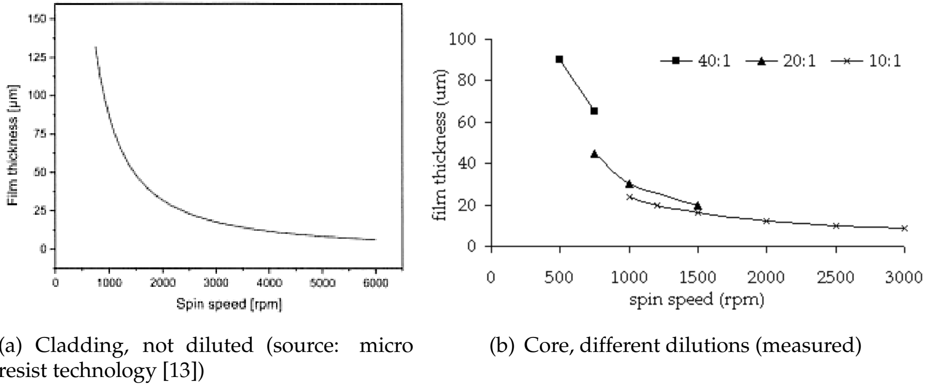


(a) Cladding, not diluted (source: micro resist technology [13])

(b) Core, different dilutions (measured)

**Figure 2.5:** Spin curves for Ormocer®

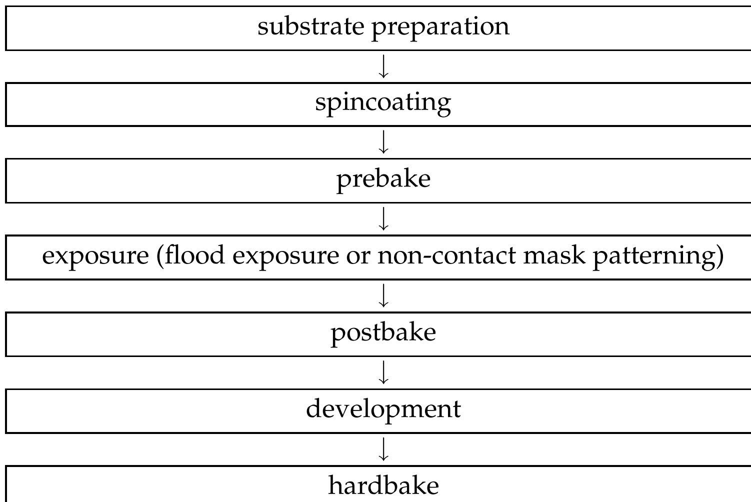


**Table 2.3:** Process flow for the application of one Ormocer® layer

Before applying the Ormocer® layers, the substrates are cleaned with aceton-IPA-DI water, and dried on a hotplate (120$^o$C) for 20 min. See Table 2.3 for an overview of the process flow. After being spun on, the layers are treated thermally (prebake) at 80$^o$C for approximately 2 min. UV exposure is used at a typical power density of 10 mW/cm$^2$ (UV lamp OmniCure, broadband) for approximately 40 sec. After the UV exposure, the samples undergo a second thermal treatment (postbake) at 80$^o$C–120$^o$C for 5 min. After a 1 min cool-down period, the layers are developed for approximately 20 sec in Ormodev [13]. Finally, the samples were treated for approximately 180 min at 150$^o$C (final curing step). This

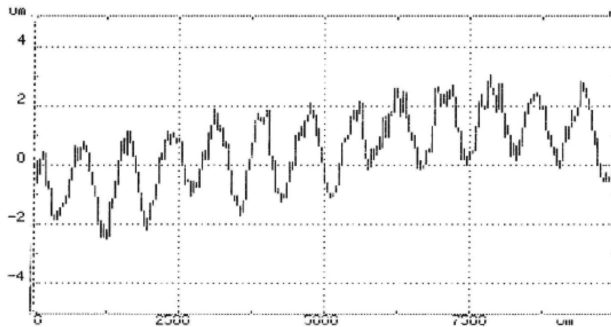


(a) Surface roughness of an FR4 substrate

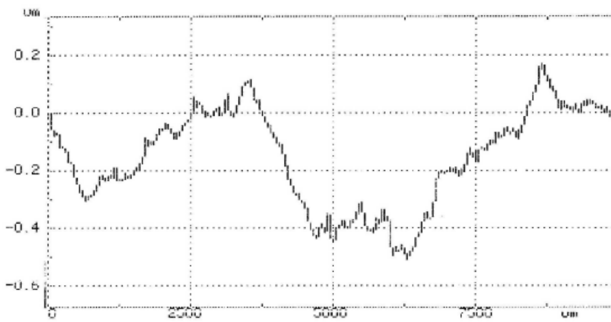


(b) Surface roughness of a 20$\mu$m thick cladding layer, spincoated on an FR4 substrate

**Figure 2.6:** Planarization properties of Ormocer®, measured using a Tencor Alphastep-200 stylus profiler

process sequence is used for both cladding and core. It seems that after final curing of the undercladding layer, the adhesion of the core layer is not very well. This is solved by using an $O_2$ plasma, but as this requires an additional processing step, an alternative solution is found. When the undercladding and core layer are cured together, no adhesion problems are observed.

One of the issues associated with optical waveguide integration onto a PCB is the surface roughness of the FR4 substrate. Figure 2.6 illustrates the planarization properties of the Ormocer®: surface profile of the FR4 substrate, and surface profile of the 20 $\mu$m thick cladding layer, spincoated on top of the FR4, measured using a surface profiler (Tencor Alphastep-200, with a scanning stylus of 12.5 $\mu$m radius). The long-period roughness is 300 nm on a 5000 $\mu$m period. There are two explanations for the good planarization properties: (1) it is a low molecular weight material that has the ability to smooth out easily and (2) shrinkage is not a major concern.

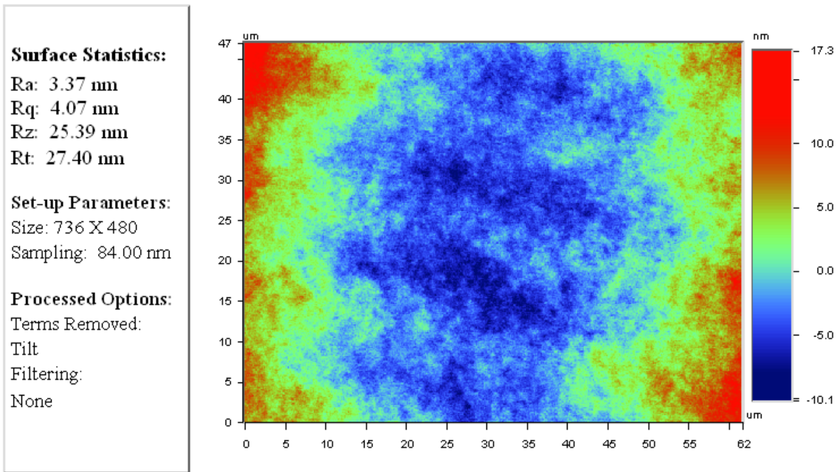


**Figure 2.7:** Surface roughness of one Ormocer® cladding layer integrated on FR4

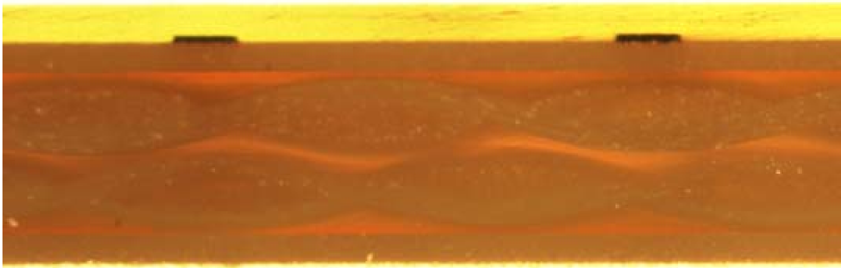

**Figure 2.8:** Cross-section showing electrical tracks covered by an Ormocer® layer integrated on a halogen-free FR4 substrate

Short-period roughness is measured using a non-contact optical profiler (WYKO NT2000), scan area of $60 \times 45\,\mu m^2$, tilt removed, gives an $R_a$ surface roughness of 3–4 nm (Figure 2.7).

A cross-sectional view of a standard FR4 based PCB with two electrical tracks covered by an optical layer is shown in Figure 2.8. The optical layer is not laminated in the PCB but is applied onto the surface. This has obviously implications on further process steps: different approaches and requirements for waveguide processing, for the creation of optical coupling and interfaces, and for the assembly of the boards.

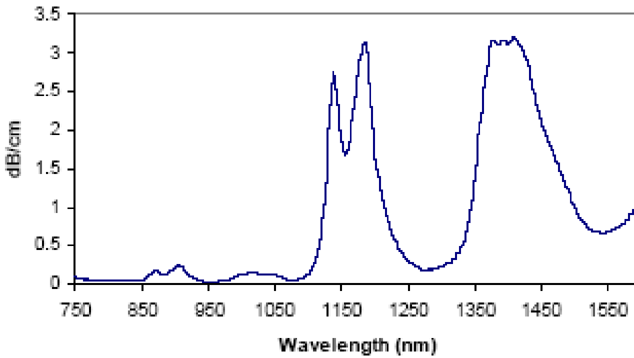


**Figure 2.9:** Optical transparency of Truemode™ (source: Exxelis [11])

## 2.5 Truemode™

### The materials

The Truemode™ family of polymers is a range of multi-functional acrylate polymers for the fabrication of low cost and high performance optical interconnects. The polymers offer a unique combination of low loss, wide-range of refractive index, photo-sensitivity, and environmental stability. They are specifically designed to be compatible with PCB manufacturing including lamination, metal coating and reflow soldering applications. As little material synthesis information is available in literature, the synthesis is illustrated by one example, described in different patents [31]:

*2.00 g phenylthioethyl acrylate (from Bimax) was added to 2.00 g methyl methacrylate (from Sigma-Aldrich) and 1.25 g ethoxylated bisphenol A dimethacrylate (from Roehm GmbH) and thoroughly mixed. 0.25 g polymethyl methacrylate powder was added to this solution and dissolved by stirring at 60°C for 12 h. This mixture was further reacted for 96 h at 60°C. 0.1838 g photo-initiator (Irgacure 184 from Ciba Specialty Chemicals) was also added to the above mixture and dissolved. This solution was filtered using a 1 μm glass pre-filter and 0.2 μm Teflon filter.*

### Processing

The optical transparency of the polymer is illustrated in Figure 2.9, showing low optical loss at datacom and telecom wavelengths. The refractive indices are 1.5266 and 1.5563 for cladding and core, respectively, at a wavelength of 850 nm. Before applying the Truemode™ layers, the substrates are cleaned with aceton-IPA-DI water, and dried on a hotplate (120°C) for 20 min. See Table 2.4 for an

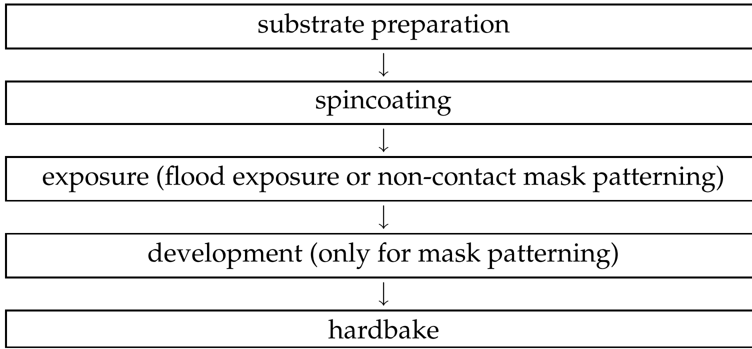


**Table 2.4:** Process flow for the application of one Truemode™ layer

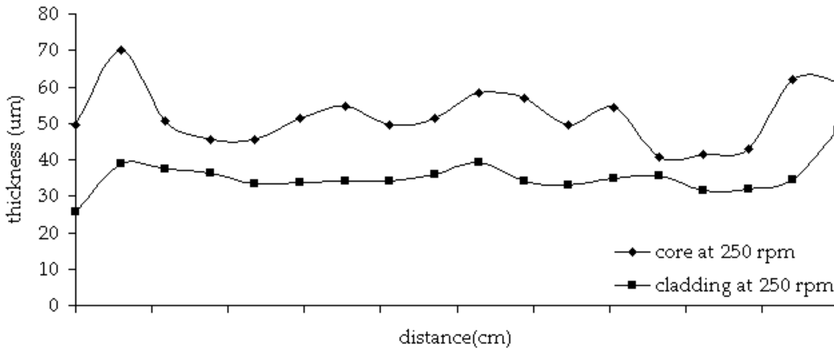


**Figure 2.10:** Non-uniformity of spincoated Truemode™ layers

overview of the process flow. The materials are applied by spincoating. Because of the low viscosity, very low spin speeds are required to obtain a layer thickness of 50 $\mu$m, and the homogeneity of the layers becomes critical. The thickness variation for a 10×10 cm$^2$ substrate is shown in Figure 2.10. The average core thickness for a spin speed of 250 rpm is 52 $\mu$m, standard deviation of 7 $\mu$m; average cladding thickness is 35 $\mu$m, standard deviation of 4 $\mu$m. By ignoring edges of 1 cm (edge bead), the average core thickness is 50 $\mu$m, standard deviation of 5 $\mu$m; average cladding thickness is 35 $\mu$m, standard deviation of 2 $\mu$m. Cladding layers are applied by subsequently spincoating two layers of 35 $\mu$m, to obtain a cladding thickness of 70 $\mu$m. In Figure 2.11 the undercladding has a thickness of 2×35 $\mu$m, the core a thickness of 50 $\mu$m, and the uppercladding a thickness of 1×35 $\mu$m.

UV exposure at a typical power density of 10 mW/cm$^2$ (UV lamp OmniCure, broadband) for 60 sec needs to be done in a nitrogen environment, to avoid the

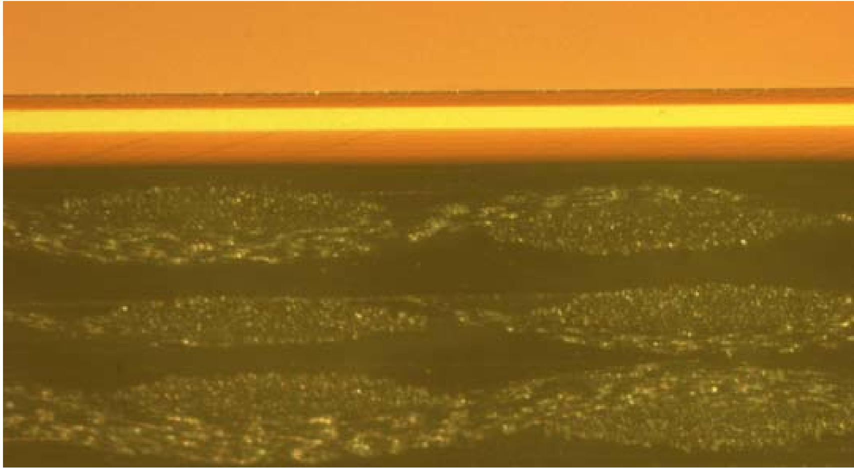

(a) 5x

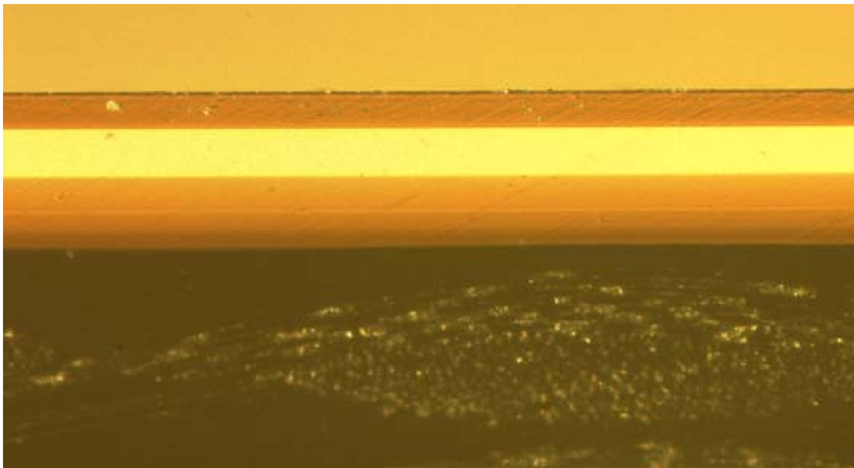

(b) 10x

**Figure 2.11:** Cross-section of a Truemode™ undercladding, core, and uppercladding stack, integrated on an FR4 substrate

presence of oxygen during acrylate crosslinking. Development is optional, and only required when using mask patterning. Subsequently each layer is baked for 1 hour at 120$^o$C. Surface roughness measured using a non-contact optical profiler, shows similar results compared to the surface roughness of an Ormocer® layer integrated on an FR4 substrate, scan area of $60\times45\,\mu m^2$, curvature and tilt removed, gives an $R_a$ surface roughness of 3–4 nm.

## 2.6 Conclusions

The requirements for optical materials to be used for board-level optical interconnections were discussed. Thin glass sheets are a very attractive material, as the temperature and humidity behaviour is superior to polymers, and they show a low optical loss over a broad window. Big challenge is the fabrication of multimode waveguides in the 70 $\mu$m thick glass foils. An overview of polymer candidates was presented, with a propagation loss $< 0.1$ dB/cm, both for datacom and telecom wavelengths. Both polysiloxanes (Ormocer®) and acrylates (Truemode$^{TM}$) are investigated within this work. This choice was mainly determined by the low optical losses at all major wavelengths, the ability to tune the indices of refraction, and the possibility to structure the materials using standard photolithography. Process parameters for the application of cladding and core layers are determined. Surface roughness of the layers has been evaluated making use of a non-contact optical profiler, showing an $R_a$ surface roughness around 3–4 nm.

# References


[1] PPC Electronic. http://www.ppc-electronic.com.

[2] PPC Electronic Optoboard. http://www.ppc-electronic.com/english/products/optoboard.html.

[3] Schott. http://www.schott.com.

[4] L. Eldada and L.W. Shacklette. Advances in polymer integrated optics. *IEEE Journal Of Selected Topics In Quantum Electronics*, 6(1):54–68, Jan 2000.

[5] H. Ma, A.K.-Y. Jen, and L.R. Dalton. Polymer-based optical waveguides: Materials, processing, and devices. *Advanced Materials*, 14(9):1339–1365, Oct 2002.

[6] M. Zhou. Low-loss polymeric materials for passive waveguide components in fiber optical telecommunication. *Optical Engineering*, 41(7):1631–1643, Jul 2002.

[7] A. Skumanich and C.R. Moylan. The vibrational overtone spectrum of a thin polymer film. *Chemical Physics Letters*, 174(2):139–144, Nov 2 1990.

[8] W. Groh. Overtone absorption in macromolecules for polymer optical fibers. *Macromolecular Chemistry And Physics*, 189(12):2861–2874, Dec 1988.

[9] E. Griese. A high-performance hybrid electrical-optical interconnection technology for high-speed electronic systems. *IEEE Transactions On Advanced Packaging*, 24(3):375–383, Aug 2001.

[10] Y.G. Zhao, W.K. Lu, Y. Ma, S.S. Kim, S.T. Ho, and T.J. Marks. Polymer waveguides useful over a very wide wavelength range from the ultraviolet to infrared. *Applied Physics Letters*, 77(19):2961–2963, Nov 6 2000.

[11] Exxelis. http://www.exxelis.com.

[12] S.Y. Cho, M.A. Brooke, and N.M. Jokerst. Optical interconnections on electrical boards using embedded active optoelectronic components. *IEEE Journal Of Selected Topics In Quantum Electronics*, 9(2):465–476, Mar-Apr 2003.

[13] micro resist technology. `http://www.microresist.de`.

[14] R. Houbertz, G. Domann, C. Cronauer, A. Schmitt, H. Martin, J.U. Park, L. Frohlich, R. Buestrich, M. Popall, U. Streppel, P. Dannberg, C. Wachter, and A. Brauer. Inorganic-organic hybrid materials for application in optical devices. *Thin Solid Films*, 442(1–2):194–200, Oct 1 2003.

[15] H. Schroder. Waveguide and packaging technology for optical backplanes and hybrid electrical-optical circuit boards. In *Photonics West'06, Proceedings SPIE 6124, Optoelectronic Integrated Circuits*, Jan 2006.

[16] M. Usui, M. Hikita, T. Watanabe, M. Amano, S. Sugawara, S. Hayashida, and S. Imamura. Low-loss passive polymer optical waveguides with high environmental stability. *Journal Of Lightwave Technology*, 14(10):2338–2343, Oct 1996.

[17] T. Watanabe, N. Ooba, S. Hayashida, T. Kurihara, and S. Imamura. Polymeric optical waveguide circuits formed using silicone resin. *Journal Of Lightwave Technology*, 16(6):1049–1055, Jun 1998.

[18] Y. Ishii, S. Koike, Y. Arai, and Y. Ando. Smt-compatible large-tolerance optobump interface for interchip optical interconnections. *IEEE Transactions On Advanced Packaging*, 26(2):122–127, May 2003.

[19] Luvantix. `http://www.luvantix.com`.

[20] Optical Crosslinks. `http://www.opticalcrosslinks.com`.

[21] Promerus. `http://www.promerus.com`.

[22] RPO. `http://www.rpo.biz`.

[23] V. Sundaram, R. Tummala, G. White, K. Lim, L. Wan, D. Guidotti, F. Liu, S. Bhattacharya, R.M. Pulugurtha, I.R. Abothu, R. Doraiswami, R.V. Pucha, J. Laskar, M. Tentzeris, G.K. Chang, and M. Swaminathan. System-on-a-package (sop) substrate and module with digital, rf and optical integration. In *ECTC'04, Proceedings Electronic Components And Technology Conference*, pages 17–23, May 2004.

[24] G. Fischbeck, R. Moosburger, C. Kostrzewa, A. Achen, and K. Petermann. Singlemode optical waveguides using a high temperature stable polymer with low losses in the 1.55 mu m range. *Electronics Letters*, 33(6):518–519, Mar 13 1997.

[25] W.S. Choi and F.W. Harris. Synthesis and polymerization of trifluorovinylether-terminated imide oligomers. *Polymer*, 41(16):6213–6221, Jul 2000.

[26] Interconnect by Optics (IO). `http://io.intec.ugent.be`.

[27] A. Neyer, S. Kopetz, E. Rabe, W.J. Kang, M. Stach, and R. Michalzik. 10 gbit/s electrical-optical circuit board based on new polysiloxane waveguide technology. In *ECOC'04, Proceedings European Conferences On Optical Communication*, pages 814–815, Sep 2004.

[28] Polysiloxane optical waveguide layer integrated in printed circuit board. `http://www-mst.e-technik.uni-dortmund.de/eocb.html`.

[29] R. Houbertz, L. Frohlich, M. Popall, U. Streppel, P. Dannberg, A. Brauer, J. Serbin, and B.N. Chichkov. Inorganic-organic hybrid polymers for information technology: from planar technology to 3d nanostructures. *Advanced Engineering Materials*, 5(8):551–555, Aug 2003.

[30] R. Buestrich, F. Kahlenberg, M. Popall, P. Dannberg, R. Muller-Fiedler, and O. Rosch. Ormocer®s for optical interconnection technology. *Journal Of Sol-Gel Science And Technology*, 20(2):181–186, Feb 2001.

[31] Patent WO0194430. `http://www.espacenet.com`.

# Chapter 3

# Laser ablation

*This chapter deals with the feasibility of KrF excimer laser-, frequency tripled Nd-YAG laser-, and $CO_2$ laser ablation for structuring Ormocer®s, Truemode$^{TM}$ and borosilicate glass sheets. The first part contains a short description of the laser ablation set-up. In the second part, the physical nature of nanosecond laser ablation of polymers will be discussed, introducing two processes, photodecomposition, and thermal ablation. Experimental results are explained by theoretical aspects, with emphasis on surface quality of the ablated structures. In the last part, structuring glass is addressed, based on dielectric breakdown.*

## 3.1 Laser set-up

### 3.1.1 Beam delivery unit

The custom-built ablation set-up [1] contains three different laser sources: a KrF excimer laser, a frequency tripled Nd-YAG laser and a $CO_2$ laser, integrated into one system (Figure 3.1), being able to structure a whole set of materials in different micro- and opto-electronic applications. In addition to the experiments related to this work, the set-up has been used for structuring stacked 2.5D optical interconnections [2], for structuring optical interconnections integrated on a flexible substrate [3], for terminating both glass and plastic optical fibers [4, 5, 6], for structuring photoresist using laser direct writing [7], within the framework of the European-Hiding Dies-project (HIgh Density INteGration of Dies Into Electronics Substrates) [8] for microvia drilling in FR4 based multilevel PCBs, and within the framework of the European-Shift-project (Smart High-Integration Flex Technologies) [9] for microvia drilling in polyimide based flexible substrates.

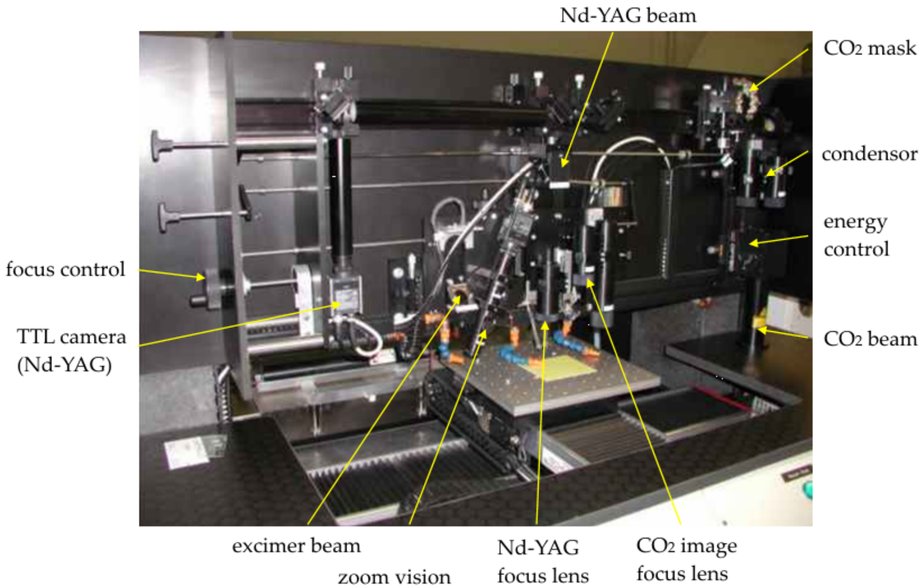


**Figure 3.1:** Laser set-up

**$CO_2$ laser**

The $CO_2$ laser (GSIL Impact SSM 2150) operates in the 9–10 $\mu$m range. The maximum optical power is 60 W, corresponding to a maximum pulse energy of 0.4 J, and a maximum pulse repetition rate of 150 Hz. The pulse length is 70 nsec. The laser emits a beam with approximately a square section, about 1 $cm^2$ with a rich mode structure, typically for TEA (Transverse Excited Atmospheric) sources. The laser radiation is concentrated on the part to an area up to approximately 1 $mm^2$, by image projection (demagnification) from an irradiated mask, with an image resolution on the order of 30 $\mu$m (proportional to $\lambda/NA$). Figure 3.2 illustrates the beam path for the $CO_2$ laser. The beam is guided through a manually operated energy controller (attenuator), with a scale ranging from 0 to 90 for minimum respectively maximum attenuation. There is a choice between two condensor lenses, to form the beam into either a spot or a ribbon shape, depending on the application. The beam waist is formed behind the mask plane. A turning mirror directs the beam to the motorized mask selector. A second turning mirror directs the beam downwards to the projection lens, which projects a demagnified image of the mask onto the part. A manual control allows the selection of one of the three image lenses, with a different demagnification: L1 10× demag. ($>125\,J/cm^2$), L2 5× demag. ($>20\,J/cm^2$), and L3 2× demag. ($>5\,J/cm^2$). An off-axis camera gives an overall 40× view of the process area. Because of this low

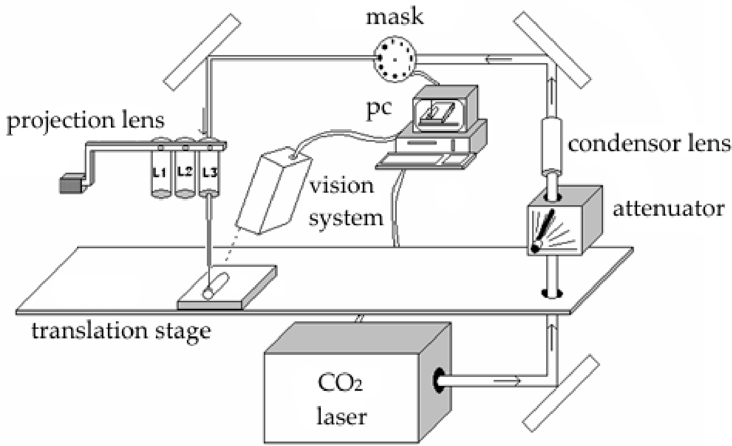


**Figure 3.2:** Schematic of the $CO_2$ laser beam path [5]

camera demagnification, and because of the low image resolution, the exploitation of $CO_2$ laser ablation for micron precision structuring is very challenging. Even for the realization of multimode optical interconnections, it will be necessary to push the image resolution to the limit.

#### Nd-YAG laser

The Nd-YAG laser (LWE 210-355-5000) emits pulsed UV radiation at 355 nm, the third harmonic of the 1.064 $\mu$m fundamental. The beam has a $TEM_{00}$ profile, and about 1 mm diameter when leaving the laser. The laser radiation is focussed on the part (direct write operation) or concentrated by image projection (demagnification) from an irradiated mask. The laser has a maximum power of 5 W, a maximum pulse energy of 500 $\mu$J, a pulse frequency between 10 and 100 kHz (externally triggered), a beam waist of 200 $\mu$m, and a pulse duration of 30 nsec. The optical path is different for either direct write or image projection operation, but one can change easily between the two configurations by selecting one out of two turning mirrors. An optional trepanning unit (via drilling), formed by two rotating optical wedges, can be placed in the optical path. The trepanning diameter is set by the angular offset of the two wedges, which are independently motorized. The beam passes through the 10× imaging lens, which projects a demagnified image of the mask aperture, or beam waist in the same plane, onto the part. The same lens is used to form a 450× through the lens (TTL) image of the part, for alignment purposes. The laser spot has typically a diameter of 20 $\mu$m, which, together with the high image resolution, is very promising for the definition of multimode waveguide structures.

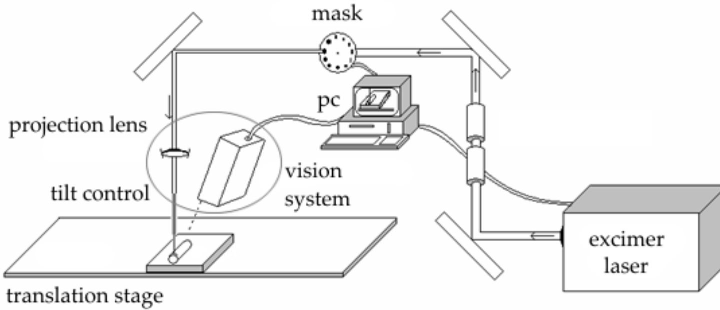


**Figure 3.3:** Schematic of the excimer laser beam path [5]

**KrF excimer laser**

The KrF excimer laser (ATL Lasertechnik SP300i) operates at a wavelength of 248 nm. The laser emits a beam with rectangular section approximately $4{\times}6\,\mathrm{mm}^2$, with a rich mode structure. The maximum pulse energy is 20 mJ, maximum repetition rate 300 Hz, and the pulse duration 3–7 nsec. Figure 3.3 illustrates the beam path for the excimer laser. The laser beam is shaped by a mask that is imaged on the sample by a demagnification of 10×, the image resolution is below 2 $\mu$m. The imaging lens has a focus and tilt control of the complete machining head that allows working at any angle. Necessarily, when tilted out of perpendicular operation, the focus control must be adjusted. A zoom microscope (30–200×) provides an angled view of the process region, with controls for magnification, focus, and centering with respect to the laser beam. The alignment accuracy due to the off-axis camera view, even for a 200× view, is limited to 3–5 nm.

### 3.1.2 Part mounting, motion, and control

The sample is positioned on a $300{\times}300\,\mathrm{mm}^2$ XY translation stage, which are linear motor driven stages with position encoder. The stages have a 1 $\mu$m positioning accuracy, and are capable of high acceleration and speed, which should allow fast structure definition, even for a serial process. Flat samples may be held in place either by suction, or using fixtures in the tapped holes provided. Due to the large deformation of standard printed circuit boards (warpage), substrate suction cannot be used. When defining micron precision structures, substrates can be attached using tape. Squaring the parts, relative to the X, Y stages, is achieved using a low profile theta trim stage located immediately below the part support. The manual micrometer screw gives $\pm\,3^o$ of precision motion, with $5'$ resolution.

During laser machining a plume will be generated at the ablated surface. The plume consists of evaporated material which can propagate towards the beam

optics, and of non-evaporated particles which can drop back on the sample near the ablated area. In order to mimimize this, fume extraction is provided.

The control software for the complete workstation is an engineering level, Windows based, program allowing control of all basic machine functions. Compatibility with industry file formats as Excellon, Gerber, HPGL, and DXF offers the opportunity to define complex patterns with a CAD tool. When doing so, the operation is fully computer controlled, without the need for an operator.

## 3.2 Ablating polymers: some fundamentals and experimental results

Several thousand journal publications are devoted to polymer laser ablation, driven by interest in the basic science as well as by numerous applications that have emerged for this high-resolution technique for material removal. A number of reviews have appeared over the years charting the progress made in polymer ablation at various stages of its development, for example, by Srinivasan [10], Yeh [11], Srinivasan and Braren [12], Lazare and Granier [13], and Dyer [14]. This section gives an overview of the basic mechanistic aspects, applied for KrF excimer laser, Nd-YAG laser, and $CO_2$ laser ablation of Ormocer® and Truemode™ materials. A more detailed description of polymer laser ablation, with emphasis on excimer laser ablation, can be found in the PhD work of Kris Naessens [15].

### 3.2.1 Ablation rate and ablation threshold

A useful starting point for the characterization of laser ablation is to measure the depth of material removed from the surface by each laser pulse, that is, the so-called ablation rate per pulse. Data is available on the variation of the ablation rate x with the laser fluence F (in $J/cm^2$) for a wide range of materials and laser wavelengths. This is usually derived by measuring the depth h of the etch crater produced by exposure to n pulses, i.e. $x = h/n$ and, as such, is an average value. It is found that a distinct threshold fluence $F_T$ must be exceeded for significant material removal to occur. This applies across a broad range of laser wavelengths, spanning the long wavelength infrared [16] to the deep ultraviolet. In the UV, the threshold for polymers can be very low, with typical values ranging from $F_T \approx 20$–$200\,mJ/cm^2$, depending on the laser wavelength as well as the polymer itself [11, 12, 13, 17]. Exposure to a large number of subthreshold fluence pulses does not produce the same degree of removal as the equivalent single-pulse dose above threshold. For excimer and solid state lasers, for which the pulse duration is usually restricted to less than $\approx 100\,ns$, the threshold fluence $F_T$ for a given polymer and wavelength appears to be independent of the pulse duration.

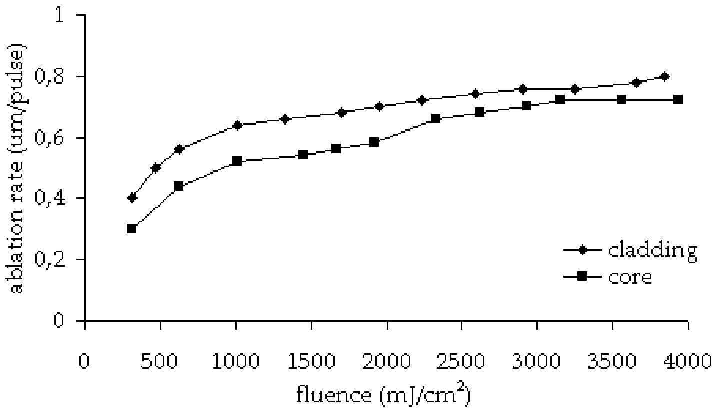


**Figure 3.4:** Excimer laser ablation rate for Ormocer® core and cladding material

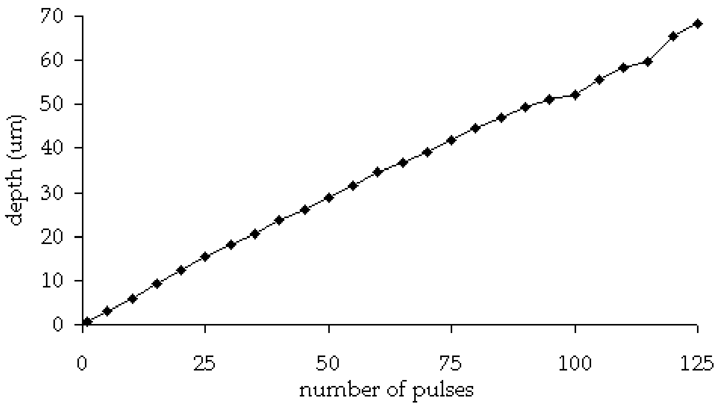


**Figure 3.5:** Linear relation between number of pulses and ablation depth for Ormocer®

The KrF excimer laser ablation rate for Ormocer® is given in Figure 3.4, showing the dependence of the ablation rate on the laser fluence F. As the minimum pulse energy is 1 mJ for a laser beam of 4×6 mm$^2$ (see Section 3.1.1), and there is no additional attenuator for the excimer laser, the minimum fluence is exceeding the threshold fluence $F_T$. It can be seen that there is a difference in ablation rate of about 0.1 $\mu$m between Ormocer® core and cladding material. The assumption that the ablation rate is independent of the number of pulses, is shown in Figure 3.5. Ablation depth varies linearly with number of pulses. This might be obvious, but is not the case for e.g. PMMA (polymethylmetacrylate).

It has been found, that, at least for a limited range of fluences above threshold, that the ablation rate obeys a form consistent with the Beer-Lambert law [18]:

$$x = \alpha^{-1} ln F / F_T \tag{3.1}$$

Here $\alpha$ is an effective absorption coefficient determined from a fit to the experimental ablation rate versus fluence data near threshold. This may differ from the low-signal absorption coefficient of the polymer determined from its transmission under low irradiance laser conditions or by using a spectrophotometer. This difference is probably not surprising given the likely physical (e.g. temperature, density) and chemical changes that can occur in the polymer under the high volumetric energy density loading corresponding to ablation.

Laser ablation allows the controlled removal of the surface of essentially any polymer, and not simply those that can be thermally evaporated. Experimentally it has been confirmed that extensive fragmentation of the main chains of even thermally robust polymers (such as the polyimide family) occurs in laser ablation, indicating that strong intra-chain covalent bonds are broken. Two specific models can be considered for the bond-breaking mechanism, photochemical and thermal [14].

### 3.2.2 Ablative photodecomposition

Srinivasan [19] proposed that the absence of significant thermal damage in polymers ablated with UV lasers could be explained by the fact that incident photons have sufficiently high energy (e.g. 4.9 eV for KrF excimer laser) to directly break main chain bonds. In this photochemical view of ablation, termed ablative photodecomposition [19], decomposition reactions would take place mainly from electronically excited states and repulsive forces between species would lead to their rapid expulsion from the surface (volume expansion). Energy absorbed in this bond-breaking process would restrict the temperature rise and the extent of thermal damage to the substrate. This is the case for KrF excimer laser ablation of Truemode$^{TM}$: a clean ablation with well-defined edges and the absence of thermal damage (Figure 3.6). Characterization based on scanning electron microscope (SEM) images shows that the laser fluence is not critical to avoid thermal damage. In Figure 3.6 the laser fluence is 2.5 J/cm$^2$, corresponding to a pulse energy of 6 mJ. Doubling the laser fluence (5 J/cm$^2$) does not significantly change the ablation behaviour, the difference is even critical to observe using SEM images.

A single pulse threshold follows from a photochemical model [20] if it is assumed that n bonds per unit volume must be broken to achieve material removal, the required fluence being estimated using:

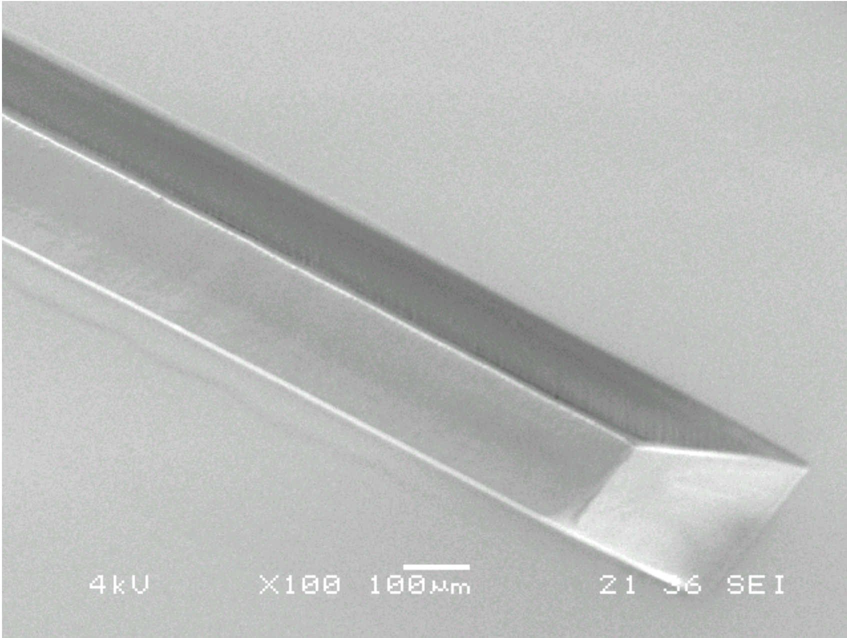


**Figure 3.6:** Ablative photodecomposition during KrF excimer laser ablation of Truemode$^{TM}$

$$F_n = nh\nu/\eta\alpha(1-R) \tag{3.2}$$

Here $\eta$ is the quantum yield for chain scission, h$\nu$ is the photon energy, which is assumed to exceed the bond energy of the polymer chain, and R is the surface reflection loss. A problem with this model is that $\eta$ is very low for many solid state polymers and the corresponding thresholds calculated from (3.2) are much larger than those found experimentally. Quantum yields can be as low as $\eta \approx 10^{-3}$, whereas $\eta \approx 1$ is needed for agreement with experiment. It might be argued that under ablation conditions $\eta$ increases dramatically (approaching unity) because the rate of bond breaking reaches a high value. Even so, the problem remains that in the run-up to this point, the polymer would be heated via non-radiative relaxation of excited electronic states unless the time constant for thermalization were significantly longer than the laser pulse duration. Hence the concept of a cold photochemical process seems difficult to justify.

Purely photochemical models of ablation have met with only limited success either because they fail to confirm the dominance of a fluence rather than irradiance threshold [21], or because they lack quantified thresholds to compare with experiment [22].

### 3.2.3 Thermal ablation

An alternative explanation of UV laser ablation can be found in terms of rapid thermal degradation of the polymer. Electronically excited states are assumed to efficiently undergo internal conversion, leading to randomisation of the absorbed energy amongst the various degrees of freedom of the molecule on a time scale that is short compared with the laser pulse. That a purely thermal process can produce effective polymer ablation has been confirmed by a number of investigations using long wavelength $CO_2$ lasers, in which the photons couple to vibrational modes of the molecule [16, 23, 24]. The general findings (threshold behaviour, dependence on absorption coefficient) mirror quite closely those for excimer lasers when account is taken of the generally lower absorption coefficient for vibrational transitions compared with resonant electronic transitions. This lower absorption coefficient for vibrational transitions seems to be the reason for the thermal damage in both Ormocer® and Truemode™ materials, making them unsuitable for far infrared based ablation. For Nd-YAG lasers operating at 355 nm, the thermal damage depends on the depth of the structures. Shallow structures of typically 10–20 $\mu$m have a well-defined shape, deeper structures of typically 50 $\mu$m are generally bothered by thermal damage, see Figure 3.7 for Truemode™ materials. The difference between the two SEM images is the pulse frequency: 20 kHz (lower pulse energy), and 15 kHz (higher pulse energy), resulting in a difference in laser fluence of a factor 4. The influence of both regulation current, ablation speed, pulse frequency, and laser spot size on the degree of thermal damage has been investigated, thermal damage could not be eliminated for deeper structures. Ablation of multimode waveguides with core dimensions of $50\times50\,\mu m^2$ will therefore not be able at 355 nm. The same result is found for Ormocer® materials, see Figure 3.8, a clean ablation, but only for limited depths. This opens a lot of possibilities for defining single mode optical waveguides using Nd-YAG laser ablation, as the laser spot size can be minimized to about 5–10 $\mu$m. However, the optimization of defining single mode optical waveguides is not within the scope of this PhD work.

A threshold-like behaviour for polymer removal can be explained by noting that the rate k at which volatile products are formed by thermal decomposition will have a very strong temperature dependence [25]. Assuming an Arrhenius expression is applicable, k will vary as:

$$k = A \exp[-E_A/RT] \tag{3.3}$$

where T is the temperature, and A and $E_A$ are the pre-exponential factor and the activation energy, respectively, for the decomposition path. An apparent threshold arises from the requirement that k must attain a sufficiently high value that measurable decomposition can occur on the time-scale that the material remains hot. This heating time is essentially defined by a combination of the laser pulse

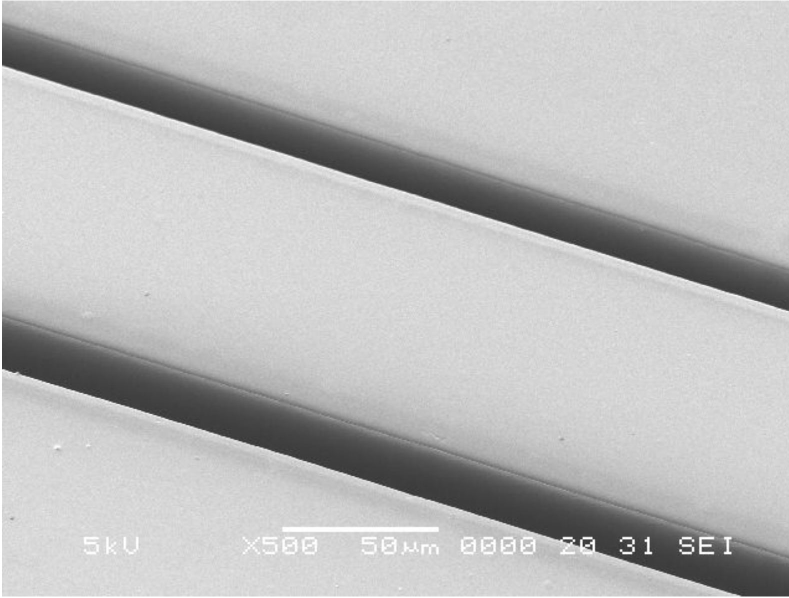


(a) Clean ablation for shallow structures

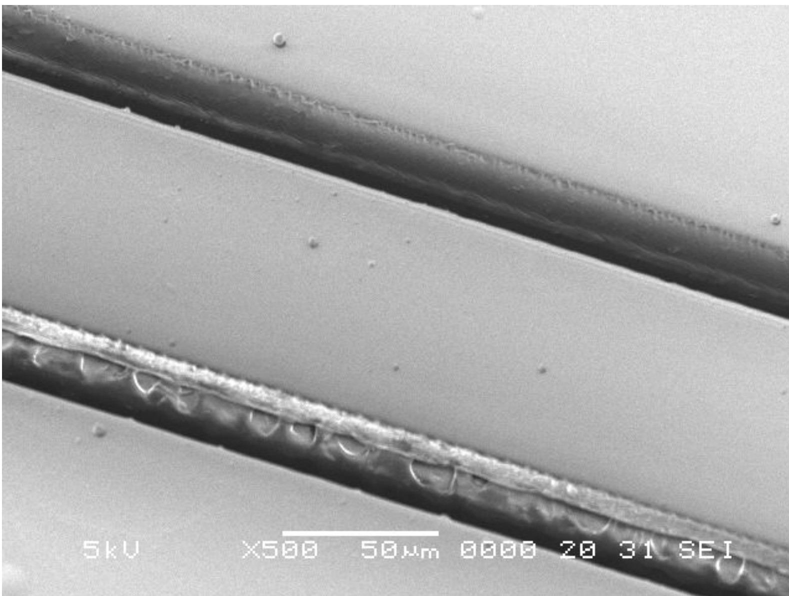


(b) Thermal damage for deeped structures

**Figure 3.7:** Nd-YAG laser ablation of Truemode$^{TM}$

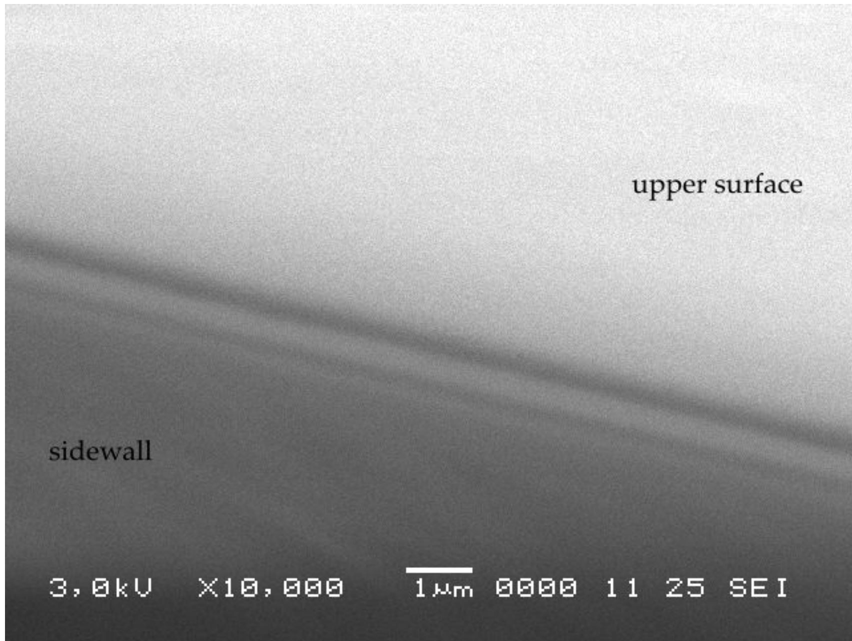


**Figure 3.8:** Nd-YAG laser ablation of Ormocer®

duration and the rate that the heated surface layer cools via conduction to the bulk underlying polymer when the pulse terminates. If a corresponding temperature for measurable decomposition is specified as $T_D$, the threshold fluence can then be estimated from [25]:

$$F_T = C(T_D - T_R)/\alpha(1 - R) \tag{3.4}$$

where C is the volumetric specific heat of the polymer, R is the surface reflection loss, and $T_R$ is the initial surface temperature. In deriving (3.4) heat loss through conduction is assumed to be negligible during the laser pulse and the thermo-optic parameters for the polymer are taken to be constants. It is likely that neither of these is a good assumption in all cases, and that more refined heating models are needed, such as those described in [26, 27].

Conversely, (3.4) can be used to estimate the temperature rise produced at the surface of a polymer with absorption coefficient $\alpha$ when it is exposed at the experimentally determined threshold fluence $F_T$. In this way it is found that typically $T_D \geq$ 800–1000 K at threshold, and under these relatively extreme conditions polymers can be expected to undergo rapid thermolysis [14]. The low extent of the heat-affected-zone, even at these elevated temperatures, can be explained by

the low thermal diffusivity D of polymers and the short duration laser pulses that are involved. For polymers with $D \approx 1 \times 10^{-3}$ cm$^2$/s and with a typical (excimer, or Nd-YAG) laser pulse duration $\tau = 10$–$20$ ns, the characteristic heat flow depth during the laser pulse is $x_d = (D\tau)^{1/2} = 31$–$44$ nm [14]. In most cases $x_d$ is small compared with the characteristic beam penetration depth $\alpha^{-1}$ so that heat flow from the optical deposition zone can be neglected on the time-scale of the laser pulse. This is implicitly assumed in deriving (3.4).

It is of interest to ask whether ablation exhibits a true physical threshold. The threshold concept was originally put forward as a convenient practical indication of the fluence at which significant material removal occurs, though it was recognised that some degree of etching could occur below $F_T$ [18]. This is confirmed in various reports in which sensitive measurement techniques have been used to study removal in the vicinity of threshold. Kuper et al. [26], for example, made a detailed investigation of the threshold region for polyimide, and found that the longer wavelength 248, 308, and 351 nm excimer lasers produced ablation rate-fluence curves that were consistent with a thermal ablation model. At these wavelengths there was no truly abrupt threshold. In contrast, for 193 nm exposure the onset of removal was sharply defined and tentatively taken to be evidence of the photochemical nature of ablation at this wavelength. Even in this latter case, however, the surface temperature at threshold was deduced to be $\approx 840$ K, implying that the photochemistry occurs on a hot surface [26]. Further discussions can be found in [28], where detailed modelling of laser-induced thermal degradation of polymers is reported.

### 3.2.4 Efficient ablation

From an applications viewpoint some useful guiding principles can be derived from the simple Beer's Law description of a threshold ablation process [14]. For $F < F_T$ there is no material removal and, in the absence of significant radiative loss from the polymer and under the condition that photochemical change (if any) is thermo-neutral, all absorbed energy should appear as heat. When $F > F_T$ the depth of material subjected to a fluence exceeding $F_T$ is ablated, thus carrying away the excess fluence $(F - F_T)$. As a consequence the thermal loading on the polymer remains clamped at $F_T A$ where A is the beam area. Experimental findings confirm, at least approximately, the validity of this simple view [25, 29].

If heat loss from the absorption zone is negligible, the product $\alpha F_T = H$ is a measure of the ablation enthalpy of the polymer, that is, the minimum volumetric energy density needed to transform the initially cool solid to volatile products. H is found to be approximately a constant, independent of laser wavelength. For example for polyimide and PET results obtained using 193, 248, and 308 nm lasers give $H \approx 3$–$4$ kJcm$^{-3}$ [25]. This is close to values obtained for polymers under long-pulse $CO_2$ laser exposure [16].

Under these conditions it then follows that the ablation threshold is inversely proportional to the absorption coefficient:

$$F_T = H/\alpha \tag{3.5}$$

This form is consistent with the predictions of the simple thermal model (3.4), provided differences in the beam penetration depth ($\alpha^{-1}$) do not significantly affect the heating-cooling cycle, so that the thermal reaction time, and hence $T_D$, remain constant.

From a practical perspective a high absorption coefficient is advantageous for several reasons [14]:

- The ablation rate per pulse varies as $\alpha^{-1}$ (3.1) so that spatial depth resolution improves.
- $F_T$, and consequently thermal loading of the irradiated surface, is reduced (3.5).
- On cessation of the laser pulse, the characteristic cooling time $\tau_c$ of the hot surface is more rapid, as $\tau_c = 1/\mathrm{D}\alpha^2$, and this falls with increasing $\alpha$. The time spent at high temperature is thus reduced, minimizing local damage.
- When processing at a laser pulse repetition rate $\nu_P$, the average thermal loading of the polymer, given by $\nu_P H/\alpha$, is reduced. This acts to restrict more widespread thermal damage such as might arise through exceeding the melting temperature in a semi-crystalline polymer or the glass temperature in an amorphous polymer.

As for UV lasers $\alpha$ values range from $\approx 1\times10^4$ to in excess of $1\times10^5\,\mathrm{cm}^{-1}$, ablation with typical nanosecond duration lasers is characterised by a low threshold fluence and precise depth control. These factors, together with a theoretical sub-micron optical spatial resolution, bring a unique advantage to micro-scale polymer machining and processing with UV lasers.

For polymers that exhibit weak absorption at a specific laser wavelength, it has been shown that deliberately doping them with absorbers to raise $\alpha$ can dramatically improve their ablation properties. Dye-doped PMMA [10] and polyimide doped PTFE (poly-tetrafluoroethylene) [30] provide good examples of this fact. An effect termed incubation has also been reported [31], for which UV laser exposure leads to photochemical modification of a (weakly absorbing) polymer, increasing its absorption coefficient and altering its ablation characteristics.

### 3.2.5 Plume effects and debris

Much useful information has been gained from studies on the dynamic behaviour and the composition of the polymer ablation plume, that is, the expanding cloud of volatile products that is expelled from the irradiated surface by each laser pulse. Using various chemical and physical techniques [12, 13], the plume composition has been found to be quite complex, with species ranging from low mass volatile gases to large polymer fragments and, in some cases, carbonrich clusters. Experimental ablation rate-fluence plots often differ from the description provided by (3.1). One explanation for this is that the laser beam must propagate through the plume of ablation products that are expelled from the surface and this may have a significantly different mass absorption coefficient to the parent solid polymer.

Re-deposition of the ablation products on or around the ablation site is commonly observed, the magnitude of this debris problem being governed by the specific polymer involved as well as the processing environment (gas, vacuum), ablation fluence, and laser wavelength. The presence of debris is found to be a significant obstacle to exploit KrF excimer laser ablation as a patterning technique for Ormocer® materials. Serious efforts have been directed at reducing this re-deposited debris, of which a summir overview is given in this section. To stress out the problem, a cross-sectional view of debris is shown in Figure 3.9, pictures taken at different distances around the ablated area.

In general, gas dynamic models have been developed that relate the plume expansion to the re-deposited debris patterns [32], and the potential benefits of using gas streams for clean-up have been explored [33]. Keeping the application in mind, structuring optical layers integrated on larger PCBs, this is not the way to proceed.

The debris is not only detrimental to the optical performance (surface roughness). In applications where components need to be mounted on the contaminated surface, the alignment becomes much more difficult. The height reference is lost, due to the non-uniformity of the debris layer thickness, see Figure 3.9. Reliability issues are a concern, because the layer might come loose in some cases (Figure 3.10).

Two complementary approaches are investigated for achieving optical quality surfaces: the avoidance of debris, and the removal of debris. The avoidance of debris is achieved by fume extraction. It has been shown that the ablation direction with respect to the fume extraction direction is important: optimum results are obtained when the debris is extracted in the opposite direction of what is already structured, which might seem obvious (Figure 3.11). The removal of debris is investigated using both excimer laser and $CO_2$ laser cleaning, with low laser fluences, in order to ablate the debris layer, without affecting the actual material surface. The poor adhesion of the debris layer could be beneficial here. Laser

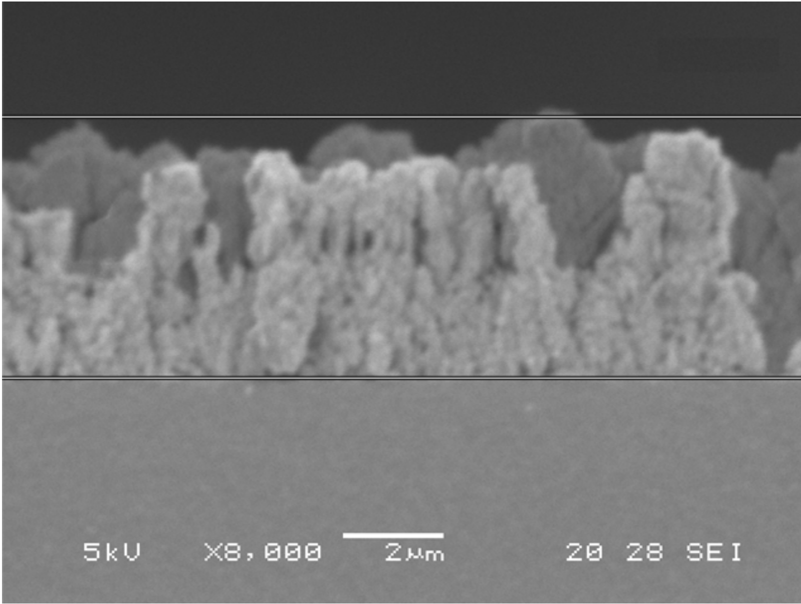


(a) Debris thickness 5.2 $\mu$m

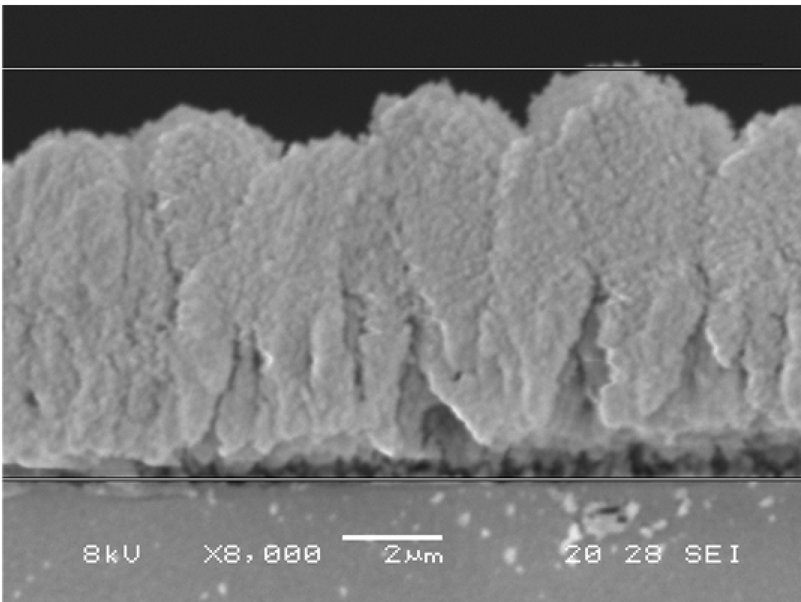


(b) Debris thickness 8.2 $\mu$m

**Figure 3.9:** Redeposition of ablation products on or around the ablated area (Ormocer®)

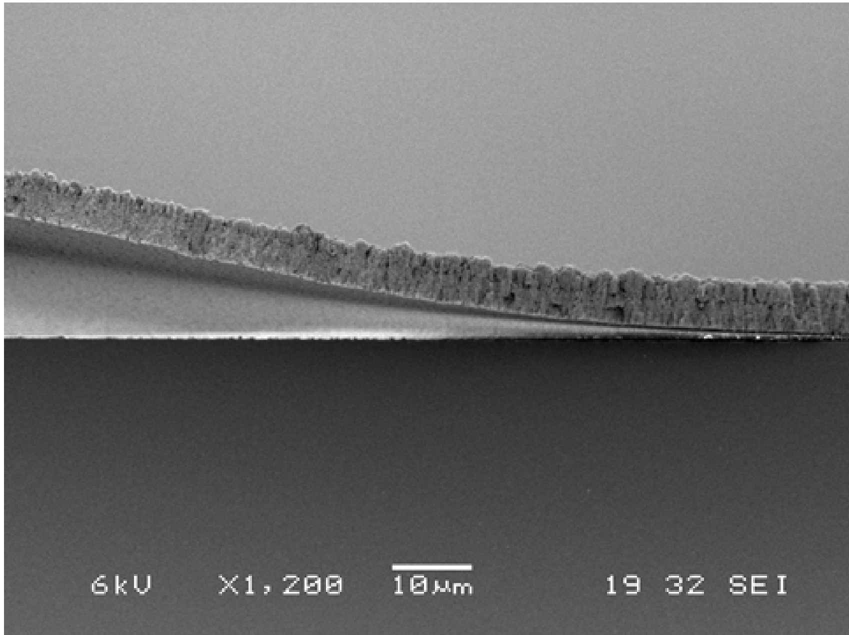


**Figure 3.10:** Poor adhesion of debris (Ormocer®)

cleaning is mainly intended to remove the debris on the upper surface. Debris removal on the vertical sidewall would require angular laser cleaning to have a sufficient impact. Representative results are shown in Figure 3.12. The figure shows KrF excimer laser ablated structures, that are subsequently cleaned with a limited number of laser pulses. Excimer laser cleaning of Ormocer® is able to remove the debris, but the bottom of excimer laser ablated areas suffer from granular-like microstructures, discussed further on. $CO_2$ laser cleaning has a different impact on the debris: due to the thermal ablation the debris layer is melted, and this way eliminated. The process is only reliable and reproducible for a limited degree of debris, and therefor the process will only be applied for cleaning excimer laser defined microlenses, discussed in Chapter 6.

The easiest way to remove the debris on top of the upper surface, it to apply a thin layer of resist (Microposit S1818) prior to ablation, and to remove (develop) the resist together with the debris. This process will be applied when defining the coupling structures in Chapter 5.

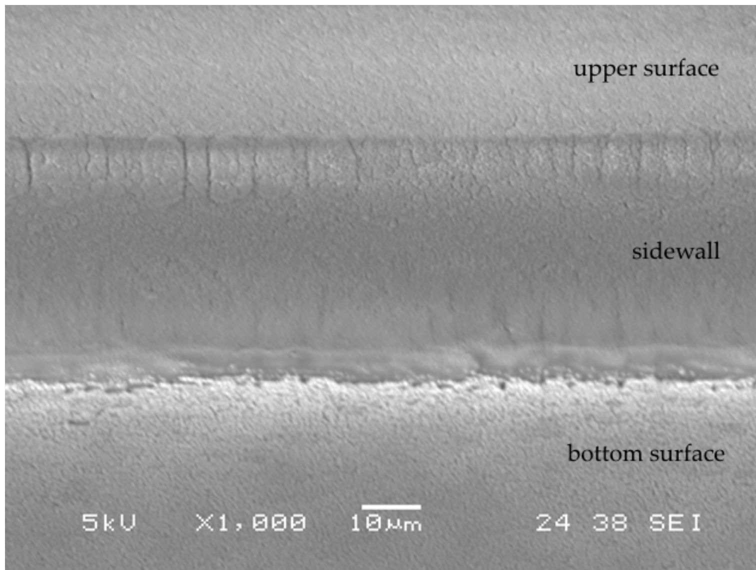


(a) Wrong direction

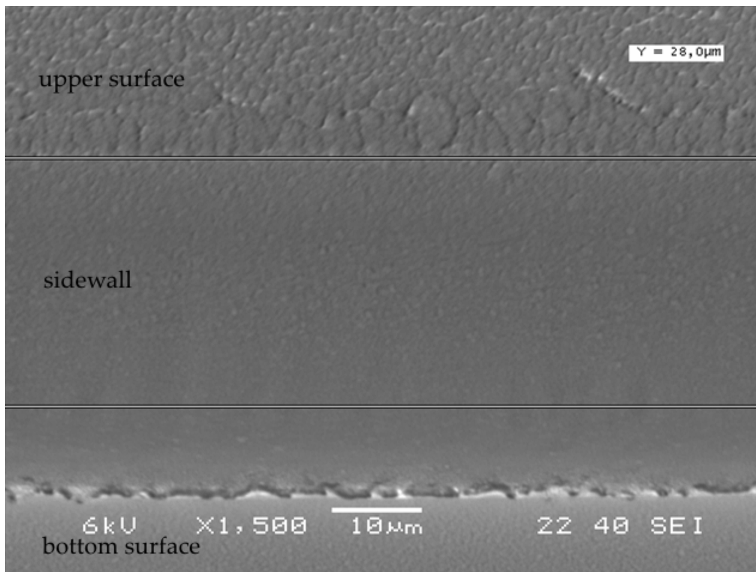


(b) Good direction

**Figure 3.11:** Influence of fume extraction direction with respect to ablation direction to the vertical sidewall surface quality (Ormocer®)

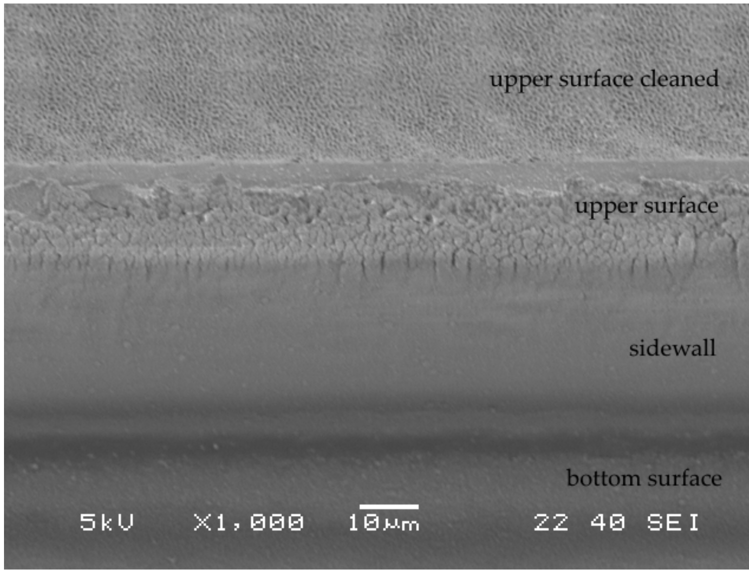


(a) KrF excimer laser cleaning

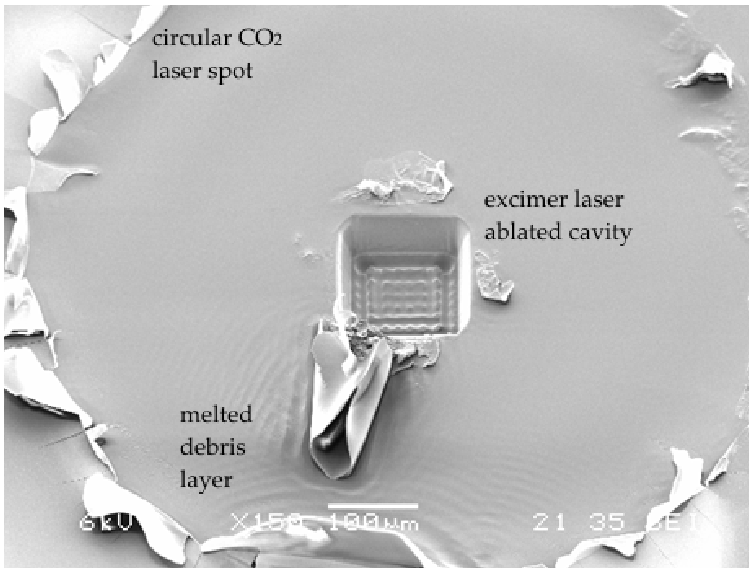


(b) $CO_2$ laser cleaning

**Figure 3.12:** Laser cleaning of surfaces contaminated with debris (Ormocer®)

### 3.2.6 Surface quality

Three types of microstructures appearing on the surface of ablated polymers have attracted a considerable deal of attention over the years [14].

One of these is the formation of well-defined cones that develop on the surface as etching proceeds [34]. There is general consensus that cones are initiated by particulate shielding and that their wall angle is controlled by the ratio $F/F_T$, i.e. fluence above threshold. The initiating particles may arise from carbon-rich fragments born in the ablation process itself or be present in the polymer as inadvertent impurities. Deliberate doping of a polymer with a high volumetric density of sub-micron-sized particles can lead to the entire ablated surface being covered with cones.

The second type of microstructures, LIPSS (Laser Induced Periodic Surface Structures), have been observed on ablated polymer surfaces [35, 36]. LIPSS have their origin in optical interference effects and appear as regular grating-like structures. These can extend over areas that greatly exceed the size of the spatial coherence patch of a typical excimer beam, and may have periods down to the order of the laser wavelength depending on exposure parameters (e.g. angle of incidence and beam polarization).

Finally, microstructures can be driven by a relaxation of stress in the hot surface layer that remains after the ablating pulse. It has been observed that the scale-size of these microstructures depends on the laser wavelength. This does not, however, appear to arise through optical interference or diffraction effects but, rather, because of differences in the threshold fluence $F_T$ and thermal loading on the surface associated with changes in wavelength. This thermal loading determines the depth over which there is a sufficiently large temperature rise to allow material flow. Although several models have been proposed to explain these effects it seems that a fully satisfactory account has yet to emerge. The effect appears for both the KrF excimer laser and for the $CO_2$ laser when applying them to Ormocer®, see Figure 3.13. The scale-size of the microstructures is indeed different, but not only the scale, also the kind of structures. That these structures are driven by a relaxation of stress, is proved by a subsequent thermal step: when the samples with the microstructures are put in a conventional oven for about 2 hour at a temperature of 170°C (approximately the final curing temperature of Ormocer®) the microstructures disappear for the $CO_2$ laser induced structures (Figure 3.14).

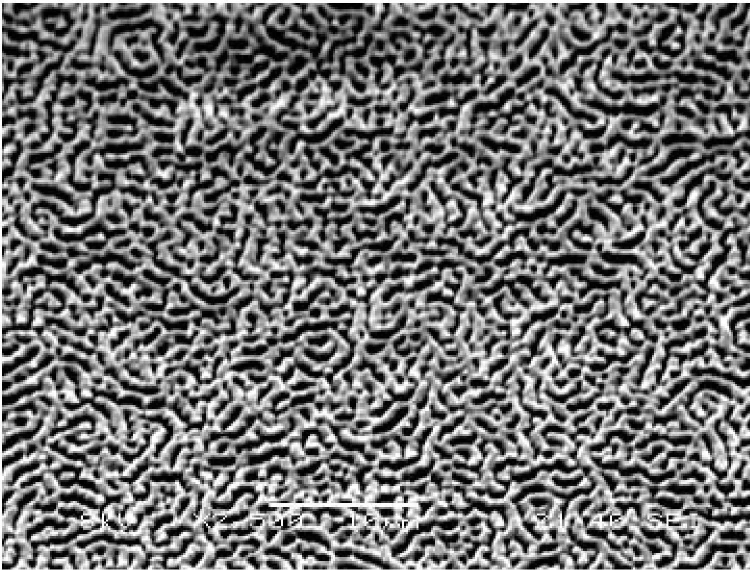

(a) KrF excimer laser, 20 pulses

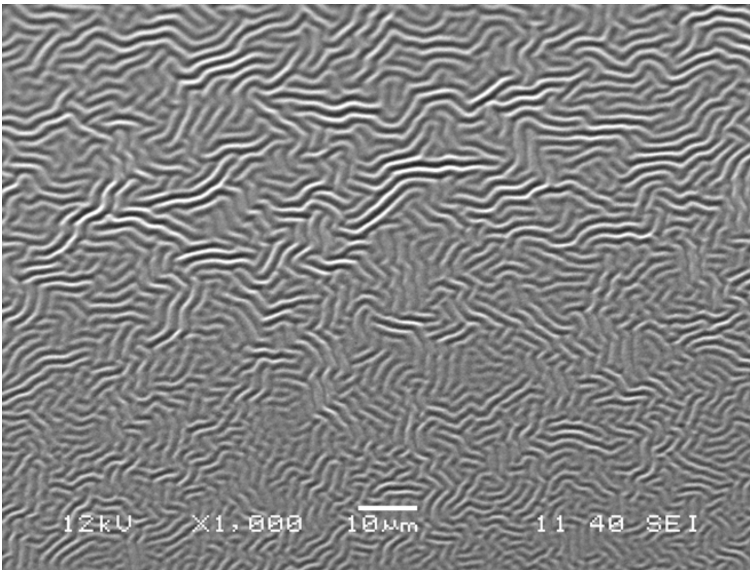


(b) $CO_2$ laser, 4 pulses

**Figure 3.13:** Formation of microstructures on the bottom surface of the ablated area (Ormocer®)

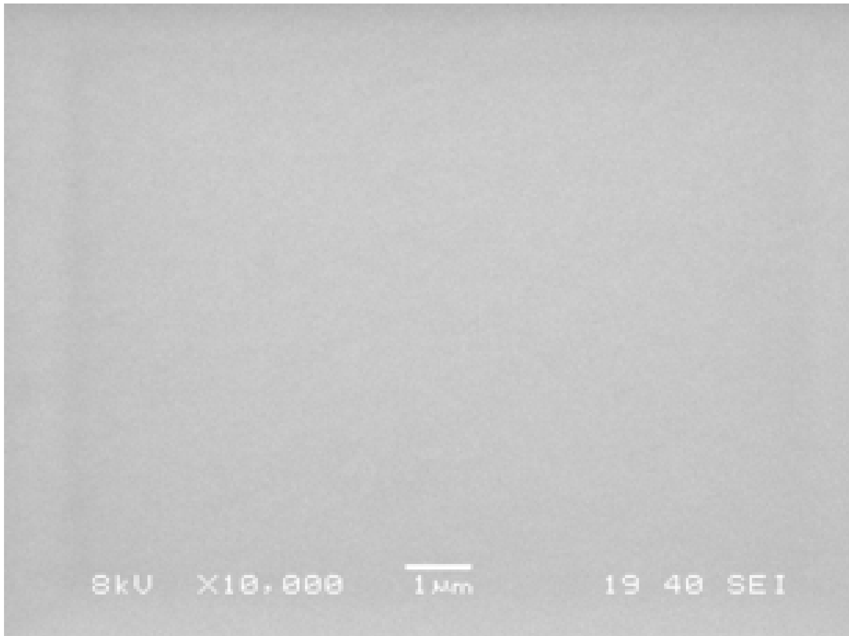


**Figure 3.14:** Smooth surface after annealing of $CO_2$ laser induced microstructures (Ormocer®)

### 3.2.7 Surface roughness

For polymers that do not suffer from stress relaxation microstructures and, under appropriate conditions, can be processed to eliminate cone formation and LIPSS, an interesting question arises as to how smooth the ablated surface will be. This is not solely of academic interest but also of practical importance in applications such as forming polymer waveguides for board-level optical interconnections. For this optical application surface roughness must be minimized to reduce scattering loss. Based on experiments with Ormocer®s, one can conclude that the surface roughness is far too high for optical waveguiding applications: the presence of both debris and microstructures are serious problems. This is different for the Truemode™ materials: no deposition of debris, and no presence of microstructures.

An analysis of the limiting factors that govern the roughness of an excimer laser ablated polymer surface needs to take account of both material aspects (e.g. intrinsic inhomogeneity) and optical factors. At the optical level it has been proposed [37] that statistical fluctuations in the spatial fluence distribution associated with the highly multimode beam of the excimer laser set a fundamental

limit. These pulse-to-pulse fluctuations produce a theoretical surface roughness in ablation that scales as $m^{1/2}$ where m is the number of exposure pulses, and for deep etching may be expected to produce roughness of hundreds of nanometers. A second more practical limitation relates to random fluence variations in a nominally uniform fluence beam which produce roughness scaling directly as m. These might easily be introduced by optical imperfections in the excimer laser beam delivery optics. Experiments with $F_2$ (157 nm) laser ablated PMMA show roughness varying as m rather than $m^{1/2}$ [37], with $R_q \approx 200$ nm for $m = 500$. This finding suggests that stationary fluence variations rather than pulse-to-pulse mode fluctuations are dominant.

This roughness refers only to the bottom of the ablated area. For the ablation of optical waveguides, not the bottom area is of interest, but the roughness of the vertical sidewalls must be minimized. The impact of both the stationary fluence variations and the pulse-to-pulse mode fluctuations are of no importance here. What determines the final roughness is the roughness of the mask that shapes the laser beam, and that is imaged on the sample (all in the assumption that debris does not contaminate the sidewall). The excimer laser imaging lens has a demagnification of 10, which means that the roughness of the mask is divided by 10. There are several ways to make suitable masks depending on the laser fluence, required accuracy, and the quality of the edge definition. The easiest approach uses a metal sheet as base material and the desired mask pattern is simply cut out with mechanical tools via drilling, sawing and milling. Although such masks can be fabricated rather rapidly, the edge definition of the apertures is generally very poor due to burring, and is unsuitable to achieve high quality sidewalls. A less conventional technique uses a polymer as mask substrate. Although polymers generally have low ablation thresholds, and thus limit the mask lifetime, they can be machined very accurately with the KrF excimer laser. Obviously, these polymer masks can not be used for shaping the $CO_2$ laser beam. In this work all masks used for shaping the KrF excimer laser beam, were fabricated using a 50 $\mu$m thick polyimide film. As the film is not self-supporting, it is glued onto a metal frame fitting in the mask holder. The resulting sidewall quality is shown in Figure 3.15 (pulse energy 6 mJ, corresponding to a laser fluence of 2.5 J/cm$^2$, ablation speed 82 $\mu$m/s). The impact of the mask quality is reduced for dynamic ablation, because the roughness of the mask is averaged during movement. Roughness measurements using a non-contact optical profiler, confirm the smoothness of the laser ablated sidewall, 18 nm $R_a$ and 23 nm RMS roughness (cylinder and tilt removed), measured on an area of $60 \times 46\ \mu m^2$ (Figure 3.16) (pulse repetition rate 200 Hz). A complete study of the impact of the ablation parameters on the resulting sidewall roughness of waveguides is included in Chapter 4.

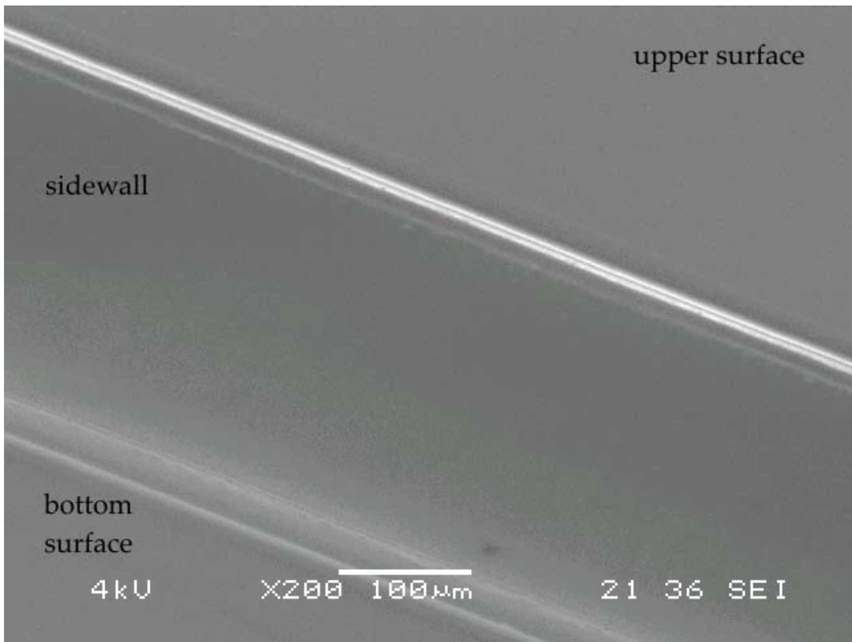


**Figure 3.15:** Smooth KrF excimer laser ablated sidewall (Truemode$^{TM}$)

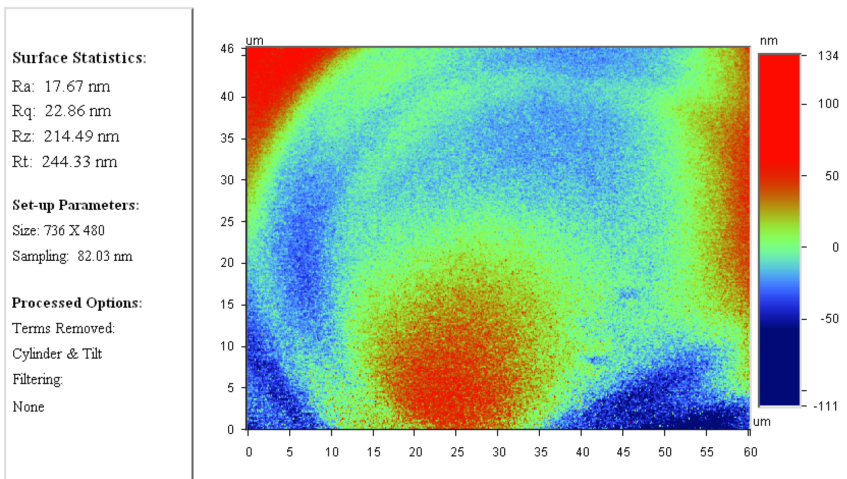


**Figure 3.16:** Roughness of a KrF excimer laser ablated sidewall (Truemode$^{TM}$)

### 3.2.8 Dynamic ablation

For static ablation the crater depth is obviously equal to the number of laser pulses, multiplied by the ablation depth per pulse x. For dynamic ablation using a rectangular beam spot of length a that moves with a constant velocity v while the laser is firing at a constant repetition rate $\nu$, the depth of the ablated groove equals:

$$depth = x\nu a/v \tag{3.6}$$

If the laser is only fired during beam translation over the substrate, the ablated groove will feature a ramp with an angle $\theta$ = atan(depth/a) at the start and the end. During ablation the surface below the laser beam has the same inclination $\theta_{ramp}$. If deep tranches are to be fabricated (e.g. 50 $\mu$m), it is generally a good idea to choose a large aperture in the scan direction. This does not only improve the ablation speed (more material is removed per pulse) but will also limit $\theta_{ramp}$. In [38] it is suggested that enhanced debris deposition occurs in the ablated groove as the ejected fragments from the ablating surface front are launched towards the groove and debris deposition can be considered as a sort of self-PLD (Pulsed Laser Deposition). An alternative is to ablate the grooves gradually by scanning several times over the same surface. Even for a small aperture, the ablating surface angle can be kept low by choosing a desired number of passes. This has been evaluated for Ormocer®: comparing SEM images of both single and multiple ablation (up to 6×) does not show improvement of sidewall surface quality.

## 3.3 Ablating glass materials

Inorganic insulators are ablated by UV laser radiation even when the photon energy does not exceed the bandgap energy (e.g. for $SiO_2$ the bandgap energy is 9.1 eV, requiring a photon wavelength of 136 nm). Ablation also occurs at laser fluences that are significantly lower than those that would be required to produce fast thermal vaporization. This can be explained by the production of defect centers or radiative interactions with existing centers or impurities. Such changes often result in an increase in optical absorption at the laser wavelength as well as at other wavelengths. With optical fibers, defect formation limits the fluence that can be transmitted. For silica glass, there have been a number of studies on the effect of UV laser radiation on this material. An example of defect absorption features induced by ArF (193 nm) laser radiation of hydroxyl-free silica is shown in Figure 3.17 [39]. The 7.6 and 5.0 eV bands are due to the intrinsic oxygen-deficient defects. The growth of the 5.8 eV band, and the decrease of the 5.0 eV band, were observed after radiation by an ArF excimer laser of 45 mJ/cm$^2$ per pulse at 30 Hz with irradiation times shown.

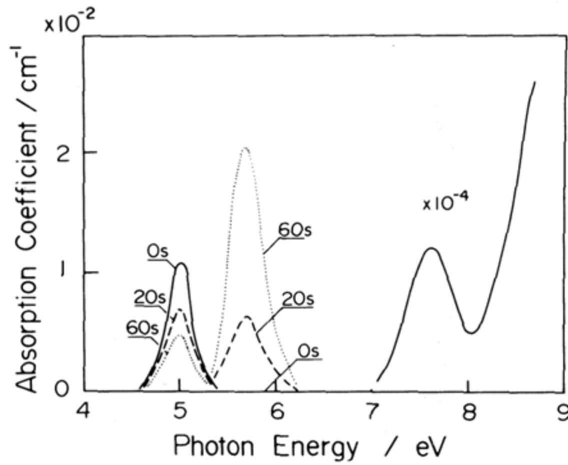


**Figure 3.17:** Optical absorption properties of dehydrated synthetic silica glass under ArF laser irradiation [39]

Laser ablation of inorganic insulators have been studied using different kind of conventional nanosecond laser sources: $F_2$ excimer laser (157 nm) ablation [40], ArF and KrF excimer laser ablation [41, 42], copper vapour laser (255 nm) ablation [43, 44], Nd-YAG laser (1064, 355, and 266 nm) ablation [45, 46, 47], and $CO_2$ laser ablation [48].

Experiments on 70 $\mu$m thick borosilicate glass are performed using the three available laser sources, KrF excimer, frequency tripled Nd-YAG, and $CO_2$ laser ablation. KrF excimer laser ablation does not allow for a clean ablation, a representative result is shown in Figure 3.18. Microcracks along the ablated vertical sidewall, and the deposition of debris prevent a clean ablation. Results on KrF excimer laser ablation of grating structures [41, 42] cannot be compared with ablated grooves of 70 $\mu$m deep, as residual stress and formation of debris increase with increasing laser fluence, and increasing number of laser pulses.

Representative results on Nd-YAG laser ablation of borosilicate glass, are shown in Figure 3.19a. Changing the pulse repetition rate from 10 to 100 kHz, the regulation current from 23 to 28 A, the number of pulses, and heating the glass sample to an elevated temperature of 100°C, did not substantially improve the result as shown in Figure 3.19a. Because of the small laser beam diameter, and the intention to use laser ablation for the definition of multimode waveguide structures, the use of the trepanning unit is also investigated, see Figure 3.19b, with similar surface roughness as without trepanning unit.

It is expected that subsequent etching of the debris using a solution of HF, together with temperature annealing would substantially improve the results, but

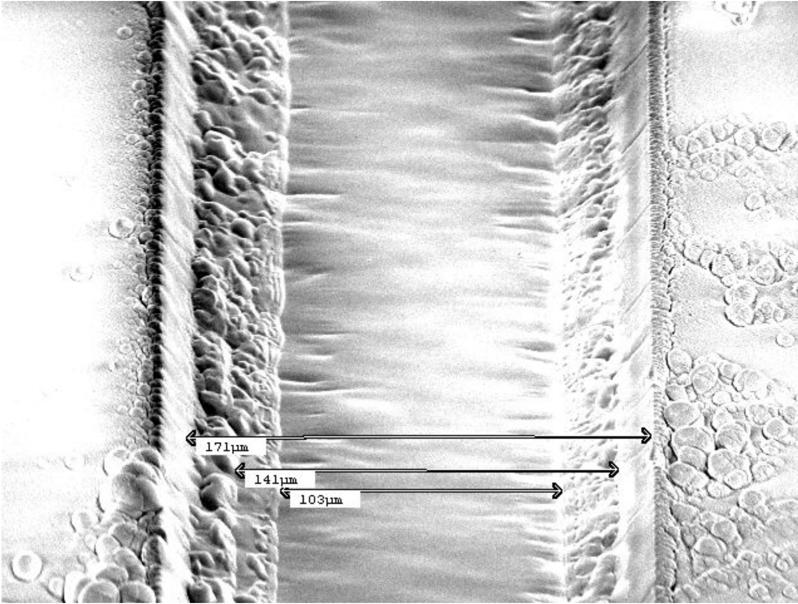


**Figure 3.18:** KrF excimer laser ablation of a 70 $\mu$m thick borosilicate glass sheet

as this requires two additional processing steps that are not compatible with standard PCB technology, this is not further investigated.

Optimum results are abtained using $CO_2$ laser ablation, shown in Figure 3.20. Smooth surfaces and the absence of microcracks are obtained when cutting through the entire glass sheet. Ablation speed is 400 $\mu$m/s, pulse repetition rate 50 Hz, and a laser spot of 200 $\mu$m diameter. This learns that 25 laser pulses are required to achieve a smooth surface, for a glass sheet thickness of 70 $\mu$m. The results as shown in Figure 3.20 are very promising, however, there are three very important limitations:

- Ablation to a certain depth ($< 70\ \mu$m) does not result in clearly defined sidewalls.
- The presence of material underneath the glass sheet (polymer cladding, FR4, or copper) might result in contamination of the sidewall.
- Starting and ending the ablation in the middle of the glass sheet results in cracks near the starting and ending point.

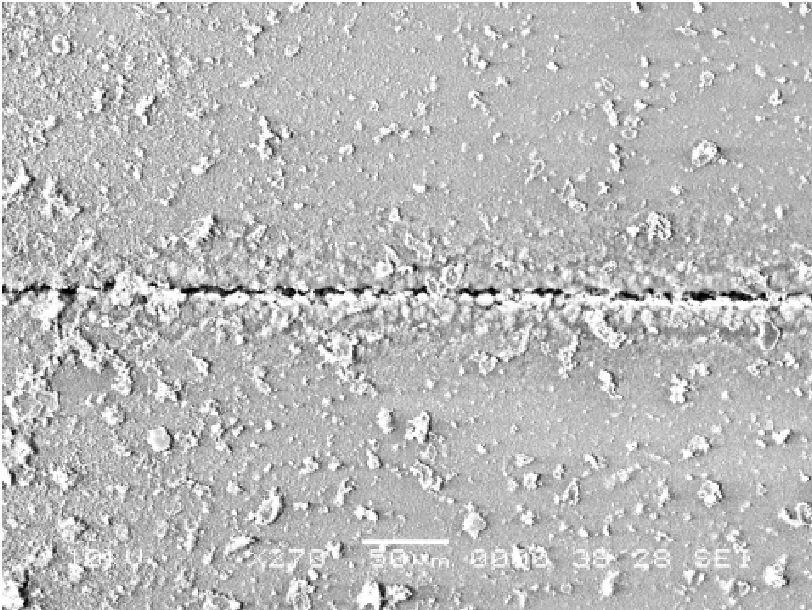

(a)

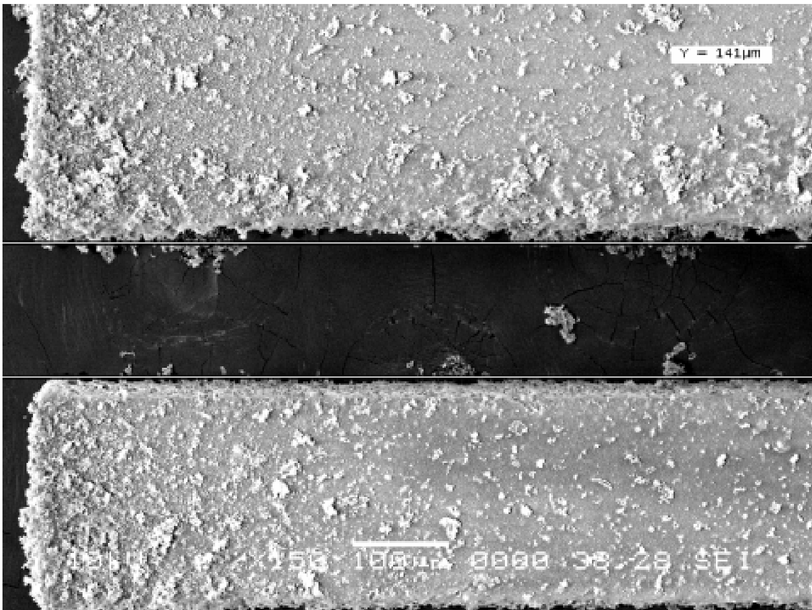


(b) Using the trepanning unit

**Figure 3.19:** Nd-YAG laser ablation of a 70 $\mu$m thick borosilicate glass sheet

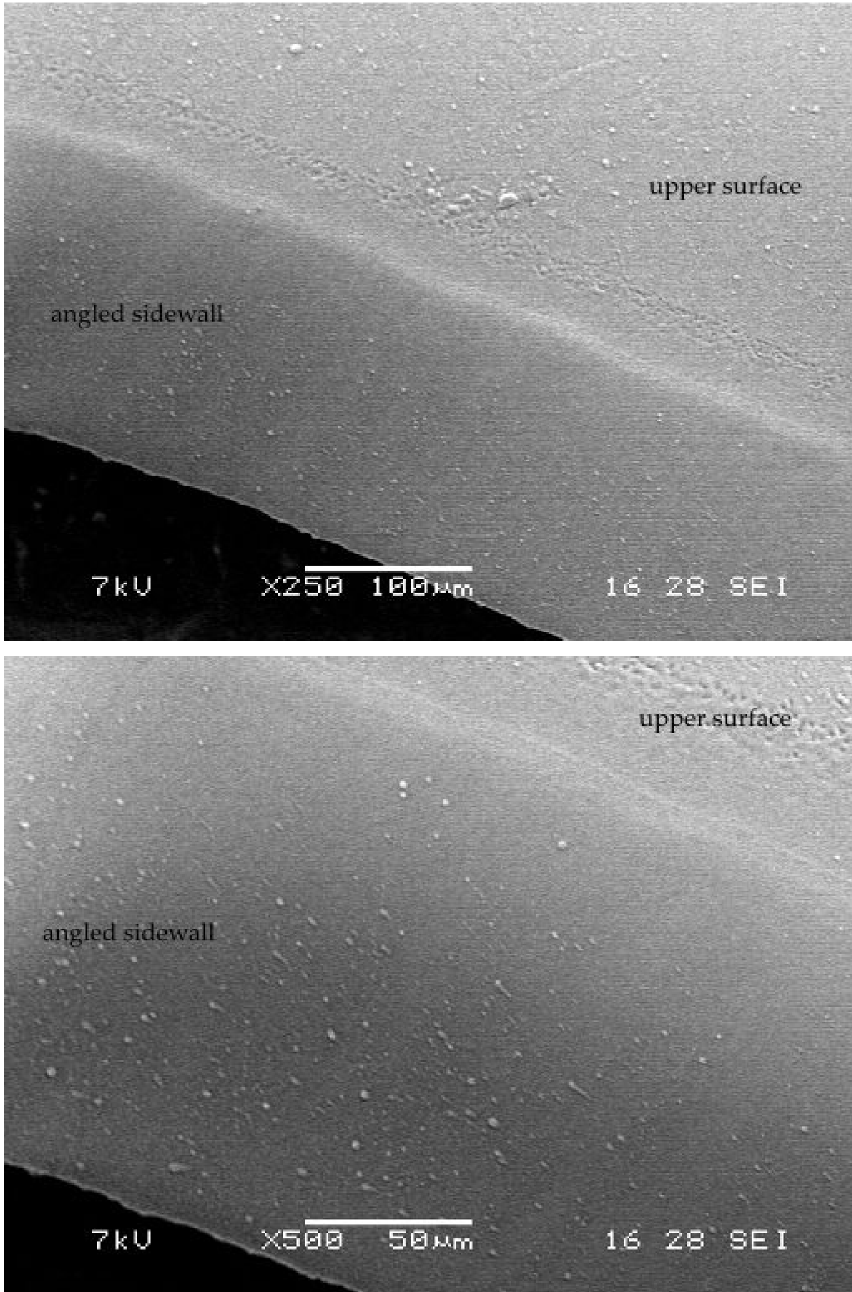


**Figure 3.20:** $CO_2$ laser cutting of a 70 $\mu$m thick borosilicate glass sheet

These limitations (especially the third one) make it impossible to use laser ablation for the definition of waveguides in glass sheets. However, ablation of a coupling facet is possible. Surface roughness of the facet is measured using a non-contact optical profiler, showing an $R_a$ roughness of 500–600 nm, on an area of $90 \times 205\,\mu m^2$.

## 3.4 Conclusions

The working principles of KrF excimer laser-, frequency tripled Nd-YAG laser-, and $CO_2$ laser ablation for structuring Ormocer®s, Truemode™ and borosilicate glass have been explained. It has been revealed that structuring multimode optical interconnections using laser ablation offers a lot of potential for the combination KrF excimer laser - Truemode™, showing very smooth sidewall surfaces, with an $R_a$ roughness around 20 nm. Generation of debris, and the presence of microstructures are two fundamental limits for structuring Ormocer® materials using KrF excimer lasers. It has been shown that frequency tripled Nd-YAG lasers are capable of structuring shallow grooves with smooth surfaces, but grooves with a depth of 50 $\mu$m introduce too much thermal damage. This offers a lot of potential for structuring single mode optical waveguides, not within the scope of this work. $CO_2$ lasers can be used for smoothening polymer surfaces, but introduce serious thermal damage when ablating polymers. Best results for structuring glass are obtained for $CO_2$ laser ablation, minimizing the presence of debris, and under the right circumstances, without microcracks.

# References


[1] Optec. http://www.optec.be.

[2] N. Hendrickx, G. Van Steenberge, P. Geerinck, and P. Van Daele. Multilayer optical interconnects integrated on a printed circuit board. In *Photonics Europe'06, Proceedings SPIE 6185, Micro-Optics, VCSELs, And Photonic Interconnects*, Apr 2006.

[3] E. Bosman, P. Geerinck, W. Christiaens, G. Van Steenberge, J.M. Vanfleteren, and P. Van Daele. Optical connections on flexible substrates. In *Photonics Europe'06, Proceedings SPIE 6185, Micro-Optics, VCSELs, And Photonic Interconnects*, Apr 2006.

[4] P. Vanroelen. *Studie van laserablatie bij de terminatie van polymere optische vezels*. Master Thesis, Ghent University, 2002–2003.

[5] E. Bosman. *Fabricage van eindfacetten aan polymere optische vezels met behulp van laserablatie*. Master Thesis, Ghent University, 2003–2004.

[6] P. Catteeuw. *Klieven van glasvezels met behulp van lasers*. Master Thesis, Hogeschool West-Vlaanderen, 2002–2003.

[7] W. Vereecken. *Flexibele patroondefinitie in foto-gevoelige lagen met behulp van UV-lasers*. Master Thesis, Ghent University, 2004–2005.

[8] HIgh Density INteGration of Dies Into Electronics Substrates (HIDING DIES). http://www.hidingdies.net/.

[9] Smart High-Integration Flex Technologies (Shift). http://tfcg.elis.ugent.be/projects/shift/welcome.html.

[10] R. Srinivasan. Ablation of polymers and biological tissue by ultraviolet-lasers. *Science*, 234(4776):559–565, Oct 31 1986.

[11] J.T.C. Yeh. Laser ablation of polymers. *Journal Of Vacuum Science And Technology A–Vacuum Surfaces And Films*, 4(3):653–658, May-Jun 1986.

[12] R. Srinivasan and B. Braren. Ultraviolet-laser ablation of organic polymers. *Chemical Reviews*, 89(6):1303–1316, Sep-Oct 1989.

[13] S. Lazare and V. Granier. Ultraviolet-laser photoablation of polymers - a review and recent results. *Laser Chemistry*, 10(1):25–40, 1989.

[14] P.E. Dyer. Excimer laser polymer ablation: twenty years on. *Applied Physics A–Materials Science And Processing*, 77(2):167–173, Jul 2003.

[15] K. Naessens. *Excimer Laser Ablation of Microstructures in Polymers for Photonic Applications*. PhD Thesis, Ghent University, Sep 2003.

[16] R.F. Cozzens and R.B. Fox. Infrared-laser ablation of polymers. *Polymer Engineering And Science*, 18(11):900–904, 1978.

[17] R. Srinivasan, B. Braren, R.W. Dreyfus, L. Hadel, and D.E. Seeger. Mechanism of the ultraviolet-laser ablation of polymethylmethacrylate at 193 and 248 nm - laser-induced fluorescence analysis, chemical-analysis, and doping studies. *Journal Of The Optical Society Of America B–Optical Physics*, 3(5):785–791, May 1986.

[18] J.E. Andrew, P.E. Dyer, D. Forster, and P.H. Key. Direct etching of polymeric materials using a xecl laser. *Applied Physics Letters*, 43(8):717–719, 1983.

[19] R. Srinivasan and W.J. Leigh. Ablative photo-decomposition - action of far ultraviolet (193-nm) laser-radiation on poly(ethylene-terephthalate) films. *Journal Of The American Chemical Society*, 104(24):6784–6785, 1982.

[20] H.H.G. Jellinek and R. Srinivasan. Theory of etching of polymers by far-ultraviolet, high-intensity pulsed laser and long-term irradiation. *Journal Of Physical Chemistry*, 88(14):3048–3051, 1984.

[21] E. Sutcliffe and R. Srinivasan. Dynamics of uv laser ablation of organic polymer surfaces. *Journal Of Applied Physics*, 60(9):3315–3322, Nov 1 1986.

[22] L.B. Kiss and P. Simon. Statistical-model for the uv laser ablation mechanism of polymers. *Solid State Communications*, 65(10):1253–1254, Mar 1988.

[23] J.H. Brannon and J.R. Lankard. Pulsed $co_2$-laser etching of polyimide. *Applied Physics Letters*, 48(18):1226–1228, May 5 1986.

[24] P.E. Dyer, G.A. Oldershaw, and J. Sidhu. $Co_2$-laser ablative etching of polythylene terephthalate. *Applied Physics B–Photophysics And Laser Chemistry*, 48(6):489–493, Jun 1989.

[25] P.E. Dyer and J. Sidhu. Excimer laser ablation and thermal coupling efficiency to polymer-films. *Journal Of Applied Physics*, 57(4):1420–1422, 1985.

[26] S. Kuper, J. Brannon, and K. Brannon. Threshold behavior in polyimide photoablation - single-shot rate, measurements and surface-temperature modeling. *Applied Physics A–Materials Science And Processing*, 56(1):43–50, Jan 1993.

[27] S.R. Cain, F.C. Burns, C.E. Otis, and B. Braren. Photothermal description of polymer ablation - absorption behavior and degradation time scales. *Journal Of Applied Physics*, 72(11):5172–5178, Dec 1 1992.

[28] N. Arnold and N. Bityurin. Model for laser-induced thermal degradation and ablation of polymers. *Applied Physics A-Materials Science And Processing*, 68(6):615–625, Jun 1999.

[29] D.P. Brunco, M.O. Thompson, C.E. Otis, and P.M. Goodwin. Temperature-measurements of polyimide during krf excimer laser ablation. *Journal Of Applied Physics*, 72(9):4344–4350, Nov 1 1992.

[30] C.R. Davis, F.D. Egitto, and S.L. Buchwalter. Dopant-induced excimer laser ablation of poly(tetrafluoroethylene). *Applied Physics B-Photophysics And Laser Chemistry*, 54(3):227–230, Mar 1992.

[31] S. Kuper and M. Stuke. Femtosecond uv excimer laser ablation. *Applied Physics B–Photophysics And Laser Chemistry*, 44(4):199–204, Dec 1987.

[32] A. Miotello, R. Kelly, B. Braren, and C.E. Otis. Novel geometrical effects observed in debris when polymers are laser sputtered. *Applied Physics Letters*, 61(23):2784–2786, Dec 7 1992.

[33] W. Spiess and H. Strack. Structuring of polyimide by arf excimer laser ablation. *Semiconductor Science And Technology*, 4(6):486–490, Jun 1989.

[34] P.E. Dyer, S.D. Jenkins, and J. Sidhu. Development and origin of conical structures on xecl laser ablated polyimide. *Applied Physics Letters*, 49(8):453–455, Aug 25 1986.

[35] H. Niino, M. Nakano, S. Nagano, A. Yabe, and T. Miki. Periodic morphological modification developed on the surface of polyethersulfone by xecl excimer laser photoablation. *Applied Physics Letters*, 55(5):510–512, Jul 31 1989.

[36] P.E. Dyer and R.J. Farley. Periodic surface-structures in the excimer laser ablative etching of polymers. *Applied Physics Letters*, 57(8):765–767, Aug 20 1990.

[37] P.E. Dyer, S.M. Maswadi, H.V. Snelling, and C.D. Walton. Glass micromachining using the vuv $f_2$ laser. In *Photon Processing in Microelectronics and Photonics, Proceedings SPIE 4637*, Jun 2002.

[38] F. Wagner and P. Hoffmann. Structure formation in excimer laser ablation of stretched poly(ethylene therephthalate) (pet): the influence of scanning ablation. *Applied Physics A–Materials Science And Processing*, 69(S):S841–S844, Dec 1999.

[39] K. Arai, H. Imai, H. Hosono, Y. Abe, and H. Imagawa. 2-photon processes in defect formation by excimer lasers in synthetic silica glass. *Applied Physics Letters*, 53(20):1891–1893, Nov 14 1988.

[40] I.A. Konovalov and P.R. Herman. Ablation-induced stresses in fused silica by 157-nm f2-laser irradiation. In *Proceedings Materials Research Society Symposium Vol. 617*, 2000.

[41] J. Ihlemann and B. WolffRottke. Excimer laser micro machining of inorganic dielectrics. *Applied Surface Science*, 106:282–286, Oct 1996.

[42] P.E. Dyer, R.J. Farley, R. Giedl, and D.M. Karnakis. Excimer laser ablation of polymers and glasses for grating fabrication. *Applied Surface Science*, 96(8):537–549, Apr 1996.

[43] A. Luft, U. Franz, A. Emsermann, and J. Kaspar. A study of thermal and mechanical effects on materials induced by pulsed laser drilling. *Applied Physics A–Materials Science And Processing*, 63(2):93–101, Aug 1996.

[44] D.M. Karnakis, M.R.H. Knowles, K.T. Alty, M. Schlaf, and H.V. Snelling. Comparison of glass processing using high repetition femtosecond (800nm) and uv (255nm) nanosecond pulsed lasers. In *Photonics West'05, Proceedings SPIE 5718, Microfluidics BioMEMs And Medical Microsystems*, Jan 2005.

[45] S. Shuttleworth. Optimisation of laser wavelength in the ablation sampling of glass materials. *Applied Surface Science*, 96-8:513–517, Apr 1996.

[46] S. Nikumb, Q. Chen, C. Li, H. Reshef, H.Y. Zheng, H. Qiu, and D. Low. Precision glass machining, drilling and profile cutting by short pulse lasers. *Thin Solid Films*, 477(1-2):216–221, Apr 22 2005.

[47] A. Salleo, T. Sands, and F.Y. Genin. Machining of transparent materials using an ir and uv nanosecond pulsed laser. *Applied Physics A–Materials Science And Processing*, 71(6):601–608, Dec 2000.

[48] G. Allcock, P.E. Dyer, G. Elliner, and H.V. Snelling. Experimental observations and analysis of $co_2$ laser-induced microcracking of glass. *Journal Of Applied Physics*, 78(12):7295–7303, Dec 15 1995.

# Chapter 4

# Planar waveguides

*In this chapter, multimode waveguides integrated on a PCB are discussed. In a short literature overview different fabrication technologies are compared. Next, the experimental results on laser ablated waveguides are presented. Special attention is given to the optimization of the sidewall roughness. Cut-back loss measurement results are given, and compared to the loss of photolithographic defined waveguides. Finally, some realized single mode waveguide structures are included.*

## 4.1 Introduction

For the guided-wave transport of optical signals on a PCB, optical propagation in fibers and waveguides have been proposed in Chapter 1. Conventional fiber is certainly the most established technology and offers the lowest losses (few dB/km). The involved materials are qualified and reliable, and the technology is readily available from multiple sources. Drawbacks are the hardness of the material which makes interface preparation a complex task. A fiber termination procedure is being developed within Chapter 7. In general, today's fiber connector technology is still too expensive, in particular with regard to the targeted large number of optical channels [1]. Small-core plastic optical fiber might be an attractive alternative in this context. In general, fibers only offer point-to-point links, i.e. the implementation of splitters is only possible in combination with additional components. Waveguides are expected to be more cost efficient than fibers, they offer a higher degree of integration compared to the individual wiring of many discrete fibers, and arrays of them can be fabricated more densely than standard fiber ribbons. Fabrication of splitters, in-plane crossings and combiners is straightforward. Attenuation (few dB/m) is ca. 1000 times higher than for fiber, which is still sufficient for a typical link length of 1 m, but which only leaves little

margin for coupling losses. A major drawback is the relative novelty (i.e. low maturity) of the involved materials, whose process compatibility, reliability and lifetime remains to be properly qualified.

One open question, both for fiber and for waveguides, is the position of the optical layer [1]. An optical layer at the surface of the PCB has the advantage of minimal impact on the existing board fabrication processes, because it can be applied at the end of a normal process chain. This is also attractive in terms of board yield and therefore cost. A potential drawback might be the required space on and above the board, since the board surface is usually densely packed, with the few open spaces being used for air flow, i.e. heat management. Especially for waveguides, another drawback might be the reduced mechanical and environmental protection of a layer at the surface. The advantages and drawbacks of a buried optical layer are obviously complementary. In addition, one needs to determine where exactly the buried optical layer should be, e.g. in the center of the board or close to the surface. Aspects that influence this decision include the board structure (number and position of other layers, structure should usually be symmetric), or the coupling approach (see Chapter 5). We have been focussing on a surface level optical layer, mainly decided by the coupling approach.

Another question is the structure of the optical layer [1]. A layer covering the whole PCB area is easier to integrate, either by in-situ fabrication, or externally as a separate sheet that is laminated together with the rest of the layer stack. A means to make reliable electrical contacts (i.e. plated vias) through such a layer, however, needs to be developed. On the other hand, a small optical band, either fabricated in-situ or externally, embedded into an FR4 layer with cutouts (inlay technique), is more complex to integrate and align. For multilayer structures, one need to determine whether all the single optical layers are stacked together to one thick optical layer or whether they are interleaved with the electrical layers. Advantage of the first method is a better layer-to-layer alignment, which is of importance for the coupling, advantage of the second method can be an improved board stability.

As explained earlier, we have been focussing on board-integrated waveguides, based on acrylates, siloxanes, and thin glass sheets. The coating of the layers has been discussed in Chapter 2. For the patterning, UV exposure (through a conventional mask, or by serial laser writing), laser ablation, moulding, diffusion, ion-exchange, reactive ion etching, and HF etching have been proposed. We have been focusing on UV exposure through a conventional mask, and laser ablation. UV exposure allows for a high throughput, but the technology is not very flexible, and is not compatible with larger board dimensions. Laser ablation on the other hand, offers a lot of flexibility, can be scaled to larger board sizes, and it offers the possibility to compensate for substrate distortions, on the fly during waveguide definition.

## 4.2 Technology overview

### Photolithography

The key process in which radiation sensitive organic materials are selectively polymerized, crosslinked, or degraded has become a backbone of current opto- and microelectronics technology. The process is based on the doping of a host material with a photoinitiator. The higher (positive resist) or lower (negative resist) solubility of the exposed regions as compared to the unradiated areas is exploited during the subsequent development step. The resolution of the definable patterns (around 0.5 $\mu$m for abundantly used mask aligners) is sufficient for the definition of multimode and single mode board-level waveguides. The main drawback is the cost of high-resolution large area masks.

A considerable variety of photodefinable polymers are available, see Table 4.1 [2]. Recently, IBM reported on both acrylate and siloxane based waveguides [1, 3], Fujitsu investigated five different polymers [4, 5], Fraunhofer IZM focusses on epoxies [6], Georgia Institute of Technology reported on system-on-a-package (SOP) substrates with integrated optical interconnections based on inorganic polymer glass [7, 8], the University of Twente is developing their own epoxy based polymers to allow for contact mask aligning [9], the OptoBump concept from NTT is based on epoxies [10, 11], and VTT reported on SU-8 waveguides [12]. The propagation loss at 850 nm is ranging from as high as 0.6 dB/cm to as low as 0.04 dB/cm. All reports on lithographic structuring of board-level waveguides are carried out with the aid of exposure devices designed for wafers, as well 4 inch as 8 inch technology. An approach to produce 24 inch$\times$24 inch large-area panels is developed by Linköping University in cooperation with the Fraunhofer Institute [13], based on a stepwise projection patterning from 4 inch$\times$4 inch masks, with a misalignment between waveguides at the border crossing of $\approx$ 5 $\mu$m. Experimental results and propagation loss of photolithographic defined waveguides based on Ormocer® materials will be discussed in Section 4.3 and Section 4.4.

### Laser direct writing

Laser direct writing is a flexible technology for direct photoresist patterning with a focussed small beam spot without the need for masks, screens, molds, stamps or resists with associated wet chemistry. It allows for rapid fabrication of microdevices and microcircuits in the application area of microelectronics, photonics, MEMS and MOEMS. For board- and backplane-level interconnections, the propagation distances are in the range of tens of centimeters and large area processing is required. Laser writing is especially suitable for features with long linear dimensions in large areas. Additionally, laser writing is possible to non-planar, rolled or flexible substrates. It permits the creation of novel structures, which are

| Manufacturer | Polymer Type [Trade Name] | Patterning technique |
|---|---|---|
| Amoco | fluorinated polyimide [Ultradel] | photolithography |
| Corning | acrylate | photolithography RIE/laser ablation |
| | halogenated acrylate | photolithography RIE/laser ablation |
| Dow Chemical | benzocyclobutene [Cyclotene] | RIE |
| | perfluorocyclobutene [XU 35121] | photolithography |
| Exxelis | acrylate [Truemode™] | photolithography laser ablation laser direct writing |
| General Electric | polyetherimide [Ultem] | RIE/laser ablation |
| Hitachi | fluorinated polyimide | photolithography |
| Micro resist technology | polysiloxane [Ormocer®] | photolithography moulding |
| | epoxy [EpoCore] [EpoClad] | photolithography laser direct writing |
| NTT | halogenated acrylate | RIE |
| | deuterated polysiloxane | RIE |
| | fluorinated polyimide | RIE |
| | epoxy | photolithography |
| Luvantix | epoxy | photolithography |
| Optical Crosslinks | acrylate [Polyguide] | diffusion |
| Promerus | polynorbornene [Core MSDS] [Clad MSDS] | moulding |
| RPO | inorganic polymer glass [IPG] | photolithography RIE |
| Telephotonics | [OASIC] | photolithography RIE/laser ablation |

**Table 4.1:** Patterning techniques for optical polymers to be used for board-level interconnections

virtually impossible with the conventional mask lithography such as waveguides with a varying refractive index along the direction of propagation. Additionally, restricted regions can be processed without affecting the surrounding areas as opposed to the other conventional planar processing technologies. Obvious benefit is rapid prototyping and small-volume manufacturing [14]. A polymer optical backplane with 1 m transmission has been manufactured by Daimler Chrysler [15, 16], based on laser written waveguides with a core section of $250\times200\,\mu m^2$. Heriot-Watt University is using a direct write system based on a HeCd (wavelength 325 nm) UV laser [17]. Fraunhofer IZM's direct write process is based on a Siemens Dematic Microbeam 3200 (wavelength 355 nm), for structuring epoxy based polymers on larger areas [6]. The results from IBM apply both for lithographic defined and laser written waveguides [1, 3].

## Diffusion and photolocking

A waveguide manufacturing process based on internal monomer diffusion and photolocking by using an acrylate polymer film is the DuPonts trademark Polyguide process, currently available at Optical CrossLink under the name GuideLink. Waveguides are defined with light-induced polymerization and monomer diffusion in the binder polymer matrix to create local higher index areas for waveguide cores within the polymer foil [18, 19]. Square step or graded index core profiles and customisable numerical aperture varying from 0.1 to 0.3 are available. Losses for multimode foils of 0.08 dB/cm at 850 nm are achieved. Fabrication is implemented on a reel-to-reel process in $30\times40\,cm^2$ flexible substrates. Structural integrity and thermo-mechanical stability is achieved by using high $T_g$ and low CTE buffer film laminates, such as Kapton polyimide.

## Moulding

Polymeric optical components have always been regarded as having the potential of low cost fabrication. Well-established industrial replication techniques such as casting, moulding, hot embossing, and soft embossing contribute to the fulfilment of such expectations.

In the hot embossing process, the waveguide structures are imprinted into the optical polymer with an embossing tool under pressure at elevated temperature. Two hot embossing processes for waveguide fabrication, groove-filling and rib-cladding, are reported. In the groove-filling approach the waveguide structures are imprinted into the cladding material and filled with a higher index core material. After curing the uppercladding is laminated. In rib-cladding process the waveguides cores are manufactured first and laminated on top of the undercladding substrate. Besides the waveguide structures, the embossing tool can contain micromechanical structures for alignment and coupling. Siemens C-LAB

[20, 21], the University of Dortmund [22], the University of Ulm [23], and Fraunhofer IZM [24] have been investigating this process for quite some years. More recently, results from research institutes in Korea have been reported [25, 26, 27].

Currently the embossed substrate size is limited to $\approx$15–20 cm substrates, using the embossing tool from Jenopik Mikrotechnik GmbH. Due to the nature of the process, the embossing tool defines ultimately the resulting physical dimensions, surface coplanarity, tolerances and sidewall roughness and is therefore the key to ensure the quality of the waveguides. Conventional CNC-machined embossing tools are suitable for larger structures ($>100\,\mu$m), but do not meet the sidewall roughness requirement realized by employing lithographic techniques. Features ranging $>1\,\mu$m are realized by making a master with combined UV-deep lithography and electroforming process. The surface roughness of an electroformed nickel tool is less than 10 nm. A patterned silicon wafer can be used as an embossing tool as well. For very high resolution and aspect ratios, X-ray lithography LIGA or laser-LIGA tool manufacturing has to be used. Good uniformity can be obtained over the whole surface, but inevitably the replication process introduces an additional degree of roughness to the waveguides which adds a significant scattering loss contribution to the overall waveguide loss. This scattering loss is typically between 0.1–0.3 dB/cm for wavelengths in the range from 633 to 850 nm [28].

Recently, the University of Dortmund reported on an adopted casting in combination with doctor blading as a polysiloxane waveguide fabrication method [29, 30]. In the reported experiments standard 6 inch technology has been applied, extension to larger formats ($300\times400\,\mathrm{mm}^2$) is under development. The technique allows simultaneous fabrication of waveguides together with integrated micromirrors. First the waveguide cores are fabricated by filling the grooves in the mould by the core polymer. This is accomplished by the doctor blade technique. Then the core material is thermally cured, and in a next step the waveguide substrate layer is fabricated by applying the liquid cladding polymer to the mould, and, subsequently, the substrate carrier is pressed against the mould. Copper structures on the substrate define the thickness of the waveguide substrate layer. The superstrate layer is applied identically. Other reports on moulded waveguide circuits include reports on soft embossing of SU-8 by the University of Texas [31], and casting of polynorbornenes by BFGoodrich [32].

## Laser ablation

Laser ablation offers basically the same advantages as laser direct writing, it allows rapid fabrication, and is scalable to larger board dimensions. The technology is compatible with standard electrical PCB manufacturing processes, as it is already used for drilling microvias and trimming resistors. Moreover, it allows to define not only waveguides [33], but also coupling structures [34], mi-

crolenses [35], and alignment marks. Reports on optical loss of laser ablated waveguides from other research groups are to our knowledge not available so far. Experimental results and propagation loss based on KrF excimer laser ablation of Truemode$^{TM}$ will be discussed in Section 4.3 and Section 4.4. As was presented in Chapter 3, other combinations between available laser source, and investigated optical material are not suited for optical waveguide applications.

## Diffusion and ion-exchange process

Processes for fabricating gradient index waveguides on glass substrates are based on diffusion and ion-exchange. Modifications to the basic processes are for example thermal diffusion, thermal ion-exchange, field-assisted ion-exchange, wet or dry ion-exchange. The ion-exchange process is one of the most widespread technologies for the fabrication of optical waveguides in glass substrates. Fraunhofer IZM reported first experimental results for electrical optical circuit boards using ion exchange in molten salts based on borosilicate glass D263T from Schott [36], the same glass foils as being investigated within this PhD dissertation. At the glass interface monovalent alkali ions, mostly sodium, become very mobile under influence of a hot salt melt. Alkali ions of the glass are exchanged by diffusion with alkali ions of the salt melt. If these ions have other ionic radii and polarizability, a variation of refractive index is possible. Therefore dopants could be Li, K, Cs, Rb, Ag, Tl and Cu. Due to the availability of the cations sodium and potassium in D263T it is possible to produce channel waveguides using the ion exchange technique. The exchange efficiency is affected by temperature, concentration of dopants in the salt and the glass and the exchange time. Increase in productivity is possible if the thermal statistic movement of ions can be enhanced by a directed force like an electrical field E or a thermal gradient.

## HF etching

PPC Electronic's OptoBoard [37] is based on HF wet etching of borosilicate glass D263T. The 70 $\mu$m thin glass sheet contains arrays of waveguides, all etched simultaneously, with the possibility to include alignment marks, see Figure 4.1. The process sequence includes glass cleaning, metal coating, photoresist coating and patterning, metal patterning by wet etching, photoresist stripping, glass wet etching with modified HF, metal mask wet etching, glass cleaning, and coating with polymer cladding material. The process has partly been developed within the European IST-IO-project (Interconnect by Optics) [38], and developed further within the European PIDEA-Orbita-project (Optical Routing Backplanes Intranetworking for Telecom/datacom Applications). The waveguide samples provided by PPC Electronic are further investigated within this work for the definition of coupling structures, using $CO_2$ laser ablation, results are presented in Chapter 5.

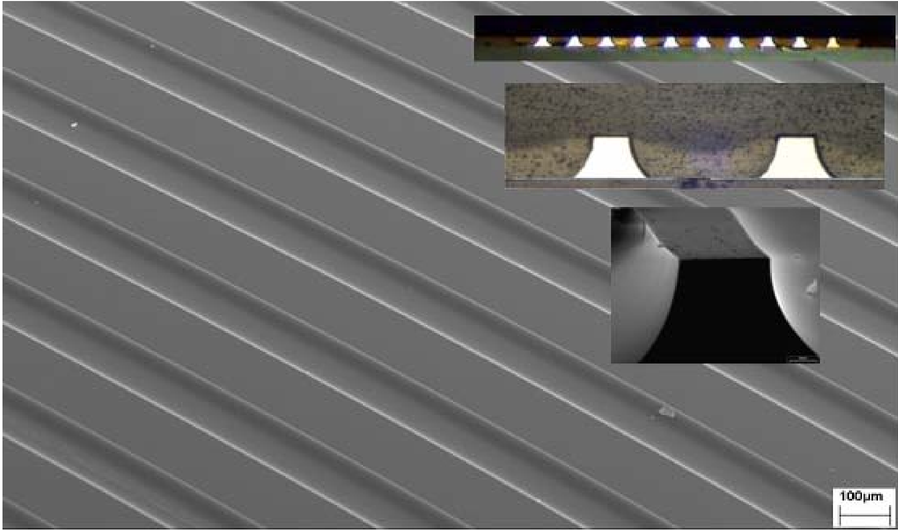


**Figure 4.1:** Array of waveguides in a 70 $\mu$m thick borosilicate glass sheet defined by HF etching (source: PPC Electronic [38])

# 4.3 Fabrication

In Chapter 3 it has been shown that KrF excimer laser ablation of Truemode$^{TM}$ has the potential of defining multimode waveguides with very smooth sidewalls, without the deposition of debris, and without the presence of microstructures. The process flow for defining waveguides using laser ablation is shown in Table 4.2. The cladding and core layers are deposited as described in Section 2.5, the core layer is structured prior to deposition of the uppercladding. An SEM image of a single waveguide fabricated using KrF excimer laser ablation is shown in Figure 4.2. The width of the waveguide is determined by the distance between the two grooves. The grooves have a depth of at least the thickness of the core layer, being 50 $\mu$m, with a standard deviation of 5 $\mu$m. Removing more material, being ablation of undercladding material, is not a problem, as the groove will be filled up with uppercladding material anyway. The starting and ending points of the grooves feature a ramp with an angle $\theta = \text{atan(depth/a)}$, with a being the length of the rectangular beam spot. These ramps do not have a function, as separate mirrors will be fabricated to allow in- and outcoupling. The final optimum ablation parameters are given by: $2.5 \pm 0.5\,\text{J/cm}^2$ laser fluence (corresponding to a pulse energy of 6 mJ), 200 Hz pulse repetition rate, $75 \times 300\,\mu\text{m}^2$ laser spot dimensions, 340 $\mu$m/s ablation speed, and 125 $\mu$m pitch to pattern an array of waveguides. The 125 $\mu$m pitch subtracted with the 75 $\mu$m width of the laser beam, results in a nominal 50 $\mu$m waveguide width. In Figure 4.3 a cross-

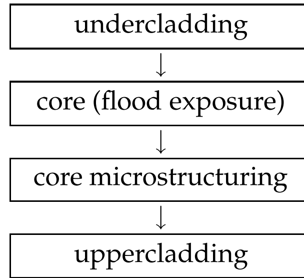


**Table 4.2:** Process flow for the definition of waveguides by laser ablation

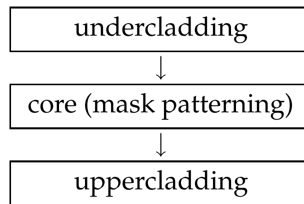


**Table 4.3:** Process flow for the definition of waveguides by photolithography

sectional view shows the non-perpendicularity of the waveguide sidewalls. The height is 52 $\mu$m, the width 52 $\mu$m and 68 $\mu$m at the top and bottom respectively. This tapering results from the limited depth of focus (DOF) of the beam delivery system, material specific ablation properties, and the laser fluence. However, the contribution of the surface roughness to the optical loss, is much more important than the cross-sectional shape [39]. For that reason, the optimization of the waveguide ablation process, is oriented towards sidewall roughness, instead of cross-sectional shape. An array of KrF excimer laser ablated waveguides on a pitch of 125 $\mu$m is shown in Figure 4.4. The pitch is chosen to be compatible with 125 $\mu$m and 250 $\mu$m standards. Smaller pitches down to 62.5 $\mu$m have not been investigated.

There are two obstacles to exploit KrF excimer laser ablation as a patterning technique for Ormocer®. The first obstacle is the re-deposition of the ablation products on or around the ablation site, and the second obstacle is the presence of surface microstructures on the bottom of the ablated cavity, as was discussed in Section 3.2. For that reason photolithography is used to pattern the waveguides. A microscope image of an array of 45×120 $\mu$m$^2$ waveguides on a pitch of 250 $\mu$m is shown in Figure 4.5. A mask opening of 50 $\mu$m results in a waveguide width of 120 $\mu$m. This arises from the requirement of a non-contact mask condition, and could be eliminated by controlling and reducing the mask-optical layer distance. As this is not supported by the available mask aligner, this has not been further investigated.

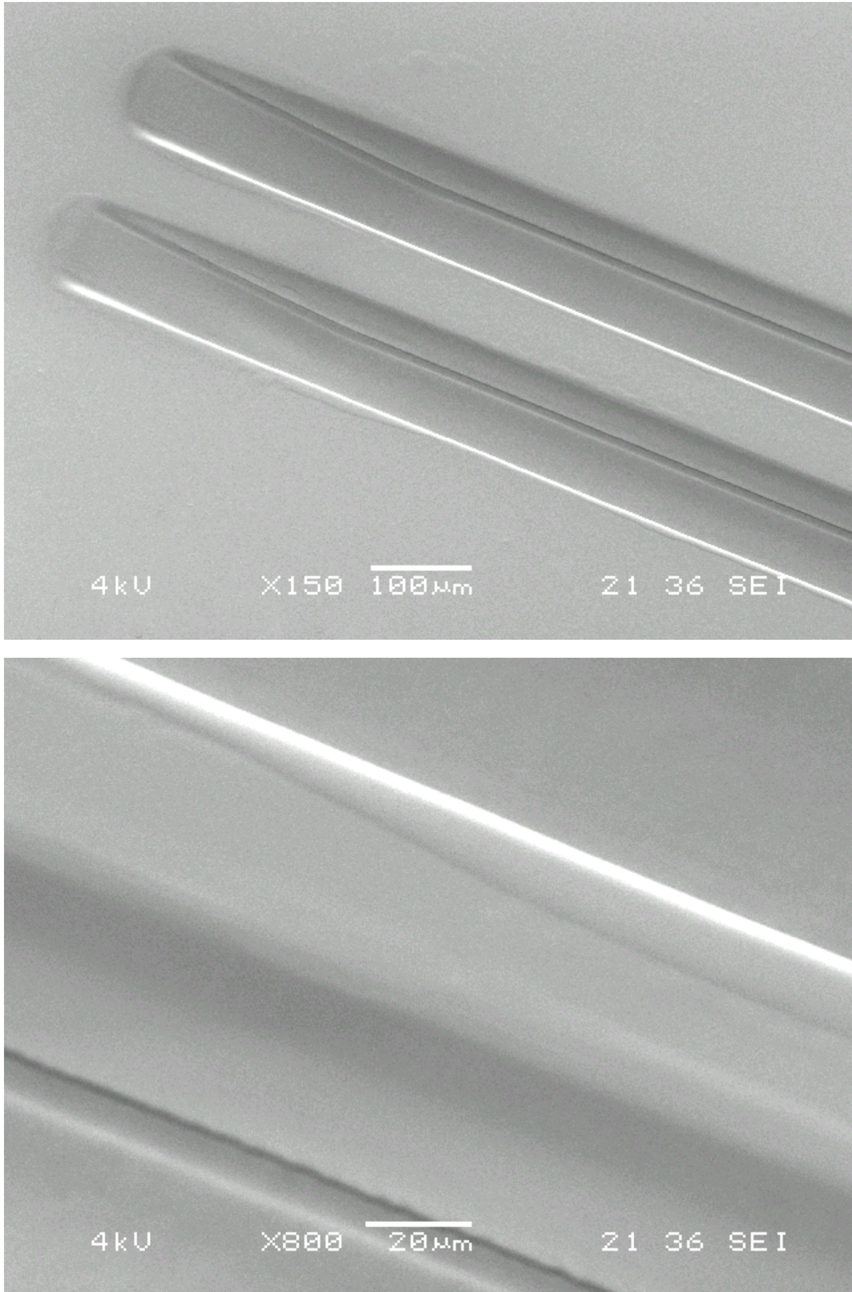


**Figure 4.2:** SEM images of excimer laser ablated waveguides (Truemode$^{TM}$)

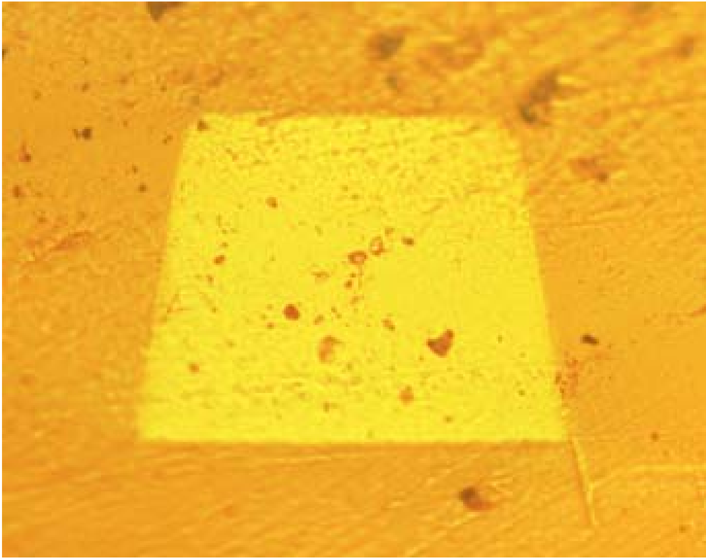

**Figure 4.3:** Cross-section of an excimer laser ablated waveguide (Truemode$^{TM}$)

**Figure 4.4:** Microscope image of an array of KrF excimer laser ablated waveguides on a pitch of 125 $\mu$m (Truemode$^{TM}$)

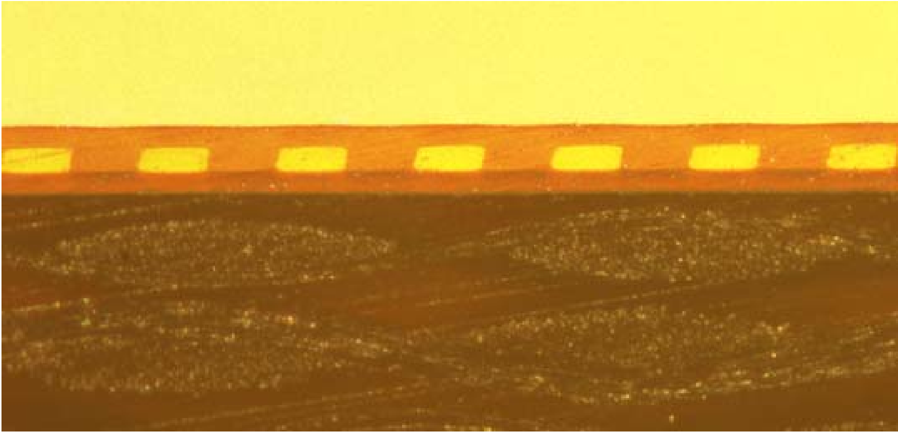

**Figure 4.5:** Microscope image of an array of 45×120 $\mu m^2$ waveguides on a pitch of 250 $\mu$m defined by photolithography (Ormocer®)

## 4.4 Characterization

### 4.4.1 Surface roughness

Roughness measurements using a non-contact optical profiler confirm the smoothness of the laser ablated sidewalls. Two different ablation parameters have a large impact on the resulting waveguide surface roughness:

- The influence of the laser pulse energy on the waveguide top surface roughness is investigated for pulse energies of 6 mJ and 12 mJ. The roughness decreases by a factor 2–2.5 for 6 mJ compared to 12 mJ.
- The influence of the laser pulse repetition rate on the sidewall roughness is shown in Figure 4.6. The roughness can be seriously reduced by increasing the pulse repetition rate: $R_a$ of 48.9 ± 6.8 nm, RMS of 61.3 ± 8.3 nm for 50 Hz, $R_a$ of 32.0 ± 7.1 nm, RMS of 41.4 ± 8.7 nm for 100 Hz, and $R_a$ of 21.0 ± 4.7 nm, RMS of 26.6 ± 5.3 nm for 200 Hz (based on two measured samples). Maximum pulse repetition rate is 300 Hz, but as this pulse frequency is detrimental for the excimer laser's life time, pulse frequencies above 200 Hz have never been used.

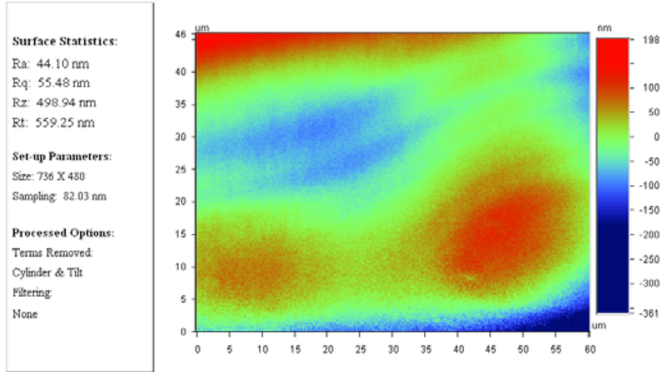


(a) 50 Hz

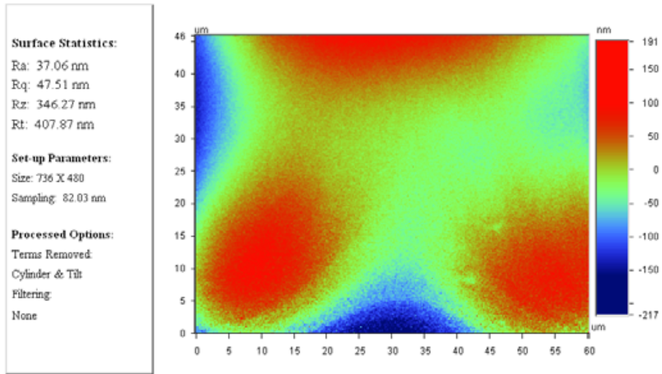


(b) 100 Hz

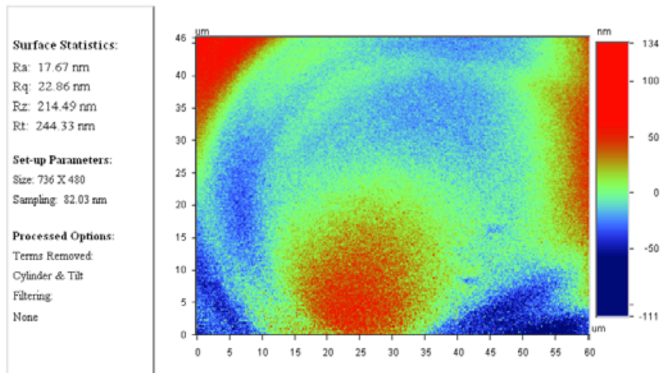


(c) 200 Hz

**Figure 4.6:** Sidewall surface roughness as a function of pulse repetition rate for KrF excimer laser ablated waveguides (Truemode$^{TM}$)

### 4.4.2 Measurement set-up

The alignment set-up (Newport) that has been built comprises motorized XYZ left and right stage stacks with manual tip/tilt movement, mounted on a vibration isolated workstation. The motorized XY stages have a travel range of 10 cm, the Z stages a travel range of 2.5 cm, all with a bidirectional repeatability of 50 nm. The long travel range is compatible with typically used PCB dimensions of $10 \times 10\,\text{cm}^2$. The six motorized axes are controlled by a motion controller, remote control is possible for quite simple positioning tasks. To take the full advantage of the advanced features and capabilities of the system, operation using GPIB communication interface is advisable. The manual tip/tilt stages are mounted on top of the XYZ stack, but they are only used for visual alignment of the sample edges with respect to the optical axes. Active tip/tilt adjustment is not used, as in this case the measurements become very time consuming. On each XYZ stack optical fibers are mounted, used for the in- and outcoupling. The optical PCB is mounted on a fixed central stage.

The alignment in YZ direction is done actively, by optimizing the measured output power, alignment in X direction (along the optical axis) is done using a vision system, with a CCD camera. The camera can switch between in- and outcoupling to allow alignment in the X direction. Another camera is used to visualize the light beam coming out of the waveguide, so enabling the YZ alignment at the incoupling. Once the incoupling is roughly aligned, the optical fiber at the out-coupling can be positioned in front of the facet, and the measured optical power can be optimized. Subsequently adjusting in- and outcoupling allows for maximizing the output power.

A laser diode light source from QPhotonics operating at 845 nm is mounted in a Newport laser diode mount (Model 742 DIL Mount), allowing the interface to a Newport (Model300B Series) temperature controller, and a Newport (Model 500B Series) laser diode driver. Measurements are performed using an operating current of 32 mA, corresponding to a reference fiber-to-fiber output power of 2.92 mW. Optical losses at other wavelengths are measured as well, laser sources operating at 980 nm and at 1310 nm are driven by a current of 16.7 mA and 40 mA, corresponding to a reference fiber-to-fiber output power of 1.92 mW and 1.85 mW respectively. The optical power is measured using a Newport photodetector (818 Series), both for 850 nm and 980 nm. At 1310 nm an adjusted photodetector is used. The Newport optical power meter (Model 1930/2930 Series) provides a continuous wave measurement. Both laser diode driver and temperature controller have a USB interface, the power meter and the motion controller are using a GPIB communication interface. A picture of the complete measurement set-up is shown in Figure 4.7.

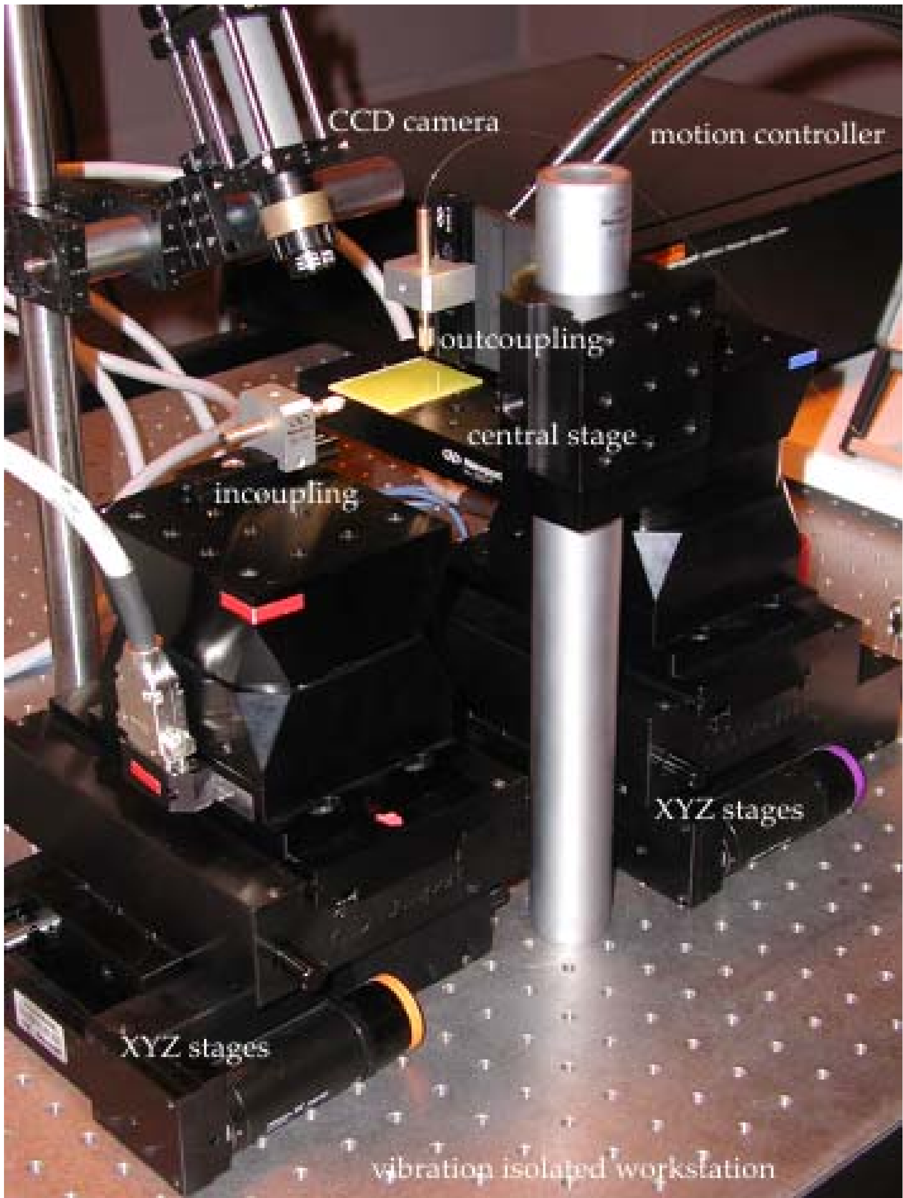


**Figure 4.7:** Optical loss measurement set-up

| | Truemode$^{TM}$ | Ormocer® |
|---|---|---|
| Wavelength | 850 nm | 830 nm |
| Cladding | 1.5266 | 1.5475 |
| Core | 1.5563 | 1.5306 |
| NA | 0.3 | 0.23 |

**Table 4.4:** Truemode$^{TM}$ and Ormocer® indices of refraction

### 4.4.3 Waveguide propagation loss

The ultimate test in the realization of polymeric optical waveguide circuits implies the measurement of their propagation and coupling loss, here determined using the cut-back method. The optical PCB is sawed to the required length, the endfaces are prepared by a polishing procedure. This consists in pushing the sample edge onto a revolving plate with decreasing grain size, flushed with water. The surface roughness of such a manually polished endfacet is characterized by an $R_a$ of 184 nm, and an $R_q$ of 234 nm. In front of the incoupling facet, a cleaved 50 $\mu$m diameter multimode fiber is positioned, with a numerical aperture of 0.2. No index matching adhesives are used. Core and cladding refractive indices are given in Table 4.4, resulting in an NA of 0.3 for Truemode$^{TM}$, and an NA of 0.23 for Ormocer®. At the out-coupling facet, light is coupled towards a cleaved 100 $\mu$m diameter multimode fiber with an NA of 0.29. For each waveguide length, losses are averaged over an array of waveguides, in order to achieve reliable results.

**KrF excimer laser ablated waveguides**

Optimization of propagation loss as a function of KrF excimer laser pulse repetition rate is shown in Figure 4.8, Figure 4.9 and Figure 4.10, and summarized in Table 4.5. The average propagation loss at a wavelength of 850 nm for a pulse repetition rate of 50 Hz is $0.68 \pm 0.12$ dB/cm, for a pulse repetition rate of 100 Hz the average propagation loss is $0.48 \pm 0.2$ dB/cm, and for a pulse repetition rate of 200 Hz the average propagation loss is $0.45 \pm 0.16$ dB/cm. Other ablation parameters are kept constant.

| Pulse frequency (Hz) | Propagation loss (dB/cm) |
|---|---|
| 50 | $0.68 \pm 0.12$ |
| 100 | $0.48 \pm 0.20$ |
| 200 | $0.45 \pm 0.16$ |

**Table 4.5:** Propagation loss optimization at 850 nm for varying KrF excimer laser pulse repetition rate (Truemode$^{TM}$)

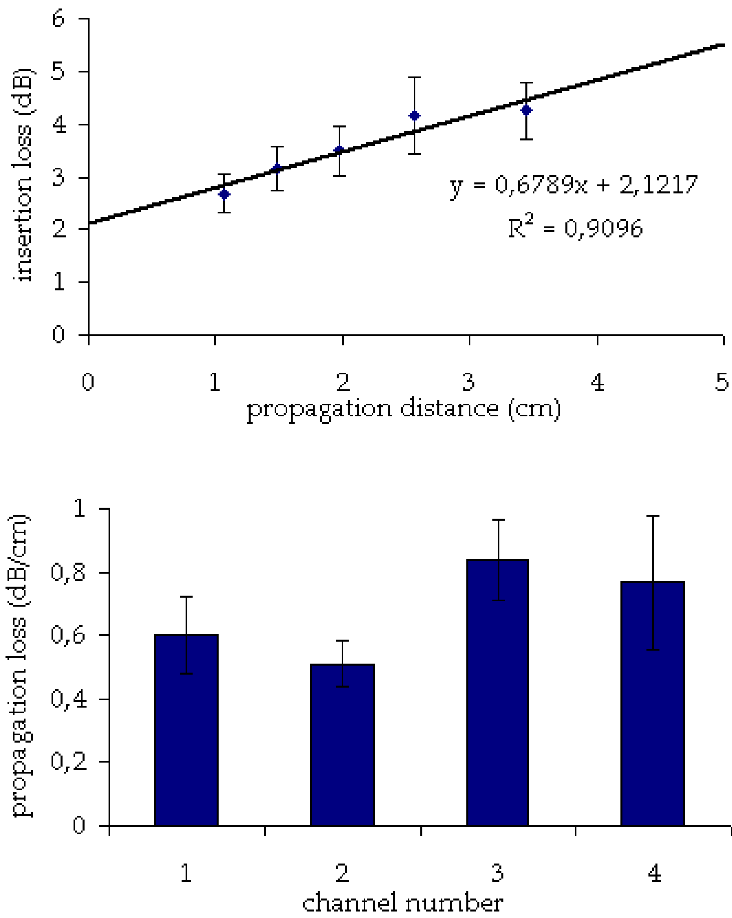


**Figure 4.8:** Loss of KrF excimer laser ablated waveguides (Truemode™) at 850 nm for a pulse repetition rate of 50 Hz

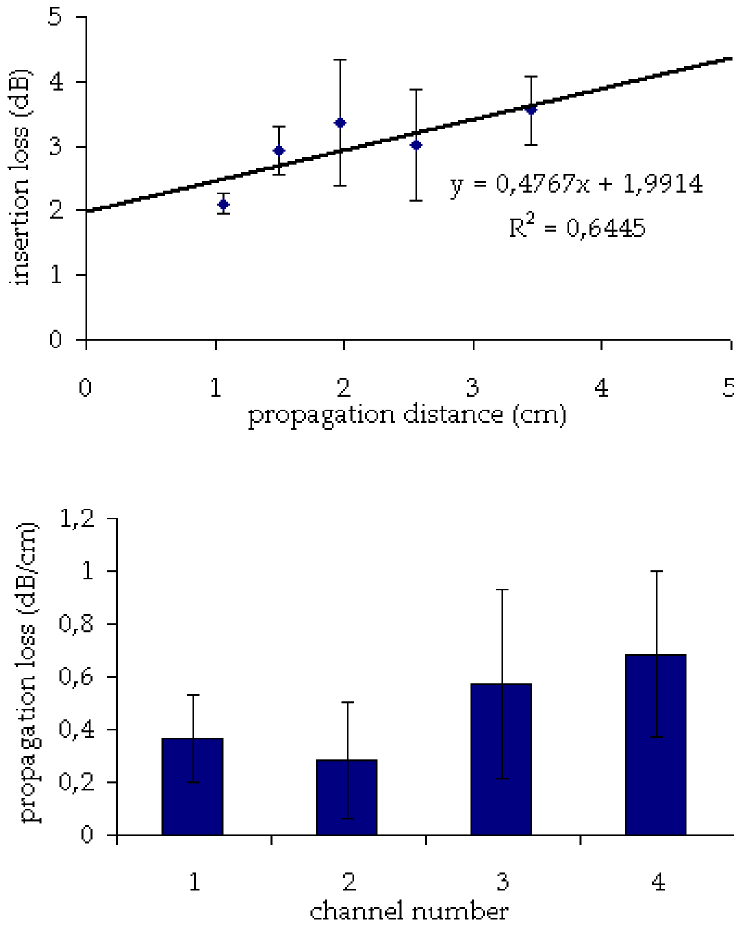


**Figure 4.9:** Loss of KrF excimer laser ablated waveguides (Truemode™) at 850 nm for a pulse repetition rate of 100 Hz

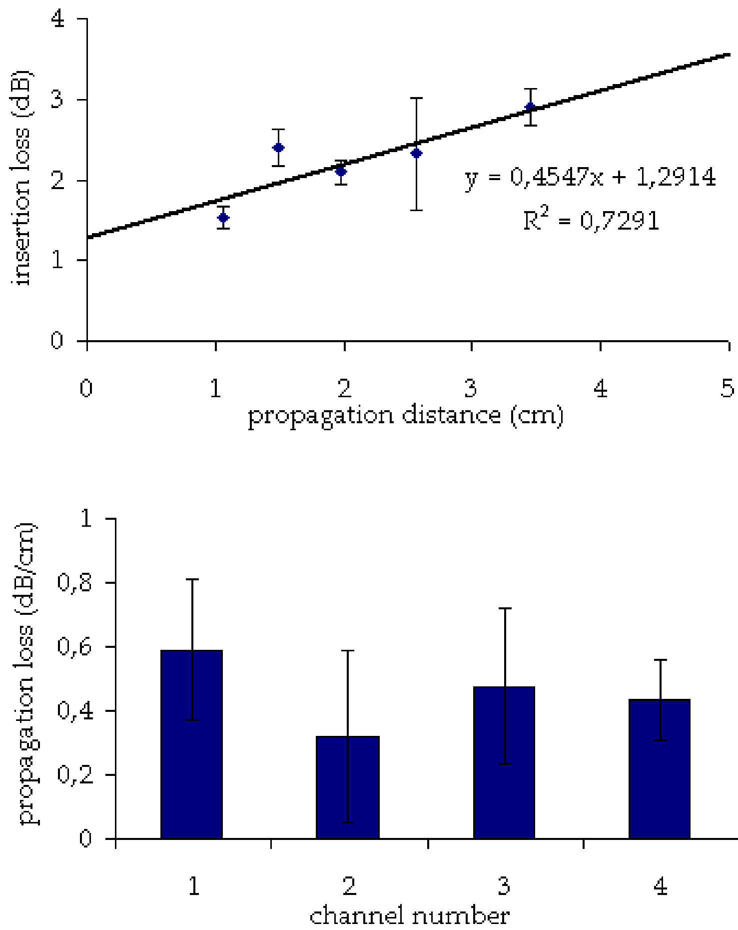


**Figure 4.10:** Loss of KrF excimer laser ablated waveguides (Truemode™) at 850 nm for a pulse repetition rate of 200 Hz

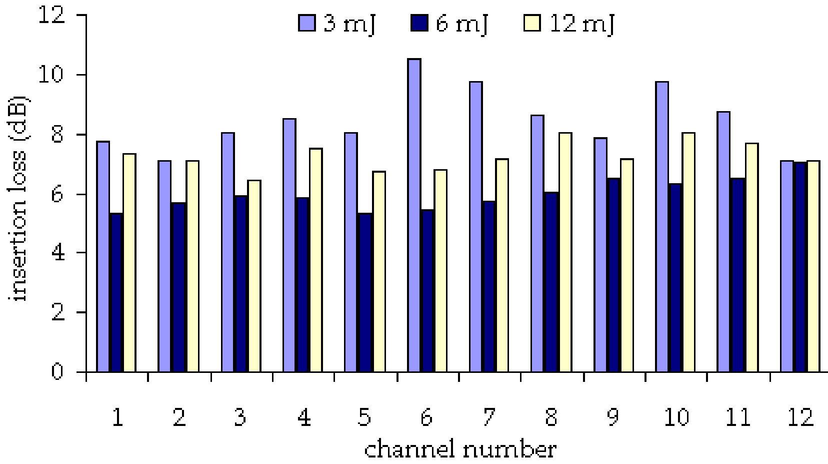


**Figure 4.11:** Loss of KrF excimer laser ablated waveguides (Truemode$^{TM}$) at 850 nm as a function of pulse energy

Optimization of propagation loss as a function of pulse energy is shown in Figure 4.11. Propagation distance of 8 cm is kept fixed. The average insertion loss, over the 12 channels, for a pulse energy of 3 mJ is $8.48 \pm 1.07$ dB, for a pulse energy of 6 mJ the average insertion loss is $5.97 \pm 0.54$ dB, and for a pulse energy of 12 mJ the average insertion loss is $7.26 \pm 0.49$ dB. A different pulse energy results in a different ablation depth per pulse. This means that for a fixed ablation depth, the ablation speed is changed together with the pulse energy, which might also have an impact on the insertion loss. However, it is clear that for the investigated combinations (pulse energy and corresponding propagation speed) a minimum insertion loss is achieved for a pulse energy of 6 mJ.

A combination of the separately defined optimum ablation parameters results in a propagation loss of $0.11 \pm 0.03$ dB/cm and an average coupling loss of $1.91 \pm 0.07$ dB, see Figure 4.12. The variation of the optical loss over the different channels is mainly due to the non-reproducibility of the manual polishing procedure of the coupling facets.

In addition to the propagation loss and coupling loss measurements, the crosstalk of laser ablated waveguides is measured. The isolation between adjacent waveguides on a pitch of 125 $\mu$m is -35 dB, for a propagation distance of 7.4 cm.

An example of a $10 \times 10$ cm$^2$ PCB with integrated optical Truemode$^{TM}$ layers containing arrays of KrF excimer laser ablated multimode waveguides with a propagation loss of 0.11 dB/cm at 850 nm can be seen in Figure 4.13.

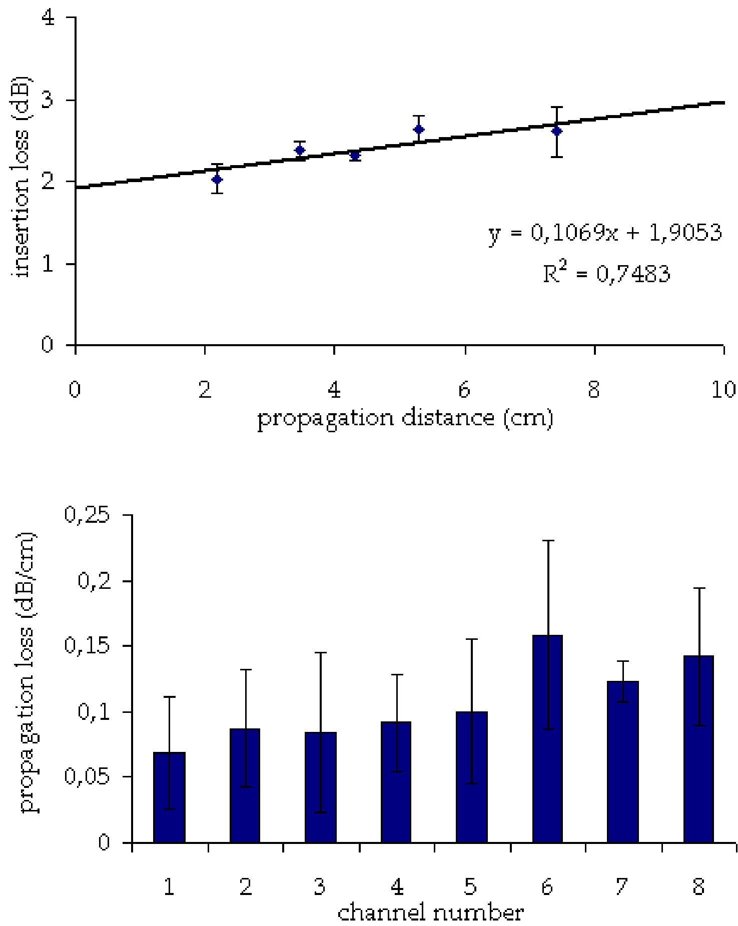


**Figure 4.12:** Loss of KrF excimer laser ablated waveguides (Truemode$^{TM}$) at 850 nm for optimum ablation parameters

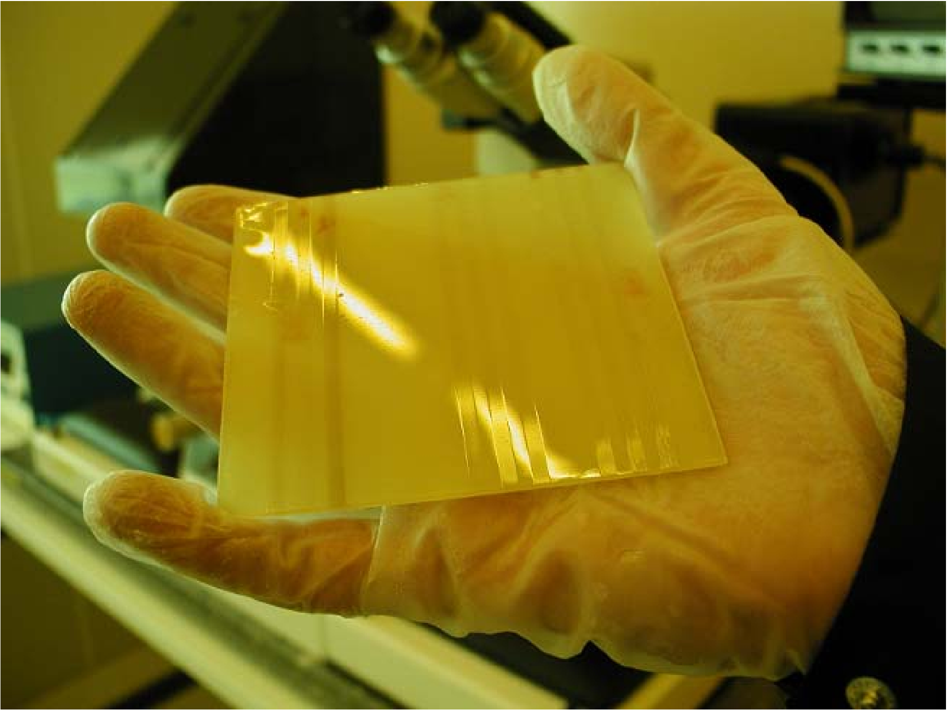

**Figure 4.13:** 1×12 arrays of KrF excimer laser ablated parallel optical interconnections integrated on a $10 \times 10\,cm^2$ PCB

### Waveguides defined by photolithography

For Ormocer®, the propagation losses of waveguides defined by photolithography are measured using the same measurement set-up. The losses are determined both at 850 nm and at 980 nm. The results can be found in Figure 4.14 and Figure 4.15. The large uncertainties at 850 nm are caused by the limited mask dimensions, together with the low propagation losses. At 850 nm the propagation loss is 0.08 dB/cm, the coupling loss is 2.10 dB. At 980 nm the propagation loss is $0.22 \pm 0.07$ dB/cm, and the coupling loss is $1.17 \pm 0.21$ dB.

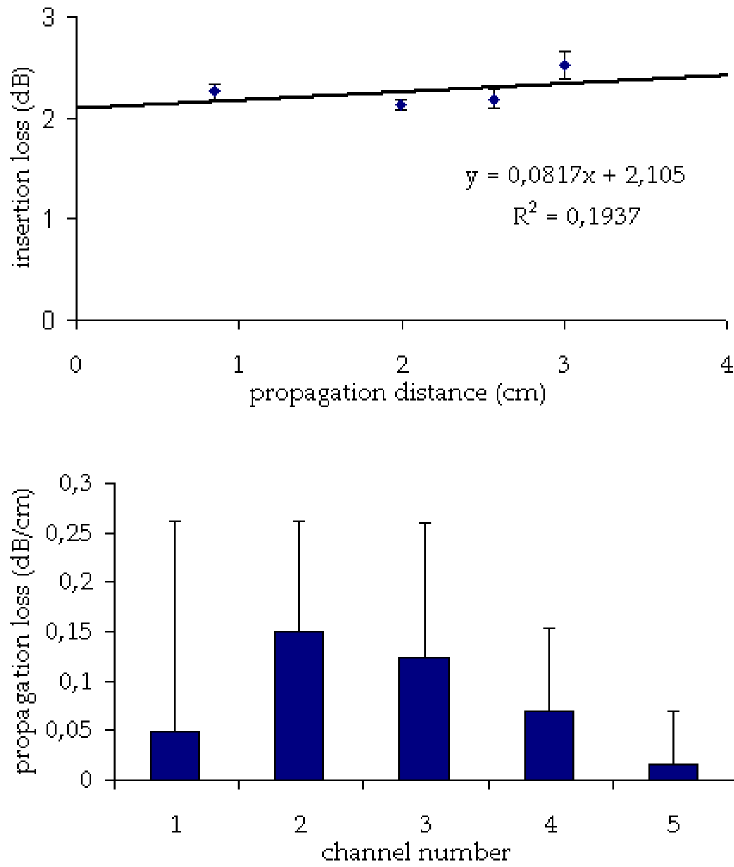


**Figure 4.14:** Loss of waveguides defined by photolithography (Ormocer®) at 850 nm

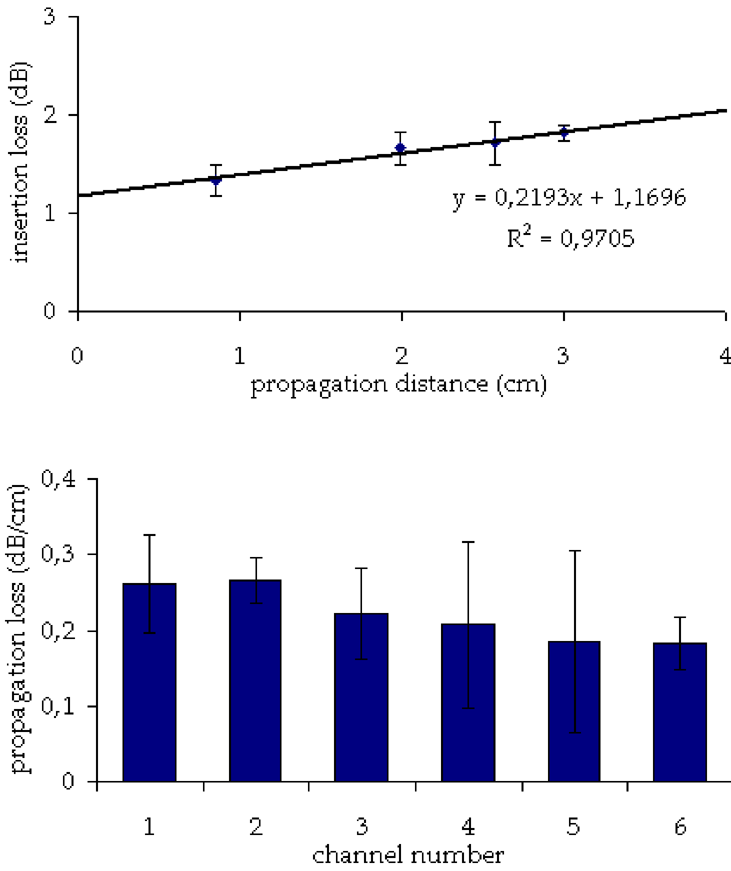


**Figure 4.15:** Loss of waveguides defined by photolithography (Ormocer®) at 980 nm

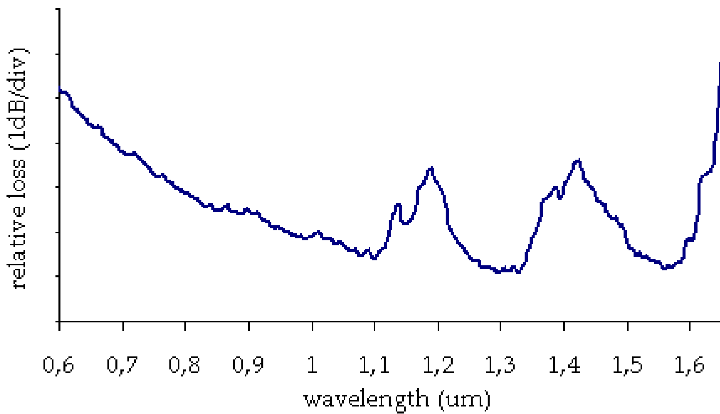


**Figure 4.16:** Relative loss spectrum of a KrF excimer laser ablated waveguide (Truemode™)

### 4.4.4 Spectral attenuation

Figure 4.16 shows the relative loss spectrum (1 dB/division) of a KrF excimer laser ablated waveguide in Truemode™. The spectrum is measured using a 50 $\mu$m fiber as input, a 100 $\mu$m fiber as output and a halogen lamp as a light source.

First conclusion is that at shorter wavelengths a yellowing effect increases the propagation loss. This yellowing is introduced by the ablation process, as it is not present in bulk material, see Figure 2.9 on page 33. As discussed in Section 2.3.2, such yellowing results from the formation of partially conjugated molecular groups characterized by broad ultraviolet absorption bands, which tail off in intensity through the visible. Thermal coloration is a common problem with organic polymers when exposed to elevated temperatures. Since during the ablation process, the temperature rise at the surface is typically found to be $\geq$ 800–1000 K (for a very short time period), it is no wonder that yellowing is introduced. The low extent of the heat-affected-zone, explains why yellowing is rather limited. In general, the power loss as a function of time for a given temperature can be measured by comparing the optical outputs before and after heating. Over a wide range of temperatures, the degradation rates or yellowing rates (losses as a function of time and temperature) were found to be well described by an Arrhenius expression of the form:

$$rate = A - exp[-(E_a/kT)] \tag{4.1}$$

where k is Boltzmanns constant, T is the absolute temperature, $E_a$ is an activation energy for the chemical degradation process, and A is a constant. These yellowing rates can be measured, and fit to the Arrhenius law.

| Wavelength (nm) | Insertion loss (dB) | Propagation loss (dB/cm) |
|---|---|---|
| 850 | reference | 0.11 |
| 980 | −0.7 | 0.11 dB/cm − 0.7 dB/7.4 cm = 0.015 |
| 1310 | + 0.3 | 0.11 dB/cm + 0.3 dB/7.4 cm = 0.15 |

**Table 4.6:** Propagation loss as a function of wavelength (Truemode$^{TM}$)

For example, for acrylates from Corning [28] this results in practical stabilities (time for thermally inducing 0.1 dB/cm loss) at 840 nm of about 65 year at 100$^o$C, 10 year at 120$^o$C, one year at 150$^o$C, two weeks at 200$^o$C, and one day at 250$^o$C.

Second conclusion out of the loss spectrum is a low loss at wavelengths of 980 nm and 1310 nm. This is verified by comparing the insertion loss of 7.4 cm long waveguides at 980 nm and 1310 nm to 850 nm as a reference wavelength, using the same set-up as is used for the cut-back measurements. Results are summarized in Table 4.6. At 980 nm the average insertion loss is decreased with 0.7 dB, at 1310 nm increased with 0.3 dB. This means a waveguide loss of 0.015 dB/cm at 980 nm, and 0.15 dB/cm at 1310 nm. At these wavelengths the loss of laser ablated waveguides is lower compared to photolithographic defined waveguides. However, further cut-back measurements are required to confirm the propagation losses at 980 nm and 1310 nm.

## 4.5 Single mode waveguides

The integration of single mode waveguides on a standard PCB is not within the scope of this PhD work. However, within the framework of a project with Motorola, the aim was to fabricate out-of-plane coupling structures for single mode waveguide samples provided by the Fraunhofer IOF Institute. The fabrication of the out-of-plane couplers will be discussed in Chapter 5. The characterization of the test-bed waveguides is described in this section. Single mode interconnections are further investigated within the ongoing PhD work of Nina Hendrickx, Ghent University.

The single mode waveguides are defined in Ormocer® by photolithography, and have a cross-sectional shape of $7 \times 8\,\mu m^2$, as is shown in the cross-section in Figure 4.17. To measure the loss of a vertical coupling structure, the propagation loss and the coupling loss for horizontal out-coupling facets must be known first. The propagation loss are determined at a wavelength of $1.3\,\mu m$. Material specifications predict a propagation loss of 0.2–0.3 dB/cm. A cleaved single mode fiber is placed in front of a polished horizontal in-coupling facet. No index matching adhesives are used. At the out-coupling facet, the detector is placed in front of the facet.

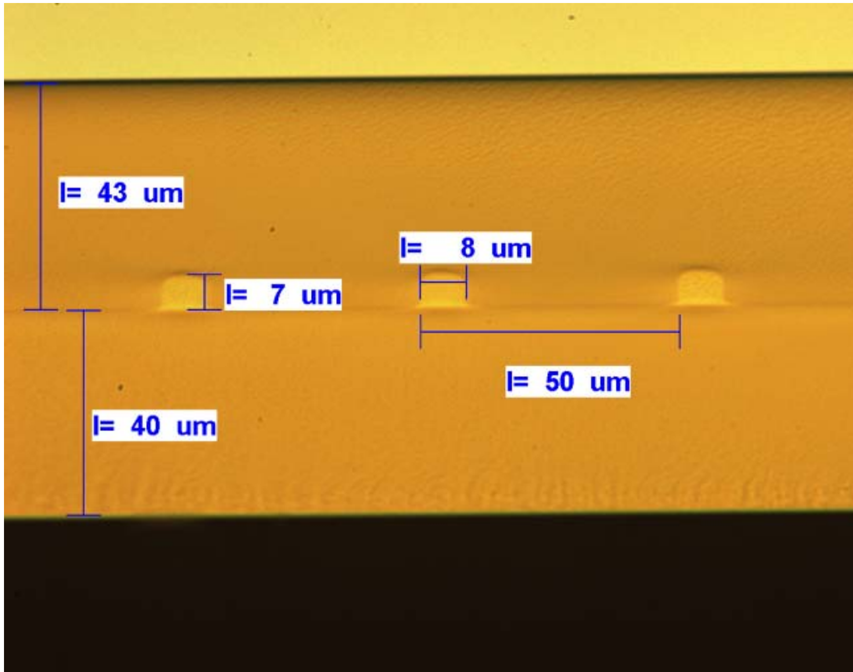


**Figure 4.17:** Microscope image of an array of single mode waveguides defined by photolithography (Ormocer®)

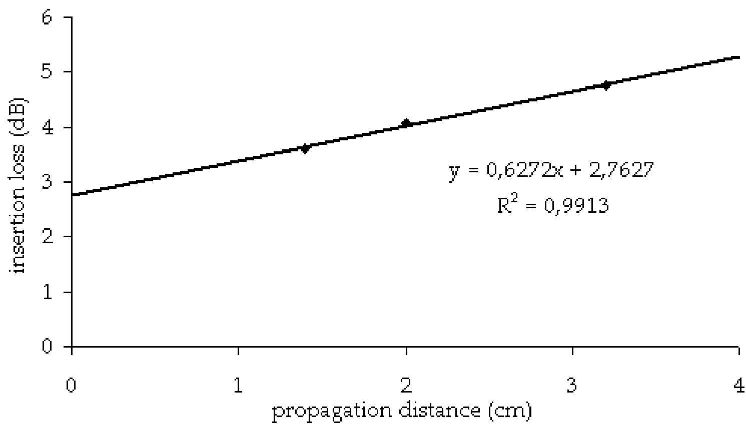


**Figure 4.18:** Loss of photolithographic defined single mode waveguides at 1310 nm (Ormocer®), based on samples provided by the Fraunhofer IOF Institute

The cut-back method is used, and the insertion losses are measured at lengths of 3.2, 2, and 1.4 cm, resulting in an average propagation loss of 0.62 dB/cm and a standard deviation of 0.08 dB/cm, as shown in Figure 4.18.

The higher attenuation loss compared to the specifications might be due to the higher surface roughness of the PCB substrate compared to that of a silicon substrate. Coupling loss for two polished facets is 2.76 dB. Coupling loss could be further reduced by using index matching adhesives. This propagation and coupling loss will be used to determine the excess loss of a vertical out-coupling $45^o$ micromirror, described in Chapter 5.

## 4.6 Conclusions

Experimental results on KrF excimer laser ablated waveguides have been presented. Using acrylate materials (Truemode$^{TM}$), multimode waveguides with a propagation loss of 0.11 dB/cm at 850 nm have been integrated on $10 \times 10\,cm^2$ PCBs. The loss spectrum revealed that longer wavelengths could be used as well, opening possibilities for telecom applications at the board-level. Comparing the insertion loss at 850 nm to the insertion loss at 980 nm and 1.3 $\mu$m, gives a propagation loss of 0.015 dB/cm at 980 nm, and 0.15 dB/cm at 1.3 $\mu$m. Even though laser ablation remains a serial process, it allows for a simultaneous fabrication of arrays of waveguides, using an array of apertures instead of a single aperture, with the size of the laser beam as the limiting factor. Multiple laser beams could be integrated into one system, in order to speed up the process.

Waveguides defined by photolithography have been structured in hybrid materials (Ormocer®), with a propagation loss of 0.08 dB/cm at 850 nm, and 0.22 dB/cm at 980 nm.

State-of-the-art waveguides described in the technology overview in Section 4.2 indicate waveguide propagation losses ranging from as high as 0.6 dB/cm to as low as 0.04 dB/cm. A standard measurement procedure for board-level multimode waveguides is emerging in order to be able to benchmark the different materials and technologies.

# References

[1] C. Berger, B.J. Offrein, and M. Schmatz. Challenges for the introduction of board-level optical interconnect technology into product development roadmaps. In *Photonics West'06, Proceedings SPIE 6124, Optoelectronic Integrated Circuits*, Jan 2006.

[2] H. Ma, A.K.-Y. Jen, and L.R. Dalton. Polymer-based optical waveguides: Materials, processing, and devices. *Advanced Materials*, 14(9):1339–1365, Oct 2002.

[3] G.L. Bona, B.J. Offrein, U. Bapst, C. Berger, R. Beyeler, R. Budd, R. Dangel, L. Dellmann, and F. Horst. Characterization of parallel optical-interconnect waveguides integrated on a printed circuit board. In *Photonics Europe'04, Proceedings SPIE 5453, Micro-Optics, VCSELs, And Photonic Interconnects*, Apr 2004.

[4] A.L. Glebov, J. Roman, M.G. Lee, and K. Yokouchi. Optical interconnect modules with fully integrated reflector mirrors. *IEEE Photonics Technology Letters*, 17(7):1540–1542, Jul 2005.

[5] A.L. Glebov, M.G. Lee, S. Aoki, D. Kudzuma, J. Roman, M. Peters, L. Huang, D.S. Zhou, and K. Yokouchi. Integrated waveguide microoptic elements for 3d routing in board-level optical interconnects. In *Photonics West'06, Proceedings SPIE 6126, Nanophotonic Packaging*, Jan 2006.

[6] H. Schroder. Waveguide and packaging technology for optical backplanes and hybrid electrical-optical circuit boards. In *Photonics West'06, Proceedings SPIE 6124, Optoelectronic Integrated Circuits*, Jan 2006.

[7] V. Sundaram, R. Tummala, G. White, K. Lim, L. Wan, D. Guidotti, F. Liu, S. Bhattacharya, R.M. Pulugurtha, I.R. Abothu, R. Doraiswami, R.V. Pucha, J. Laskar, M. Tentzeris, G.K. Chang, and M. Swaminathan. System-on-a-package (sop) substrate and module with digital, rf and optical integration. In *ECTC'04, Proceedings Electronic Components And Technology Conference*, pages 17–23, May 2004.

[8] Y.J. Chang, G.K. Chang, T.K. Gaylord, D. Guidotti, and J. Yu. Ultra-high speed transmission of polymer-based multimode interference devices for board-level high-throughput optical interconnects. In *Photonics West'06, Proceedings SPIE 6126, Nanophotonic Packaging*, Jan 2006.

[9] M. Diemeer, R. Dekker, L. Hilderink, A. Leinse, M. Balakrishnan, M. Faccini, and A. Driessen. Polymeric components for telecom and datacom. In *ICOO'05, Proceedings SPIE 5956, Integrated Optics*, Sep 2005.

[10] Y. Ishii. Optoelectronic system-in-package for next-generation optical interconnections. *IEEE LEOS Newsletter*, Jun 2005.

[11] Y. Ishii, S. Koike, Y. Arai, and Y. Ando. Smt-compatible large-tolerance optobump interface for interchip optical interconnections. *IEEE Transactions On Advanced Packaging*, 26(2):122–127, May 2003.

[12] M. Immonen, M. Karppinen, and J.K. Kivilahti. Fabrication and characterization of polymer optical waveguides with integrated micromirrors for three-dimensional board-level optical interconnects. *IEEE Transaction On Electronics Packaging Manufacturing*, 28(4):304–311, Oct 2005.

[13] S. Uhlig, L. Frohlich, M.X. Chen, N. Arndt-Staufenbiel, G. Lang, H. Schroder, R. Houbertz, M. Popall, and M. Robertsson. Polymer optical interconnects–a scalable large-area panel processing approach. *IEEE Transactions On Advanced Packaging*, 29(1):158–170, Feb 2006.

[14] L. Eldada and J.T. Yardley. Integration of polymeric micro-optical elements with planar waveguiding circuits. In *Photonics West'98, Proceedings SPIE 3289, Micro-Optics Integration And Assemblies*, Jan 1998.

[15] B. Lunitz, J. Guttmann, H.P. Huber, J. Moisel, and M. Rode. Experimental demonstration of 2.5 gbit/s transmission with 1 m polymer optical backplane. *Electronics Letters*, 37(17):1079–1079, Aug 16 2001.

[16] J. Moisel, J. Guttmann, H.P. Huber, O. Krumpholz, M. Rode, R. Bogenberger, and K.P. Kuhn. Optical backplanes with integrated polymer waveguides. *Optical Engineering*, 39(3):673–679, Mar 2000.

[17] A. McCarthy, H. Suyal, and A.C. Walker. $45^o$ out-of-plane turning mirrors for optoelectronic chip carriers based on multimode polymer waveguides. In *ECOC'04, Proceedings European Conferences On Optical Communication*, Sep 2004.

[18] B.L. Booth, J.E. Marchegiano, C.T. Chang, R.J. Furmanak, D.M. Graham, and R.G. Wagner. Polyguide polymeric technology for optical interconnect circuits and components. In *Photonics West'97, Proceedings SPIE 3005, Optoelectronic Interconnects And Packaging*, Apr 1997.

[19] Optical Crosslinks. `http://www.opticalcrosslinks.com`.

[20] E. Griese. A high-performance hybrid electrical-optical interconnection technology for high-speed electronic systems. *IEEE Transactions On Advanced Packaging*, 24(3):375–383, Aug 2001.

[21] E. Griese. Optical interconnection technology for pcb applications. *PC FAB*, 25(6):20–36, Jun 2002.

[22] S. Lehmacher and A. Neyer. Integration of polymer optical waveguides into printed circuit boards. *Electronics Letters*, 36(12):1052–1053, Jun 8 2000.

[23] F. Mederer, R. Jager, H.J. Unold, R. Michalzik, K.J. Ebeling, S. Lehmacher, A. Neyer, and E. Griese. 3-gb/s data transmission with gaasvcsels over pcb integrated polymer waveguides. *IEEE Photonics Technology Letters*, 13(9):1032–1034, Sep 2001.

[24] D. Krabe, F. Ebling, N. Arndt-Staufenbiel, G. Lang, and W. Scheel. New technology for electrical/optical systems on module and board level: The eocb approach. In *ECTC'00, Proceedings Electronic Components And Technology Conference*, pages 970–974, May 2000.

[25] E.H. Lee, S.G. Lee, B.H. O, S.G. Park, and K.H. Kim. Fabrication of a hybrid electrical-optical printed circuit board (eo-pcb) by lamination of an optical printed circuit board (o-pcb) and an electrical printed circuit board (e-pcb). In *Photonics West'06, Proceedings SPIE 6126, Nanophotonic Packaging*, Jan 2006.

[26] K.B. Yoon, I.K. Cho, and S.H. Ahn. 10-gb/s data transmission experiments over polymeric waveguides with 850-nm wavelength multimode vcsel array. *IEEE Photonics Technology Letters*, 16(9):2147–2149, Sep 2004.

[27] C.G. Choi, S.P. Han, B.C. Kim, S.H. Ahn, and M.Y. Jeong. Fabrication of large-core 1×16 optical power splitters in polymers using hot-embossing process. *IEEE Photonics Technology Letters*, 15(6):825–827, Jun 2003.

[28] L. Eldada and L.W. Shacklette. Advances in polymer integrated optics. *IEEE Journal Of Selected Topics In Quantum Electronics*, 6(1):54–68, Jan 2000.

[29] A. Neyer, S. Kopetz, E. Rabe, W.J. Kang, M. Stach, and R. Michalzik. 10 gbit/s electrical-optical circuit board based on new polysiloxane waveguide technology. In *ECOC'04, Proceedings European Conferences On Optical Communication*, pages 814–815, Sep 2004.

[30] Polysiloxane optical waveguide layer integrated in printed circuit board. `http://www-mst.e-technik.uni-dortmund.de/eocb.html`.

[31] C.C. Choi, L. Lin, Y.J. Liu, J.H. Choi, L. Wang, D. Haas, J. Magera, and R.T. Chen. Flexible optical waveguide film fabrications and optoelectronic devices integration for fully embedded board-level optical interconnects. *Journal Of Lightwave Technology*, 22(9):2168–2176, Sep 2004.

[32] K. Glukh, J.H Lipian, R. Mimna, P.S. Neal, R. Ravikiran, L.F. Rhodes, R.A. Shick, and X.M. Zhao. High-performance polymeric materials for waveguide applications. In *SPIE's Annual Meeting'00, Proceedings SPIE 4106, Linear, Nonlinear, And Power Limiting Organics*, Jul 2000.

[33] G. Van Steenberge, N. Hendrickx, E. Bosman, J. Van Erps, H. Thienpont, and P. Van Daele. Laser ablation of parallel optical interconnect waveguides. *Photonics Technology Letters*, 18(9):1106–1108, May 2006.

[34] G. Van Steenberge, P. Geerinck, S. Van Put, J. Van Koetsem, H. Ottevaere, D. Morlion, H. Thienpont, and P. Van Daele. Mt-compatible laser-ablated interconnections for optical printed circuit boards. *Journal Of Lightwave Technology*, 22(9):2083–2090, Sep 2004.

[35] K. Naessens, H. Ottevaere, R. Baets, P. Van Daele, and H. Thienpont. Direct writing of microlenses in polycarbonate with excimer laser ablation. *Applied Optics*, 42(31):6349–6359, Nov 1 2003.

[36] H. Schroder, N. Arndt-Staufenbiel, M. Cygon, and W. Scheel. Planar glass waveguides for high performance electrical-optical-circuit-boards (eocb) – the glass-layer-concept–. In *ECTC'03, Proceedings Electronic Components And Technology Conference*, pages 1053–1059, May 2003.

[37] PPC Electronic Optoboard. `http://www.ppc-electronic.com/english/products/optoboard.html`.

[38] Interconnect by Optics (IO). `http://io.intec.ugent.be`.

[39] T. Bierhoff. Influence of the cross sectional shape of board-integrated optical waveguides on the propagation characteristics. In *IEEE Workshop On Signal Propagation On Interconnects*, May 2002.

# Chapter 5

# Coupling structures

*This chapter deals with the fabrication of out-of-plane coupling structures. Different approaches are given, with emphasis on the fabrication of 45$^o$ micromirrors. A process for embedding metal coated mirrors is being developed. Characterization results based on surface roughness, angle accuracy, and coupling loss are presented. Next, the fabrication of optical vias allowing the introduction of a pluggable component is described. Finally, the use of laser ablation to acces the optical layers through fiber reinforced epoxy is discussed.*

## 5.1 O/E coupling

Light coupling structures are crucial to couple light in and out of the planar waveguides. At the incoupling, low cost vertical cavity surface emitting lasers are being considered worldwide, in order to convert the electrical signals into light. Telecom-class lasers are not considered for possible applications because of their cost. VCSELs operating at 850 nm and at 980 nm are available as 1D and 2D arrays, which is necessary in order to provide the large number of required channels, and they can be processed and tested on the wafer-level, which is important for cost reasons. VCSELs have been on the market for several years, i.e. the technology is rather mature. Commercial devices are available at 10 Gbps [1], and experimental devices have been operated at 25 Gbps [2]. On the other end, to convert the optical signal back to an electronic signal, various types of matching photodiode arrays are available [3].

One of the most complex parts of the technology is the interface between the electrical domain and the optical domain. Amongst others, the complexity is due to the fact that the electrical interface, the optical interface and the mechanical interface, plus eventually a thermal interface have to be combined in one single

package. Additionally, many interlocked factors come into play, which are partially still unknown or undecided. They include for example the type of the data link, the position of the optical layer (surface versus buried), or the location of the E/O- and O/E-conversion with respect to the digital chip [4]:

- The closest possible location is obviously on-chip, e.g. by flip-chip attachment of an OE-device on top of the digital chip [5, 6, 7]. Advantages include very short electrical paths (low power consumption) and the possibility for a 2D distribution of I/O ports over the whole chip area. Drawbacks include heat and lifetime issues, as well as material incompatibilities, e.g. a mismatch in thermal expansion coefficients.

- The next closer option is to place the O/E-conversion next to the digital chip, but still on the same package or multi-chip module (MCM), that will need to be expanded for this purpose [8]. Advantages include still very short electrical paths, dense electrical connections and a more manageable thermal situation than for flip-chip attachment. Drawbacks include the need for development of new packages/MCMs, and the fact that the reliability of the whole package is now determined by the reliability of the optoelectronics, which has to be addressed with improved reliability & lifetime and/or with appropriate redundancy concepts.

- The next option is to place the optoelectronics in a separate package close to the processor package. This is probably the most established method, and it avoids the integration issues mentioned above. Drawbacks include the need to electrically leave the processor package through PCB pads, which results in a reduction of the overall data density that can be achieved, i.e. giving away much of the density advantage that the use of optics could provide. Several proposals have been made to embed the optoelectronics into the PCB with integrated optical layers [9, 10, 11]. The motivation is to hide the use of board-level optics from the user and solve all the alignment questions during fabrication. Drawbacks include the fact that the previously passive and therefore very reliable PCB is now subject to reliability & lifetime issues, heat management during operation (assuming the drivers are embedded too) or electrical connection issues (assuming the drivers are at the surface, separated from the optoelectronics), as well as testability issues during assembly.

- Finally, the optoelectronics can be placed at the card edge, e.g. in an optical connector [12], basically avoiding an optical channel on the card. Drawbacks are similar to the situation with separate packages close to the digital chip (data density), plus longer electrical connections and limited freedom in the heat management, since the location of the packages is now fixed at the card edge.

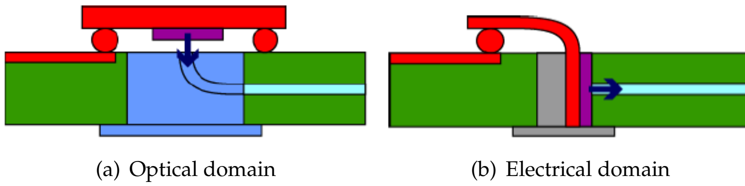

(a) Optical domain (b) Electrical domain

**Figure 5.1:** The use of vertical emitters calls for an additional $90^o$ bend in the signal path (source: IBM [4])

Another, related question is the orientation of the opto-electronic chip with respect to the optical layer. In case of vertically emitting opto-electronic devices, the incoming electrical signal as well as the outgoing optical signal both run parallel to the card, a $90^o$ bend in the signal path, either in the optical domain or in the electrical domain need to be provided, see Figure 5.1 [4]. In the first case, the opto-electronics and drivers are oriented parallel to the card, and the emitted beam has to be reflected or guided by $90^o$ before it can be coupled into the optical channel. In the second case, the opto-electronics and–due to the required short distance between them–probably also the driver chips are inserted perpendicularly into the board, emitting more or less directly into the optical channel. In this case, the $90^o$ bend has to be made by a piece of flexible printed circuit that connects the opto-electronic subassembly with the PCB.

Advantages of the $90^o$-in-electronics approach [4] include the fact that an architecture with an electrical flex-circuit is already being used in commercial fiber-optic transceiver modules, which allows to build upon that experience. Since the lasers emit in the direction of the waveguides, there is no need for a mirror. As 850 nm VCSELs are usually topemitters (modified devices with bottom emission have been reported, but they suffer from reduced reliability and lifetime), they cannot be directly placed on the waveguide facets, i.e. through-substrate waveguides or microlenses are still required. In [13], reported by IBM, the light is guided through the Si module by integrated waveguides based on holes etched through the silicon, which are then oxidized and filled with a polymer, a total optical loss of 1 dB was measured, through the transceiver module. An extension to 2D arrays is straightforward, at least as far as the optics is concerned. In practice, the degree of 2D-scalability will be limited by the available opto-electronics (lower yield for larger arrays), by the electrical routing to the driver and the connections between driver and opto-electronics, as well as by the number of optical layers that can actually be stacked in a board with the required precision and board stability [14]. Drawbacks of the approach include the open access slot in the PCB, which makes dust protection, cleaning and servicing more complex. In a pure butt-coupling configuration without additional imaging optics, module insertion requires a 2-step process (first into the slot and then onto the waveguide facet), which requires

a more complex housing mechanics. Moreover, more careful waveguide facet preparation is required in the absence of additional imaging optics. Without a mechanical de-coupling (e.g. by a pair of lenses), the whole module (including driver chips and heat sink) will physically interface to the waveguide facet, which is a potential stability risk. Other reports on butt-coupled optoelectronic modules include those from Fraunhofer IZM [15], and Siemens C-LAB [16], among others.

Advantages of the $90^o$-in-optics approach [4] include better compatibility with standard packaging and assembly processes, the possibility for a clear separation of the OE-package and the passive PCB, and the option to realize large packages with multiple densely packed opto-electronic components in close vicinity of the rest of the electronics. Potential drawbacks depend on the nature of the optics that performs the $90^o$ bend. For a lens & mirror module, there is a distance limitation, that is related to the ratio of waveguide core size to lens size, which determines how far a collimated beam can propagate before it penetrates into a neighbouring channel, causing loss and/or crosstalk. For a 50 $\mu$m waveguide and a 235 $\mu$m lens, the distance between waveguide exit and detector surface is roughly limited to 2.5 mm, which is sufficient for waveguides on or close to the surface [4]. The distance limitation can in particular become important when 2D arrays are imaged over a single mirror, because this requires longer propagation distances. For 4$\times$N arrays, however, one can also map a sparse 2D array (250 $\mu$m pitch) to a dense 1D array (62.5 $\mu$m pitch), which allows to circumvent the issue, but requires a more complex mirror array structure. Reports on collimated beam coupling include results from Daimler Chrysler [17, 18], and NTT [19]. For very short free-space distances, collimated beams are not necessary, as shown by Intel [8]. Alternatively, the $90^o$ bend can be done using other optical elements, for example optical pins which are essentially short pieces of waveguides with a $45^o$ mirror on one end, assembled vertically into the board, as reported by Fraunhofer IZM [20], and the Information and Communications University Korea [21], or 2D waveguide cubes consisting of stacked waveguide plates, reported by NTT [22]. While such approaches can eliminate the distance limitation, they clearly suffer from a more complex (and therefore more costly) board-side optics. Another approach that has been proposed by the Tokyo University of Technology is the so-called self-organized lightwave network [23], which enables selfaligned optical couplings between misaligned optical devices by introducing write beams from the devices into photorefractive materials placed between them, resulting in self-written waveguides in the vertical direction.

We have been focussing on the $90^o$-in-optics approach, making use of embedded $45^o$ mirrors [24]. This coupling configuration is compatible both with O/E coupling and with board-backplane-board links, discussed in Chapter 6. An additional advantage of using embedded mirrors is the elimination of the alignment in Z direction, which allows more standard mounting in XY direction only. Several technologies have been proposed for the fabrication of $45^o$ reflector mi-

cromirrors, such as dicing, tilted exposure, grey-scale lithography, reactive ion etching (RIE), laser ablation, and laser direct writing. Fabrication of a standalone mirror can be performed by many techniques, however, integration of micromirrors into a backplane with waveguides and optical connectors poses a number of strict requirements on the mirror characteristics. The requirements include, high reflectivity, precise mirror plane positioning control, symmetrical layout for in- and outcoupling, ability to direct light up and down out of the propagation plane, full integration with planar waveguides, and a robust and cost effective manufacturing process [25].

## 5.2 Embedded 45$^o$ micromirrors

### 5.2.1 Technology overview

#### Dicing

The 45$^o$ mirror can be fabricated using a mechanical dicing saw with a 90$^o$ V-shaped diamond blade. Commercial dicing saws, available in semiconductor assembly fabs, can control the positioning of the cut within several $\mu$m in the vertical and lateral directions. The dicing saws can be programmed to perform the cuts at multiple locations without realignment. However, due to the physical size of the machining tool, it is difficult to cut individual waveguides on the same substrate. NTT reported on the fabrication of 45$^o$ mirrors in polymer optical waveguide films [26, 27, 19]. Fujitsu reported on the fabrication of wedge-diced micromirrors [28, 25], that allows to embed the mirror in the optical layer. First, the lower cladding is deposited, second, the wedge layers are deposited and the wedge base is patterned, third, one side of the wedge base is tapered to 45$^o$ by microdicing and a thin gold (Au) film is deposited on the tapered wedge side, fourth, the waveguide core layer is deposited and the channel waveguide is pattered, fifth, the top cladding is coated on top of the formed waveguide and mirror structure. Two major contributions to the mirror reflection losses of 0.8 dB were reported, the roughness of the diced 45$^o$ sloped wedge surface and the Au metal film. The surface roughness is inherent to the process, and is difficult to eliminate.

#### Inclined exposure

Waveguides with mirror facets can be fabricated by tilting the incoming beam from the UV source with respect to the patterning mask. The tapering angle of the mirrors is controlled by changing the incoming beam angle. When the incoming light is tilted 50$^o$–60$^o$ mirror angles are 36$^o$–45$^o$, as reported by VTT [29]. Surface roughness below 100 nm was achieved, the mirror excess loss was 1.8–2.3 dB. The disadvantage of UV light when using a tilted exposure is that the reflections of

the incoming radiation at the glass mask are increased with the tilting angle. For this reason, X-rays, have been proposed instead [30], resulting in a mirror loss of 0.43 dB. The limited degree of freedom inherent to inclined exposure, makes this technology not attractive for the fabrication of optical PCBs containing mirrors in several outcoupling directions.

#### Laser direct writing

Simultaneous fabrication of multimode polymer waveguide cores, and $45^o$ polymer structures have been reported by Heriot-Watt University based on a HeCd (325 nm) UV laser [31]. A combination of three beams (at normal and $\pm 45^o$ angles) are used, with equalized optical power in the three different channels, in combination with an oil-immersion technique (sample positioned in an oil bath containing silicon oil), to form internal angles greater than $\approx 40^o$, impossible for beams coming from air into a polymer with $n = 1.56$. Features with vertical sidewalls are written with the normal incident beam while angled features are produced by the $45^o$ beams. A flat-top intensity profile was achieved by placing an aperture on the axis of the Gaussian beam and imaging it on to the polymer surface. No coupling loss values were reported so far.

#### Reactive ion etching

Micromirror couplers formed by reactive ion etching (reported by the University of Texas [32]) require the deposition of a protective mask during the RIE process. Using photolithography and wet etching a window can be opened in the mask at the end of each waveguide, where the mirror is to be etched. During the RIE process, the sample is placed at an angle of $45^o$ with respect to the electrode in the chamber. The directional high-speed ions attack the polymer at a $45^o$ angle with respect to the substrate through the mask openings. The limited directional freedom of the angled RIE process, is limiting the practical application of this process. Obviously, the process can provide vertical endfacets as well [33], with a sidewall surface roughness of $\approx 30$ nm (measured on an area of $5 \times 5\,\mu m^2$), and a sidewall angle accuracy of $\pm 1^o$.

#### Moulding

The basic idea here is to realize the mirror structures already at the masterform-level, and apply the waveguide layer fabrication, as described in Section 4.2. The University of Dortmund [34, 35] reported on the fabrication of micromirrors integrated into the masterform at SU-8-level by diamond micromilling the end faces of the cured SU-8 ridges under an angle of $45^o$. Surface roughness of 70–80 nm

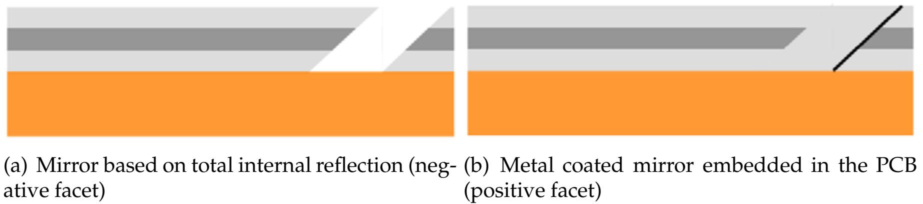

(a) Mirror based on total internal reflection (negative facet)
(b) Metal coated mirror embedded in the PCB (positive facet)

**Figure 5.2:** Schematic view of two coupling concepts

has been reported. A slightly adapted approach was reported by the University of Texas [9]. No mirror loss values have been published so far.

**Laser ablation**

The use of KrF excimer laser ablation for the definition of 45$^o$ micromirrors is widely known by the Polyguide polymeric technology, developed by DuPont, and currently available at Optical Crosslinks under the name GuideLink [36]. They have been used within several projects [37], and more recently Intel [8] reported on their optical interconnect system integration for ultra-short-reach applications using GuideLink.

The use of laser ablation for the definition of coupling structures within this PhD work will be described in the next paragraphs.

### 5.2.2 Fabrication

Two basic coupling structures are proposed in Figure 5.2. The first coupling structure is based on total internal reflection (TIR) at the interface between the polymer material and the air gap (negative facet), in the second coupling structure the light beam is reflected on a metal coated mirror (positive facet), embedded in the PCB.

The development of a technology for fabricating micromirrors was established using Ormocer® materials, once the technology was available, the Truemode™ materials were investigated. An SEM picture of a micromirror based on total internal reflection is shown in Figure 5.3. The tapering of the edges is in agreement with the tapering of the ablated waveguides. This tapering effect is shown to be highly reproducible, therefore this effect can be compensated for in order to achieve an angle of 45$^o$ at the negative facet, crucial for the TIR condition. An overview of the ablation parameters: laser fluence $2.5 \pm 0.5\,J/cm^2$, pulse repetition rate 200 Hz, number of pulses 290, tapering compensation 9$^o$, fabrication time of one mirror is about 1 sec. In Section 3.1.1 the generation of debris and the presence of microstructures on the bottom of the ablated cavity were two main obstacles to exploit KrF excimer laser ablation for the definition of waveguides

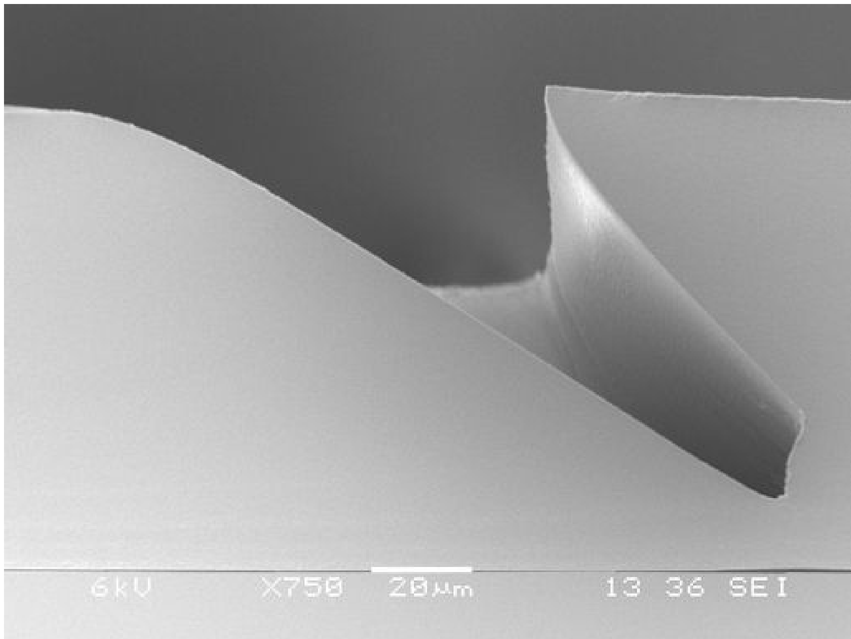


**Figure 5.3:** SEM image of a cross-section of a TIR micromirror fabricated in Ormocer® using a KrF excimer laser

in Ormocer®. The difference here is the static ablation of a mirror, compared to the dynamic ablation of a waveguide. When using static ablation, the debris being deposited on the mirror sidewall is removed contineously, and debris is only deposited in the surroundings of the ablation area. Moreover, the requirements for a micromirror are somewhat different: the sidewall quality is less important compared to the sidewall quality of a waveguide, roughness $< \lambda/10$ is often used as a criterium here.

The condition for TIR of the light beam at the negative facet is very critical, and light will not be reflected when the condition is not reached. The Vrije Universiteit Brussel, FirW-TONA, calculated that the use of a metal reflection coating on the micromirror significantly increases the coupling efficiency, be it for a slightly different coupling configuration [38]. The largest gain (almost 20%) is obtained in the case of waveguides with a large NA (0.3 for Truemode$^{TM}$), the smaller the NA, the smaller the TIR loss at the mirror and thus the smaller the gain when applying a coating on the micromirror. Additional loss might arise when an adhesive penetrates into the optical via during a later mounting phase, humidity or dust could also be a problem. For these reasons it is necessary to apply a metal reflection coating.

The reflection characteristics of a metal coating applied on an Ormocer® layer are investigated for Au, Al, Ni, Cr, and Ti. The complex indices of refraction $n_t$ are available for different wavelengths [39]. From the Fresnel equations, the amplitude reflection coefficients for an electrical field respectively perpendicular and parallel to the plane of incidence can be calculated. Eliminating $\theta_t$ using Snells law of refraction results in the following equations:

$$r_\perp \equiv \left(\frac{E_{0r}}{E_{0i}}\right)_\perp = \frac{\cos(\theta_i) - i\sqrt{\sin^2(\theta_i) - n^2}}{\cos(\theta_i) + i\sqrt{\sin^2(\theta_i) - n^2}}$$

$$r_{//} \equiv \left(\frac{E_{0r}}{E_{0i}}\right)_{//} = \frac{n^2\cos(\theta_i) - i\sqrt{\sin^2(\theta_i) - n^2}}{n^2\cos(\theta_i) + i\sqrt{\sin^2(\theta_i) - n^2}}$$

where $E_{0i}$ is the amplitude of the incident field, $E_{0r}$ the amplitude of the reflected field, and $n = n_t/n_i$, with $n_i = n_{ormocer}$. The reflectance coefficients are defined as:

$$R_\perp \equiv \left(\frac{I_r}{I_i}\right)_\perp = \left(\frac{E_{0r}}{E_{0i}}\right)^2_\perp = r_\perp r^*_\perp$$

$$R_{//} \equiv \left(\frac{I_r}{I_i}\right)_{//} = \left(\frac{E_{0r}}{E_{0i}}\right)^2_{//} = r_{//} r^*_{//}$$

where $^*$ denotes the complex conjugate.

The reflectance coefficients as a function of wavelength are shown in Figure 5.4, for an angle of incidence $\theta_i = 0$, perpendicular to the surface. It is clear that Au is the best choice as coating material. The reflectance coefficients $R_\perp$(Au) and $R_{//}$(Au) as a function of the angle of incidence $\theta_i$ are given in Figure 5.5, using $n_t$(Au) = 0.188 + 5.39 i at a wavelength of 826.6 nm [39].

The overview of the process flow for the fabrication of a coated mirror embedded in the optical layers is given in Table 5.1. Selective coating of only the positive facet is possible using a lift-off process. A photoresist layer is applied prior to ablation of the angled optical via, with a thickness of 1.8 $\mu$m (Microposit S1818). Evaporation of 50 nm Ti (improved adhesion) and 200 nm of Au is used as coating process. Due to the directional selectivity of the evaporation process, the negative facet is not coated. After development of the resist (AZ400K) a coated positive facet can be used as deflecting mirror.

For a reliable functioning it was assumed that the presence of air bubbles in the cavity would be detrimental due to the temperature dependence of the pressure

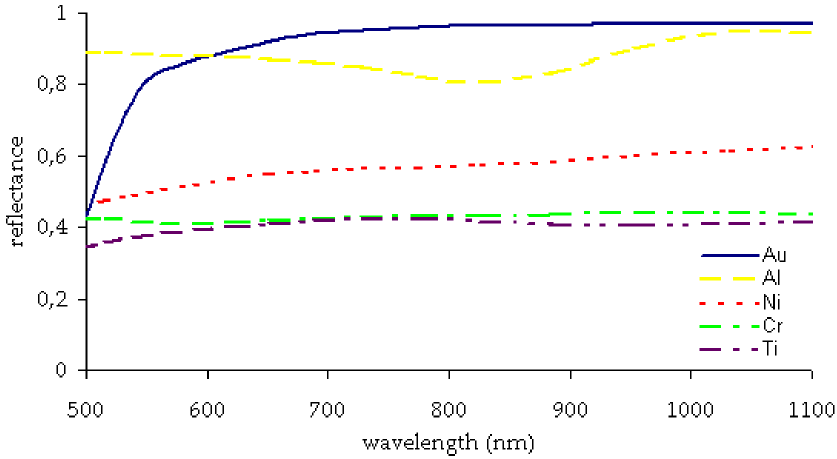


**Figure 5.4:** Reflectance of different metals to be used for mirror coating

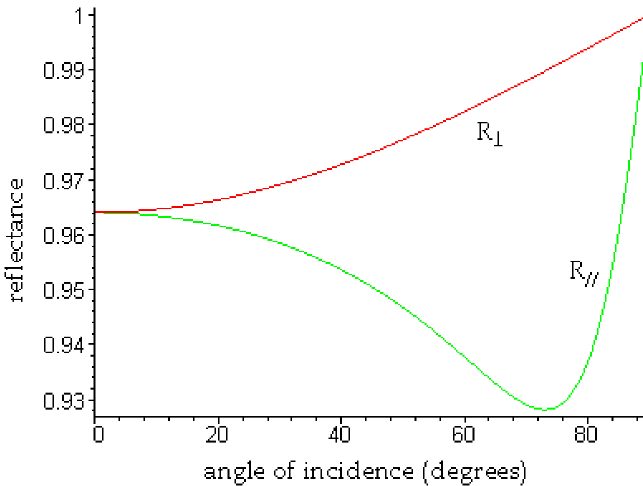


**Figure 5.5:** Au reflectance as a function of angle of incidence $\theta_i$

within the bubbles. Therefore, ways of filling up the cavity without the presence of air bubbles were studied. At the same time, providing a flat surface above the mirror is another important feature required for subsequent processes and has to be regarded as well. It was found that filling the cavity without air bubbles was only possible by enhancing the cladding deposition process with ultrasound agitation. During the investigation it could be shown that even small air bubbles

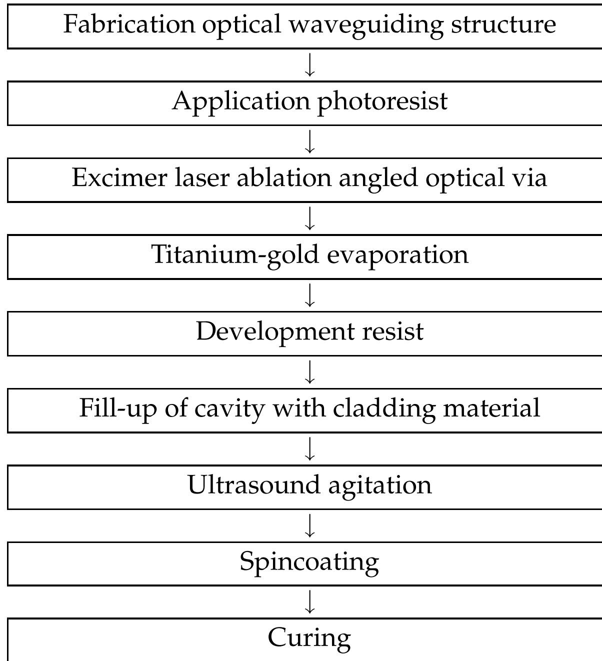


**Table 5.1:** Process flow for the fabrication of metal coated mirrors embedded in the optical layer (Ormocer®)

**Figure 5.6:** Process flow for the fabrication of a metal coated mirror embedded in the optical layer

will cause reliability problems. The final curing step of the additional cladding material at 170$^o$C will lead to a volume expansion of the air bubble, resulting in a surface elevation (Figure 5.7). Ultrasound agitation is needed for at least 8 min to avoid the presence of air bubbles at the bottom of the cavity. Afterwards, a spincoating step is necessary to achieve a flat surface. Spincoating speed was increased to 8000 rpm, resulting in an additional layer thickness of 2 $\mu$m, hardly influencing the initial uppercladding layer thickness. The final result is shown in Figure 5.8. Mechanical stresses introduced during cleaving the sample (GaAs substrate to ease making a cross-section) caused the crack in between the gold mirror and the additional cladding material, this is not the case in real life situations.

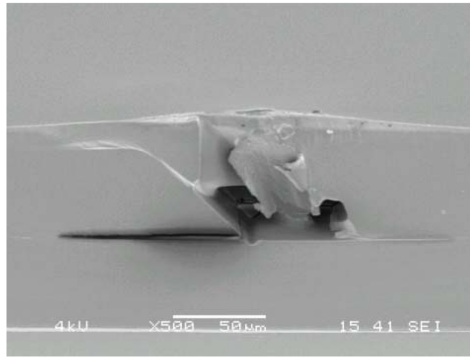


(a) No ultrasound agitation

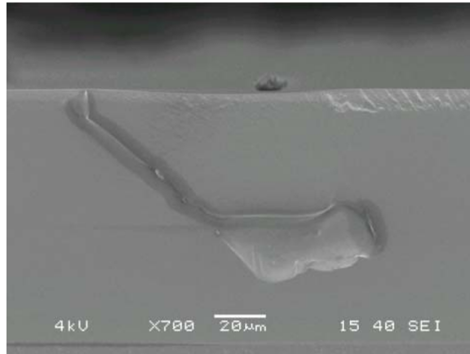


(b) 1 minute ultrasound agitation

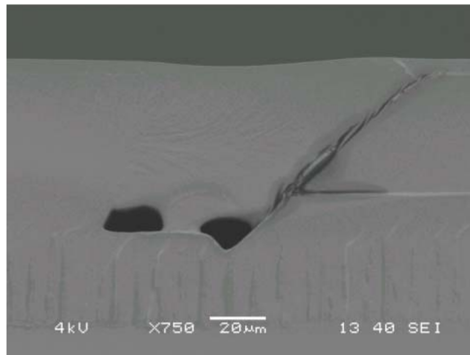


(c) 5 minutes ultrasound agitation

**Figure 5.7:** Result of ultrasound agitation and spincoating at 4000 rpm on filling up an angled optical via with Ormocer® cladding

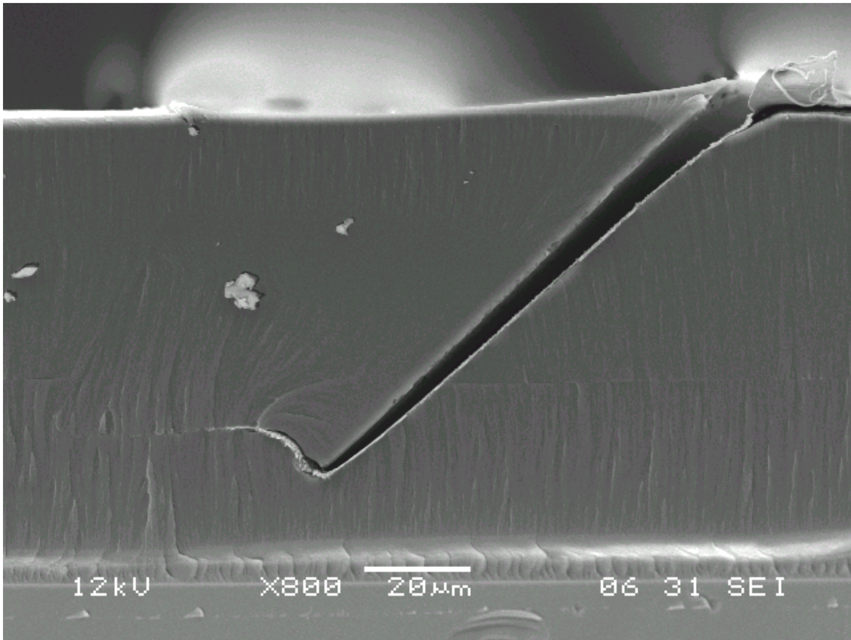


**Figure 5.8:** SEM image of a cross-section of a metal coated micromirror fabricated in Ormocer®

The flatness of the upper cladding surface above the embedded mirror has been investigated using a non-contact optical profiler. The result is shown in Figure 5.9. A height difference of 6 $\mu$m on a distance of 200 $\mu$m (X direction) or 400 $\mu$m (Y direction) can be observed, corresponding to a surface angle of 1.72$^o$, and 0.85$^o$, which should be sufficient to provide a mounting surface for any opto-electronic component.

Ablation of a positive facet has slightly different parameters compared to ablation of a negative facet. Due to the tapering, the actual ablation angle is 34$^o$, the number of pulses is 270. The variation of the 45$^o$ mirror surface is $\pm 2^o$, which should be sufficient, both for total internal reflection, and for a metal coated mirror, as is measured in Section 5.2.3.

The technology sequence for the fabrication of metal coated micromirrors in Truemode$^{TM}$ is somewhat different: due to the very smooth sidewall of the ablated structures ($R_a = 18$ nm for a vertical sidewall, Figure 3.16) the adhesion of Au or Ti is very poor, and during development of the photoresist, the coating comes loose. Because of this, the use of an external mask was considered, being a polyimide film with rectangular openings on the locations of the mirrors. This film is attached to the optical PCB during the coating process (using high temper-

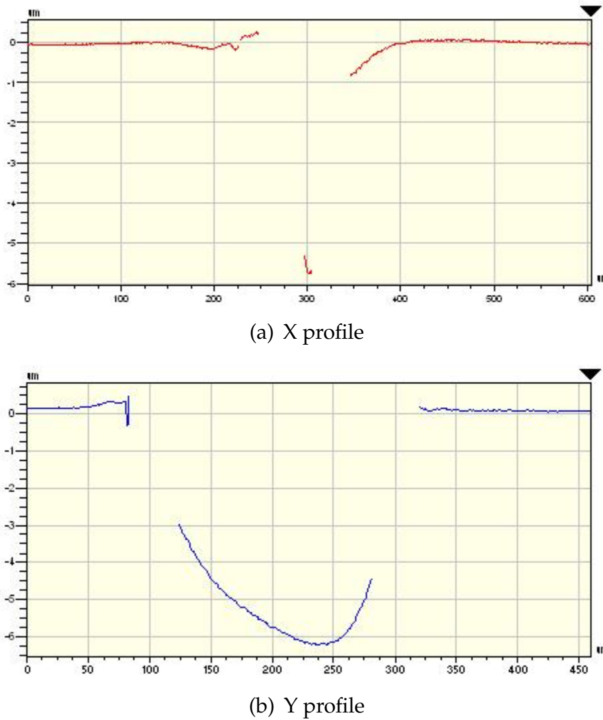


(a) X profile

(b) Y profile

**Figure 5.9:** WYKO plot to analyze surface flatness above an embedded metal coated mirror

ature resistant tape), which results in a coated area around the mirrors. Once the mirrors have been coated, the polyimide mask film is removed, and the second uppercladding layer is applied, which secures the adhesion of the TiAu coating. Because of the low viscosity of Truemode$^{TM}$, additional ultrasound agitation is not required. The final technology sequence is shown in Table 5.2. For the ablation of mirrors in Truemode$^{TM}$, static or dynamic ablation give both excellent results. Dynamic ablation if favoured in this case, as the surface roughness of the imaging mask is averaged while moving the laser spot.

### 5.2.3 Characterization

#### Surface roughness

Using an optical interferometer system, the surface roughness of $45^o$ micromirrors can only be measured for positive facets while tilting the sample under an angle of $45^o$. This way, it is assumed that for mirrors based on total internal

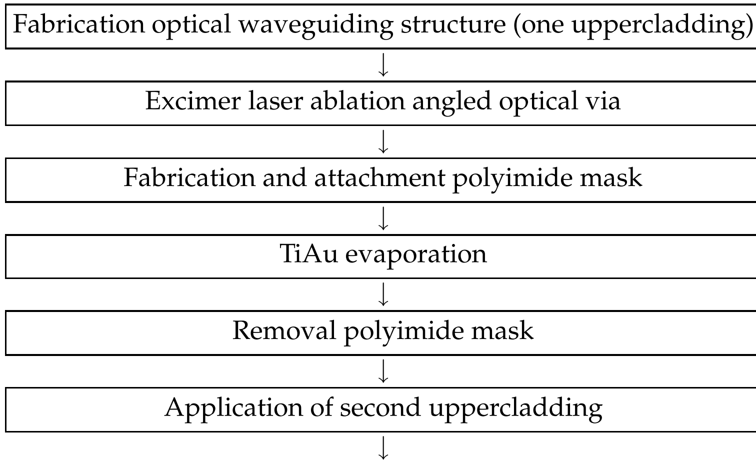


**Table 5.2:** Process flow for the fabrication of metal coated mirrors embedded in the optical layer (Truemode$^{TM}$)

reflection, the surface roughness of the negative facet is comparable to the surface roughness of the positive facet. Static ablated mirrors defined in Ormocer® (laser fluence $2.5 \pm 0.5\,J/cm^2$) result in a surface roughness of 81 nm $R_a$ and 110 nm RMS, as shown in Figure 5.10. The additional technology steps necessary to apply the metal coating, are detrimental for the surface quality, as shown in Table 5.3.

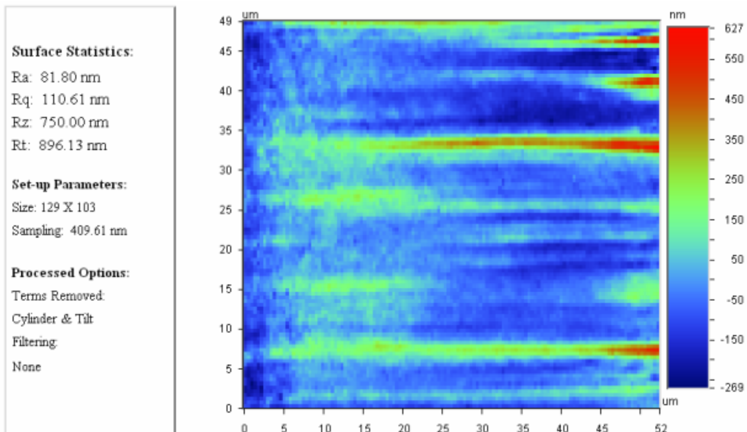


**Figure 5.10:** Surface roughness of a micromirror fabricated in Ormocer® using KrF excimer laser ablation

| | **sample 1** | | **sample 2** | | **average** | | **st dev** | |
|---|---|---|---|---|---|---|---|---|
| | **$R_a$** | **RMS** | **$R_a$** | **RMS** | **$R_a$** | **RMS** | **$R_a$** | **RMS** |
| **50 Hz** | | | | | | | | |
| **140** | 185.3 | 237.4 | 157.5 | 201.2 | 171.4 | 219.3 | 19.6 | 25.6 |
| **160** | 187 | 235.9 | 140.3 | 182.0 | 163.6 | 209.0 | 32.9 | 38.1 |
| **180** | 135.3 | 237.4 | 173.8 | 227.6 | 154.5 | 232.5 | 27.2 | 6.9 |
| **200** | 117.9 | 152.6 | 105.0 | 140.9 | 111.5 | 146.8 | 9.0 | 8.2 |
| **100 Hz** | | | | | | | | |
| **140** | 171.1 | 213.9 | 150.1 | 187.8 | 160.6 | 200.8 | 14.8 | 18.4 |
| **160** | 194.0 | 244.8 | 137.2 | 174.0 | 165.6 | 209.4 | 40.2 | 50.0 |
| **180** | 126.1 | 163.5 | 153.2 | 203.5 | 139.6 | 183.5 | 19.1 | 28.2 |
| **200** | 118.0 | 149.8 | 140.0 | 171.9 | 129.0 | 160.9 | 15.5 | 15.6 |
| **150 Hz** | | | | | | | | |
| **140** | 195.9 | 247.5 | 155.3 | 197.3 | 175,6 | 222.4 | 28.7 | 35.4 |
| **160** | 151.4 | 185.6 | 185.6 | 236.3 | 168,5 | 210.9 | 24.1 | 35.8 |
| **180** | 159.2 | 202.8 | 111.8 | 151.2 | 135,5 | 177.0 | 33.5 | 36.4 |
| **200** | 143.5 | 175.9 | 162.1 | 205.4 | 152,8 | 190.6 | 13.2 | 20.8 |
| **200 Hz** | | | | | | | | |
| **160** | 126.9 | 169.9 | 173.1 | 225.0 | 150.0 | 197.4 | 32.6 | 38.9 |
| **180** | 142.6 | 180.2 | 142.7 | 180.7 | 142.6 | 180.5 | 0.1 | 0.3 |
| **average (nm)** | | | | | 151.5 | 195.8 | 22.2 | 25.6 |

**Table 5.3:** Surface roughness optimization of 45$^o$ coated mirrors (Ormocer®)

The surface roughness of two samples are investigated while varying the pulse frequency (50 Hz, 100 Hz, 150 Hz, and 200 Hz), and the number of pulses (140, 160, 180, and 200). Pulse energy is kept constant at 5 mJ, corresponding to a laser fluence of 2 J/cm$^2$. The $R_a$ and RMS surface roughness is given, measured on an area of 50×50 $\mu$m$^2$, curvature and tilt removed, without data filtering. Generally, the higher the number of laser pulses, the smoother the mirror. The influence of the pulse frequency shows some conflicting measurements, depending on the number of pulses. An overall $R_a$ average of 151 nm, with a standard deviation of 22 nm, and an overall RMS average of 196 nm, with a standard deviation of 26 nm was achieved.

Micromirrors defined in Truemode$^{TM}$ show an $R_a$ surface roughness of 42 nm, and an RMS roughness of 53 nm, measured on an area of 174×52 $\mu$m$^2$, cylinder and tilt removed, no data filtering, for mirrors ablated with a laser pulse energy of 6 mJ (laser fluence of 2.5 J/cm$^2$), and a pulse frequency of 200 Hz.

### Stylus angle measurement

KrF excimer laser ablation for the definition of 45$^o$ mirrors, requires compensation of the ablation angle to the tapering inherent to ablation, in order to have the resulting mirror under an angle of 45$^o$. Measuring the mirror angle is done by different methods, optical microscopy, SEM, Tencor Alphastep-200, and Dektak 8 Stylus profiler, most accurate is the Dektak. This stylus profiler can only be used for optimizing the angle of the positive facet, because the negative facet is hidden under the surface. For Ormocer®, the tapering is measured to be 8–9$^o$, resulting in an actual ablation angle of 36–37$^o$ and 53–54$^o$, for positive and negative facets respectively. For Truemode$^{TM}$ it has been decided to focus on the coated mirrors using the positive facet, actual ablation angle was 26$^o$, which results in a tapering of 19$^o$. The reason for this high tapering was a decreased laser pulse energy (corresponding to a higher tapering angle), at the time of optimizing the mirror angle. The flexibility in changing the ablation angle, allows us to tune the angle as a function of laser pulse energy. An example of a Dektak measurement of a positive facet is shown in Figure 5.11, resulting in an angle of 45.52$^o$.

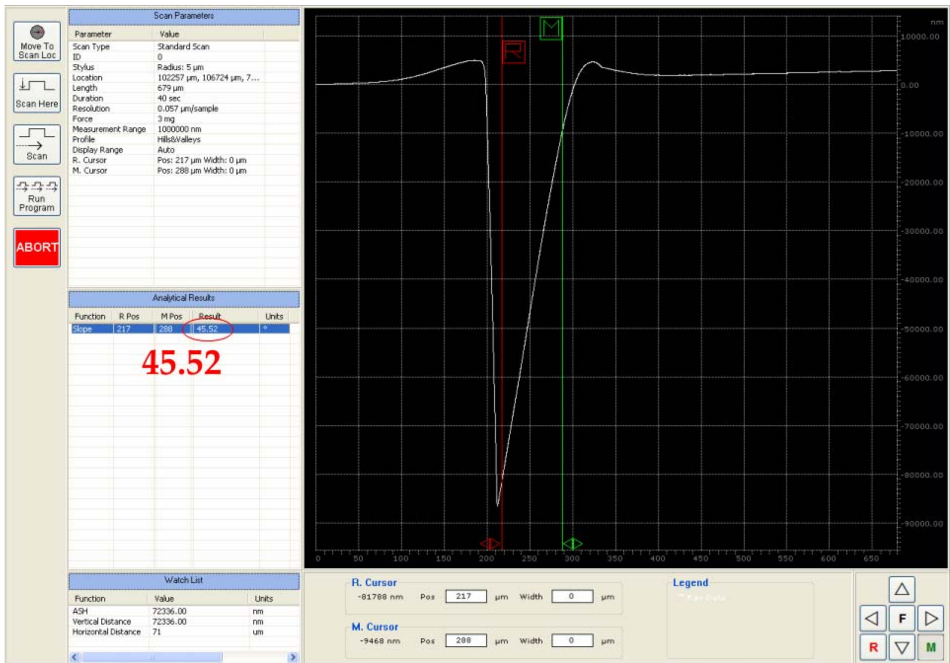


**Figure 5.11:** Dektak stylus angle measurement of a 45$^o$ micromirror

**Coupling loss**

The insertion loss of KrF excimer laser ablated waveguides in Truemode$^{TM}$ was discussed in Section 4.4.3, resulting in a propagation loss of 0.11 dB/cm and a coupling loss of 1.90 dB for two interfaces, at a wavelength of 850 nm. Comparing these loss values to the loss measured for vertical in- and outcoupling, results in the excess mirror loss. The measurement sample with coated mirrors is shown in Figure 5.12, the results are presented in Table 5.4. The results show that a lot depends on the coupling condition. A 50 $\mu$m fiber (NA of 0.2) at the incoupling, and a 100 $\mu$m fiber (NA of 0.29) at the outcoupling, results in an excess mirror loss of 7.59 dB. Replacing the outcoupling fiber by the detector head, results in an excess mirror loss of 3.17 dB. Replacing the multimode fiber at the incoupling by a single mode fiber (NA of 0.13), further reduces the mirror loss to 2.2 dB. Although the mirror loss seems quite high, it is in correspondance with state-of-the-art, as described in the technology overview in Section 5.2.1 and as reported by IBM [40] (average excess loss of 2.4 dB). The main contributions to the mirror loss are investigated within the ongoing PhD work of Nina Hendrickx, Ghent University [14]. In practical situations the coupling losses can be further reduced by the introduction of microlenses, even when the optical layers are located on top of the PCB. This will be discussed in Chapter 6.

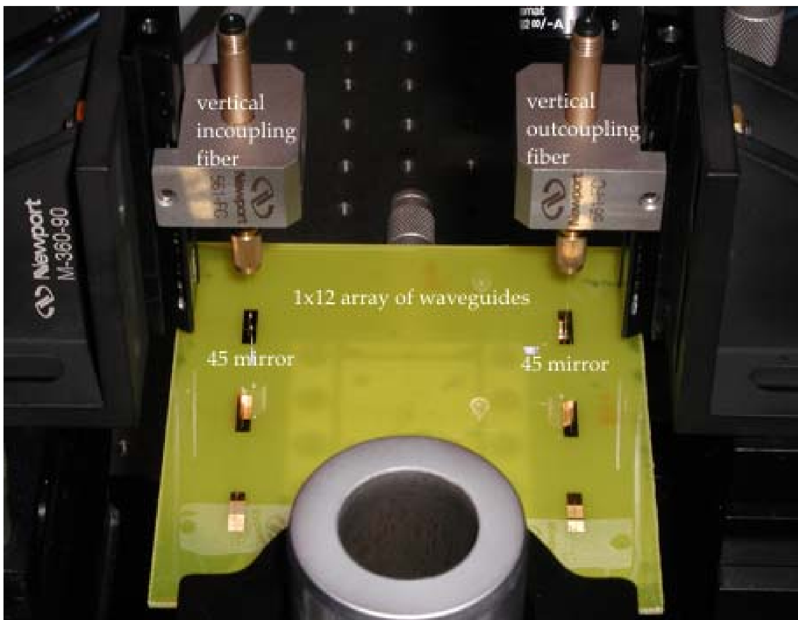


**Figure 5.12:** Vertical coupling loss measurements performed on a 10×10 cm$^2$ optical PCB

| | insertion loss | 2× mirror | 1× mirror |
|---|---|---|---|
| **MM fiber to MM fiber** | 17.93 | 15.18 | 7.59 |
| **MM fiber to detector** | 9.09 | 6.34 | 3.17 |
| **SM fiber to detector** | 7.15 | 4.40 | 2.20 |

**Table 5.4:** Mirror coupling loss (dB)

The characterization of single mode coupling structures defined in Ormocer® is based on the waveguide samples described in Section 4.5, delivered by the Fraunhofer IOF Institute, in the framework of a bilateral project with Motorola. A cleaved single mode fiber is positioned in front of a manually polished incoupling facet, the detector head is positioned above a metal coated mirror defined at the end of the 3.3 cm long waveguides. The excess mirror loss has an average of 2.29 dB, with a standard deviation of 0.54 dB, based on 4 measurements. Optimum excess mirror loss is 1.55 dB.

## 5.3 Laser ablated cavities for hybrid integration

### 5.3.1 Inserts with in-plane optical functionality

The fabrication of optical vias in a polymer layer integrated on a PCB, to allow the introduction of an insert, is developed during a project with Motorola. The complete description of the final demonstrator that has been built, is out of the scope of this PhD dissertation. Important to know is that optical cavities had to be defined, well aligned with respect to single mode waveguides, facing the alignment limits of the ablation set-up. Part of the final board is shown in Figure 5.13, containing 10 laser ablated cavities, corresponding to 10 chips. The size of one chip is 10×30 $mm^2$.

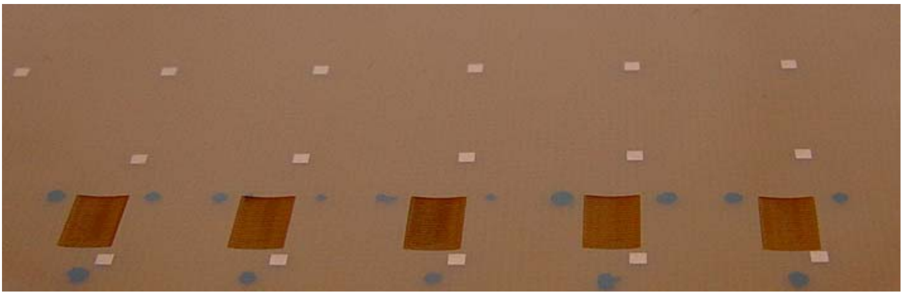

**Figure 5.13:** Laser ablated cavities defined in Ormocer®

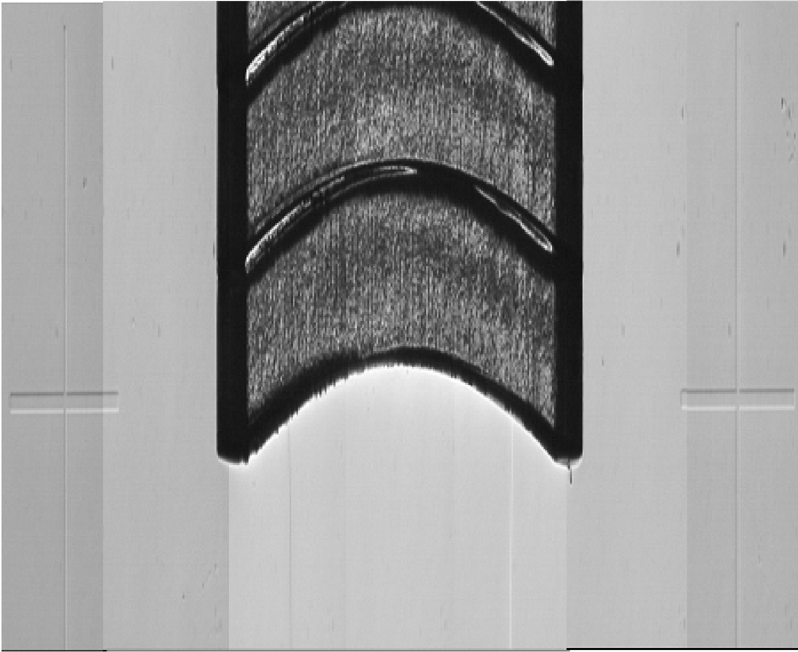

**Figure 5.14:** Microscope image of a KrF excimer laser ablated large area cavity

The insert is attached on a glass plate that is flip chip mounted onto the PCB substrate, where the top of the uppercladding acts as a reference plane in height. The laser ablation area is slightly larger than the size of the insert, $3\times2.5\,mm^2$. Reference marks both for aligning the laser beam, and aligning the insert, are metallized. The marks have a length of 1 mm, the line width is $20\,\mu m$. The optical via is rounded with a sag of $75\,\mu m$. The total tickness of the optical layer stack is $95\,\mu m$, the remaining Ormocer® layer in the ablated cavity is $20 \pm 5\,\mu m$. This buffer layer should protect the optical quality sidewall from contaminating ablated FR4 particles. Also important, is the perpendicularity of the waveguide endfacet, which results in an actual ablation angle of $8^o$. To ablate a larger area, subsequent ablated acrs are required, using a square aperture with dimensions $260\times260\,\mu m^2$. The laser pulse energy is 10 mJ, pulse repetition rate 200 Hz, number of pulses 225, and the distance between two arcs $250\,\mu m$, $10\,\mu m$ smaller than the width of the laser spot, because of the tapering of the sidewalls. The different arcs can be seen in Figure 5.14. Debris being generated during KrF excimer laser ablation of Ormocer® is removed making use of a thin photoresist layer, which is developed after ablation. This way, the top of the uppercladding surface can act as a reference plane in height.

### 5.3.2 Inserts with out-of-plane coupling optical functionality

The laser ablated cavity fabricated in the optical PCB can be used for the insertion of a pluggable deflecting component, providing for out-of-plane coupling. This approach is similar to the use of embedded $45^o$ mirrors, as described in Section 5.2. One of the advantages is that additional functionalities can be included as well, such as microlenses and mechanical alignment structures. This concept is proposed in the European IST-project-Nemo, Network of Excellence on Micro-Optics, within the workpackage on Micro-Optics for PCB and MCM-level interconnects [41].

The out-of-plane coupling component is fabricated with Deep Lithography with Protons (DLP), an in-house technology of the Vrije Universiteit Brussel, FirW-TONA. DLP is a prototyping technology that allows fast fabrication of micro-mechanical and micro-optical elements [42, 43]. The DLP fabrication process consists of the following steps:

- First a collimated 8.3 MeV proton beam is used to irradiate an optical grade PMMA sample according to a predefined pattern by translating the PMMA sample, changing the physical and chemical properties of the material in the irradiated zones.
- As a next step, a selective etching solvent is applied for the development of the irradiated regions. This allows for the fabrication of (2D arrays of) micro-holes, optically flat micromirrors and microprisms, as well as alignment features and mechanical support structures.
- On the other hand, an organic monomer vapour can be used to expand the volume of the bombarded zones through an in-diffusion process. This enables the fabrication of spherical (or cylindrical) microlenses with well-defined heights.
- These processes are shown in Figure 5.15. If necessary, both processes can be applied to different regions of the same sample, yielding micro-optical structures combined with monolithically integrated microlenses.

The fabrication of the out-of-plane coupling component is described in [38]. For the irradiation, PMMA with a thickness of 500 $\mu$m is being used, which allows the protons to completely traverse the sample. The PMMA sample is continuously translated perpendicularly to the beam in steps of 500 nm using Burleigh inchworms with an accuracy of 50 nm. PMMA is a negative resist, which means that protons impinging on it will cause scissions in the long polymer chains and thus a material degradation in the irradiated zones, and that during the etching process the irradiated zones will be removed. This means that the entire contour of the designed component has to be irradiated. A proton beam collimating aperture of

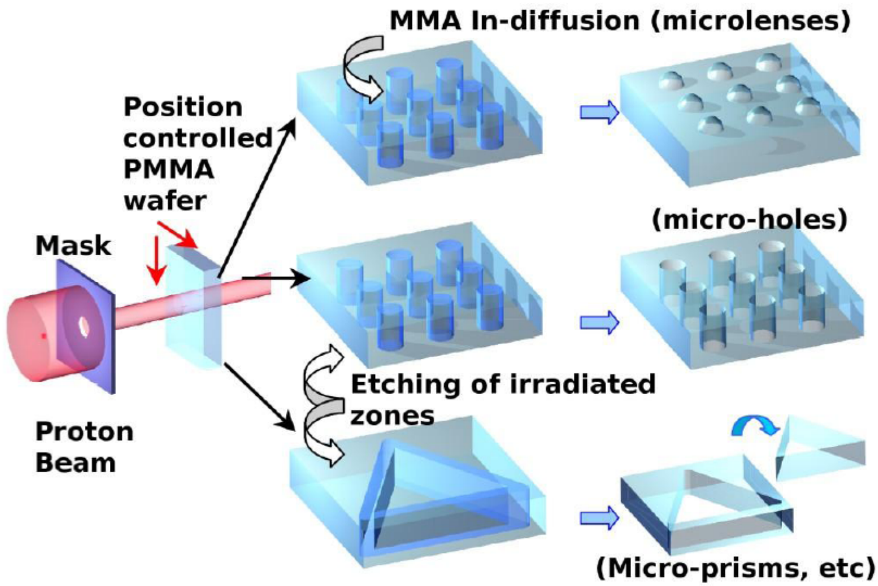


**Figure 5.15:** Basic fabrication processes of deep lithography with protons (source: VUB, FirW-TONA [42])

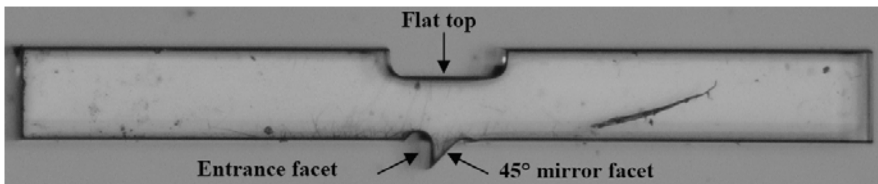


**Figure 5.16:** Microscope image of an out-of-plane coupling component fabricated with DLP (source: VUB, FirW-TONA [38])

125 $\mu$m is being used, which causes some rounding in the corners of the component, but this does not affect its optical functionality. The fabrication process has been optimized as such that a minimal roughness of the fabricated optical surfaces is achieved. Of course, fabrication with DLP is only suited for prototyping purposes, but the compatibility with standard mass-replication techniques, such as injection moulding and hot embossing has been shown [44].

Figure 5.16 shows a microscope image of the fabricated out-of-plane coupling component. The flat top exit facet is introduced for minimizing the free space travel distance. For the characterization of the critical optical surfaces of the component, being the entrance facet, the 45$^o$ mirror facet, and flat top exit facet, a

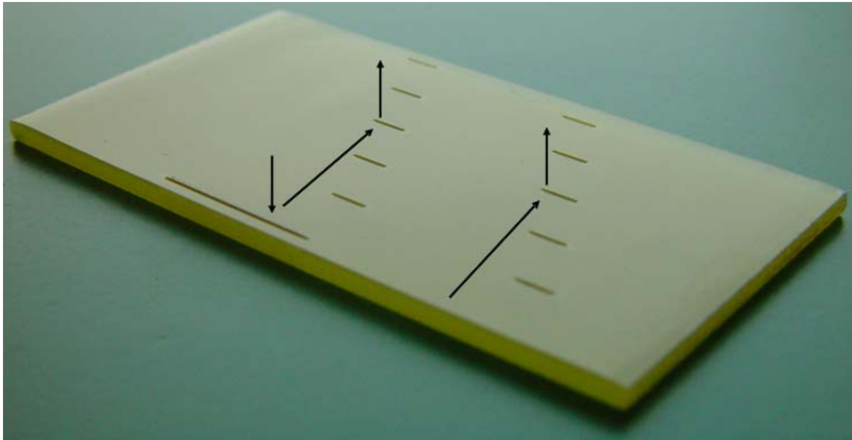

**Figure 5.17:** Demonstrator board containing laser ablated cavities for the introduction of out-of-plane coupling DLP inserts

non-contact optical surface profiler has been used. Since the entrance facet is not accessible with the microscope objective, this surface was not measured, but its surface roughness will be analogous to the two others. The surface analysis reveals that the flat top part has an average local RMS surface roughness of $34.19 \pm 4.90$ nm (for component 1) and $25.10 \pm 1.29$ nm (for component 2), measured over an area of $60 \times 46\,\mu\text{m}^2$, averaged over 5 randomly chosen positions. Applying the same measurement method to the $45^o$ angled facet reveals an RMS roughness of $29.24 \pm 3.96$ nm and $29.21 \pm 3.96$ nm for component 1 and 2 respectively. One can conclude that the developed surfaces have a very reproducible optical quality.

The demonstrator board shown in Figure 5.17 consists of $50 \times 50\,\mu\text{m}^2$ waveguides defined in Truemode$^{TM}$, in which cavities have been defined to allow for the insertion of the DLP out-of-plane coupling components. It allows for horizontal-in-, vertical-outcoupling measurements (using one DLP out-of-plane coupler), and vertical-in-, vertical-outcoupling measurements (using two DLP out-of-plane couplers). A top view of the DLP insert mounted in the laser ablated cavity is shown in Figure 5.18.

The parameters for the fabrication of the cavity: laser beam angle $6^o$ (vertical wall at the waveguide end-facet), laser fluence $2 \pm 0.5\,\text{J/cm}^2$, laser spot dimensions $280 \times 280\,\mu\text{m}^2$, ablation speed $82\,\mu\text{m/s}$, laser pulse frequency 100 Hz.

Currently, the coupling loss measurements are ongoing. Previous measurements indicated a coupling efficiency of 20.9% or -6.80 dB, which should be a measure of the coupling efficiency of the DLP out-of-plane coupler itself. This value is, however, significantly lower than the coupling efficiency of the DLP component mea-

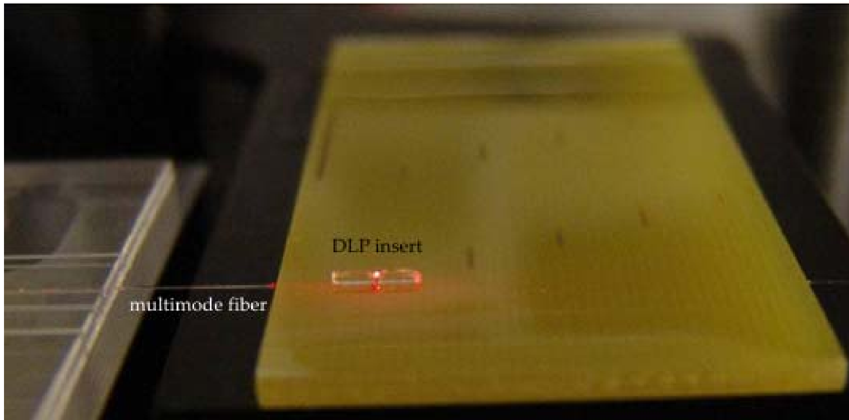


**Figure 5.18:** Out-of-plane coupler inserted in the laser ablated cavity (source: VUB, FirW-TONA)

sured using fiber-to-fiber coupling (47.5%) and the simulated coupling efficiency of 41.7%. This is mainly due to the insertion loss when light from a multimode fiber is coupled into the Truemode$^{TM}$ waveguides, in reason of the lack of use of index matching gel, the larger surface roughness of the polished input facets, and the non-optimal cross-sectional dimensions of the waveguides that were being used during those initial measurements.

## 5.4 Accessing embedded optical layers

In cooperation with different partners within the European-PIDEA-Project-Orbita (Optical Routing Backplanes Intranet-working for Telecom/datacom Applications) the aim is to realize board-to-board optical interconnections based on PCB embedded waveguides defined in glass sheets. The fabrication of the $70 \times 70\,\mu m^2$ optical waveguides is performed by PPC-Electronic. The optical layers are laminated between two $200\,\mu m$ thick layers of fiber reinforced epoxy. The window to access the optical layers through the base material will be fabricated using laser ablation. Other options may include the use of milling, as described in [20].

Both KrF excimer laser and $CO_2$ laser ablation are considered to ablate the access window in the base material. The fibers embedded in the epoxy layer cannot be ablated using our KrF excimer laser, even at higher laser pulse energies of 20 mJ ($8.3\,J/cm^2$), see Figure 5.19. The $CO_2$ laser can be used instead, see Figure 5.20 where the base material is ablated down to the glass sheet.

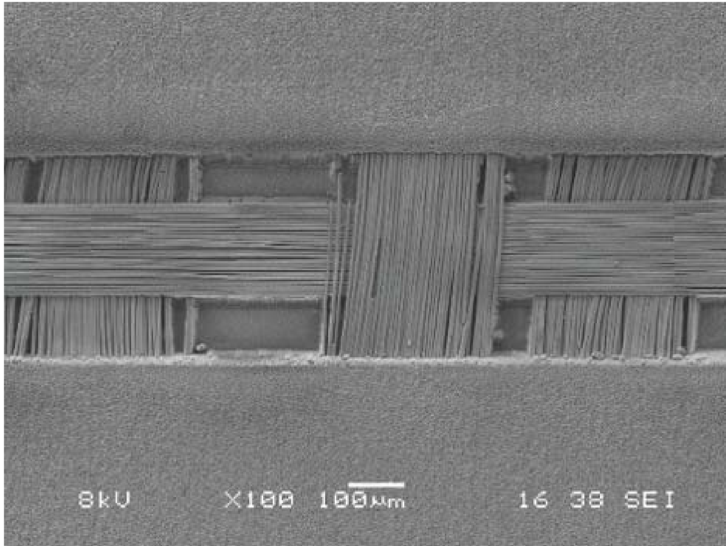


**Figure 5.19:** SEM image of KrF excimer laser ablated fiber reinforced epoxy, laminated on top of a thin glass sheet

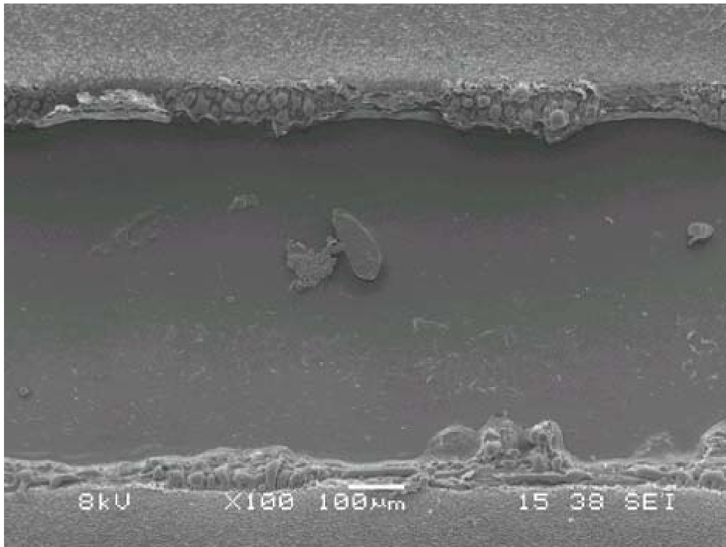


**Figure 5.20:** SEM image of $CO_2$ laser ablated fiber reinforced epoxy, laminated on top of a thin glass sheet

The glass sheet acts as an ablation stop, without damage. Laser parameters: energy level 1, minimum attenuation, focus lens L2, pulse frequency 100 Hz, ablation speed 6 mm/s. The position and dimensions of the access window are determined by an etched window in a copper foil on top of the base material. This way, the low positioning accuracy of the $CO_2$ laser beam is not an issue.

In Section 3.3 it was proved experimentally that $CO_2$ laser ablation can be used for patterning borosilicate glass. This will be explored for the fabrication of a coupling facet in a next phase, and the work is subject to further investigation.

## 5.5 Conclusions

Different approaches for out-of-plane coupling structures have been discussed. Special attention was given to the fabrication of metal coated micromirrors embedded in the optical layer. The process being developed can be applied both for Ormocer® and for Truemode$^{TM}$ materials. Surface roughness measurements revealed that for Truemode$^{TM}$ the $R_a$ surface roughness of the mirrors can be as low as 42 nm, and the RMS roughness as low as 53 nm, measured on an area of $174 \times 52\,\mu m^2$. Coated mirrors in Ormocer® show an overall $R_a$ average of 151 nm, and an overall RMS average of 196 nm. The $45^o$ angle has been verified using a Dektak 8 stylus profiler, indicating an angle accuracy of $\pm 2^o$. Coupling loss measurements were performed both using multimode and single mode waveguides as testbed structures. An excess mirror loss of 2.2 dB has been achieved, depending on the in- and outcoupling fiber being used.

The fabrication of optical vias allowing the introduction of an insert with in-plane or out-of-plane coupling optical functionality was described. Finally, the use of $CO_2$ laser ablation to acces the optical layers through fiber reinforced epoxy was discussed.

# References

[1] Avalon Photonics. `http://www.avap.ch`.

[2] N. Suzuki, H. Hatakeyama, K. Fukatsu, T. Anan, K. Yashiki, and M. Tsuji. 25-gbps operation of 1.1-$\mu$m-range ingaas vcsels for high-speed optical interconnections. In *OFC'06, Proceedings Optical Fiber Communication Conference*, Mar 2006.

[3] Albis. `http://www.albisopto.com`.

[4] C. Berger, B.J. Offrein, and M. Schmatz. Challenges for the introduction of board-level optical interconnect technology into product development roadmaps. In *Photonics West'06, Proceedings SPIE 6124, Optoelectronic Integrated Circuits*, Jan 2006.

[5] Interconnect by Optics (IO). `http://io.intec.ugent.be`.

[6] M.B. Venditti, E. Laprise, J. Faucher, P.O. Laprise, J. Eduardo, A. Lugo, and D.V. Plant. Design and test of an optoelectronic-vlsi chip with 540-element receiver-transmitter arrays using differential optical signaling. *IEEE Journal Of Selected Topics In Quantum Electronics*, 9(2):361–379, Mar-Apr 2003.

[7] C. Cook, J.E. Cunningham, A. Hargrove, G.G. Ger, K.W. Goossen, W.Y. Jan, H.H. Kim, R. Krause, M. Manges, M. Morrissey, M. Perinpanayagam, A. Persaud, G.J. Shevchuk, V. Sinyansky, and A.V. Krishnamoorthy. A 36-channel parallel optical interconnect module based on optoelectronics-on-vlsi technology. *IEEE Journal Of Selected Topics In Quantum Electronics*, 9(2):387–399, Mar-Apr 2003.

[8] E. Mohammed, A. Alduino, T. Thomas, H. Braunisch, D. Lu, J. Heck, A. Liu, I. Young, B. Barnett, G. Vandentop, and R. Mooney. Optical interconnect system integration for ultra-short-reach applications. *Intel Technology Journal*, 8(2):115–128, May 2004.

[9] C.C. Choi, L. Lin, Y.J. Liu, J.H. Choi, L. Wang, D. Haas, J. Magera, and R.T. Chen. Flexible optical waveguide film fabrications and optoelectronic devices integration for fully embedded board-level optical interconnects. *Journal Of Lightwave Technology*, 22(9):2168–2176, Sep 2004.

[10] N.A. Jokerst, T.K. Gaylord, E. Glytsis, M.A. Brooke, S. Cho, T. Nonaka, T. Suzuki, D.L. Geddis, J. Shin, R. Villalaz, J. Hall, A. Chellapa, and M. Vrazel. Planar lightwave integrated circuits with embedded actives for board and substrate level optical signal distribution. *IEEE Transactions On Advanced Packaging*, 27(2):376–385, May 2004.

[11] E. Bosman, P. Geerinck, W. Christiaens, G. Van Steenberge, J.M. Vanfleteren, and P. Van Daele. Optical connections on flexible substrates. In *Photonics Europe'06, Proceedings SPIE 6185, Micro-Optics, VCSELs, And Photonic Interconnects*, Apr 2006.

[12] J. Moisel, H.P. Huber, J. Guttmann, O. Krumpholz, B. Lunitz, M. Rode, and R. Schoedlbauer. Optical backplane. In *ECOC'01, Proceedings European Conferences On Optical Communication*, pages 254– 255, Sep 2001.

[13] L. Dellmann, T. Lamprecht, S. Oggioni, M. Witzig, R. Dangel, R. Beyeler, C. Berger, F. Horst, and B.J. Offrein. Butt-coupled optoelectronic modules for high-speed optical interconnects. In *CLEO/Europe '05, Proceedings Conference On Lasers And Electro-Optics Europe*, page 476, Jun 2005.

[14] N. Hendrickx, G. Van Steenberge, P. Geerinck, and P. Van Daele. Multilayer optical interconnects integrated on a printed circuit board. In *Photonics Europe'06, Proceedings SPIE 6185, Micro-Optics, VCSELs, And Photonic Interconnects*, Apr 2006.

[15] D. Krabe, F. Ebling, N. Arndt-Staufenbiel, G. Lang, and W. Scheel. New technology for electrical/optical systems on module and board level: The eocb approach. In *ECTC'00, Proceedings Electronic Components And Technology Conference*, pages 970–974, May 2000.

[16] E. Griese. A high-performance hybrid electrical-optical interconnection technology for high-speed electronic systems. *IEEE Transactions On Advanced Packaging*, 24(3):375–383, Aug 2001.

[17] J. Moisel, J. Guttmann, H.P. Huber, O. Krumpholz, M. Rode, R. Bogenberger, and K.P. Kuhn. Optical backplanes with integrated polymer waveguides. *Optical Engineering*, 39(3):673–679, Mar 2000.

[18] B. Lunitz, J. Guttmann, H.P. Huber, J. Moisel, and M. Rode. Experimental demonstration of 2.5 gbit/s transmission with 1 m polymer optical backplane. *Electronics Letters*, 37(17):1079–1079, Aug 16 2001.

[19] Y. Ishii, S. Koike, Y. Arai, and Y. Ando. Smt-compatible large-tolerance opto-bump interface for interchip optical interconnections. *IEEE Transactions On Advanced Packaging*, 26(2):122–127, May 2003.

[20] H. Schroder. Waveguide and packaging technology for optical backplanes and hybrid electrical-optical circuit boards. In *Photonics West'06, Proceedings SPIE 6124, Optoelectronic Integrated Circuits*, Jan 2006.

[21] B.S. Rho, M.H. Cho, H.S. Cho, S. Kang, H.H. Park, S.W. Ha, and B.H. Rhee. Low-crosstalk and high-efficiency optical interconnection using 45 deg-ended connection rods. *Electronics Letters*, 40(12):730–732, Jun 10 2004.

[22] S. Hiramatsu and M. Kinoshita. Three-dimensional waveguide arrays for coupling between fiber-optic connectors and surface-mounted optoelectronic devices. *Journal Of Lightwave Technology*, 23(9):2733–2739, Sept 2005.

[23] T. Yoshimura, T. Inoguchi, T. Yamamoto, S. Moriya, Y. Teramoto, Y. Arai, T. Namiki, and K. Asama. Self-organized lightwave network based on waveguide films for three-dimensional optical wiring within boxes. *Journal Of Lightwave Technology*, 22(9):2091–2100, Sep 2004.

[24] G. Van Steenberge, P. Geerinck, S. Van Put, J. Van Koetsem, H. Ottevaere, D. Morlion, H. Thienpont, and P. Van Daele. Mt-compatible laser-ablated interconnections for optical printed circuit boards. *Journal Of Lightwave Technology*, 22(9):2083–2090, Sep 2004.

[25] A.L. Glebov, M.G. Lee, S. Aoki, D. Kudzuma, J. Roman, M. Peters, L. Huang, D.S. Zhou, and K. Yokouchi. Integrated waveguide microoptic elements for 3d routing in board-level optical interconnects. In *Photonics West'06, Proceedings SPIE 6126, Nanophotonic Packaging*, Jan 2006.

[26] R. Yoshimura, M. Hikita, M. Usui, S. Tomaru, and S. Imamura. Polymeric optical waveguide films with 45 mirrors formed with a 90 v-shaped diamond blade. *Electronics Letters*, 33(15):1311–1312, Jul 17 1997.

[27] M. Hikita, S. Tomaru, K. Enbutsu, N. Ooba, R. Yoshida, M. Usai, T. Yoshida, and S. Imamura. Polymeric optical waveguide films for short-distance optical interconnects. *IEEE Journal Of Selected Topics In Quantum Electronics*, 5(5):1237–1242, Sept-Oct 1999.

[28] A.L. Glebov, J. Roman, M.G. Lee, and K. Yokouchi. Optical interconnect modules with fully integrated reflector mirrors. *IEEE Photonics Technology Letters*, 17(7):1540–1542, Jul 2005.

[29] M. Immonen, M. Karppinen, and J.K. Kivilahti. Fabrication and characterization of polymer optical waveguides with integrated micromirrors for

three-dimensional board-level optical interconnects. *IEEE Transaction On Electronics Packaging Manufacturing*, 28(4):304–311, Oct 2005.

[30] J.S. Kim and J.J. Kim. Fabrication of multimode polymeric waveguides and micromirrors using deep x-ray lithography. *IEEE Photonics Technology Letters*, 16(3):798–800, Mar 2004.

[31] A. McCarthy, H. Suyal, and A.C. Walker. $45^o$ out-of-plane turning mirrors for optoelectronic chip carriers based on multimode polymer waveguides. In *ECOC'04, Proceedings European Conferences On Optical Communication*, Sep 2004.

[32] Y. Liu, L. Lin, C. Choi, B. Bihari, and R.T. Chen. Optoelectronic integration of polymer waveguide array and metal-semiconductor-metal photodetector through micromirror couplers. *IEEE Photonics Technology Letters*, 13(4):355–357, Apr 2001.

[33] W.M. Diffey, R.H. Trimm, M.G. Temmen, and P.R. Ashley. Fabrication of low-loss optical-quality polymer waveguide facets in multilayer polymer devices using an inductively coupled plasma. *Journal Of Lightwave Technology*, 23(4):1787–1790, Apr 2005.

[34] A. Neyer, S. Kopetz, E. Rabe, W.J. Kang, M. Stach, and R. Michalzik. 10 gbit/s electrical-optical circuit board based on new polysiloxane waveguide technology. In *ECOC'04, Proceedings European Conferences On Optical Communication*, pages 814–815, Sep 2004.

[35] Polysiloxane optical waveguide layer integrated in printed circuit board. `http://www-mst.e-technik.uni-dortmund.de/eocb.html`.

[36] Optical Crosslinks. `http://www.opticalcrosslinks.com`.

[37] B.L. Booth, J.E. Marchegiano, C.T. Chang, R.J. Furmanak, D.M. Graham, and R.G. Wagner. Polyguide polymeric technology for optical interconnect circuits and components. In *Photonics West'97, Proceedings SPIE 3005, Optoelectronic Interconnects And Packaging*, Apr 1997.

[38] J. Van Erps, G. Van Steenberge, N. Hendrickx, P. Geerinck, B. Volckaerts, C. Debaes, P. Van Daele, and H. Thienpont. Deep lithography with protons to prototype pluggable micro-optical out-of-plane coupling structures for multimode waveguides. In *ICOO'05, Proceedings SPIE 5956, Integrated Optics*, Sep 2005.

[39] E.D. Palik. *Handbook of Optical Constants of Solids*. Academic, Jan 1985.

[40] M.A. Taubenblatt. Challenges and opportunities for integrated optics in computing systems. In *Photonics West'06, Proceedings SPIE 6124, Optoelectronic Integrated Circuits*, Jan 2006.

[41] Network of Excellence on Micro-Optics (Nemo). `http://www.micro-optics.org`.

[42] C. Debaes, M. Vervaeke, B. Volckaerts, J. Van Erps, L. Desmet, H. Ottevaere, P. Vynck, V. Gomez, A. Hermanne, and H. Thienpont. Low-cost plastic micro-optics for board level optical interconnections. In *Photonics West'06, Proceedings SPIE 6126, Nanophotonic Packaging*, Jan 2006.

[43] C. Debaes, M. Vervaeke, V. Baukens, H. Ottevaere, P. Vynck, P. Tuteleers, B. Volckaerts, W. Meeus, M. Brunfaut, J. Van Campenhout, A. Hermanne, and H. Thienpont. Low-cost microoptical modules for mcm level optical interconnections. *IEEE Journal Of Selected Topics In Quantum Electronics*, 9(2):518–530, Mar-Apr 2003.

[44] P. Tuteleers, P. Vynck, H. Ottevaere, C. Debaes, A. Hermanne, I.P. Veretennicoff, and H. Thienpont. Replication of refractive micro-optomechanical components made with deep lithography with protons. In *DTIP'01, Proceedings SPIE 4408, Symposium On Design, Test, Integration And Packaging On MEMS/MOEMS*, pages 329–337, Apr 2001.

# Chapter 6

# Board-to-board coupling interface

*In this chapter the interface to allow coupling between waveguides located on different PCBs will be discussed. Excimer laser ablation of an intermediate alignment plate containing microlenses and mechanical alignment holes is described. A proof-of-principle demonstrator is presented. A brief alignment tolerance study is included.*

## 6.1 Introduction

To set up a complete optical interconnection system in addition to the interconnection between O/E module and optical waveguide, a purely optical interconnection between board and backplane is needed. For this task different approaches are considered:

- Free space optical interconnection with focusing elements. The Daimler Chrysler optical backplane concept is based on this approach [1]. Large core multimode polymer waveguides in combination with an expanded free space beam coupling between board and backplane allows for a 1 dB loss lateral displacement tolerance of 500 $\mu$m, which makes the system useful for plug-and-play mechanisms of the boards.

- Fiber ribbon optical interconnection. This concept has been evaluated within the German-OptiCon-project [2]. The backplane architecture from Fujitsu using pluggable optical jumpers consisting of glass or polymer fiber ribbons with MT type connectors is another example [3]. No board-to-board losses have been reported so far.

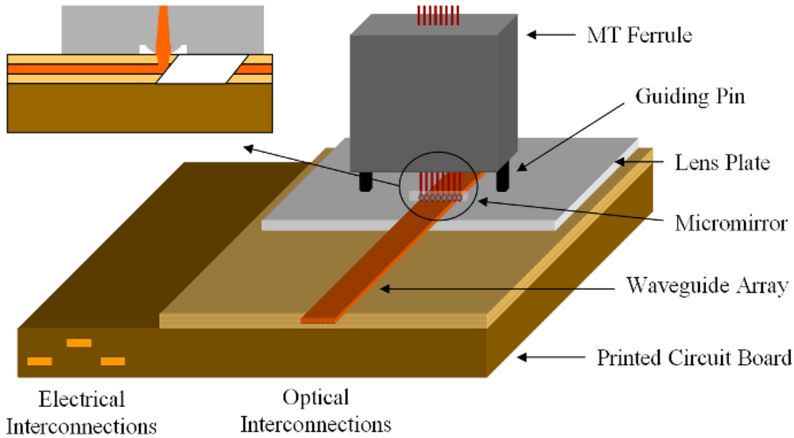


**Figure 6.1:** Coupling approach based on passive and mechanical alignment of a standard MT type connector

- Pluggable optical connector. The connector developed within the European-IO-project [4] is further modified by FCI France within the European-Orbita-project for this purpose. The German-NeGIT-project is based on an MT like optical connector containing laser written vertical waveguiding structures [5].

The coupling approach developed within this work is a modification of the second option: the coupling interface towards a standard MT type fiber ribbon allows for a passive alignment making use of an intermediate plastic plate containing holes for the insertion of the alignment pins of the MT ferrule, and containing microlenses for an increased coupling efficiency (Figure 6.1). The microlenses can also be structured directly into the optical layer. In addition to the waveguides, and the micromirrors, the microlenses and the mechanical alignment holes are fabricated using laser ablation, which allows us to fabricate the entire optical interconnection using only one technology.

## 6.2 Microlenses

### 6.2.1 Technology overview

Most of the microlens fabrication methods yield microlens arrays that satisfy many of the optical quality requirements [6]. They differ however in that some fabrication methods are more suitable either for rapid prototyping or for mass-

fabrication or for monolithic integration than others. Some methods are relatively inexpensive and are based on existing technologies while others require dedicated processing tools and/or new materials with special properties.

Lens arrays made of glass have been studied for a relatively long time compared to those made in other materials and various fabrication techniques have been proposed for this purpose: photothermal expansion [7], ion exchange [8], $CO_2$ laser irradiation [9] and reactive ion etching [10]. More recently fabrication techniques of micro-optical components in optical grade polymers have become a research topic of interest. They include techniques like photoresist reflow [11], laser beam shaping [12], deep lithography with protons [13], LIGA-processing [14], photopolymerization [15], microjet printing [16], laser ablation [17] and direct laser [18] or e-beam writing [19].

### 6.2.2 Excimer laser ablation

The in-house technology to fabricate microlenses using laser ablation has been developed within the PhD work of Kris Naessens [20]. A short description of the principle is included in this work. The process is based on circular concentric movements of the translation stage. Depending on the relation between contour and laser beam radius, a trench with a certain profile is realized. Keeping the laser beam parameters (fluence, pulse frequency and circular beam aperture) constant, leaves two variables for varying the trench profile: contour velocity and radius. The contour speed is related to the depth while the radius will determine the location and shape of the trench. By ablating several of these concentric trenches, one is able to approximate an arbitrary, circular-symmetric lens shape. Since ablation is essentially an erosive process, the resulting lens will consequently be buried below the sample surface. Based on simulated annealing, an algorithm calculates an optimal set of contour speeds and radii in order to approximate a desired lens profile taking some boundary values into account, e.g. a maximum value for the contour speed to prevent the translation stage from unstable operation and to ensure sufficient overlap between successive pulses. The maximum number of contours is determined by the user but the algorithm decides how many eventually will be used, during the calculation of a suitable set of contours.

Once an optimal set has been calculated, it is translated into control code for the translation stage and laser. In this phase, a decision has to be made concerning the sequence of the contours. The trenches can be written in random order, in order of increasing and of decreasing radius. From a processing point of view, it is not clear which approach is best. For instance writing the central part of the lens first allows accurate profiling of this area since we start with a flat surface free of debris and do not ablate steep edges in this region. However, as the ablation progresses towards the outer region of the lens, a lot of debris is deposited on the central part. On the other side, the inverse approach first ablates the deeper parts

of the lens and gradually moves towards the central part. Although the central part will be initially covered with debris, towards the end of the processing it will become clear again due to ablation in that area. However, the present debris can cause the surface shaping to be less accurate centrally, which in turn degrades the optical functionality. In order to ensure that the contour velocity remains constant during ablation, there is a small delay between triggering of the laser and stage motion in order to allow the latter to ramp to the desired speed.

The optical finish of the lens surface is achieved by ablation of the entire lens area with a large beam aperture. During this process the sample is contouring with a small diameter (typically 20–30 $\mu$m). In this way a structure is ablated on top of the lens with a central flat part at least equaling the lens area. Three distinct effects are achieved in this way: debris is ejected from the lens surface, forced to leave the lens area and deposited near the ablated zone. Secondly, as spatially rapidly varying features ablate faster than smooth surfaces, the surface gradually becomes smoother. It is believed that this smoothing during material removal is due to the presence of a thermal component in the photoablation process. Thirdly, as during the surface smoothing a layer of polymer is physically removed, it is important that the large laser beam is as homogeneous as possible in order not to deform the lens shape. Since the set-up lacks a beam homogenizer, the contouring of the smoothing beam ensures that the laser fluence is spatially averaged over the lens area. During this process, a layer of typically 15–20 $\mu$m is removed. Drilling the lens structure less deep does not eliminate the discrete pulse pattern in the surface.

The described technique has been applied for the fabrication of spherical microlenses of 100 $\mu$m diameter with a radius of curvature of 100 $\mu$m. Microlenses are written directly into the Ormocer® layer integrated on top of the PCB. Since the bottom of an excimer laser defined cavity in Ormocer® suffers from microstructures (see Section 3.2), an alternative to the above mentioned smoothing step is developed within this PhD work, using the thermal energy of the $CO_2$ laser.

### 6.2.3 $CO_2$ laser polishing

Figure 6.2 illustrates the result of the $CO_2$ laser assisted smoothing procedure, requiring only a very limited number of laser pulses, and avoiding the lens surface from being buried into the surface. The microlens as shown in Figure 6.2a, is fabricated with following parameters: pulse energy 420 mJ, energy transmission 8%, demagnification of the imaging lens 5, repetition rate 20 Hz, aperture 250 $\mu$m. The parameters for $CO_2$ laser smoothing: energy level 1, demagnification of the imaging lens 2 (L3), maximum attenuation, repetition rate 50 Hz, aperture 2000 $\mu$m. As can be seen, only 3 to 5 $CO_2$ laser pulses are required to remove the discrete pulse pattern in the lens surface.

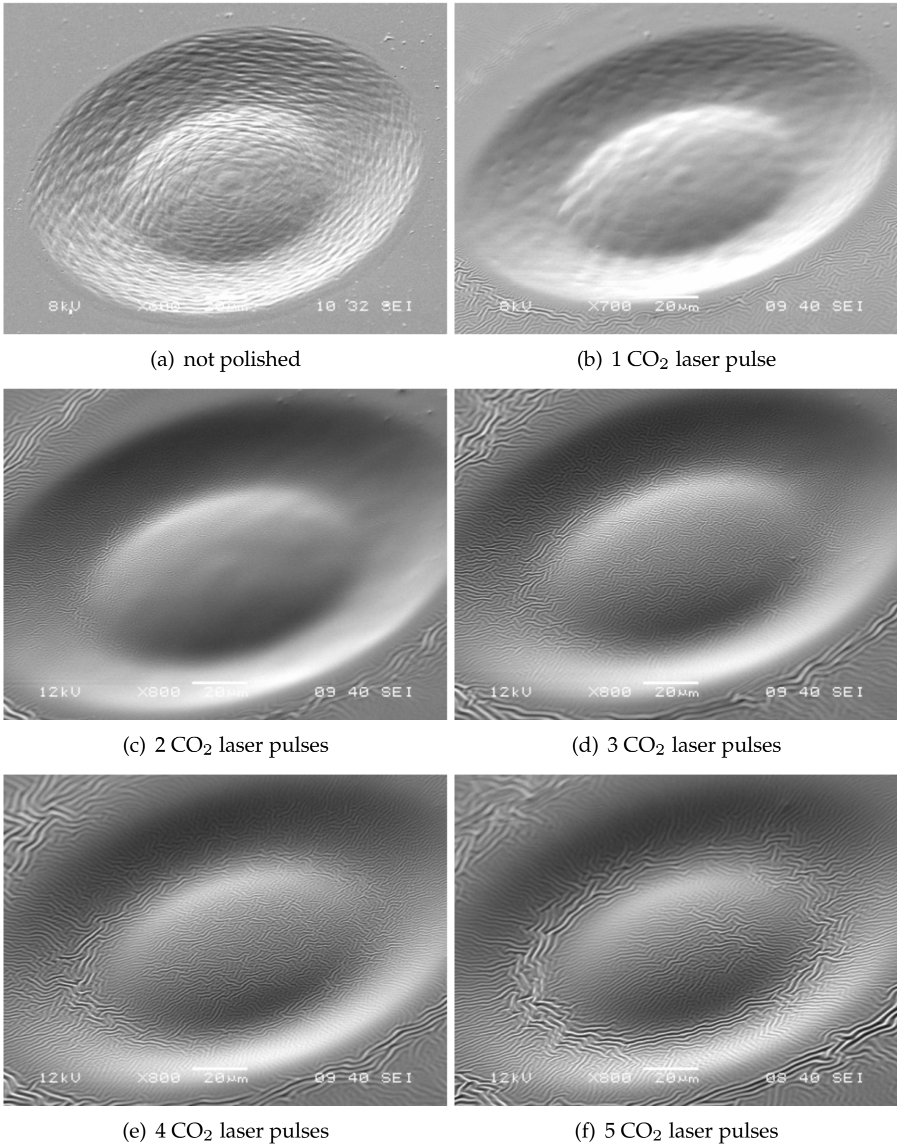

(a) not polished

(b) 1 $CO_2$ laser pulse

(c) 2 $CO_2$ laser pulses

(d) 3 $CO_2$ laser pulses

(e) 4 $CO_2$ laser pulses

(f) 5 $CO_2$ laser pulses

**Figure 6.2:** $CO_2$ laser polishing of KrF excimer laser ablated microlenses in Ormocer®

The surface microstructures that do appear using $CO_2$ laser ablation of Ormocer® can be eliminated using an annealing step, as was shown in Figure 3.14 on page 61. This annealing step has been applied to the $CO_2$ laser polished microlenses,

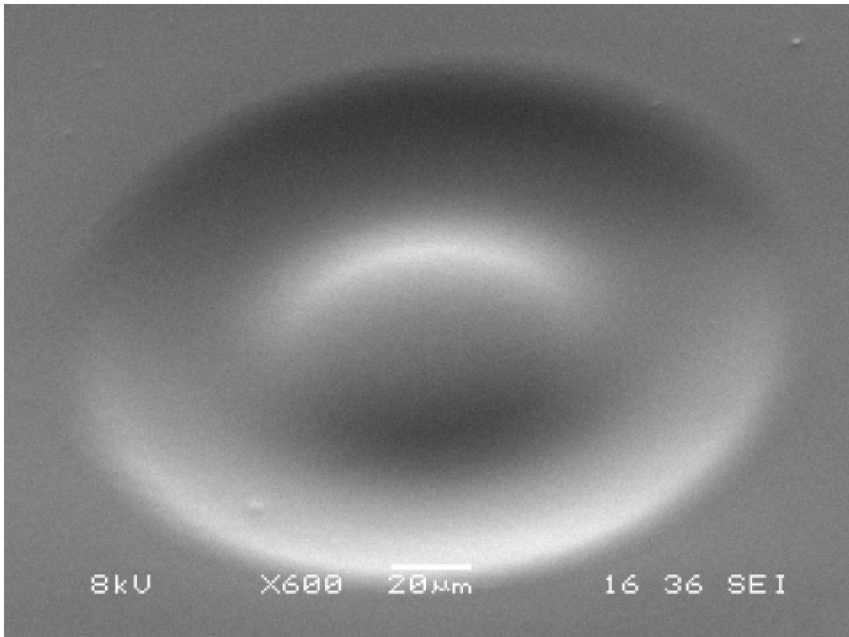


**Figure 6.3:** Ormocer® microlens fabricated by KrF excimer laser ablation, $CO_2$ laser polishing, and thermal annealing

with the intention to remove the surface microstructures. The result is shown in Figure 6.3, after an annealing step of 2 hours in a conventional oven at a temperature of 170°C. The $CO_2$ laser polishing step included 5 laser pulses.

The microlenses defined in the Ormocer® layer on top of the PCB can be ablated perfectly aligned with respect to the coupling structure. Locating the center of this coupling structure (micromirror) is achieved actively, by sending light into the waveguides, and locating the outcoupling light spots under the ablation setup. Because of the minimum diameter of the microlenses, it is clear that only embedded metal coated mirrors can be considered as coupling structure to be combined with microlenses, as is shown in Figure 6.4 for a mirror based on total internal reflection.

In what follows, microlenses are ablated not in the optical layer, but in a separate polycarbonate (PC) plate, together with additional mechanical alignment structures. This makes the coupling approach compatible with lens plates fabricated using low cost mass-replication technologies.

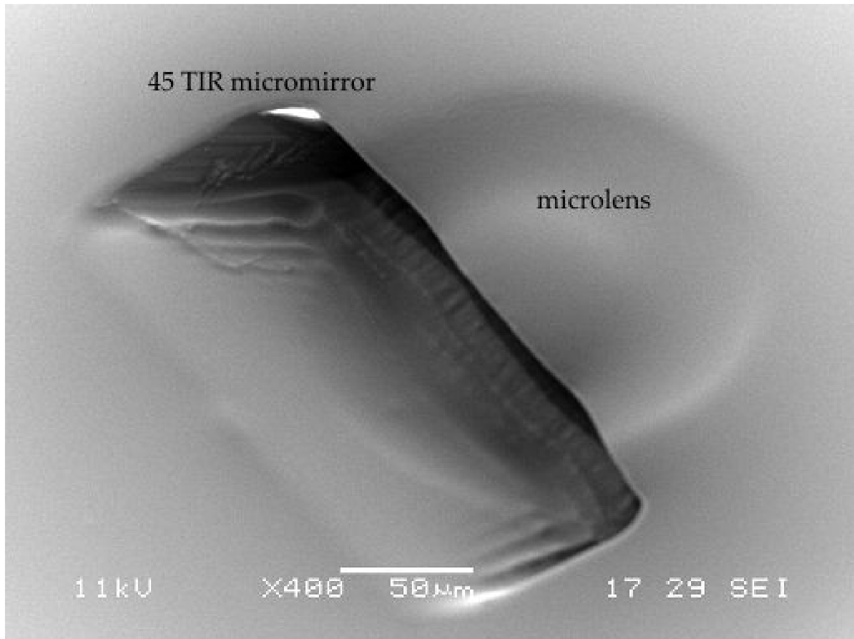


**Figure 6.4:** Microlens aligned with a TIR micromirror

### 6.2.4 Characterization

Within this work SEM is used for visual inspection of laser written microlenses. A complete characterization of excimer laser ablated microlenses (PC substrate) can be found in [20, 21]. Radius of curvature, lens height, diameter, and surface roughness are derived from surface measurements using a white light interference profilometer. The evaluation of the optical performance of the lenses in terms of wavefront aberrations is measured using a Mach-Zehnder interferometer. The knowledge of these wavefront anomalies gives an indication of the expected imaging qualities by comparing them to the Maréchal and Rayleigh criterion. In addition, the Strehl ratio of the lens is estimated by calculating the standard deviation of the aberrations. It is expected that the modifications that have been made to the lens fabrication process (Ormocer® substrate, and $CO_2$ laser polishing) will give comparable characterization results.

**Figure 6.5:** Active writing of microlenses in a 250 $\mu$m thick PC plate

# 6.3 MT compatible coupling

## 6.3.1 Fabrication

Within the project Coupling from Opto-Boards (bilateral project between UGent, Intec Department and FCI 's Hertogenbosch), a connector interface has been developed to allow coupling between waveguides located on different boards. The interface is based on the MT connector technology, that has been proved to be a very suitable technology for both 1D and 2D parallel optical interconnections. The connector ferrule (fiber aligning part of the connector) contains 125 $\mu$m fibers positioned in 250 $\mu$m pitch fiber capillaries. The guiding pins ($699 \pm 0.5\,\mu$m) on either end of the fiber row help to align the connector ferrules during mating, fitting in very precise alignment pin holes. The dimensional tolerances on the aligning features are within 1 $\mu$m. The pre-alignment of the ferrules is guaranteed by the surrounding connector housing (MPO or MTP). The mating between the MPO connector and the MPO connector adapter interface is realized by a simple push-pull mechanism (MTP: push-on connector).

The alignment of the MT ferrule with respect to the waveguides and micromirrors on the PCB is realized making use of a PC plate containing an array of microlenses well aligned to two 700 $\mu$m holes that match the pins of the MT ferrule. Index alignment is used for aligning the PCB and the PC plate. The alignment marks on the PCB are defined in the same processing step as for ablation of the mirrors, without removing the substrate from the ablation set-up, and using the same laser spot. The same principle is used for the marks on the PC plate, well aligned to the microlenses. Aligning the PC plate and the MT ferrule is achieved by two 700 $\mu$m laser ablated holes in the PC plate, that guide the pins of the MT ferrule [22]. The array of microlenses is written actively with respect to the fibers of the MT ferrule. The principle is demonstrated in Figure 6.5. An MT ferrule, coupled to a fiber ribbon, is mounted vertically on the ablation stage, making use of a special

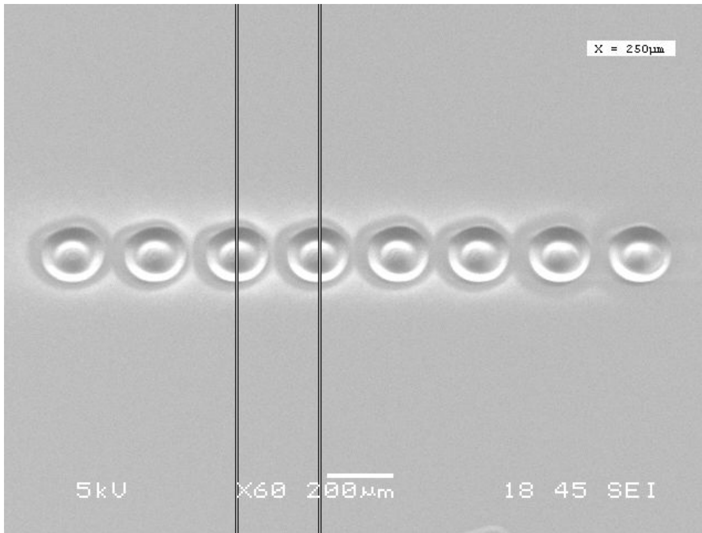


**Figure 6.6:** 1×8 microlens array defined in a PC plate

holder. The 250 $\mu$m thick PC plate is mounted on top of the ferrule. The 700 $\mu$m holes that match the pins of the ferrule were ablated using the excimer laser, prior to mounting the plate on the MT ferrule. The tapering of the holes, due to excimer laser ablation, will ease the insertion of the pins. When light is shined through the fibers, the laser ablation set-up is used to detect the light at the end facet of the fibers in the MT ferrule and through the PC plate that will serve as the substrate for the microlenses. This way, the microlenses are fabricated perfectly aligned with respect to the light spots, visually aligned under the microscope.

The microlenses are compatible with a 250 $\mu$m pitch of the optical channels. An array of maximum 1×6 lenses is written in one single step, using a 1×6 array of apertures instead of one single aperture for shaping the laser beam. The homogeneity of the laser fluence within the entire array area is the limiting factor for not extending to simultaneously writing 1×12 arrays of microlenses. Figure 6.6 shows the result for a 1×8 array, again the $CO_2$ laser is used for polishing. During ablation of the microlenses, reference marks written on the PC plate allow the alignment of the PCB and the PC plate.

The parameters for the ablation of two 700 $\mu$m holes on a distance of 4600 $\mu$m in a PC plate with a thickness of 500 $\mu$m are: laser pulse energy 14 mJ, circular aperture with a diameter of 800 $\mu$m, pulse repetition rate 100 Hz, translation speed 20 $\mu$m/s. For each hole, the laser beam describes three contours with a radius of 340 $\mu$m. An SEM image is shown in Figure 6.7. A 3D Coordinate Measurement Microscope (CCM) is used to measure the accuracy of the 700 $\mu$m holes. In

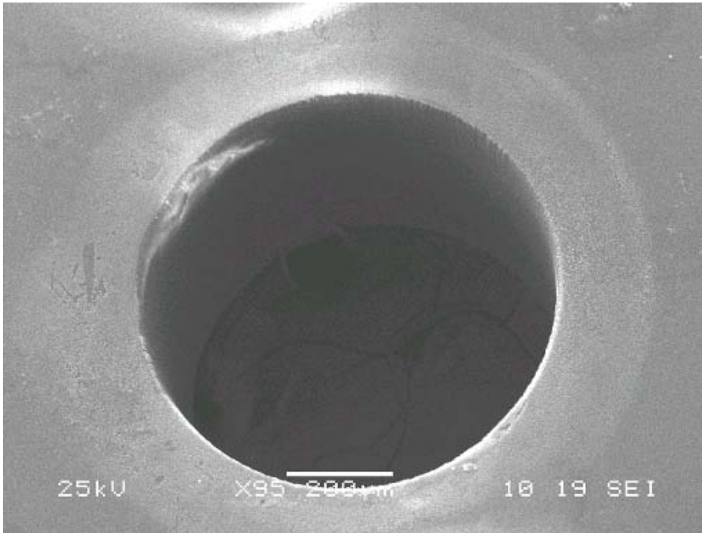


**Figure 6.7:** 700 $\mu$m hole matching the pins of the MT ferrule

general a 3D CMM allows to measure the XYZ coordinates of individual points in its entire machine coordinate system. With the help of vision software, this simple basic task can be forged into a powerful tool for measuring the exact XYZ coordinates of any feature on the surface of a sample: squares, circles, crosses, lines, planes... The average hole diameter was 700.1 $\mu$m with a standard deviation of 1 $\mu$m, based on 10 measured holes, average distance between the holes was 4599.2 $\mu$m with a standard deviation of 1.1 $\mu$m.

A mechanical stable connection is achieved by attaching the pins into the board. This is realized by mechanically drilling holes into the PCB. The alignment of these holes is not critical, as these holes have a diameter of 900 $\mu$m, the center of the holes is marked by the laser beam, after ablating the micromirrors. The alignment is achieved by the 700 $\mu$m holes in the PC plate, the mechanical stable attachment of the pins is achieved by the 900 $\mu$m holes in the PCB. The reason for drilling the 900 $\mu$m holes mechanically, is the thickness of the PCB stack. Laser drilling using the Nd-YAG laser in combination with the $CO_2$ laser is investigated, but introduces too much thermal damage. The use of a thinner PCB stack would allow laser drilling.

The PC plate and the optical PCB are aligned using the optical reference marks. In general, alignment with marks becomes more difficult as the processed surfaces of substrate and device including the precise marks face each other. Two main alignment principles can be used for this purpose, commercially available as flip-chip bonders:

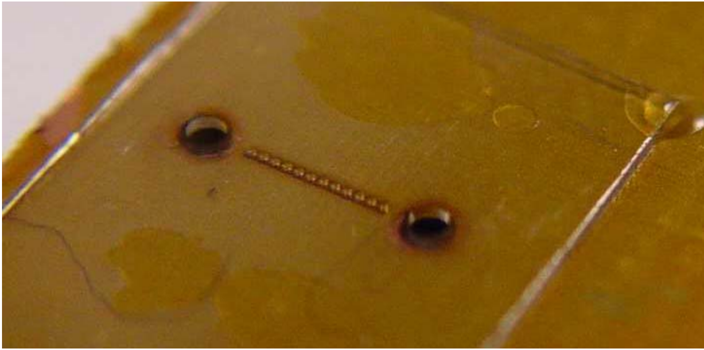

**Figure 6.8:** PC plate containing an array of 1×12 microlenses (250 $\mu$m pitch) and two 700 $\mu$m holes that match the pins of the MT ferrule

- The first type of flip-chip bonder uses infrared light in transmission, such light can be used to visualize metallic marks by light transmission trough substrate and device (Si, GaAs and InP related applications). Parallelism of substrate and device can be controlled with an autocollimator. Magnified images of substrate and device marks are used for rotational and lateral alignment. Before attachment, only a small movement is needed to close the gap between device and mounting board.

- The second type of flip-chip bonder, using double magnifying optics in between the components to align them, needs large high-precision translation stages. As both surfaces of device and board are made visible, no restrictions for substrate and device materials apply and standard optics and cameras for visible light are used.

The available flip-chip bonder is one of the second type, with an accuracy of $\pm 5\,\mu$m. After rotational (1 degree) and lateral (2 degrees) alignment, the PC plate is moved towards the PCB, and contact pressure can be controlled. The plate is fixed to the PCB using a UV curable adhesive which is dispensed before alignment and cured right after both parts are brought into contact. The mirrors used within the project Coupling from Opto-Boards were based on total internal reflection, as the process for embedding metal coated mirrors has been developed later on. This means that special attention is required not to fill up the angled via with UV curable glue. Different adhesives have been investigated for this purpose: OP21, OP61 (Dymax), Vitralit 7106, and NOA83H (Norland). Using the low viscosity adhesives OP21, and NOA83H it was difficult to prevent adhesive from flowing into the angled optical via. Using the low shrinkage adhesive OP61, optimum results are obtained. The PC plate mounted on the optical PCB can be seen in Figure 6.8.

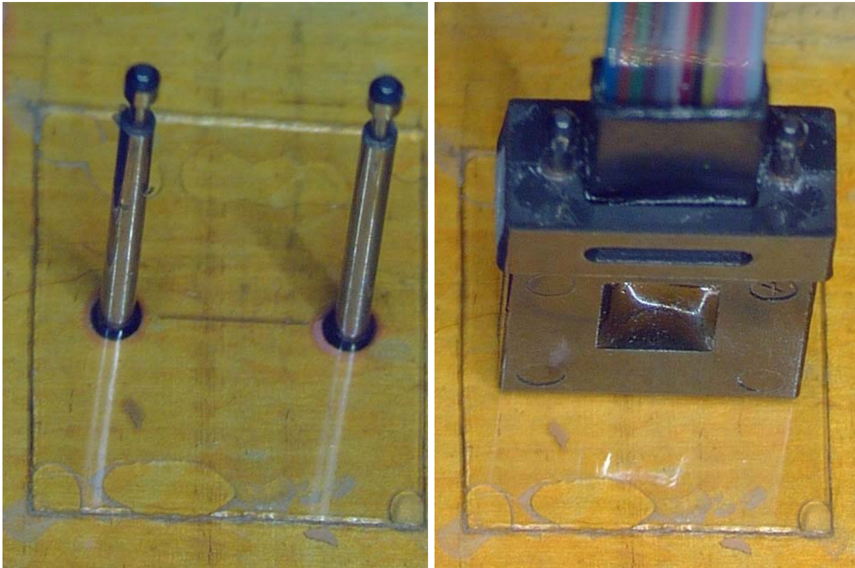

**Figure 6.9:** Mechanical alignment of the MT ferrule with respect to the lens plate

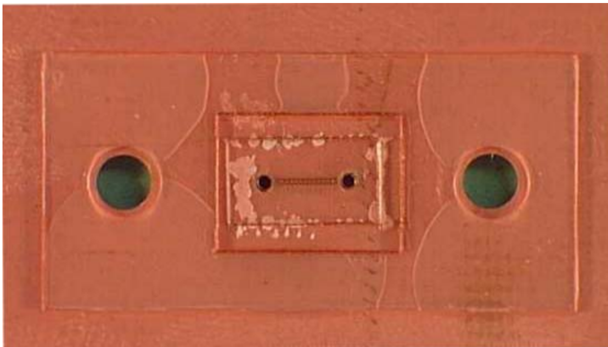

**Figure 6.10:** PC plate of 500 $\mu$m thickness surrounding the lens plate to reduce the stress on the optical layers

Once the alignment plate is fixed, the guiding pins are inserted, and glued at the back of the PCB, in the 900 $\mu$m holes. The MT ferrule is mounted during fixation of the pins, to ensure the perpendicularity of the pins with respect to the optical plane. Figure 6.9 shows the alignment pins attached into the optical PCB, aligning the MT ferrule.

The coupling concept must fulfill the demands for reproducible coupling con-

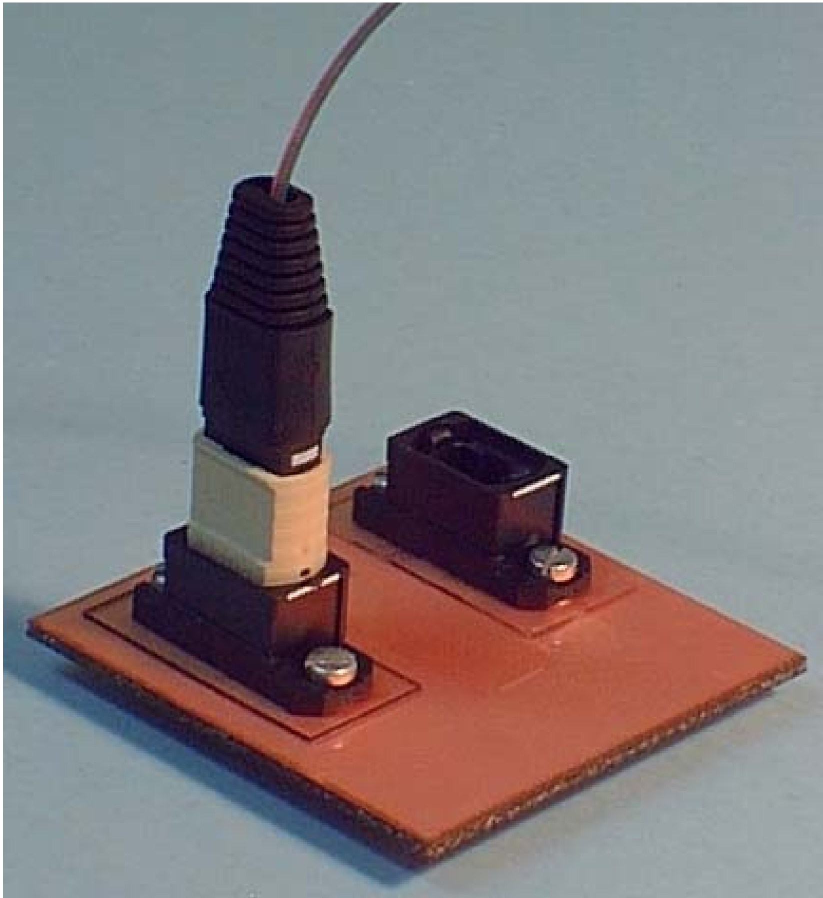

**Figure 6.11:** Proof-of-principle demonstrator board providing for board-to-board coupling

ditions while connecting the MT ferrule of the fiber ribbon, and avoid bringing physical stress into the optical layer. So it was decided to surround the 250 $\mu$m thick PC plate by a 500 $\mu$m thick PC plate, as a footprint of the MPO plug adaptor interface (Figure 6.10), reducing the stress in the optical layers. The large holes for the screws of the MPO plug adaptor interface are mechanically drilled, large enough to overcome alignment issues. In Figure 6.11, the final demonstrator board is shown, with plug-and-play possibilities. The loss introduced by the coupling interface has not been measured, but in what follows simulation results indicate what might be expected.

**Figure 6.12:** Ray-tracing simulation of the coupling interface

### 6.3.2 Misalignment tolerances

To estimate the coupling loss and the misalignment tolerances of the coupling structure, a ray-tracing simulation is carried out using the photonics design software ZEMAX. The simulation is based on coupling between a $50\times50\,\mu\text{m}^2$ Ormocer® waveguide and a $50\,\mu$m diameter detector making use of a TIR mirror (Figure 6.12). A microlens with a diameter of $100\,\mu$m and a radius of curvature of $150\,\mu$m is defined in a $250\,\mu$m thick PC plate. An indication of the tolerances is given in Figure 6.13 for the worst-case scenario where both misalignments in the X and Y direction are applied. The most critical alignment of the fiber array to the PC plate is determined by the accuracy of the $700\,\mu$m holes ($\pm\,1$–$2\,\mu$m), and the accuracy of the active alignment of the laser beam prior to lens writing ($\pm\,5\,\mu$m), as was shown in Figure 6.5. The alignment of the PC plate and the PCB is determined by the accuracy of the reference marks ($\pm\,5\,\mu$m), when defining the microlenses and micromirrors respectively, and by the accuracy of the flip-chip mounting procedure ($\pm\,5\,\mu$m). To estimate the loss introduced by the entire coupling scheme, based on the alignment accuracy of the individual steps, and based on the simulation results, it is assumed that the loss introduced by one coupling interface is below 2 dB. This has not been proven experimentally, as both the waveguide fabrication process, and the micromirror fabrication process, was not yet optimized at the time of establishing the coupling interface.

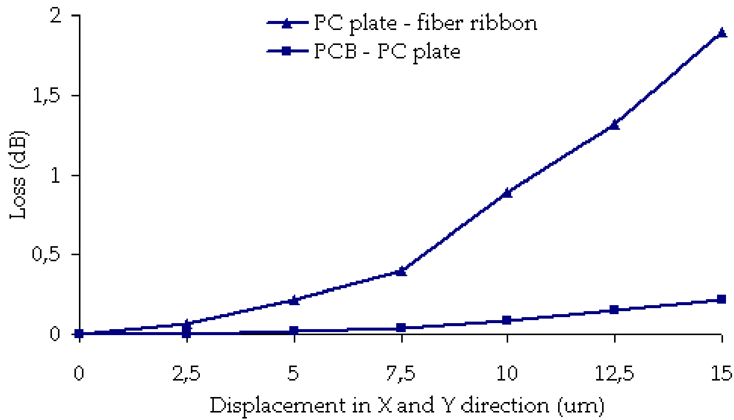


**Figure 6.13:** Simulated alignment tolerances of the coupling interface

## 6.4 Conclusions

KrF excimer laser ablation of microlenses has been described, both using PC and Ormocer® substrates, and using $CO_2$ laser assisted polishing. Coupling between optical waveguides located on different PCBs was shown to be feasible. The coupling approach was based on both passive and mechanical alignment making use of a 250 $\mu$m thick PC plate. The alignment between the optical PCB and the PC plate was achieved by index alignment, the alignment of the MT ferrule and the PC plate was achieved by the two 700 $\mu$m holes that match the pins of the MT ferrule. A misalignment tolerance study was performed estimating the loss introduced by the coupling scheme.

# References

[1] B. Lunitz, J. Guttmann, H.P. Huber, J. Moisel, and M. Rode. Experimental demonstration of 2.5 gbit/s transmission with 1 m polymer optical backplane. *Electronics Letters*, 37(17):1079–1079, Aug 16 2001.

[2] M. Franke and F.P. Schiefelbein. Optical interconnects on printed circuit board level - results based on the german funded project opticon. In *ECTC'04, Proceedings Electronic Components And Technology Conference*, pages 1542–1546, May 2004.

[3] A.L. Glebov, M.G. Lee, S. Aoki, D. Kudzuma, J. Roman, M. Peters, L. Huang, D.S. Zhou, and K. Yokouchi. Integrated waveguide microoptic elements for 3d routing in board-level optical interconnects. In *Photonics West'06, Proceedings SPIE 6126, Nanophotonic Packaging*, Jan 2006.

[4] Interconnect by Optics (IO). `http://io.intec.ugent.be`.

[5] H. Schroder. Waveguide and packaging technology for optical backplanes and hybrid electrical-optical circuit boards. In *Photonics West'06, Proceedings SPIE 6124, Optoelectronic Integrated Circuits*, Jan 2006.

[6] H. Ottevaere. *Refractive Microlenses and Micro-Optical Structures for Multi-Parameter Sensing: a Touch of Micro-Photonics*. PhD Thesis, Vrije Universiteit Brussel, Feb 2003.

[7] N.F. Borrelli, D.L. Morse, R.H. Bellman, and W.L. Morgan. Photolytic technique for producing microlenses in photosensitive glass. *Applied Optics*, 24(16):2520–2525, 1985.

[8] M. Oikawa, K. Iga, T. Sanada, N. Yamamoto, and K. Nishizawa. Array of distributed-index planar microlens prepared from ion-exchange technique. *Japanese Journal Of Applied Physics*, 20(4):L296–L298, 1981.

[9] M. Wakaki, Y. Komachi, and G. Kanai. Microlenses and microlens arrays formed on a glass plate by use of a $co_2$ laser. *Applied Optics*, 37(4):627–631, Feb 1 1998.

[10] M.T. Gale. *Micro-optics: elements, systems and applications, Chapter 6: Replication*. Ed. H.P. Herzig, Taylor and Francis, 1997.

[11] Z.D. Popovic, R.A. Sprague, and G.A. Neville Connell. Technique for monolithic fabrication of microlens arrays. *Applied Optics*, 27(7):1281–1284, 1988.

[12] T.R. Jay and M.B. Stern. Preshaping photoresist for refractive microlens fabrication. *Optical Engineering*, 33(11):3552–3555, Nov 1994.

[13] H. Ottevaere, B. Volckaerts, J. Lamprecht, J. Schwider, A. Hermanne, I. Veretennicoff, and H. Thienpont. 2d plastic microlens arrays by deep lithography with protons: fabrication and characterization. *Journal Of Optics A–Pure And Applied Optics*, 4(4):S22–S28, 2002.

[14] C. Ossmann, J. Gottert, M. Ilie, J. Mohr, and P. Ruther. Fabrication of pmma based microlenses using the liga process. In *Proceedings Microlens Arrays EOS Topical Meeting*, pages 54–58, 1997.

[15] C. Croutxé-Barghorn, O. Soppera, and D.J. Lougnot. Fabrication of refractive microlens arrays by visible irradiation of acrylic monomers: influence of photonic parameters. *European Physical Journal-Applied Physics*, 13(1):31–37, Jan 2001.

[16] D.L. MacFarlane, V. Narayan, W.R. Cox, and D.J. Chen, T. and. Hayes. Microjet fabrication of microlens arrays. *IEEE Photonics Technology Letters*, 6(9):1112–1114, Apr 1994.

[17] S. Mihailov and S. Lazare. Fabrication of refractive microlens arrays by excimer laser ablation of amorphous teflon. *Applied Optics*, 32(31):6211–6218, 1993.

[18] M.T. Gale. *Micro-optics: elements, systems and applications, Chapter 4: Direct writing of continuous relief micro-optics*. Ed. H.P. Herzig, Taylor and Francis, 1997.

[19] E.B. Kley, T. Possner, and R. Gring. Realization of micro-optics and integrated optic components by electron-beam lithographic surface profiling and ion exchange in glass. *International Journal Of Optoelectronics*, 8:513–527, 1993.

[20] K. Naessens. *Excimer Laser Ablation of Microstructures in Polymers for Photonic Applications*. PhD Thesis, Ghent University, Sep 2003.

[21] K. Naessens, H. Ottevaere, R. Baets, P. Van Daele, and H. Thienpont. Direct writing of microlenses in polycarbonate with excimer laser ablation. *Applied Optics*, 42(31):6349–6359, Nov 1 2003.

[22] A. Van Hove, K. Vandeputte, K. Naessens, B. Dhoedt, R. Baets, and P. Van Daele. Mt compatible red vcsel module for parallel optical interconnections. In *Photonics West'00, Proceedings SPIE 3952, Optoelectronic Interconnects, Photonics Packaging And Integration*, pages 134–143, Jan 2000.

# Chapter 7

# Fiber cleaving

*In this chapter a UV excimer laser based cleaving procedure for silica fiber is introduced, enabling automated cleaving for high volume production of fiber optic assemblies. Experimental results are discussed for single fiber, and for ribbon configurations. End angle is evaluated using a non-contact optical interferometer system, and insertion loss after splicing is given. The developed cleaving process is presented to enable termination of optical fibers embedded in a PCB. Finally, $CO_2$ laser polishing of fiber facets is shown to be feasible.*

## 7.1 Introduction

The work reported on laser cleaving of optical glass fibers has been developed within the IWT-project-LIAM (high-performance low-cost interconnection components for a new generation of access network products, manufactured using new micro-optical fabrication technologies), enabling automated cleaving for high volume production of fiber optic assemblies [1]. The laser cleaving procedure is investigated for the termination of optical glass fibers embedded in a PCB, within the European-project-Nemo, Network of Excellence on Micro-Optics, in the workpackage on Micro-Optics for PCB and MCM-level interconnects [2].

## 7.2 Termination of optical fibers

### 7.2.1 Using mechanical cleavers

A mechanical fiber cleave is typically accomplished by first putting the fiber under tension, and then using a mechanical blade that scores the fiber in order to

initiate the crack propagation. The stress pattern present in the fiber determines to a large extent the direction of this crack propagation and the surface morphology of the obtained cleave facet. At present, this mechanical cleave procedure is still intensively used in field situations but also in manufacturing environments, in spite of the fact that it exhibits some serious drawbacks. Mechanical cleaving parts are sensitive to wear over time and the operation of mechanical cleavers primarily relies on precision moving parts, including a sharp cutting blade. Sharp blades in particular are prone to physical damage like e.g. chipping and to misalignment which requires re-adjustment over time. As a result, mechanical cleaving procedures, in their current form, are hardly considered for automation. They turn out to be processes where operator skills and experience are critical factors for success of the final product. However, cleave quality is critical for ensuring low reflectance terminations and enabling optimum performance fiber optic components and systems. Poor cleaves can cause cracks and scratches at the end of the fiber, which adversely affects the optical performance. Cracks and scratches can sometimes be corrected by polishing, but polishing is time consuming and generally increases the cost of the product. Furthermore, in the case of ferrule configurations, cracks caused by a poor cleave can sometimes extend below the surface of the ferrule.

### 7.2.2 Using $CO_2$ lasers

Initially, $CO_2$ laser cutting was explored to cut excess optical fiber that protruded from a ferrule, prior to mechanical polishing. Soon it became apparent that laser based methods, as an alternative to mechanical procedures, might have the potential to provide unprecedented accuracy and versatility for terminating and shaping fiber ends in a manufacturing environment. In contrast to mechanical methods, cutting under an angle of $45^o$ was shown to be feasible, opening up possibilities for VCSEL coupling to fibers and waveguides [3]. In addition to cutting, $CO_2$ laser stripping was found to be more attractive than mechanical and chemical/thermo-chemical or acid strip procedures. The advantage of laser assisted non-contact strip methods lies in the fact that precise ends or windows can be stripped without altering the tensile strength properties of the stripped fibers. Finally, low power density continuous wave $CO_2$ laser light exposure to optical fiber ends was found to result in a decrease of the surface roughness by more than one order of magnitude [4].

The mechanism is absorptive, with strong thermal heating, so when $CO_2$ lasers are used in a cutting arrangement where the focused beam is translated across the fiber in order to realize a progressive cut of the glass, unwanted thermal conduction and diffusion effects can come into play. Ultimately, this can lead to fiber end flare, uncontrolled core diffusion and a curved fiber facet. Improved cut results were reported when using an asymmetric beam profile of the 9.4–9.8 $\mu$m lines in-

stead of the generally used 10.6 $\mu$m line, paying attention that the heat affected zone is fairly reduced [5].

### 7.2.3 Using UV lasers

Despite of the fact that silica glass is still fairly transparent for the UV excimer wavelengths, when used in a short pulse regime, ablation phenomena preferentially can take place [6]. This can be exploited to selective removal of the silica material in order to induce a scratch or cleave. Due to the typical interaction of UV excimer laser light with silica glass, thermal effects resulting in local melting of the fiber do hardly occur as is the case with $CO_2$ lasers. A selective ablation of the glass in the form of a small rectangular cavity can serve as a fracture initiator when the fiber is put under stress. The position of the UV excimer laser induced scratch can be more precisely than with a classic diamond tool.

## 7.3 Excimer laser ablation of glass fiber

In general for photon energies exceeding a materials bandgap, absorption becomes stronger as wavelengths become shorter. Thus nanosecond pulses from ArF (at 193 nm) and KrF (at 248 nm) excimer lasers are commonly used for micromachining a wide range of materials having bandgap energies $\leq 6.4$ eV. However materials that have higher bandgap energies (e.g. silica) have remained notoriously difficult to micromachine with high resolution using ArF or KrF lasers. The bandgap of $SiO_2$ is 9.1 eV, requiring a photon wavelength of 136 nm. However, some very moderate absorption peaks can be detected between 4 and 7 eV due to contamination and defects or impurities, allowing ablation with nanosecond excimer pulses, see also Section 3.3.

It is however observed that the circular geometry of the fiber acts as a lens for the laser beam and focuses the incident light somewhere underneath the fiber. As a result, the laser spot size is highly concentrated on the lower fiber surface and the threshold ablation intensity of the fiber is reached, for a relatively low fluence of the incident laser beam. This initiates the ablation of a small cavity with rectangular shape. In order to study this phenomenon in more detail, it has been simulated for a standard 125 $\mu$m glass fiber, assuming that the incident laser rays are parallel, and that the laser fluence is homogeneous over the entire beam area. The laser rays are traveling perpendicular to the fiber axis. An end view of the fiber shows the refraction of the laser light (Figure 7.1). The size of the ablated cavity at the bottom of the fiber is 19 $\mu$m for 248 nm laser light. This is proven experimentally, but the size of the cavity using a KrF laser was highly dependent on the ablation parameters (fluence, number of laser pulses). In [7] the intensity profile at the bottom of the glass fiber is calculated for KrF laser

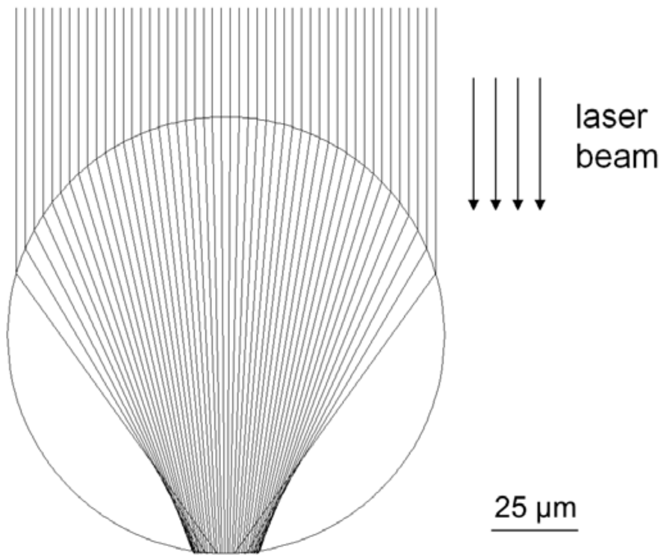


**Figure 7.1:** Refraction of the laser light in the glass fiber due to the circular geometry of the fiber that acts as a lens

light, it is found that the positions that receive the highest laser intensity are not at the center but at the two ends of the narrow focused region. This has been experimentally observed and will be discussed below.

## 7.4 Design of the fiber holder

Current art in mechanical cleaving is focused on the combination of two principal ways of cleaving an optical fiber: the score-and-bend technique and the tension-and-score technique. In the score-and-bend approach, a flaw is created in the optical fiber using a sharp blade (diamond or tungsten carbide). The fiber is then stressed in the area of this flaw, by bending, such that the tension created by the bend serves to open up the crack, propagating across the fiber, so cleaving it. In the tension-and-score approach the optical fiber is clamped at two points and tensioned with a force of around 200 grams. The tensioned fiber is then nicked with a sharp edge and resultant crack propagates automatically due to the already applied tension in the fiber. This method produces cleaved ends that are typically flatter than the score-and-bend method, with less cracking in the region of the blade strike. However, this method does not readily lend itself to cleave multiple fibers at one time. For that reason the score-and-bend technique is chosen, with the possibility to introduce pure tension (Figure 7.2), which might be necessary

**Figure 7.2:** Schematic cross-section of the fiber holder, the fiber is stretched over an anvil in order to generate stress that opens up the crack

to produce an angled cleaved facet.

The stress introduced by stretching the fiber over an anvil is tensile on the outside bend of the fiber and zero on the inside bend of the fiber. This is not the same as simply bending the fiber: pure bending would give compression on the inside of the bend, with a neutral axis half way across the fiber. In stretching the fiber over an anvil, compression on the inside of the bend is countered by the tension generated by the lengthening of the fiber, required to stretch it over the anvil. When the crack is initiated at the outside of the bend, the tension is high, so the necessary initiation scratch is small, but as the cleave progresses, the tension decreases, preventing the cleave from traveling too fast and produce hackle. The crack will travel perpendicularly across the fiber because it always experiences positive tension.

The fibers are clamped into a single fiber holder of Newport with V-grooves (Figure 7.3). This has the effect of providing secure clamping of the fiber and decreases the possibility that the fiber will rotate during clamping, which would introduce torsion into the cleaved fiber. The fiber holder is slightly adapted to cleave multiple fibers. Using laser ablation we fabricated an array of U-grooves in PMMA to clamp the array of fibers. This is discussed below. Using an XYZ translation stage, the anvil can be translated with very high accuracy. The height of the anvil is varied in order to optimize the cleaved facet. All experiments are done using non-dispersion shifted glass fiber (ITU-T G.652). The fiber coating is removed prior to laser cleaving by a mechanical method and the fiber is cleaned using isopropyl alcohol.

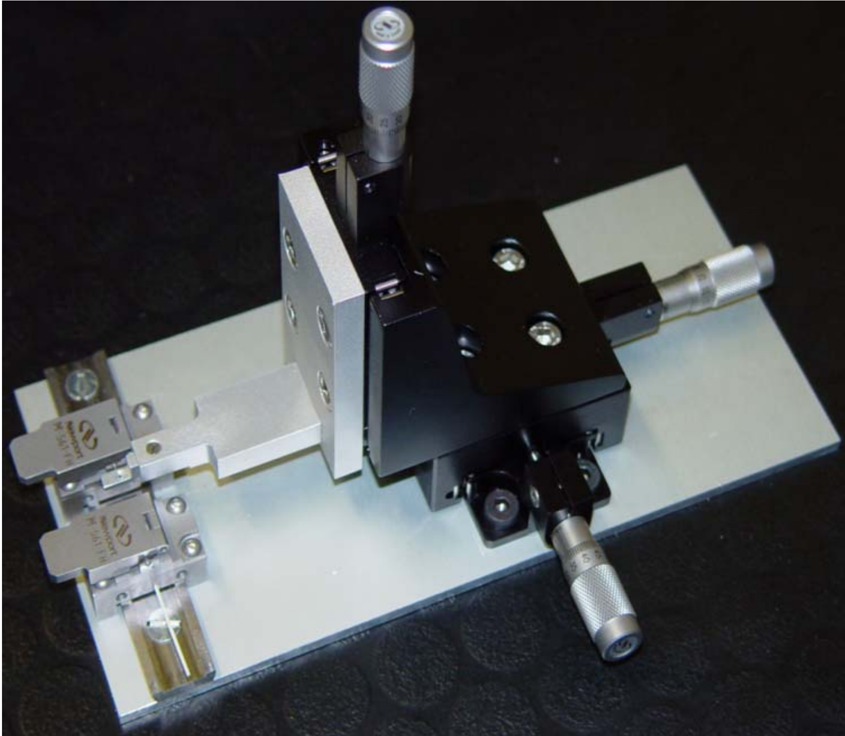

**Figure 7.3:** Picture of the fiber holder which is placed on the translation table of the laser ablation set-up

# 7.5 Experimental results

## 7.5.1 Single fiber

Despite of the fact that silica glass is still fairly transparent for the KrF excimer laser wavelength, when used in a short pulse regime (3–7 ns), ablation phenomena preferentially can take place in order to induce a scratch or cleave. Best results are obtained by applying only a single shot to cleave the fiber. For that reason the laser fluence must be high enough to reach the ablation threshold at the bottom of the fiber, $7\,\mathrm{J/cm^2}$ to allow single shot cleavages (corresponding to a pulse energy of 17 mJ). The mask that is used for shaping the laser beam must not be too small: the projection lens with a demagnification of 10, projects the mask with a width of $200\,\mu$m to a scratch of $20\,\mu$m. A smaller mask does not allow single shot cleavages. In the direction perpendicular to the fiber axis, the laser beam covers the full width of the fiber, but as discussed in a previous section, the circular ge-

| | |
|---|---|
| Laser fluence (J/cm$^2$) | $7 \pm 0.5$ |
| Number of pulses | 1 |
| Laser spot size ($\mu$m$^2$) | $20 \times 125$ |
| Anvil travel ($\mu$m) | 200 |

**Table 7.1:** Parameters for a KrF excimer laser induced scratch

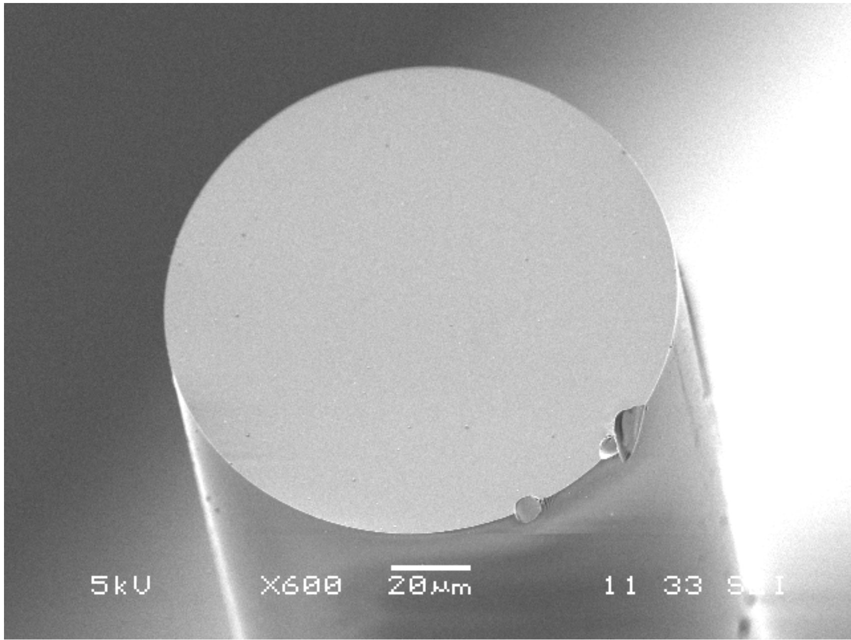


**Figure 7.4:** SEM image of an end facet of a laser cleaved glass fiber

ometry of the fiber acts as a lens for the laser beam in that direction. Using the score-and-bend technique the anvil is stretched over the fiber after the ablation of the score. A travel of 200 $\mu$m of the anvil is sufficient to cleave the fiber. Typical parameters are listed in Table 7.1.

As can be seen in Figure 7.4, the scratch at the bottom of the fiber is divided into two parts. This is the effect that is described in the previous section: the highest energy intensities are not located in the center, but at the two ends of the narrow focused region. By using only one pulse, the ablation threshold is only reached there, thus minimizing the size of the scratch. The quality of the fiber end facet, as seen under the SEM, is comparable to that obtained with mechanical cleaved fibers.

Another approach that has been investigated is the bend-and-score approach.

The fiber is tensioned by stretching the anvil over the fiber and then nicked with the laser. Resultant crack propagates automatically due to the already applied tension in the fiber. The results obtained by using this method are worse compared to the score-and-bend method. The reason could be that the laser pulse is not yet finished in time when the crack already starts to propagate, resulting in a lip that breaks off at the top of the fiber.

### 7.5.2 Fiber ribbon

The above described approach is not limited to single fibers: exactly the same principle can be used to cleave arrays of fibers. The coating of the fiber ribbon is removed by a thermo-mechanical method. Note that it is possible to strip fiber ribbons using UV laser ablation [8, 9], but this was not used in this work. The fiber holder is slightly adapted to cleave multiple fibers. Using laser ablation we fabricated an array of U-grooves in PMMA to clamp the array of fibers. This PMMA plate containing the U-grooves is mounted on the fiber holder set-up (Figure 7.3).

In Figure 7.5 an SEM image is shown of a laser cleaved fiber ribbon. The same score-and-bend method as used for single fibers is used for fiber arrays. In a first step the scratches are applied on the individual fibers, this can be done very fast by the motorized ablation stage. In a second phase the anvil is stretched over the array of fibers and the fibers are all cleaved at the same time. An important defect that is introduced during fiber ribbon cleaving is lip/roll-off, not present during single fiber cleaving, and most probably caused by stress present in the individual fibers of the array. The mechanical set-up was modified in a number of ways such as different clamping of the fibers, different coating of the fiber clamps, modification of the anvil and the introduction of tensile stress to the fibers. None of these modifications seemed to improve the results significantly, and thus eliminating lip/roll-off.

## 7.6 Characterization

The end angle of the cleaved optical fiber is measured using a non-contact optical interferometer system (DORC). This measuring set-up is designed to measure submicron variations in the surface contours of fiber optic connectors. In order to measure fiber cleave facets, prior to measurement, the fibers are inserted into a bare fiber adapter AQ-9302 from ANDO. This configuration can be inserted into the connector mount of the non-contact interferometric system. The latter operates in the red light mode ($\lambda = 660\,\text{nm}$) exploiting phase shift interferometry to map the surface of the cleaved facet. The cleave angle is calculated by finding the best fit plane inside the region, where the interference fringes are apparent. The shape and distribution of the fringes also provide valuable data on the topogra-

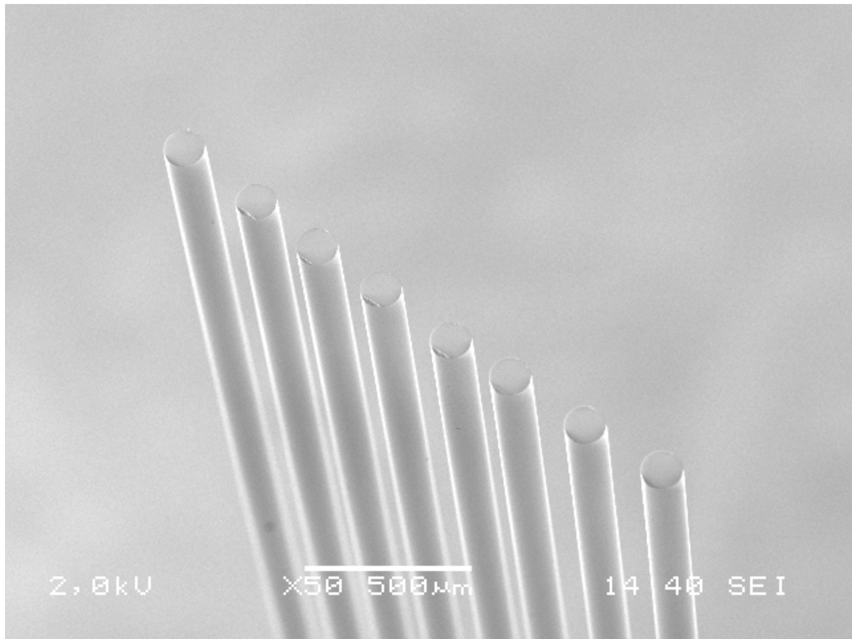


**Figure 7.5:** SEM image of a 1×8 array of laser cleaved glass fibers

phy of the fiber end facet.

Figure 7.6 represents a statistical distribution of the surface profile of laser cleaved facets. In order to be able to understand these figures, an overview of all possible defects on the fiber end face facets is given, with the description whether the defect is visible on the measured samples. Figure 7.7 [10] represents three specific defects with the typical interference fringes. Note that these pictures indicate severe defects, which did not show up in the measurements in such a way.

- Indent (Figure 7.7a): The intentionally introduced flaw in the fiber from which the controlled fracture propagates. An effective indent must have smooth, definable borders and a minimal depth. For that reason the scratch is ablated using only one single laser pulse, reducing the size of the indent. The defect is visible for laser cleaved fibers (Figure 7.6).

- Lip/Roll-off (Figure 7.7b): A sharp protrusion from the edge of the cleaved fiber, excessive lip height is conducive to fiber damage. The opposite condition of lipping, excessive roll-off can cause high insertion or splice losses. This defect appeared using the bend-and-score approach, but is eliminated using the score-and-bend method. For fiber ribbon cleaving the defect is minimized, but not completely eliminated.

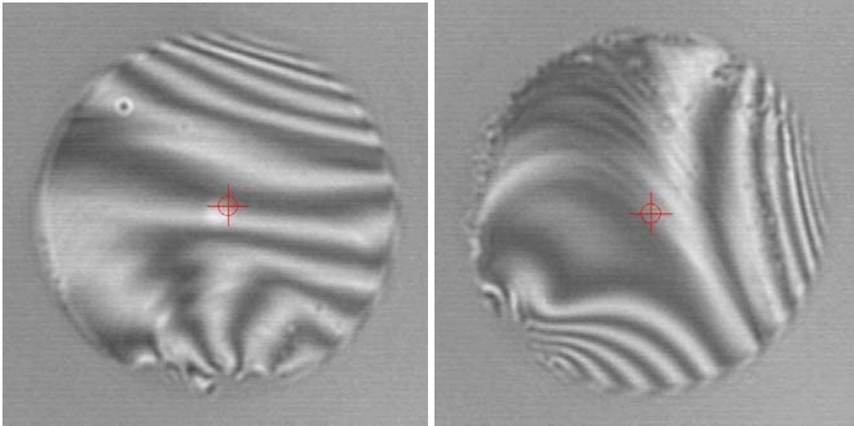

(a) x-tilt = 0.042$^o$, y-tilt = 0.789$^o$, $R_a$ = 178 nm, RMS = 236 nm

(b) x-tilt = 0.486$^o$, y-tilt = 0.269$^o$, $R_a$ = 203 nm, RMS = 271 nm

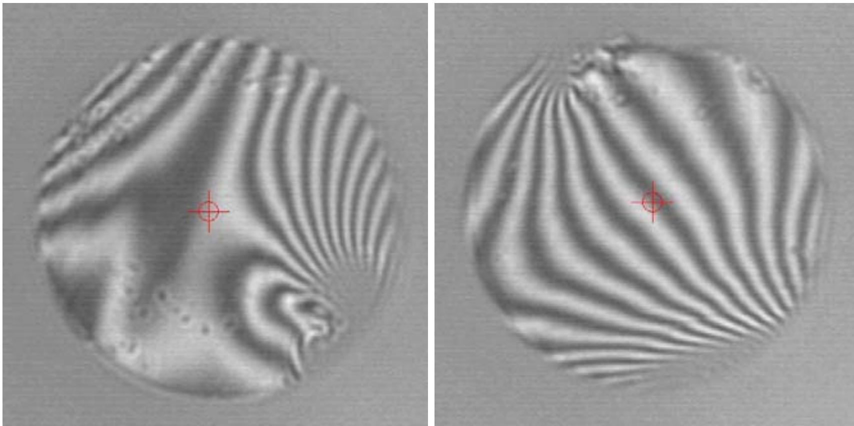

(c) x-tilt = 0.833$^o$, y-tilt = 0.071$^o$, $R_a$ = 344 nm, RMS = 468 nm

(d) x-tilt = 1.257$^o$, y-tilt = 0.788$^o$, $R_a$ = 186 nm, RMS = 261 nm

**Figure 7.6:** Statistical distribution of the surface profile of laser cleaved fibers

- Hackle/Mist (Figure 7.7c): Forms of surface irregularities occurring during the fracture. Hackle is severe surface aberration, very detrimental to light transmission, while mist is a less severe manifestation. Defect not visible in a severe way.

- Spiral/Step: An abrupt change in the topology of the fiber end face surface. The impact on connectors and mechanical splices is application dependent. Defect did not show up.

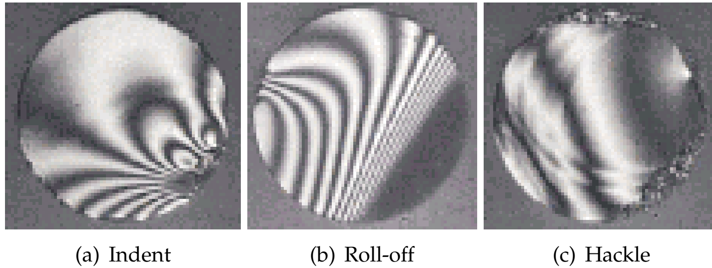

(a) Indent (b) Roll-off (c) Hackle

**Figure 7.7:** Typical interference fringes of some defects (source: Arden Photonics [10])

| | Average | Standard deviation |
|---|---|---|
| Mechanical cleave Fitel | 0.69 | 0.40 |
| Mechanical cleave Sumitomo | 1.01 | 0.61 |
| Laser cleave | 1.06 | 0.47 |

**Table 7.2:** Angle deviation for perpendicular cleaved fibers

- Shattered: The result of an uncontrolled fracture or breakage does not have a definable cleave or surface characteristics. The reproducibility of the laser cleaving is very good; the fracture is always controlled, so this defect did not show up.
- Concave/Convex: Characterized by curving interferometric patterns, indicating gradual changes in the surface height. Minor curvatures have little impact on most applications. Defect not visible using the laser cleaving approach.

The end angle of the cleaved optical fiber can be derived from the number of fringes, and is compared in Table 7.2 for laser cleaved and mechanical cleaved fibers, all for perpendicular cleavages. Average and standard deviation are based on 8 measured samples. The laser cleaved fibers had an average angle deviation of $1.06^o$ and a standard deviation of $0.47^o$. This can be compared to an average of $1.01^o$ or $0.69^o$ (depending on the manufacturer of the mechanical cleaver) and a standard deviation of $0.61^o$ or $0.40^o$ for mechanical cleaved fibers. In general, an end angle less than two degrees yield acceptable fusion splices. Measurements have proven that insertion loss is in the range of 0.03 dB, which is compatible with mechanical cleaved fibers.

The modification of the mechanical set-up for angled cleaving of fibers was studied. A number of tests were carried out to obtain such angled facets by varying the distance between the anvil and the point were the scratch was introduced. The cleaved facets were measured with the DORC set-up in order to obtain more information on the distribution of the angles. These measurements showed all

fibers having angled surfaces but most of the angles were less than 3–4$^o$, instead of 8$^o$. The fibers also showed important defects such as lip/roll-off. Further modification of the set-up such as the introduction of tensile stress to the fiber was studied but it is clear that a more refined mechanical set-up will be needed to obtain better and reproducible results.

## 7.7 Termination of PCB embedded optical fibers

As an alternative to planar waveguides integrated on an electrical PCB, standard multimode glass fibers can be embedded into the layer stack of a multilayer PCB, an approach proposed by FZK [11]. The fibers are embedded between top and bottom layers of the stack, openings are milled to get access to the end facets of the optical fibers. Along the path of the fiber copper pads are placed on the top and bottom layers to guide the fiber and ensure the proper distance between the layers during the lamination process. Electrical tracks, vias, throughplatings, and solder stop can be fabricated subsequently. Fiber cleaving is done at the very end, to be sure not to damage the cleaved facets. Figure 7.8 shows a prototype board fabricated by FZK, the openings are quite large ($4\times5\,\text{mm}^2$) to allow the use of the developed cleaving procedure. The coupling element being developed by FZK, allows for a passive alignment. The alignment structure consists of a V-groove for the fiber alignment, and an additional security clip, which holds the fiber in place. The part is fabricated with deep X-ray lithography [12], and allows for high volume production using inexpensive injection molding or hot embossing.

## 7.8 $CO_2$ laser polishing and splicing of fibers

Mechanically cleaved fibers are investigated for $CO_2$ laser polishing. Therefore the fibers are attached on the edge of the translation table of the laser set-up and positioned in the path of the $CO_2$ laser beam. Laser polishing was carried out while varying imaging lens (L1, L2, L3), attenuation (scale 90, 60, 30) and number of pulses. After visually inspecting the fiber facets using a stereo-zoom microscope, the fiber ends that were noticeably damaged were rejected (the ones using the higher demagnification lenses L1, and L2), the others (using L3) were prepared for evaluation by DORC measurement, see Figure 7.9 for an example. These measurements proved the $CO_2$ laser to have a smoothing effect on the surface of the fiber facet compared to non-polished fiber facets, reducing the average surface roughness $R_a$ from 50 nm to 27 nm within a range of 60 $\mu$m from the center of the fiber. An overview of the tests using L3 is given in Table 7.3, for varying attenuation and number of laser pulses. An overall optimum parameter combination was not found. Reason for this might be the pulse-to-pulse $CO_2$ laser energy variations.

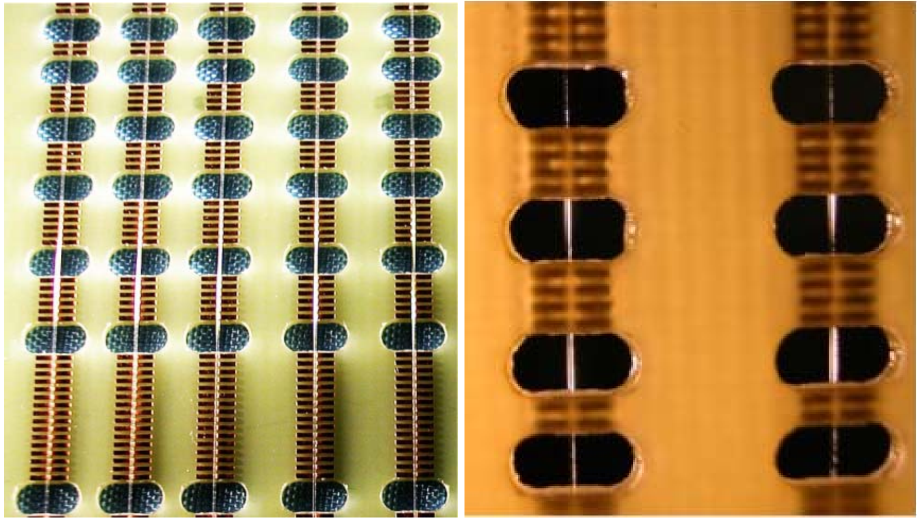

**Figure 7.8:** Optical glass fibers embedded in a PCB (source: FZK [11])

| | | sample 1 | | sample 2 | |
|---|---|---|---|---|---|
| **attenuation** | **pulses** | **$R_a$ (nm)** | **RMS (nm)** | **$R_a$ (nm)** | **RMS (nm)** |
| 90 | 4 | 24 | 31 | 33 | 44 |
| 90 | 5 | 29 | 37 | 18 | 23 |
| 90 | 6 | 10 | 13 | 51 | 68 |
| 60 | 3 | 46 | 60 | 48 | 59 |
| 60 | 4 | 23 | 29 | 16 | 21 |
| 60 | 5 | 12 | 15 | 23 | 30 |
| 30 | 1 | 22 | 28 | 14 | 19 |
| 30 | 2 | 28 | 34 | 31 | 39 |
| 30 | 3 | 54 | 71 | 10 | 13 |

**Table 7.3:** Surface roughness of $CO_2$ laser polished fiber facets

For the feasibility testing of laser assisted splicing of fibers, two mechanically cleaved fiber ends were clamped using the same set-up as for laser cleaving. The two fiber ends were brought into contact and positioned under the $CO_2$ laser beam. When subject to low energy no fusion of the fiber ends was noticed. When increasing the laser beam energy fusion did occur but at the same time the higher energy, apparently ablating the fiber, caused noticeable damage to the fiber side facing the laser beam. It was not possible to control the energy level in such a way

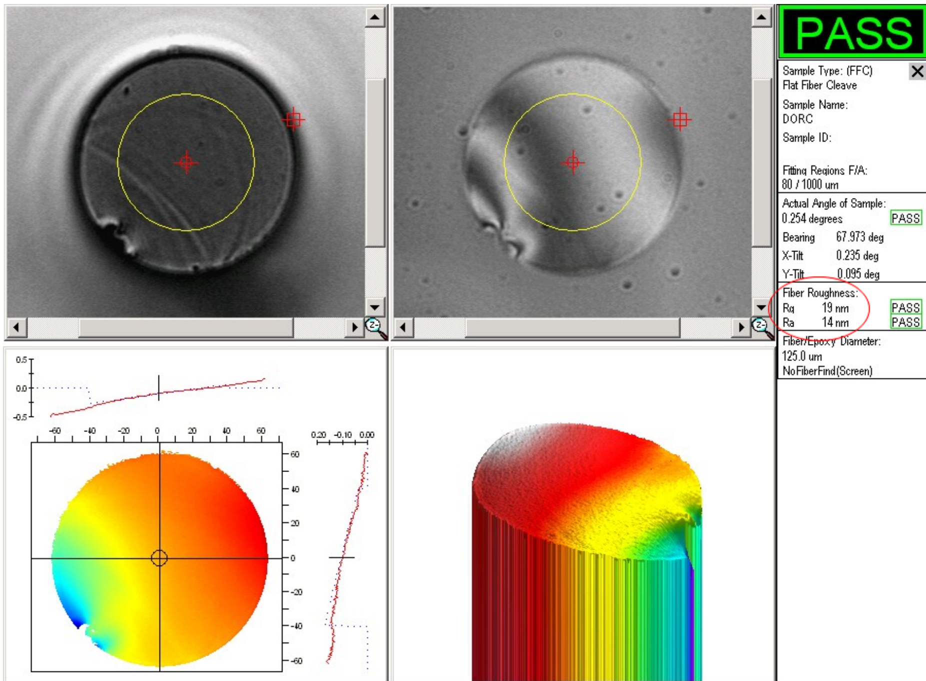


**Figure 7.9:** Surface profile of a $CO_2$ laser polished fiber endfacet

that there was sufficient energy to induce fusion splicing without having ablation and thus causing damage to the fiber.

## 7.9 Conclusions

In this chapter, a UV excimer laser based cleaving procedure for silica fiber has been developed that enables automated cleaving for high volume production of fiber optic assemblies. Due to the typical interaction of UV excimer laser light with silica glass, thermal effects resulting in local melting of the fiber do hardly occur, as is the case with $CO_2$ lasers. A selective ablation of the glass in the form of a small rectangular cavity can serve as a fracture initiator when the fiber is placed under stress. The position of the laser induced scratch can be more precise than with a classic diamond tool used in mechanical cleavers. The system is operator independent and provides consistent high-quality cleaves on single fiber, further investigation is required to minimize lip/roll-off for ribbon configurations. The end angle of the cleaved optical fiber is measured using a non-contact optical interferometer system and had an average of $1.06^o$ and a standard deviation of

$0.47^o$ for perpendicular cleavages. Insertion loss after splicing is in the range of 0.03 dB, which is compatible with mechanical cleaved fibers. The developed cleaving process is presented to enable termination of optical fibers embedded in a PCB, for which currently no cleaving process exists. Finally, $CO_2$ laser polishing of fiber facets is shown to be feasible, reducing the average surface roughness $R_a$ from 50 nm to 27 nm within a range of 60 $\mu$m from the center of the fiber.

# References


[1] G. Van Steenberge, P. Geerinck, S. Van Put, J. Watte, H. Ottevaere, H. Thienpont, and P. Van Daele. Laser cleaving of glass fibers and glass fiber arrays. *Journal Of Lightwave Technology*, 23(2):609–614, Feb 2005.

[2] Network of Excellence on Micro-Optics (Nemo). `http://www.micro-optics.org`.

[3] H. Karstensen, J. Wieland, R. Dal'Ara, and M. Blaser. Parallel optical link for multichannel interconnections at gigabit rate. *Optical Engineering*, 37(12):3119–3123, Dec 1998.

[4] M. Udrea, H. Orun, and A. Alacakir. Laser polishing of optical fiber end surface. *Optical Engineering*, 40(9):2026–2030, Sep 2001.

[5] Patent US2004/0047587. `http://www.espacenet.com`.

[6] J. Greuters and N.H. Rizvi. Laser micromachining of optical materials with a 157-nm fluorine laser. In *Photonics Fabrication Europe'02, Proceedings SPIE 4941, Laser Micromachining For Optoelectronic Device Fabrication*, pages 77–83, Oct 2002.

[7] T.M. Yue, S.M. Mei, and K.C. Chan. Excimer laser ablation of glass fiber in reinforced polymer. *Materials Manufacturing Processes*, 17(3):783–788, Jun 2002.

[8] G. Ogura. Laser stripping of optical fibers opens up new applications. *Laser Focus World*, pages 169–176, Jun 2001.

[9] Resonetics. `http://www.resonetics.com/`.

[10] Arden Photonics. `http://www.ardenphotonics.com/products/vf20_gallery.htm`.

[11] M. Schneider and T. Kuhner. Optical interconnects on printed circuit boards using embedded optical fibers. In *Photonics Europe'06, Proceedings SPIE 6185,*

*Micro-Optics, VCSELs, And Photonic Interconnects: Fabrication, Packaging, And Integration*, Apr 2006.

[12] J. Mohr. Liga - a technology for fabricating microstructures and microsystems. *Sensors And Materials*, 10(6):363–373, Jun 1998.

# Chapter 8

# Conclusions and outlook

## 8.1 Main achievements

The main objective of this PhD work was the development of a flexible technology for the fabrication of low cost board-level optical interconnections, based on the use of optical waveguides.

The use of KrF excimer laser-, frequency tripled Nd-YAG laser-, and $CO_2$ laser ablation was investigated for structuring optical waveguiding layers integrated on a printed circuit board. Both polysiloxanes (Ormocer®), acrylates (Truemode$^{TM}$), and thin glass sheets were selected because of their low optical losses, environmental stability, and compatibility with standard electrical board manufacturing.

Arrays of $50\times50\,\mu m^2$ multimode waveguides on a pitch of $125\,\mu m$ were integrated on $10\times10\,cm^2$ PCBs. KrF excimer laser ablation parameters were optimized towards minimum surface roughness, and minimum propagation loss. Making use of Truemode$^{TM}$ materials, waveguide sidewall roughnesses $< 20$ nm were attained, and propagation losses $< 0.11$dB/cm at 850 nm were achieved. Photolithographic defined waveguides were realized making use of Ormocer® materials. Propagation loss $< 0.08$ dB/cm at 850 nm, and $< 0.22$ dB/cm at 980 nm was obtained. Proof-of-principle was shown for the integration of single mode waveguides on FR4 based PCBs, propagation loss $< 0.62$ dB/cm was measured at $1.3\,\mu m$. It was proved that frequency tripled Nd-YAG lasers offer a lot of potential for structuring single mode waveguides with smooth surfaces.

A process for embedding metal coated $45^o$ micromirrors in the optical layer was developed. Mirrors are selectively metallized using a lift-off process. It was shown that filling up the angled via without the presence of air bubbles and providing a flat surface above the mirror is only possible by enhancing the Ormocer® cladding deposition process with ultrasound agitation. Mirror sur-

face roughness $< 42$ nm, and angle accuracy $< 2^o$ was attained. An excess mirror loss of $< 2.2$ dB was achieved, depending on the coupling fibers being used.

It was shown that $CO_2$ laser ablation can be used to access optical waveguiding layers embedded in the FR4. The fabrication of optical vias that allow the introduction of an insert with in-plane or out-of-plane coupling optical functionality, was successfully demonstrated.

A novel board-to-board coupling interface was established, making use of a 250 $\mu$m thick lens plate, and based on both passive and mechanical alignment. Both optical alignment marks, and mechanical alignment holes were defined by KrF excimer laser ablation. An existing process for writing microlenses was adapted to Ormocer® materials, smoothing of the lenses was achieved by using $CO_2$ laser assisted polishing. A misalignment tolerance study estimating the loss of the coupling configuration, proved the validity of the approach.

An excimer laser based cleaving procedure for glass fiber was developed, enabling automated cleaving for high volume production of fiber optic assemblies. An end angle average of $1.06^o$ and a standard deviation of $0.47^o$ was achieved for perpendicular cleavages. Insertion loss after splicing was in the range of 0.03 dB, compatible with mechanical cleaved fibers. The developed cleaving process was presented to enable termination of optical fibers embedded in a PCB, for which currently no cleaving process exists. Finally, $CO_2$ laser polishing of fiber facets was shown to be feasible, with a reduction of the average surface roughness from 50 nm to 27 nm.

## 8.2 Future work

The work described in this PhD thesis can be considered as generic and widely applicable. Most of the developed technology steps can be transferred to other interesting optical materials that would become available in the near future.

Extention of the work to 2.5D optical waveguiding structures would drastically increase the interconnection density and routing possibilities, fully exploiting the 2D character of opto-electronic components. Transition to single mode waveguides is very challenging. The very tight alignment tolerances will make the coupling approach more complicated, a first impulse is given within this work. Both multilayer structures, and single mode interconnecions are investigated within the ongoing PhD work of Nina Hendrickx, Ghent University.

The use of flexible instead of rigid substrates offers a lot of new applications, e.g. optical sensing based on waveguide type distributed sensors. Embedding thin optoelectronic chips in the optical layer for the realization of ultra-compact packages, can find a basis in this work. Flexible substrates combined with embedded optoelectronic chips are investigated within the ongoing PhD work of Erwin Bosman, Ghent University.